THE NATURE AND EVOLUTION OF GALAXIES SELECTED VIA GAS CROSS SECTION

by

Daniel Brant Nestor

B. S. in Physics, Massachusetts Institute of Technology, 1996

Submitted to the Graduate Faculty of

the Department of Physics and Astronomy in partial fulfillment

of the requirements for the degree of

Doctor of Philosophy

University of Pittsburgh

2004

UNIVERSITY OF PITTSBURGH

DEPARTMENT OF PHYSICS AND ASTRONOMY

This dissertation was presented

by

Daniel Brant Nestor

It was defended on

August 25, 2004

and approved by

David A. Turnshek, Professor

Allen I. Janis, Professor Emeritus

D. John Hillier, Associate Professor

Andrew J. Connolly, Assistant Professor

Sandhya M. Rao, Research Assistant Professor

Richard Griffiths, Professor, Carnegie Mellon University

Dissertation Director: David A. Turnshek, Professor

THE NATURE AND EVOLUTION OF GALAXIES SELECTED VIA GAS CROSS SECTION

Daniel Brant Nestor, PhD

University of Pittsburgh, 2004

This dissertation consists of several projects designed to further our understanding of galaxies and galactic structures associated with intervening quasar absorption lines – i.e., those selected via gas cross section.

Surveys for Mg II absorption were conducted using quasar spectra from the Sloan Digital Sky Survey and data collected at the 6.5m Multiple Mirror Telescope Observatory on Mount Hopkins, AZ. The first survey expands the number of studied Mg II systems by an order of magnitude, while the second extends the statistics to weaker systems and lower redshifts. The results provide high-precision measurements (relative to previous results) of the statistics and evolution of Mg II absorbers. It is shown that the distribution of rest equivalent width steepens with decreasing redshift, especially at redshifts $z < 1$, such that the total absorption co-moving cross section decreases at a rate proportional to rest equivalent width. This is interpreted as an evolution in the kinematic properties of the absorbing galaxy population. Evidence for multiple physical populations comprising Mg II absorbers is presented and discussed.

Early survey results were used to investigate the cosmic neutral-gas-phase metallicity and dust content. Quasar spectra selected due to the presence of strong intervening Mg II absorption were stacked in the absorption rest frame to create high signal-to-noise ratio composites with which to measure Zn and Cr abundances. It was found that metallicity of high-$N_{H\,I}$ gas is highly correlated with the kinematic properties of galaxies and both metallicity and dust content for these systems increase with decreasing redshift.

Two projects were completed that involved the imaging of six low-redshift damped Lyman-α galaxies. Detailed properties of the identified absorber galaxies are described. They are shown to be drawn from a variety of morphological types with a range of luminosities, environments, and impact parameters.

TABLE OF CONTENTS

LIST OF TABLES

LIST OF FIGURES

PREFACE

I would like to thank Dave and Sandhya, who have not only given me great opportunities and support, but have also been exceptional professional role models.

Andy Connolly contributed greatly to some of the techniques developed in this dissertation, and his help and advice is greatly appreciated.

Also, I give **much** thanks to my family.

1.0 INTRODUCTION

One of the major goals of modern astronomy is to understand the detailed nature of galactic structures and their evolution from the era of the earliest star formation to the present epoch. To this end, astronomers have been studying the light emitted from galaxies for more than two centuries. The stellar luminosity of galaxies is now directly observed across the electromagnetic spectrum. However, any such work is necessarily biased, for studying galaxies via their stellar luminous output preferentially selects the most luminous systems. Furthermore, this bias grows with increasing distance, and therefore look-back time.

In addition to their stellar component, galaxies consist of dark matter, the dust and metals[1] produced by stars, and the reservoir of gas from which stars may form. A satisfactory picture of galaxy formation and evolution must involve a consistent understanding of all of these aspects over the complete range of redshift. Modern instruments and techniques have produced large amounts of new data, though there remain large gaps in redshift and in the types of structures studied. Theory, and especially simulations, have also advanced greatly in recent times. Thus, the immediate goal is to extend the current body of data to all redshifts and types of galactic structures, and form consistent interpretations of the empirical and theoretical results.

Below, I summarize some of the techniques and the status of our understanding of the nature and evolution of galaxies from high-redshift to the present. Since this dissertation is comprised of studies concerning galactic structures selected via gas absorption cross section, particular attention is given to quasar absorption line studies.

[1] Metals include all elements other than H and He.

1.1 DARK MATTER

Evidence for large amounts of non-luminous matter in galaxies began to accumulate in the 1930s with Oort concluding that the amount of mass in Galactic stars was inconsistent with the velocities of stars in the solar neighborhood (Oort, 1932), and similar conclusions by Zwicky from the study of the velocity dispersions of galaxies in rich clusters. Today, dark matter in galaxies is observed indirectly, as it was in the past with galaxy rotation curves and cluster velocity dispersions, and with modern techniques such as determining the masses of clusters through their x-ray emission and lensing signatures. It is now believed that $\approx 85\% - 95\%$ of matter in the universe is "dark".

Dark matter is the key ingredient in simulations of structure formation in the Universe (see Bertschinger, 1998, for a review). These simulations typically use up to many millions of cold dark matter (CDM) particles and implement gravity using algorithms such as: hierarchical trees, which divide space into a hierarchy of cells; particle-mesh, which solves Poisson's equation on a Cartesian grid; and so called particle-particle/particle-mesh hybrid algorithms. Physical processes (e.g., adiabatic gas dynamics) are often implemented as well, using methods such as smooth-particle hydrodynamics. As the complexity of CDM models has grown rapidly in recent years, so has the robustness of their results and predictions. Discrepancies between these predictions and the results of observations provide direction for both theorists and observers. One such discrepancy has been the over prediction of power on small structure-scales (Moore et al., 1999; Klypin et al., 1999).

The over prediction of small-scale structure by CDM simulations is generally thought to be a weakness of the simulations. For example, many simulations predict ≈ 50 satellites with masses $\gtrsim 10^8\,\mathrm{M}_\odot$ for Milky Way-like galaxies (Klypin et al., 1999), as apposed to the approximately dozen presently known. However, observations may, to a large extent, be missing many faint galaxies. There is much uncertainty in the slope of the faint end of the galaxy luminosity function. Dark matter halos that have not (yet) formed significant amounts of stars are easily missed in luminosity- or surface-brightness-limited studies. Also, halos that have formed stars but are relatively diffuse low-surface-brightness (LSB) galaxies are also easily missed. Thus, the true picture may actually lie in between the current state

of observation and simulation.

1.2 H I IMAGING

It is possible to trace halos that have LSB or have formed few stars, but contain large amounts of neutral hydrogen gas, with radio surveys (see, e.g., Barnes et al., 2001; Ryan-Weber et al., 2002). The gaseous components of galaxies can be studied via 21 cm radio emission from neutral hydrogen gas down to $\approx 10^6\,M_\odot$, without the stellar luminosity bias of optical studies. However, 21 cm studies have their own set of biases. Most importantly, 21 cm imaging is limited to redshifts $z \lesssim 0.1 - 0.2$.

Radio surveys of the local Universe find that Sbc-Sc galaxies are the most dominant contributers to the local H I mass function, with large column density H I often extending out to many times the optical radii, though other galaxy types do contain significant amounts H I gas. For example, Zwaan et al. (2003) claim that LSB galaxies contribute $\sim 15\%$ of the cosmic H I mass density at $z = 0$. Even some dwarf Es, E/S0s, and S0s are known to have substantial H I halos (e.g., Lake et al., 1987; Sadler et al., 2000), extending up to ≈ 5 times the optical radius. The projected cross section for large H I column density gas at $z = 0$ is, however, dominated by spirals (Rao and Briggs, 1993).

1.3 HIGH-REDSHIFT GALAXIES

Several techniques have allowed direct study of galaxies at high ($z \gtrsim 1 - 2$) redshift. The earliest successes were studies of galaxies detected because of their large radio luminosities (see McCarthy, 1993, for a review), with redshifts determined with optical spectroscopy (e.g., via measurement of Lyα emission). More recently, 8-m class telescopes have allowed narrow-band imaging with filters tuned to redshifted Lyα to find high-redshift galaxies. The most effective technique, though, has been the "Lyman-break" technique (see Giavalisco, 2002, for a review). This technique takes advantage of the unique colors of high-redshift galaxies caused by the discontinuity in the integrated stellar spectra of galaxies below 912Å due to

the hydrogen ionization edge. In multi-band optical imaging data, high-redshift galaxies "drop-out" of the bluer filters as the rest-frame 912Å edge is redshifted past each filter. The effect is stronger due to photoelectric absorption in young galaxies with significant H I gas, and in star-forming galaxies which typically contain significant amounts of dust that preferentially attenuates the bluer wavelengths.

The Hubble Deep Fields (HDF, Williams et al., 1996; Casertano et al., 2000) provided very deep high-resolution images of a narrow field of sky, revealing a wealth of information on galaxy colors, sizes and morphologies, down to unprecedented brightness limits. Ensuing spectroscopic and photometric redshifts have enabled the study of the evolution of these properties. An important HDF result has been the discovery of an abundance of disturbed and irregular galaxies at high redshift.

The study of faint blue galaxy population has also been important to our understanding of galaxy evolution (see Ellis, 1997, for a review).

1.4 QUASAR ABSORPTION LINES

Quasar absorption lines provide a tool for the study of galaxies selected via their gas cross sections, independent of distance. The chance alignment of galactic gas with the line of sight to a distant quasar produces an absorption signature in the quasar spectrum, allowing an often detailed examination of the absorbing gas. Identification of the atomic species giving rise to absorption features allows for the precise determination of the redshift of the host galaxy without having to acquire an emission-line or composite stellar spectrum of the galaxy – or even the visual identification of the galaxy itself.

The great advantage of quasar absorption line surveys is that they do not suffer from the types of biases found in optical galaxy surveys, and they are practical out to the redshift of the highest-z quasars. They do, however, contain their own set of biases – most notably they select galaxies/galactic structure based on gas cross section. Useful past reviews of this work can be found in Weymann et al. (1981), Blades et al. (1988), Petitjean and Charlot (1997), and Rauch (1998).

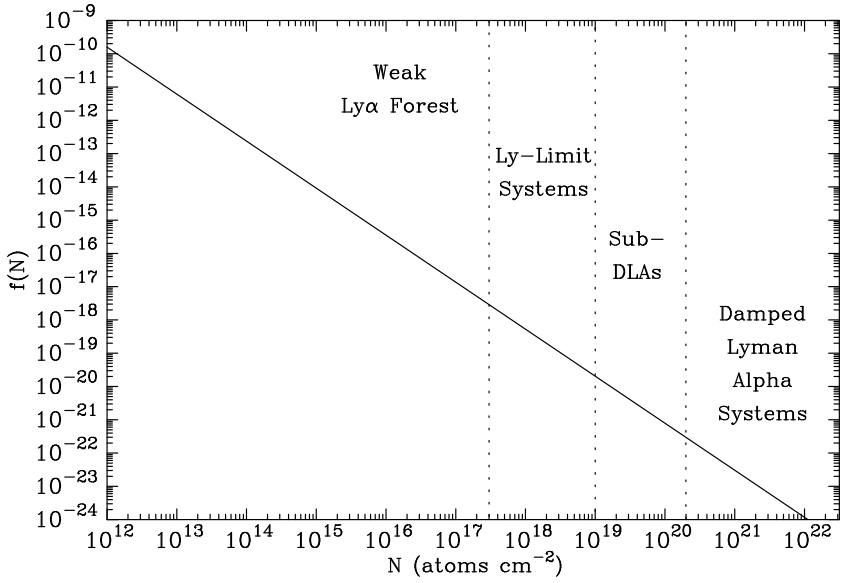

Figure 1.1: Schematic of the column density distribution for H I Lyα absorbers, at high ($z \sim 2$) redshift.

1.4.1 Hydrogen Lyα Absorbers

As galaxy evolution is, to a large extent, the conversion of H I into stars, the evolution of the H I component of galaxies is of particular interest. The regions blueward of the redshifted Lyα emission in quasar spectra contain a very high density of H I Lyα (λ1216) absorption features – the so-called Lyα forest (Weymann et al., 1981). The large incidence of these lines, together with the ability to measure them out to the largest quasar redshifts, makes them useful tools for the study of the formation of large-scale structure, the distribution of gas in the inter-galactic medium (IGM), the cosmological baryon density, etc. Figure 1.1 shows a schematic of the number of H I Lyα absorption lines per unit column density and redshift, at high ($z \sim 2$) redshift. For column densities below $N_{H\,I} \approx 10^{17}$ atoms cm^{-2}, the absorbers are optically thin at wavelengths below the Lyman limit and are ionized by the metagalactic UV flux. The term "Lyα forest" is often used to refer just these ubiquitous, weaker lines. Systems that are optically thick below the Lyman limit are less ionized or neutral, and sample denser gas that is generally associated with galaxies. While the weak lines may also

be associated with galaxies (see below), they sample relatively large galactocentric distances.

1.4.1.1 The Lyα Forest The Lyα forest in the spectra of quasar pairs has been used to estimate the sizes of the forest absorbers (Smette et al., 1992; Fang et al., 1996). It is found that their extents are large (hundreds of kpc) and therefore have low densities, which implies a high ionization correction (Tytler, 1997). The Lyα forest is believed to contain a large fraction of the baryonic content of the Universe. Penton et al. (2004) claim that Lyα forest gas is responsible for $\approx 30\%$ of the baryon content at $z = 0$.

The relationship between Lyα forest lines and galaxies is not yet well understood. There does exist a correlation between the strength of Lyα absorption and the impact parameter of the closest galaxy to the line of sight (Lanzetta et al., 2002), implying that at least relatively strong absorbers have a relationship with galaxies. CDM simulations often have gas follow the dark matter distribution and implement *ad hoc* star formation. The detailed nature of the relationship between Lyα forest clouds, dark matter, and galaxies, however, is not known. Additionally, there is evidence for weak Lyα absorbers in voids (Penton et al., 2002). Whether these are true void absorbers or related to very LSB or stellar-poor galaxies is not clear.

The number of Lyα forest lines per unit redshift at high-z ($\gtrsim 1.7$) decreases rapidly with decreasing redshift. At lower-z, however, the incidence is fairly constant with redshift (Weymann et al., 1998). Coincidently, this transition occurs at the redshift for which H I Lyα falls into the optical/UV. Davé et al. (1999) claim that the steep decline in the incidence at high-z is driven by the expansion of the Universe, but at lower-z this is offset by the fading UV background due to the decline in the population of quasars.

The incidence of Lyα forest lines at a given redshift has little dependence on the sightline for well-separated sightlines, indicating uniformity on large scales (Dobrzycki et al., 2002). However, there is evidence for weak clustering on smaller ($\Delta v \lesssim 250$ km s^{-1}) scales at high ($1.7 \lesssim z \lesssim 4$) redshift, and stronger clustering on slightly larger ($250 \lesssim \Delta v \lesssim 500$ km s^{-1}) scales at lower ($\langle z \rangle \approx 0.7$)) redshift (Ulmer, 1996, and references therein).

1.4.1.2 Damped Lyman Alpha Absorbers The number n of Lyα systems with column densities between $N_{H\,I}$ and $N_{H\,I} + dN_{H\,I}$ at high redshift is described reasonably well by a power law $\partial n/\partial N_{H\,I} \propto N_{H\,I}^{-1.5}$ over approximately ten orders of magnitude in $N_{H\,I}$, from $10^{12}\,\mathrm{cm}^{-2} \lesssim N_{H\,I} \lesssim 10^{22}\,\mathrm{cm}^{-2}$ (Hu et al., 1995). Thus, $\int_{N_{min}}^{N_{max}} N_{H\,I}\,\frac{\partial n}{\partial N_{H\,I}}\,dN_{H\,I} \propto N_{H\,I}^{0.5}|_{N_{min}}^{N_{max}} \sim N_{max}^{1/2}$, indicating that the bulk of the H I at high redshift is contained in the systems with the largest $N_{H\,I}$. Damped Lyα (DLA) systems are defined to have $N_{H\,I} \geq 2\times10^{20}$ atoms cm^{-2}. This definition (see Wolfe et al., 1986) was practical for the surveys at the time, but does not represent any distinct physically identifiable regime. Accurate column densities can be measured for systems with $N_{H\,I} \gtrsim 10^{19}$ atoms cm^{-2} (for which the Lyα absorption is above the flat, or so-called saturated, part of the curve of growth). Systems with 10^{19} atoms cm$^{-2} < N_{H\,I} < 10^{20.3}$ atoms cm^{-2} are commonly referred to as sub-DLAs. Column densities $N_{H\,I} \gtrsim 3\times10^{17}$ atoms cm^{-2} are opaque below the Lyman limit. Such absorption systems are called Lyman-limit systems. Because the strongest systems dominate any column density weighted statistics, studies of galactic H I gas in DLAs are not sensitive to the lower limit of $N_{H\,I}$ in their definition.

The Lyα λ1216 UV transition is the longest wavelength H I absorption feature short of the radio wavelength 21cm line. Therefore, ground based spectroscopy can only directly observe H I in absorption for $z \gtrsim 1.65$, when the Lyα line appears in the optical. This corresponds to when the Universe was less than 30% of its current age. Lyα absorption lines are ubiquitous, but the strongest systems are rare. For example, the number of DLAs per unit redshift is approximately $dn/dz \simeq 0.2$ at $z > 1.65$ (Wolfe et al., 1995). Blind searches for large $N_{H\,I}$ systems therefore have low efficiency, making space based surveys impracticably time-expensive. The *Hubble Space Telescope* (HST) quasar absorption line Key Project (e.g., Weymann et al., 1998) found only a single DLA.

DLA surveys at high redshift indicate that the cosmic mass density of H I evolves little over the redshift range $z = 3.5$ to $z = 1.65$ (Wolfe et al., 1995). However, the density decreases by $\approx 60\%$ by $z = 0$ (Rao and Briggs, 1993; Zwaan et al., 2003). Furthermore, studies of the global star formation rate in the Universe indicate a slow increase in star formation down to $z = 1$, and a steep decrease in star formation from $z \lesssim 1$ to $z = 0$ (see Hopkins, 2004, and references therein). Thus, the window $0 \leq z \leq 1.65$ is of great

importance to the understanding of the evolution of H I.

1.4.2 Metal-line Absorbers

Although the metal abundances of stars span four orders of magnitude, and the gas-phase abundances in a single galaxy may likewise vary greatly, galactic gas is never pristine. Figure 1.2 shows the absorption-line spectrum of a high redshift ($z = 2.462$) quasar from the Sloan Digital Sky Survey. Several emission features are recognizable, such as H I Lyα at $\lambda_{obs} = 4210$Å, N V at $\lambda_{obs} = 4285$Å, C IV at $\lambda_{obs} = 5365$Å, and C III] around $\lambda_{obs} = 6610$Å. The noise around $\lambda \approx 8400$Å and $\lambda \approx 8500$Å is due to poor subtraction of night sky lines. All absorption features visible in the spectrum are due to three intervening absorbers, at redshifts $z = 0.817, 1.634$ and 2.269. The $z = 0.817$ absorber (lines marked in blue) is recognizable via the Mg II$\lambda\lambda 2796, 2803$ doublet near $\lambda_{obs} = 5090$Å. The $z = 1.634$ system (lines marked in green) exhibits the Mg II$\lambda\lambda 2796, 2803$ doublet near $\lambda_{obs} = 7375$Å, Fe II lines spread over the interval $6100 \leq \lambda_{obs} \leq 6900$Å, Al II $\lambda 1670$ near $\lambda_{obs} = 4400$Å, C I $\lambda 1656$ near $\lambda_{obs} = 4360$Å, the C IV $\lambda\lambda 1548, 1550$ doublet near $\lambda_{obs} = 4080$Å and Si II $\lambda 1526$ near $\lambda_{obs} = 4020$Å. The $z = 2.269$ system's (lines marked in red) most notable absorption is the Mg II $\lambda\lambda 2796, 2803$ doublet near $\lambda_{obs} = 9150$Å and H I Lyα $\lambda 1216$ near $\lambda_{obs} = 3975$Å. This single quasar spectrum identifies three galaxies by virtue of their gas cross sections, at epochs 6.9, 9.6 and 10.6 Gyrs in the past, corresponding to when the universe was approximately 50%, 30% and 20% its current age, respectively[2].

Metals in enriched H I gas manifest absorption features at longer rest wavelengths than H I Lyα, allowing such systems to be studied from the ground at lower redshifts and therefore more recent epochs. As all significant columns of H I associated with galaxies are thought to contain detectable amounts of metals, these lines can serve as proxies for H I Lyα in tracing the neutral hydrogen content of galaxies. Relatively strong absorption from several atomic species, such as C IV, Fe II and Mg II are common in strong H I absorption systems. Bootstrapping from the statistics on the incidence of Mg II absorbers, Rao and Turnshek

[2]Ages calculated using rounded WMAP (Spergel et al., 2003) values for $(\Omega_\lambda, \Omega_M, h)$ of $(0.7, 0.3, 0.7)$. The corresponding age of the Universe is 13.5 Gyrs. All cosmology-dependent values in this dissertation are calculated using these values (except for Chapter 5.) See appendix A for details.

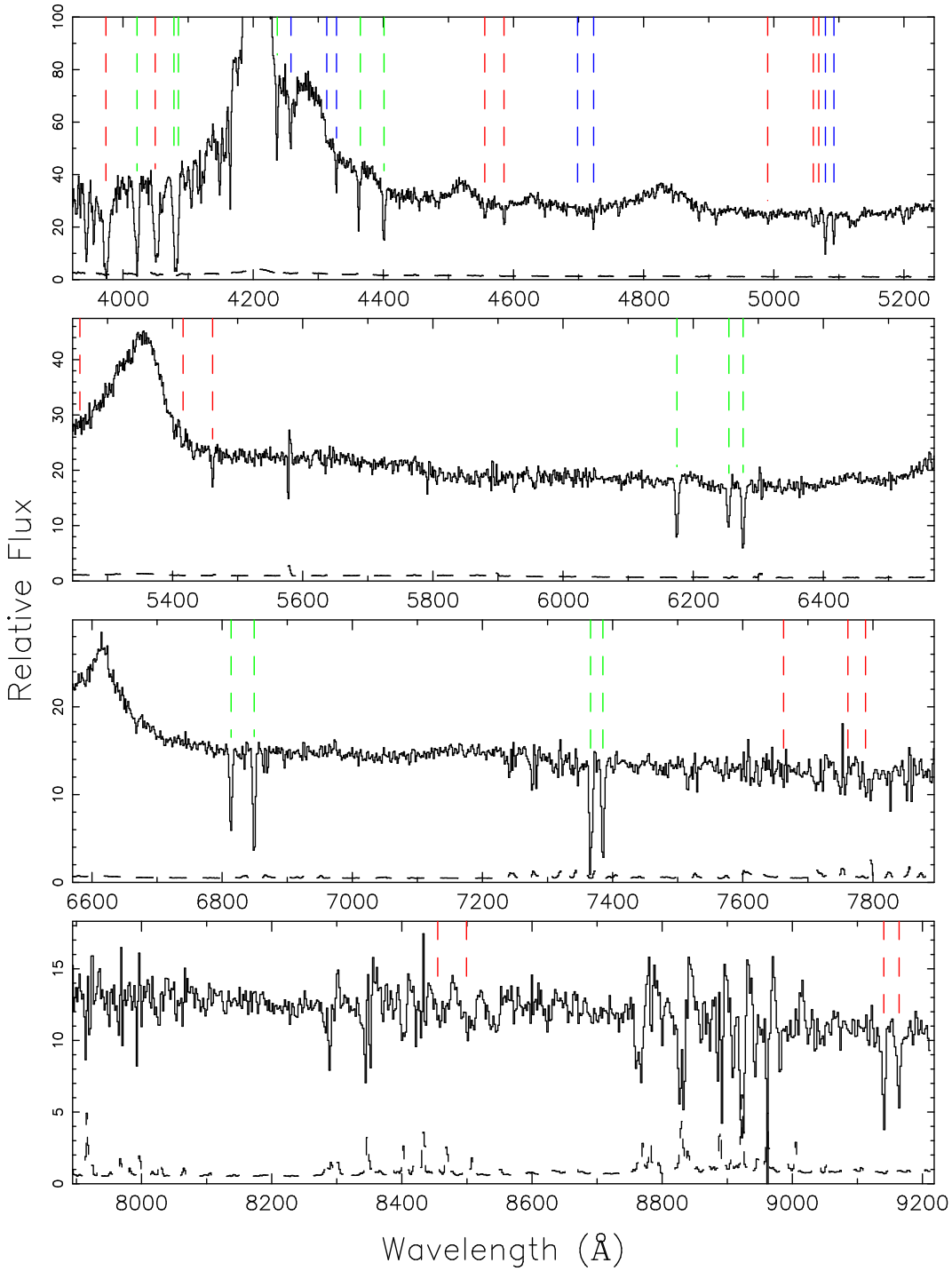

Figure 1.2: Spectrum of a $z = 2.462$ quasar with intervening absorption systems at $z = 0.817$ (lines marked in blue), $z = 1.634$ (green), and $z = 2.269$ (red.)

(2000, hereafter RT00) have used HST UV spectroscopy to estimate the incidence of DLAs and the cosmic mass density of H I, Ω_{DLA}, at redshifts $z \leq 1.65$. Their results are consistent with no evolution in Ω_{DLA} down to a redshift of $z \approx 0.5$, though their uncertainties are large.

Surveys for C IV and Mg II systems have been used to trace the gaseous cross sections of galaxies (Sargent et al., 1988a; Steidel and Sargent, 1992; Nestor et al., 2004). The lower-ionization Mg II systems tend to associate with cooler and/or denser gas and smaller impact parameters than the higher-ionization C IV systems. Their relative incidence and strengths give clues to the ionization-level history and sizes of these regions. Although DLA and sub-DLA absorption is opaque over the kinematic extent of the Lyα absorption profile, metal lines can be resolved into kinematic subcomponents with high resolution spectroscopy, thus allowing the study of the individual kinematic subsystems that comprise the absorbers (see Charlton and Churchill, 1998; Churchill et al., 1999; Churchill and Vogt, 2001, for example).

The stronger metal line features typically suffer from saturation in high $N_{H\,I}$ systems, but measurements of the strength of weaker transitions, such as lines due to Zn II and Si II, allow for the determination of neutral-gas-phase metallicity (e.g., see Pettini et al., 1990, 1999; Prochaska and Wolfe, 1999; Nestor et al., 2003). Such measurements at high redshift find DLA systems to have typical abundances that are $\approx 1-10\%$ solar, with a slight tendency to larger abundances at lower redshift (Prochaska et al., 2003; Nestor et al., 2003). Cosmic abundance evolution is intimately tied to cosmic star formation history, and is therefore an important diagnostic in galaxy evolution.

The longest rest wavelengths amongst common strong metal line absorbers are due to the Mg II $\lambda\lambda 2796, 2803$ doublet, which can be studied from the ground down to $z = 0.11$, or a look-back time of only 1.5 Gyrs. All Mg II absorbers are associated with columns of H I, and the largest H I columns almost always exhibit relatively strong Mg II absorption (RT00), making Mg II a good tracer of high column density H I absorption systems.

Strong and intermediate strength Mg II absorbers typically are at least partially saturated. Thus, their Mg II column densities cannot be determined. The absorption strength is, however, correlated with the number of individual kinematic components comprising the absorber (Petitjean and Bergeron, 1990), and therefore the projected velocity dispersion along the line of sight through the absorber (Churchill et al., 2000).

1.5 DLA GALAXIES

Although there is much data on the incidence, metallicity, and kinematics of large H I column density absorbers at redshifts $z > 1.65$, it is difficult for imaging studies to identify the galaxies associated with the absorption. The apparent surface brightness of an extended object decreases as $(1+z)^{-4}$, and reasonable impact parameters to the line of sight often correspond to small angular separations from the bright background quasar at these redshifts. Furthermore, in order to confirm an absorption galaxy candidate, a spectrum containing emission features must be obtained to confirm $z_{gal} = z_{abs}$, which is exceedingly difficult for high redshift galaxies using 4-m class telescopes. Thus, the physical interpretation of the high redshift data has largely been limited to theoretical models and simulations. Motivated by the kinematic asymmetries of the absorption profiles and the results placing the bulk of the $z = 0$ high-H I cross section in spirals, early models viewed high-redshift DLAs as rotationally supported disks that are the progenitors of present-day spirals (Prochaska and Wolfe, 1997, 1998; Wolfe and Prochaska, 2000). However, other models such as protogalactic clumps have been demonstrated to be equally successful alternatives to the disk-picture (Haehnelt et al., 1998). More recently, models have invoked a combination of components and processes such as disks, tidal streams, and halo clouds (Maller et al., 2001; Steidel et al., 2002).

The situation at redshifts $z < 1.65$ is different. Initially, there was a dearth high H I column density absorbers at low redshift. However, imaging studies are more practicable for these low-redshift systems. Now, the number of confirmed low redshift DLAs found in unbiased surveys is increasing, providing the opportunity for imaging studies to identify the galaxy associated with the DLA absorption. Initial results have found that a mix of morphological types contribute to the DLA galaxy population (Le Brun et al., 1997; Rao and Turnshek, 1998; Turnshek et al., 2001; Rao et al., 2003), though the number of systems yet studied is low.

1.6 SUMMARY OF DISSERTATION

This dissertation is comprised of five projects designed to further the understanding of the nature of galactic structures – specifically those selected via their gas cross section – and their evolution in redshift.

Two of the projects involve large surveys for intervening Mg II absorption in quasar spectra. The first, described in Chapter 2, uses data from the Sloan Digital Sky Survey (SDSS) Early Data Release (EDR). The results from this project were prepared for publication concurrently with the preparation of this dissertation, with co-authors D. Turnshek and S. Rao. The goal of this survey was to provide a Mg II absorption data set large enough to accurately determine the statistics of Mg II absorbers over a large range of the relevant parameters, as well as to accurately measure any evolution in redshift of the statistics. The second project, described in Chapter 3, uses data that I have collected at the Multiple Mirror Telescope (MMT) on Mt. Graham, AZ. The goal of the MMT survey was to extend the SDSS EDR results to lower redshift and higher sensitivity. Results from this survey will be published in the near future.

As a corollary to this work, I have used early results of the SDSS survey to measure the cosmic neutral-gas-phase metallicity and dust content of DLA absorbers at high redshift. This project is discussed in Chapter 4, and was published in reduced form as a letter with co-authors S. Rao, D. Turnshek and D. Vanden Berk.

Finally, Chapter 5 describes two imaging projects to study the nature of DLA galaxies. The first of these studies was published with D. Turnshek as the primary author; the second with S. Rao as the primary author.

Much of the text in this dissertation is identical to the text used in the published works, especially in Chapters 2 and 5. In Chapter 6, I discuss the results of the preceding chapters, and present conclusions and a summary of the work.

2.0 MG II ABSORBERS IN THE SDSS EDR QUASAR SPECTRA

2.1 INTRODUCTION

Intervening quasar absorption lines provide an opportunity to study the evolution of galaxies selected via their gas cross sections, independent of their stellar luminosities, from the earliest era of galaxy formation up to the present epoch. The chance alignment of galactic gas with the line of sight to a distant quasar allows the unique opportunity to study the gaseous phase of galaxies, without the biases involved in luminosity limited studies. In particular, low-ion metal lines and strong H I lines can be used to sample the low-ionization and neutral gas bound in galactic systems. Surveys for intervening Mg II absorption systems are particularly useful, since the Mg II doublet at rest wavelengths $\lambda\lambda 2796, 2803$ allows ground based surveys to track them down to relatively low redshift ($z = 0.11$). Strong Mg II systems are good tracers of large columns of neutral hydrogen gas RT00 and are useful probes of the velocity structure of the neutral gas components of galaxies, including DLA galaxies. Furthermore, unsaturated low-ionization metal lines associated with strong Mg II systems can be used to deduce neutral-gas-phase metal abundances (Pettini et al., 1999; Nestor et al., 2003; Prochaska et al., 2003).

Many surveys have studied the statistical properties of Mg II absorption systems. Lanzetta et al. (1987) presented the first significant survey and provided the benchmark results for the statistics of Mg II absorbers at relatively high redshift ($1.25 < z < 2.15$). They found marginal evidence for evolution in the number density of absorbers, but no significant evidence for evolution of the $\lambda 2796$ rest equivalent width ($W_0^{\lambda 2796}$) distribution, which they fit equally well with an exponential and a power law. Tytler et al. (1987) and Sargent et al. (1988b) provided data on Mg II systems at lower redshift ($0.2 \lesssim z \lesssim 1.5$) and found that the

comoving number density of absorbers (dn/dz) increases with redshift, consistent within the errors with no evolution. Caulet (1989) compared the Lanzetta, Turnshek, & Wolfe results to results at lower redshift, finding more moderately strong systems and fewer weak systems at $\langle z \rangle = 1.6$ as compared to $\langle z \rangle = 0.5$. The study by Steidel and Sargent (1992) (hereafter SS92), which contained 107 doublets with rest equivalent widths $W_0^{\lambda 2796} \geq 0.3$Å over the redshift range $0.23 \leq z \leq 2.06$, has served as the standard for the statistics of the distribution of Mg II λ2796 rest equivalent widths $n(W_0^{\lambda 2796})$, redshift number density dn/dz, and redshift evolution for the past decade. Their conclusions included the following:

1. The $W_0^{\lambda 2796}$ distribution can be fit equally well with either an exponential or power law.
2. dn/dz for systems with $W_0^{\lambda 2796} \geq 0.3$Å increases with redshift in a manner consistent with no evolution.
3. The redshift number density dn/dz for the strongest lines does show evidence for evolution, with dn/dz decreasing from the no evolution prediction with decreasing redshift.
4. The mean $W_0^{\lambda 2796}$ increases with redshift.
5. There is no evidence for correlation between the doublet ratio $W_0^{\lambda 2796}/W_0^{\lambda 2803}$ and redshift.

Churchill et al. (1999, hereafter CRCV99) presented a study of 30 "weak" ($W_0^{\lambda 2796} \leq 0.3$Å) systems, describing $n(W_0^{\lambda 2796})$ and dn/dz for the weak extreme of the Mg II $W_0^{\lambda 2796}$ population. They favored a power law over an exponential for the parameterization of $n(W_0^{\lambda 2796})$.

The SDSS (York et al., 2000) provides an opportunity to improve the statistics of Mg II and other low-ion absorption systems by expanding the number of measured systems by multiple orders of magnitude. The statistics and evolution of the absorber number density, which is the product of the space density and the absorption cross section, and the distribution of line strengths, which correlate with the number of kinematic subsystems and absorber velocity dispersion, are important factors in understanding the physical nature of Mg II systems and their evolution. Furthermore, the strong connection to DLA and sub-DLA systems (RT00; Rao, Turnshek & Nestor, in prep) makes the parameterization of the Mg II properties key to the study of large H I column density systems. Finally, only large surveys provide statistically relevant numbers of rare, ultra-strong systems for complementary imaging and

high-resolution kinematic studies.

In this Chapter, the results from a Mg II $\lambda\lambda 2796, 2803$ survey in quasar spectra from the SDSS EDR (Stoughton et al., 2002) are presented. These results, using only a small fraction of the final SDSS database, is of interest because with the large number of Mg II doublets identified (over 1,300 with $W_0^{\lambda 2796} \geq 0.3$Å), systematic errors already compete with Poissonian errors in the measured statistics. In §2.2 the SDSS EDR data set, the doublet finding algorithm, and tests for systematic biases are described. In §2.3, the results of the analyses are presented, the absorber statistics and their parameterizations described, and sources of systematic errors considered. Conclusions re presented in §2.4.

2.2 ANALYSIS

2.2.1 The Data

The SDSS EDR provides 3814 quasar spectra, approximately 3700 of which are of quasars with sufficiently high redshift ($0.37 \leq z_{QSO} \leq 5.30$, $\langle z_{QSO} \rangle \simeq 1.53$) to allow detection of intervening Mg II $\lambda\lambda 2796, 2803$ doublets. All available spectra were analyzed, regardless of quasar magnitude, as only a small number were too faint to detect the strongest systems in the catalog. This data set combines a large number of sightlines with a wide spectral coverage: from 3800 Å at a resolution of 1800, to 9200 Å at a resolution of 2100. This corresponds to a Mg II absorption redshift coverage of $0.37 \leq z_{abs} \leq 2.27$. Typical signal to noise ratios in the SDSS EDR quasar spectra are such that the survey is most sensitive to doublets with $W_0^{\lambda 2796} \gtrsim 0.6$Å, though the catalog includes systems down to $W_0^{\lambda 2796} = 0.3$Å. The strongest system found has $W_0^{\lambda 2796} = 5.68$Å. At all of these strengths, the Mg II $\lambda 2796$ line is typically saturated. Thus, no column density information can be gleaned from $W_0^{\lambda 2796}$. However, large $W_0^{\lambda 2796}$ does track high H I columns and exhibits correlation with line of sight velocity dispersion and metallicity (Nestor et al., 2003, also Chapter 3). Although the EDR quasar catalog selection properties are not homogeneous, and therefore not appropriate for statistical analyses, the quasar selection criterion should have little affect on the analysis of intervening absorption. Effects related to the quasar selection that could impact the results

are discussed in §2.3.4.

2.2.2 Continuum Fitting

In order to search the spectra for Mg II doublets, continua were first fitted to the data using the following algorithm. Data below the quasar rest-frame Lyα emission were excluded to avoid the unreliable process of searching for lines in the Lyα forest, as were data longward of the Mg II $\lambda\lambda 2796, 2803$ emission feature. As the only interest is in detecting and measuring the strength of absorption features, a continuum was defined to be the spectrum as it would appear in the absence of absorption features, i.e., the true continuum plus broad emission lines. An underlying continuum was fitted with a cubic spline, and broad emission and broad and narrow absorption features were fitted with one or more Gaussians and subtracted. This process was iterated several times to improve the fits of both the spline and Gaussians. Except for a few problematic areas in a small number of spectra, this technique provided highly satisfactory results. Note that by avoiding the Lyα forest, the difficulties that arise in trying to define a continuum in that region are not experienced. The fluxes and errors in flux were then normalized by the fitted continua, and these normalized spectra were used for subsequent analyses.

2.2.3 Mg II Doublet Finding Algorithm

The continuum-normalized SDSS EDR quasar spectra were searched for Mg II $\lambda\lambda 2796, 2803$ doublet candidates. All candidates were interactively checked for false detections, satisfactory continua fits, blends with absorption lines from other systems, and other special cases. An optimal extraction method (see Schneider et al., 1993) was used to measure each W_0:

$$(1+z)\,W_0 = \frac{\sum_i P(\lambda_i - \lambda_0)\,(1-f_i)}{\sum_i P^2(\lambda_i - \lambda_0)}\,\Delta\lambda, \tag{2.1}$$

$$(1+z)\,\sigma_{W_0} = \frac{\sqrt{\sum_i P^2(\lambda_i - \lambda_0)\,\sigma_{f_i}^2}}{\sum_i P^2(\lambda_i - \lambda_0)}\,\Delta\lambda, \tag{2.2}$$

where $P(\lambda_i - \lambda_0)$ represents the line profile, and f_i and σ_{f_i} the normalized flux and flux error per pixel. The sum is performed over an integer number of pixels that cover at least ± 3

characteristic Gaussian widths. Many of the lines found were unresolved. For these, it was appropriate to use the line spread function for the optimal extraction profile, and a Gaussian with a width corresponding to the resolution generally provided a very satisfactory fit. A large proportion of the lines, however, were at least mildly resolved. For these systems, a profile obtained by fitting a Gaussian whose width is only constrained to be greater than or equal to the unresolved width was appropriate. For the large majority of the mildly resolved lines, single Gaussians were satisfactory fits and the method for measuring W_0 gave results consistent with, and with higher significance than, other methods such as direct integration over the line. In rare cases ($\approx 4\%$), a single Gaussian was a poor description of the line profile, and more complex profiles, such as a displaced double-Gaussian, were employed.

Identifying Mg II systems requires the detection of the λ2796 line and at least one additional line, the most convenient being the λ2803 doublet partner. A $5\,\sigma$ significance level requirement was imposed for all λ2796 lines. However, a $3\,\sigma$ significance level requirement was also imposed for the corresponding λ2803 line, in order to ensure identification of the doublet. In order to avoid a selection bias in $W_0^{\lambda 2796}/W_0^{\lambda 2803}$ doublet ratio (DR), which has a maximum value of $DR = 2.0$, a detection limit for $W_0^{\lambda 2796}$, called W_0^{lim}, was defined by taking the larger of 5.0 times the error in $W_0^{\lambda 2796}$ or 6.0 times the error in $W_0^{\lambda 2803}$. The errors were computed using the unresolved profile width at the given redshift to avoid selection bias in the Gaussian fit-width. Only systems 3,000 km s^{-1} blueward of z_{QSO} and redward of Lyα emission were accepted. Systems with separations less than 500 km s^{-1} were considered single systems. This value was chosen to match the width of the broadest systems found, and is consistent with the window used in the CRCV99 study. Mg I $W_0^{\lambda 2852}$ and Fe II $W_0^{\lambda 2600}$ were also measured for confirmed systems, when possible.

2.2.4 Monte Carlo Simulations

Monte Carlo simulations of the absorber catalog were run to test the efficiency of the detection technique and to identify biases and systematic effects. For each detected system, a simulated doublet having the same redshift, and similar $W_0^{\lambda 2796}$, DR, and fit width, was put into many randomly selected EDR spectra. Each spectrum containing a simulated dou-

blet was then run through the entire non-interactive and interactive pipelines, and z and $W_0^{\lambda 2796}$ were measured for detected systems. Thus, there are two simulated catalogs: the input catalog containing over 9100 simulated doublets, though only ≈ 4500 of these appear in regions of spectra with sufficient signal to noise ratio to meet the detection threshold for the input $W_0^{\lambda 2796}$, and the simulated output catalog, containing ≈ 4400 doublets recovered from the simulation. Measurement error in $W_0^{\lambda 2796}$ and any subtle systematic effects can cause systems with $W_0^{\lambda 2796} < W_0^{lim}$ to scatter into the output catalog as well as systems with $W_0^{\lambda 2796} \geq W_0^{lim}$ to scatter out. However, if the input distribution of $W_0^{\lambda 2796}$ does not match the true distribution, the ratio of the ≈ 4400 recovered systems to the ≈ 4500 input with $W_0^{\lambda 2796} \geq W_0^{lim}$ is not necessarily an accurate estimate of the biases. Therefore, a trial $W_0^{\lambda 2796}$ distribution must be specified according to which lines are chosen from the simulated input catalog. The trial distribution must then be adjusted so that the simulated output best represents the data.

As the form of the input distribution is necessarily motivated by the data, further discussion of the simulations and their use for estimating systematic errors is discussed in §2.3.

2.3 RESULTS

In total, 1331 Mg II doublets with $W_0^{\lambda 2796} \geq 0.3$Å were identified and measured. A small number of additional possible doublets were also discovered ($\lesssim 1\%$ of the sample), but only allowed limits on $W_0^{\lambda 2796}$ to be determined or had questionable identifications and were not used in the analyses.

2.3.1 $W_0^{\lambda 2796}$ Distribution

Figure 2.1 shows the distribution of $W_0^{\lambda 2796}$ for the sample. Only those systems with $W_0^{\lambda 2796} \geq 0.3$Å which were used in the analyses are shown. The distribution has a smooth tail out to $W_0^{\lambda 2796} \approx 4.6$Å, with the largest value $W_0^{\lambda 2796} = 5.68$Å.

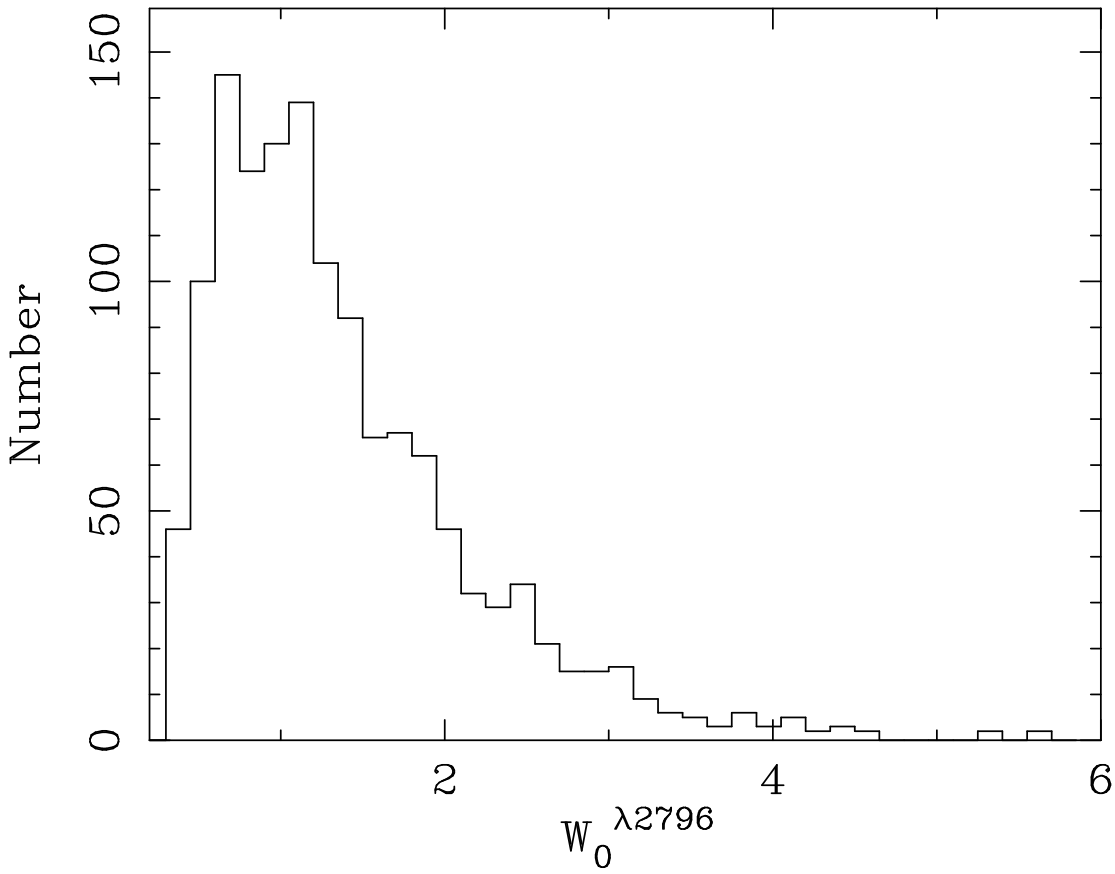

Figure 2.1: The distribution of rest equivalent widths, $W_0^{\lambda 2796}$, for Mg II systems found in the survey with $W_0^{\lambda 2796} \geq 0.3$.

The total redshift path covered by the sample for each value of $W_0^{\lambda 2796}$ is given by

$$\Delta Z\,(W_0^{\lambda 2796}) = \int_{z_{min}}^{z_{max}} \Delta Z(W_0^{\lambda 2796}, z)\,dz = \sum_{N_{spec}} \int_{z_{min}}^{z_{max}} g(W_0^{\lambda 2796}, z)\,dz, \qquad (2.3)$$

where $g(W_0^{\lambda 2796}, z) = 1$ if $W_0^{lim}(z) \leq W_0^{\lambda 2796}$ and $g(W_0^{\lambda 2796}, z) = 0$ otherwise, and the redshift limits are defined to be 3,000 km s^{-1} above Lyα emission and 3,000 km s^{-1} below Mg II emission, or the limits of the data. Broad absorption line regions were masked out. The redshift path coverage is shown in Figure 2.2. Figures 2.1 and 2.2 were combined to form an unbiased $W_0^{\lambda 2796}$ distribution, which is shown in Figure 2.3. The distribution is fit very well by an exponential,

$$n(W_0^{\lambda 2796}) = \frac{N^*}{W^*} e^{-\frac{W_0}{W^*}}, \qquad (2.4)$$

with the maximum likelihood value $W^* = 0.702 \pm 0.017$ and corresponding $N^* = 1.187 \pm 0.052$. The reduced χ^2 comparing the maximum likelihood fit to the binned data is close to unity, independent of the choice of bin size. Also shown are data from CRCV99 with $W_0^{\lambda 2796} < 0.3$Å and SS92 with $0.3\,\text{Å} \leq W_0^{\lambda 2796} \leq 2.9$Å. All three data sets have similar average absorption redshifts: the CRCV99 data have $\langle z_{abs} \rangle = 0.9$, and the SDSS EDR and SS92 data have $\langle z_{abs} \rangle = 1.1$. The SS92 best-fit exponential closely agrees with the EDR results, though the EDR normalization, N^*/W^*, is slightly ($\approx 1\sigma$) lower than the SS92 value ($W^* = 0.66 \pm 0.11$, $N^* = 1.55 \pm 0.20$). The reason for this offset, as well as the lack of scatter as compared to the size of the error bars in the SS92 data, is not clear. Both the EDR survey and the CRCV99 study consider systems within 500 km s^{-1} as a single system, while the SS92 study uses a 1,000 km s^{-1} window. This cannot be the source of the normalization offset, however, as it would have the opposite effect, reducing the number of systems found by SS92.

A power law fit of the form $n(W_0^{\lambda 2796}) = C\,W_0^{-\delta}$ with the SS92 values of $C = 0.38$ and $\delta = 1.65$ is shown as a long-dash line in Figure 2.3. It is a good fit to the EDR results for $0.5\,\text{Å} \lesssim W_0^{\lambda 2796} \lesssim 2.0$Å. For large values of $W_0^{\lambda 2796}$, however, the SS92 power law over-predicts $n(W_0^{\lambda 2796})$ by almost an order of magnitude. CRCV99 also fit a power law to their binned data combined with the SS92 binned data, but excluding the highest SS92 bin. This is shown as a dotted line. The combined data sets suggest a transition in the $n(W_0^{\lambda 2796})$ distribution occurring near $\approx 0.3\,\text{Å}$.

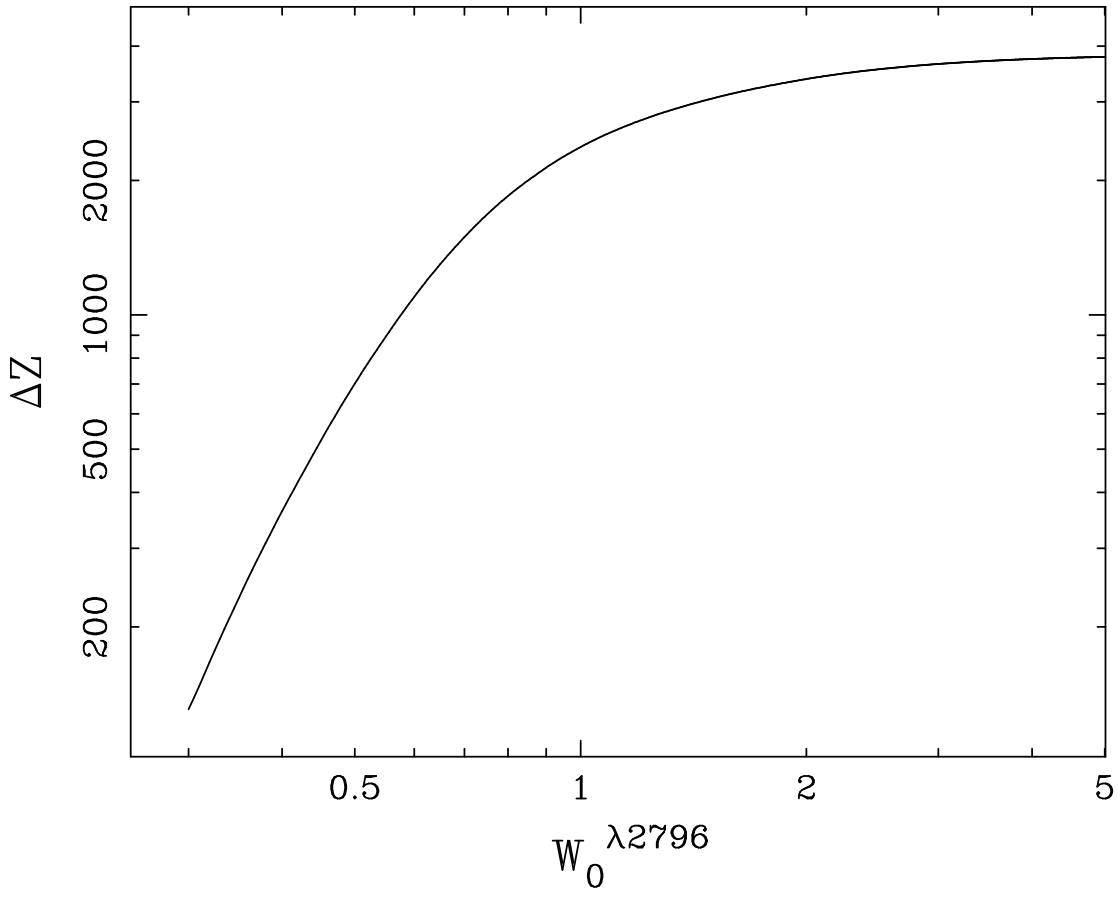

Figure 2.2: The redshift-path covered by the survey, $\Delta Z\,(W_0) = \sum_i^{N_{spec}} \int_{z_{min}}^{z_{max}} g(W_0, z)\, dz$, as a function of $W_0^{\lambda 2796}$.

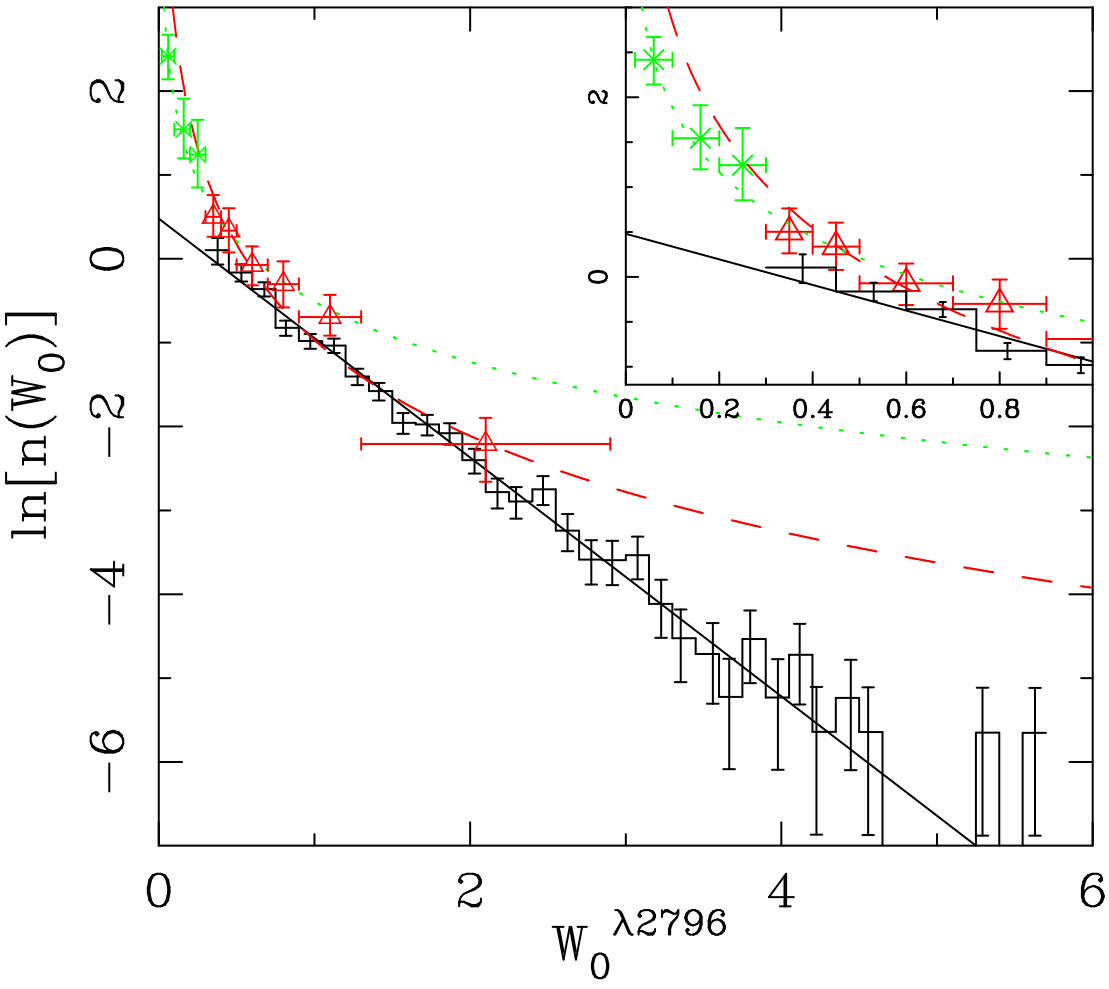

Figure 2.3: Histogram of the $W_0^{\lambda 2796}$ distribution from the EDR survey. The solid line is a maximum likelihood fit of the form $n(W_0) = \frac{N^*}{W^*} e^{-\frac{W}{W^*}}$ with $W^* = 0.702 \pm 0.017$ and $N^* = 1.134 \pm 0.069$. The open triangles are from SS92. The dashed line is their best fit power law. The $\times$ symbols represent data from CRCV99. The dotted line is their power law fit to their binned data plus the SS92 data, excluding the highest-W_0 SS92 bin. The inset shows the $W_0^{\lambda 2796} < 1.0$Å region in more detail. The power laws greatly over-predict the incidence of strong ($W_0^{\lambda 2796} > 2$Å) systems, while the exponential under-predicts the incidence of $W_0 < 0.3$Å systems. This suggests a transition in the $n(W_0)$ distribution around $W_0 \sim 0.3$Å, possibly indicative of two distinct populations.

The simulated catalogs (§2.2.4) were used to test for biases in the $W_0^{\lambda 2796}$ distribution. Lines were chosen randomly from the input catalog according to a distribution of the form $n(W_0^{\lambda 2796}) \propto e^{-\frac{W_0}{W^*_{in}}}$, with an initial guess for W^*_{in}, until the number of lines recovered was equal to that of the actual catalog, which determines N^*_{in}. Lines with input $W_0^{\lambda 2796} < 0.3$Å were used, though only lines with recovered $W_0^{\lambda 2796} \geq 0.3$Å were retained. A maximum-likelihood value was determined for W^*_{out} using the recovered $W_0^{\lambda 2796}$ values. The guess for W^*_{in} was then corrected to minimize $|W^*_{out} - W^*_{data}|$. The process was repeated several times with different seeds of the random number generator to determine variance.

Except for the weakest systems in the catalog, which were under-predicted, this simulation was able to match the actual data well. The under-prediction could be a weakness of the simulation, as there are few systems with $W_0^{\lambda 2796} < 0.3$Å with which to model the low $W_0^{\lambda 2796}$ end of the distribution. Alternatively, the actual distribution could diverge from the simulated exponential for $W_0^{\lambda 2796} < 0.3$Å, as suggested by the CRCV99 data. Thus, though the entire range $W_0^{\lambda 2796} \geq 0.3$Å was simulated, the calculation of W^*_{out} was limited to $W_0^{\lambda 2796} \geq 0.5$Å. Motivated by the CRCV99 results, a second exponential was then added to the input distribution while holding fixed the primary distribution. The values of W^* and N^* for this second exponential were adjusted to minimize a χ^2 statistic calculated by comparing the binned simulated output to the binned data. Thus, the input distribution was modeled with separate "weak" and "strong" components:

$$n(W_0^{\lambda 2796}) = \frac{N^*_{wk}}{W^*_{wk}} e^{-W_0/W^*_{wk}} + \frac{N^*_{str}}{W^*_{str}} e^{-W_0/W^*_{str}}. \tag{2.5}$$

The resulting best fit values are $N^*_{wk} = 1.71 \pm 0.02$ and $W^*_{wk} = 0.072 \pm 0.001$, and $N^*_{str} = 0.932 \pm 0.011$ and $W^*_{str} = 0.771 \pm 0.014$, where the errors are the square root of the variances from different choices of random number generator seed. These results are shown in Figure 2.4. The "weak" values were very stable under changes in the seed, producing small variances. Since the "weak" component was constrained by only a small region of $W_0^{\lambda 2796}$-space in the data, the actual uncertainties in the parameters are much larger than the variances.

Although most all of the systems in the sample are at least partially saturated, the distribution of DR values (see section §2.3.5) indicates that the typical degree of saturation increases from a mixture of saturation levels at $W_0^{\lambda 2796} \lesssim 1$Å to virtually all systems being

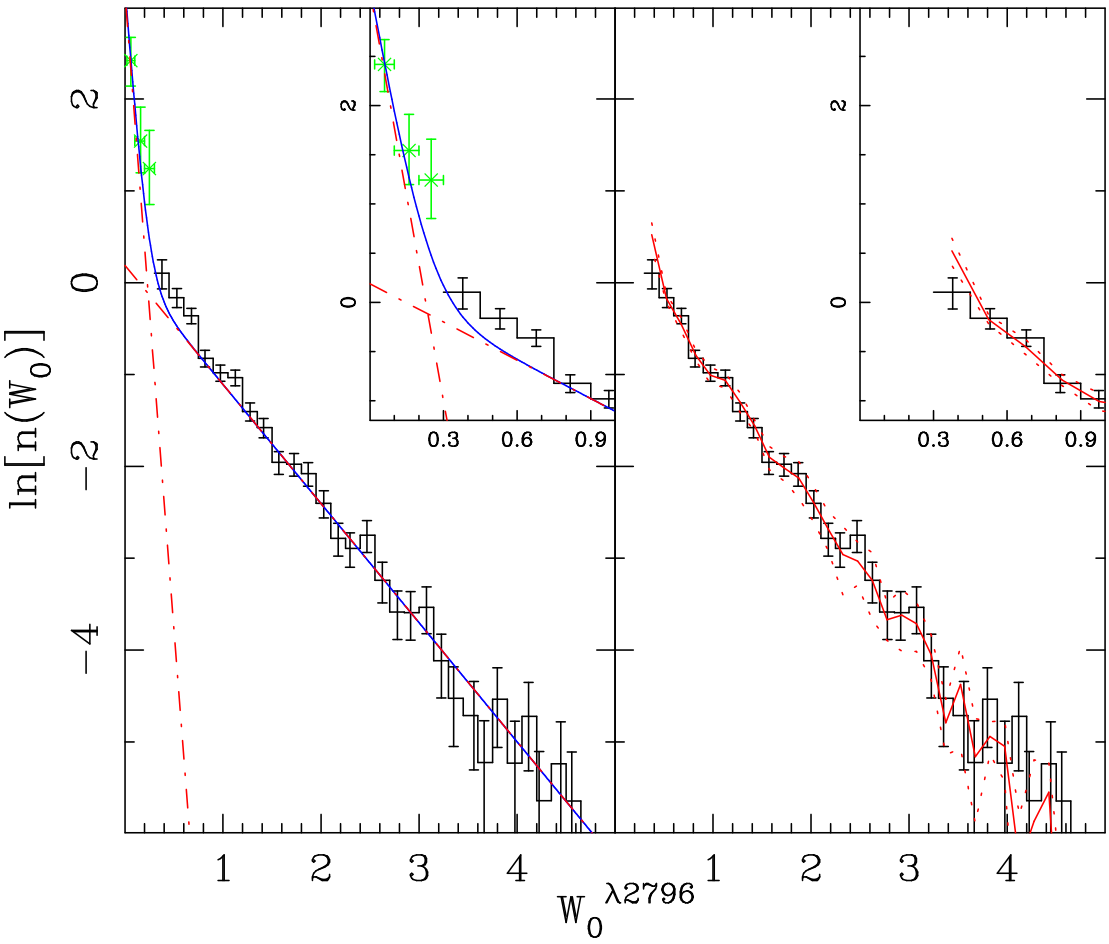

Figure 2.4: Monte Carlo results. The histograms represent the data. The points are from CRCV99. The left panel shows the input exponential distributions. The shallower exponential ($W^* = 0.771$ and $N^* = 0.932$) was chosen such that the simulated output distribution had $W^*_{out} = W^*_{data}$ for $W_0 \geq 0.5$Å. The steeper exponential ($W^* = 0.072$ and $N^* = 1.71$) was then chosen to minimize the χ^2 computed by comparing the total simulated binned data to the real binned data. The right panel shows the simulated output (solid line) over-plotted on the data. The dotted lines represent the square root of the variance.

highly saturated at $W_0^{\lambda 2796} \gtrsim 2$Å. Thus, there exists the possibility that if the column density distribution (which is *not* measurable with the SDSS data) is described by a power law over the range of line strengths in the sample, curve-of-growth effects could conceivably cause the corresponding $n(W_0^{\lambda 2796})$ to deviate from a power law at $W_0^{\lambda 2796} \gtrsim 2$Å, consistent with the SDSS results. Nonetheless, the directly measurable $n(W_0^{\lambda 2796})$ is parameterized very well by a single exponential for systems with $0.3\text{Å} \leq W_0^{\lambda 2796} \lesssim 5\text{Å}$, and by two exponentials for $W_0^{\lambda 2796} \geq 0.02$Å.

2.3.1.1 Redshift Evolution of W^*

In order to investigate evolution in W^*, the sample was split into three redshift bins, $0.366 \leq z < 0.871$, $0.871 \leq z < 1.311$, and $1.311 \leq z < 2.269$, chosen such that there are an equal number of systems in each bin. The three $n(W_0^{\lambda 2796})$ distributions are shown in Figure 2.5. Figure 2.6 shows the resulting W^* for each redshift bin (circles) and the Monte Carlo input values (squares). The curve in Figure 2.6 is the power law fit described in §2.3.3.

2.3.2 Distribution of Absorption Redshifts

Figure 2.7 shows the absorption redshift distribution for the sample. Absorption redshifts span the range $0.367 \leq z \leq 2.269$. The total number of sightlines with sufficient signal to noise ratio to detect lines with $W_0^{\lambda 2796} \geq W_0^{min}$ for several values of W_0^{min} is shown in Figure 2.8 as a function of redshift. The conspicuous features at $z > 1.5$ are due to poor night sky subtractions in many of the spectra. The feature near $z = 1.1$ is due to the dichroic (Stoughton et al., 2002).

The incidence and variance of lines in an interval of $W_0^{\lambda 2796}$ over a specified redshift range are given by

$$\frac{dn}{dz} = \sum_i \frac{1}{\Delta Z\left(W_0^i\right)}, \quad \sigma^2_{\frac{dn}{dz}} = \sum_i \left(\frac{1}{\Delta Z\left(W_0^i\right)}\right)^2, \tag{2.6}$$

where the sum is over systems with W_0^i in the given interval and $\Delta Z\left(W_0^i\right)$ represents the path contained in the specified redshift range. Traditionally, dn/dz has been plotted versus redshift for lines stronger than a specified W_0^{min}. In Figure 2.9, dn/dz is shown as a function of redshift for $W_0^{\lambda 2796} \geq 0.3$, 0.6, 1.0, 1.5, 2.0, 2.5, 3.0 and 3.5 Å. Also shown in Figure 2.9

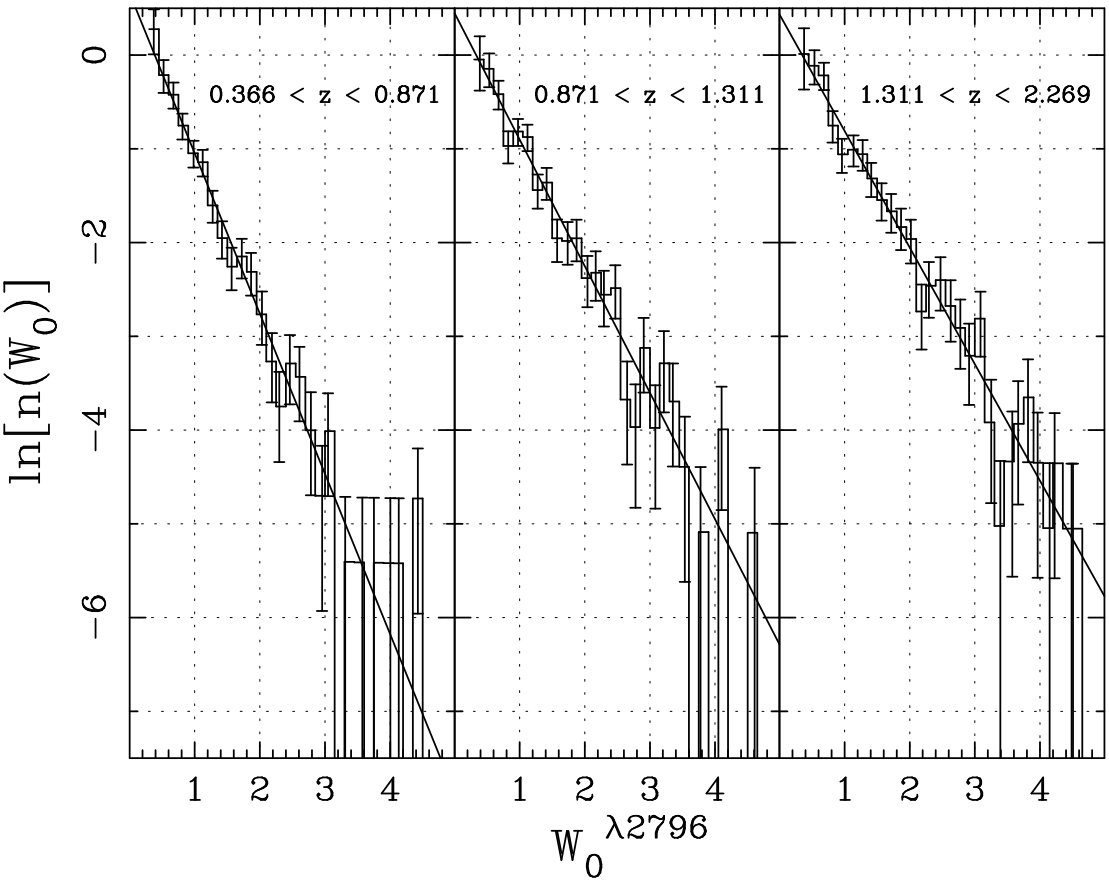

Figure 2.5: The redshift evolution of $n(W_0)$. The solid lines are maximum likelihood fits of the form $n(W_0) = \frac{N^*}{W^*} e^{-\frac{W}{W^*}}$. Left: $0.366 \leq z < 0.871$, with maximum likelihood value $W^* = 0.585 \pm 0.024$ and corresponding $N^* = 1.134 \pm 0.124$. Center: $0.871 \leq z < 1.311$, with maximum likelihood value $W^* = 0.741 \pm 0.032$ and corresponding $N^* = 1.160 \pm 0.121$. Right: $1.311 \leq z < 2.269$, with maximum likelihood value $W^* = 0.804 \pm 0.034$ and corresponding $N^* = 1.243 \pm 0.126$. Note the steepening of the slope with lower redshifts.

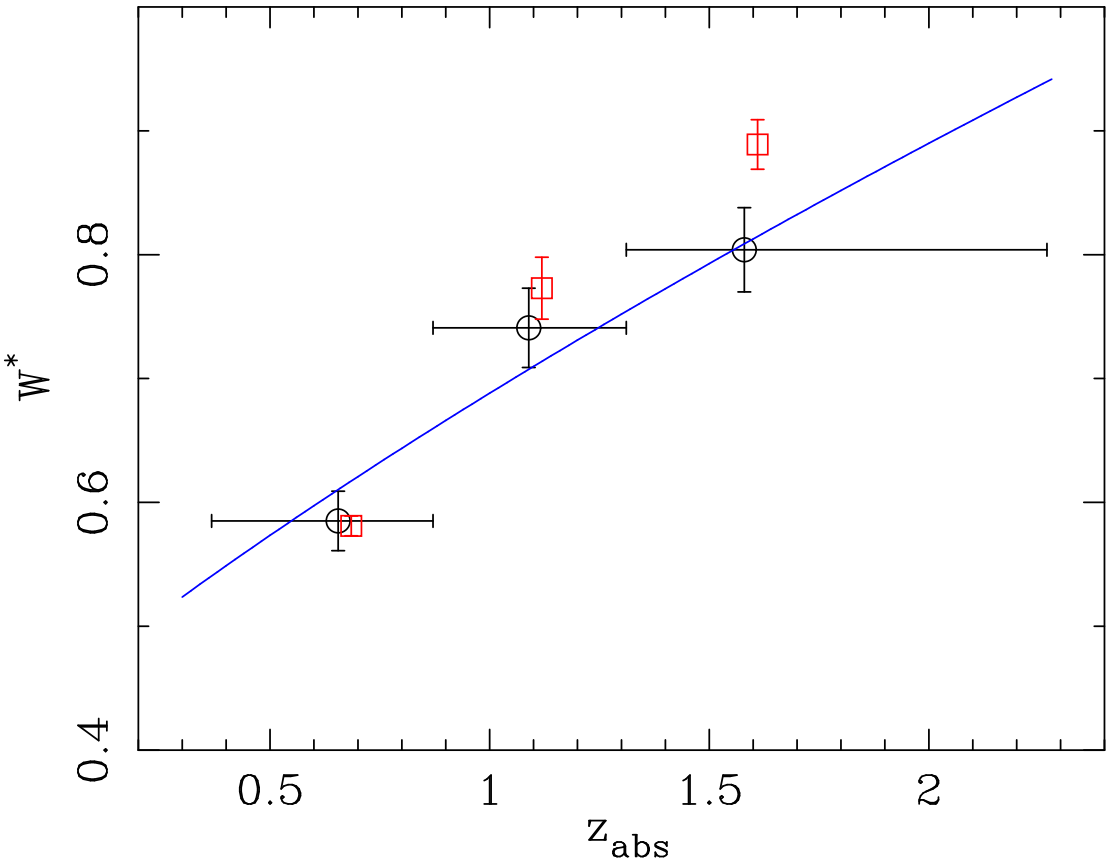

Figure 2.6: The redshift evolution of W^*. The horizontal bars represent the bin sizes. The open circles are from the data, while the squares represent the Monte Carlo input values (see text, §3.1). The points are offset slightly in z_{abs} for clarity. The solid line is the prediction for W^* for a fit of the form $W^*(z) = W^*\,(1+z)^{\alpha}$ described in §2.3.3.

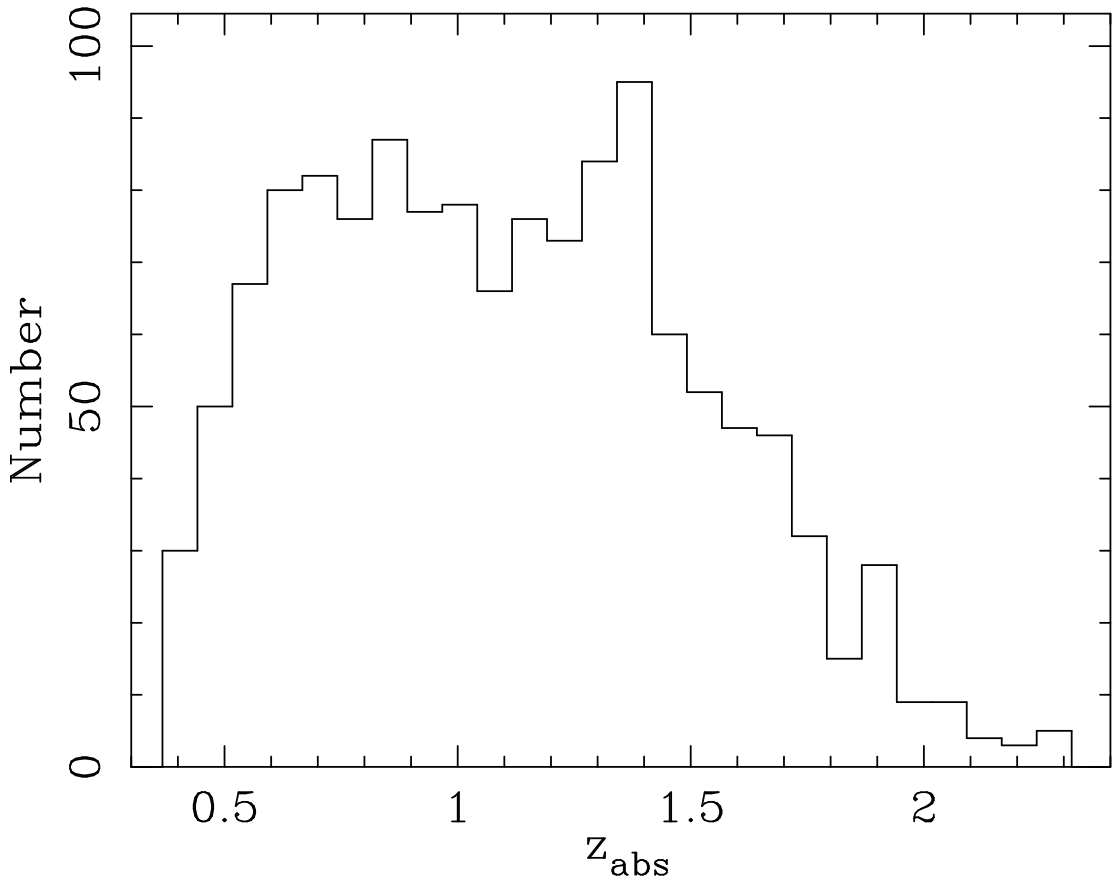

Figure 2.7: The distribution of absorption redshifts for Mg II systems with $W_0^{\lambda 2796} \geq 0.3$ found in the survey.

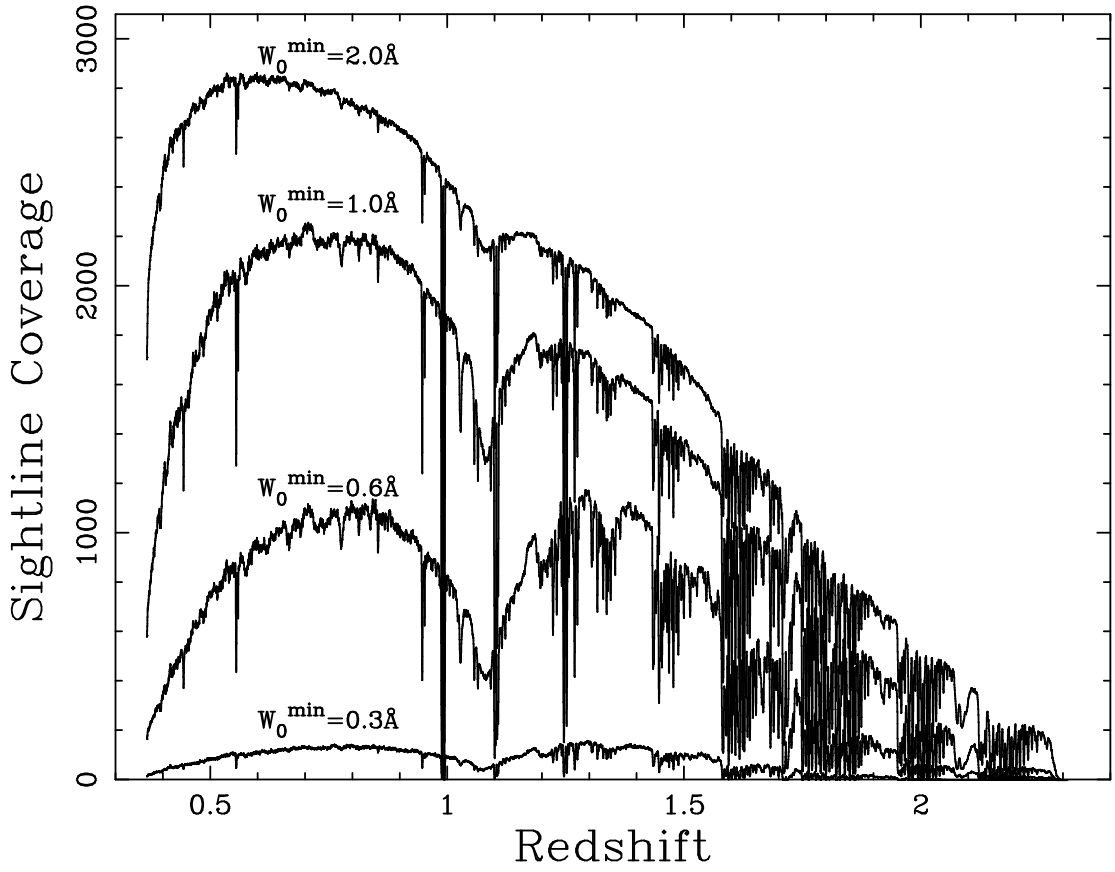

Figure 2.8: The total number of sightlines with sufficient signal to noise ratio to detect lines with $W_0^{\lambda 2796} \geq W_0^{min}$ as a function of redshift, for W_0^{min} = 2.0Å, 1.0Å, 0.6Å, and 0.3Å. The conspicuous features at $z > 1.5$ are due to poor night sky line subtractions in many of the spectra. The feature near $z = 1.1$ is due to the dichroic.

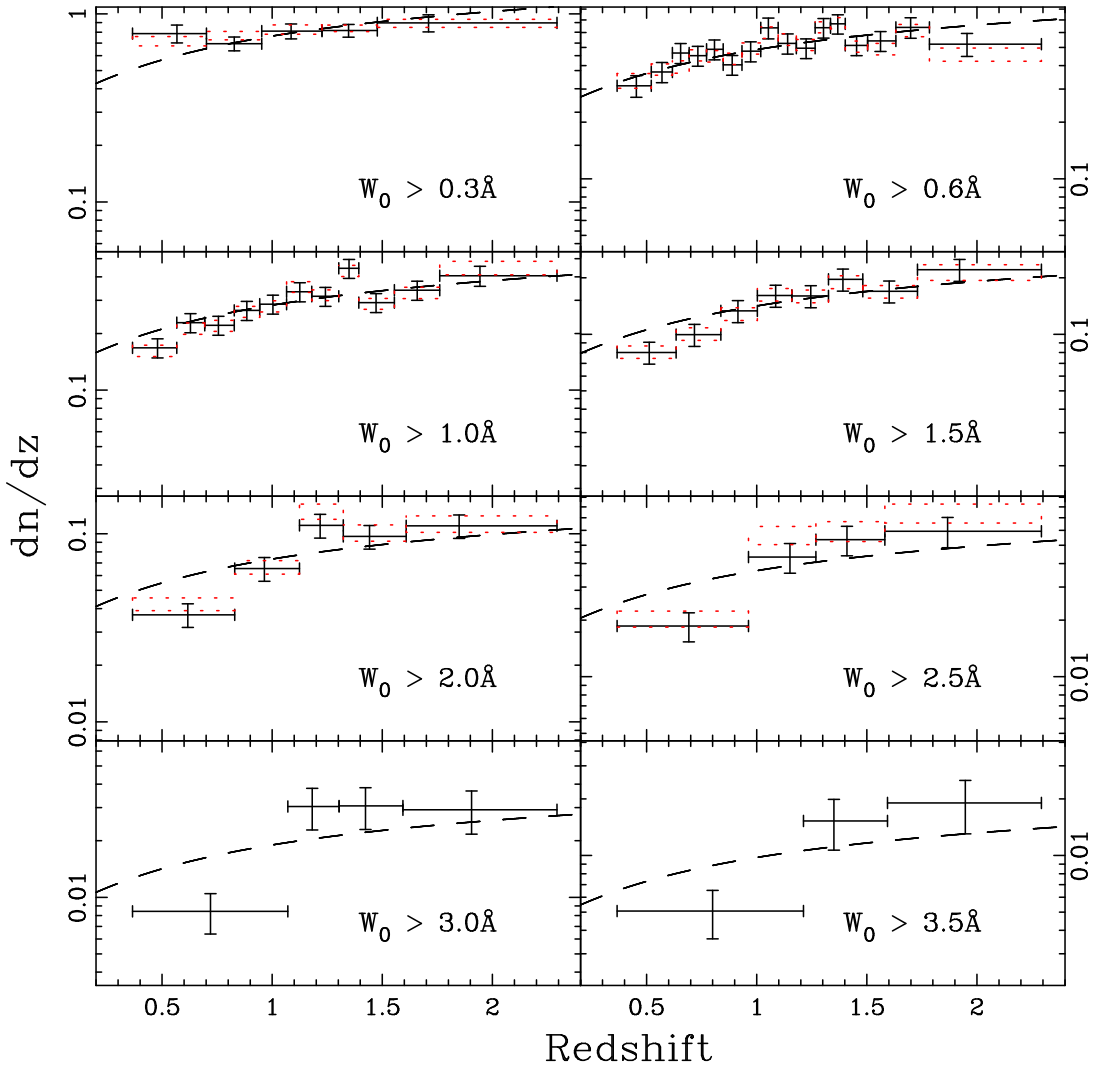

Figure 2.9: Number density evolution of Mg II absorbers for $W_0^{\lambda 2796} \geq W_0^{min}$ samples. The dashed lines are the no-evolution curves for a "WMAP" cosmology, $(\Omega_M, \Omega_\Lambda, h_0) = (0.3, 0.7, 0.7)$. The curves are normalized to minimize the χ^2 to the binned data. The $W_0^{min} = 0.3\,\text{Å}$, $0.6\,\text{Å}$, $1.0\,\text{Å}$, and $1.5\,\text{Å}$ samples have χ^2 values that are consistent with no evolution. The $W_0^{min} = 2.0\,\text{Å}$, $2.5\,\text{Å}$, and $3.0\,\text{Å}$ samples are inconsistent with the no evolution curves at $\gtrsim 3\sigma$, while the $W_0^{min} = 3.5\,\text{Å}$ sample is inconsistent at $\simeq 2\sigma$. The dotted boxes represent the results of the Monte Carlo simulation. The widths correspond to the bin sizes and the heights to the $\pm 1\sigma$ values. The $W_0^{min} = 3.0\,\text{Å}$ and $3.5\,\text{Å}$ samples were not large enough to permit meaningful Monte Carlo simulations.

are the no-evolution curves (NECs) for a cosmology with WMAP results, $(\Omega_M, \Omega_\Lambda, h) = (0.3, 0.7, 0.7)$[1], scaled to minimize the χ^2 to the binned data. The $W_0^{min} = 0.3$ Å, 0.6 Å, 1.0 Å, and 1.5 Å samples have χ^2 values that are consistent with no evolution. The $W_0^{min} =$ 2.0 Å, 2.5 Å, and 3.0 Å samples are inconsistent with the NECs at $\gtrsim 3\sigma$, while the $W_0^{min} =$ 3.5 Å sample is inconsistent at $\approx 2\sigma$. The dotted-boxes in Figure 2.9 show the results of the Monte Carlo simulation described in §2.2.4.

The large size of the data set allows investigation of dn/dz not only for distributions cumulative in $W_0^{\lambda 2796}$, but also for ranges of $W_0^{\lambda 2796}$. This is potentially important, as evolution in the largest $W_0^{\lambda 2796}$ values is not necessarily negligible in cumulative dn/dz distributions. Thus, the above analysis was repeated for the following ranges: $0.3 \leq W_0 < 0.6$ Å, $0.6 \leq W_0 < 1.0$ Å, $1.0 \leq W_0 < 1.5$ Å, $1.5 \leq W_0 < 2.0$ Å, $2.0 \leq W_0 < 2.5$ Å, $2.5 \leq W_0 < 3.0$ Å, $3.0 \leq W_0 < 3.5$ Å, and $W_0 \geq 3.5$ Å. The results are shown in Figure 2.10. The 0.6-1.0 Å, 1.0-1.5 Å, 1.5-2.0 Å, 2.0-2.5 Å and 2.5-3.0 Å samples have χ^2 values that are consistent with no evolution. The NEC for the 0.3-0.6 Å sample is ruled out at $\approx 2.5\sigma$ and for the 3.0-3.5 Å sample at $\approx 2.0\sigma$.

Since the NEC normalization is a free parameter, plots cumulative in redshift comparing dn/dz from the data to the NEC are more instructive. These plots, shown in Figures 2.11 and 2.12, highlight the skew of the dn/dz curves from the NEC prediction that is not necessarily manifested in the χ^2 analysis. The NECs over-predict dn/dz at low redshift for small W_0^{min} and under-predict dn/dz at low redshift for large W_0^{min}. The transition occurs for the cumulative $W_0^{\lambda 2796}$ plots between $W_0^{min} = 0.6$ and 1.0 Å and the effect is stronger for increasingly larger values of W_0^{min}. The plots using ranges of $W_0^{\lambda 2796}$ show that the transition from over- to under- predicting dn/dz at lower redshift occurs around 1 Å, and significant detection of evolution is seen in systems with $W_0^{\lambda 2796} \gtrsim 2.0$ Å. The evolution signal is strong ($\approx 4\sigma$) for lines with $W_0^{\lambda 2796} \geq 3.5$ Å. Although these plots do give a clearer indication of the deviation from the NECs, it is difficult to ascribe a K-S probability to the curves in Figures 2.11 and 2.12 because systems contribute to dn/dz in a non-uniform manner, i.e., inversely proportional to $\Delta Z\,(W_0^i, z)$.

The dn/dz point in the lowest redshift bin for the $W_0^{\lambda 2796} \geq 0.3$Å sample in Figure 2.9,

[1]See Appendix A (Figure A.1) for comparison of NECs with alternative cosmologies.

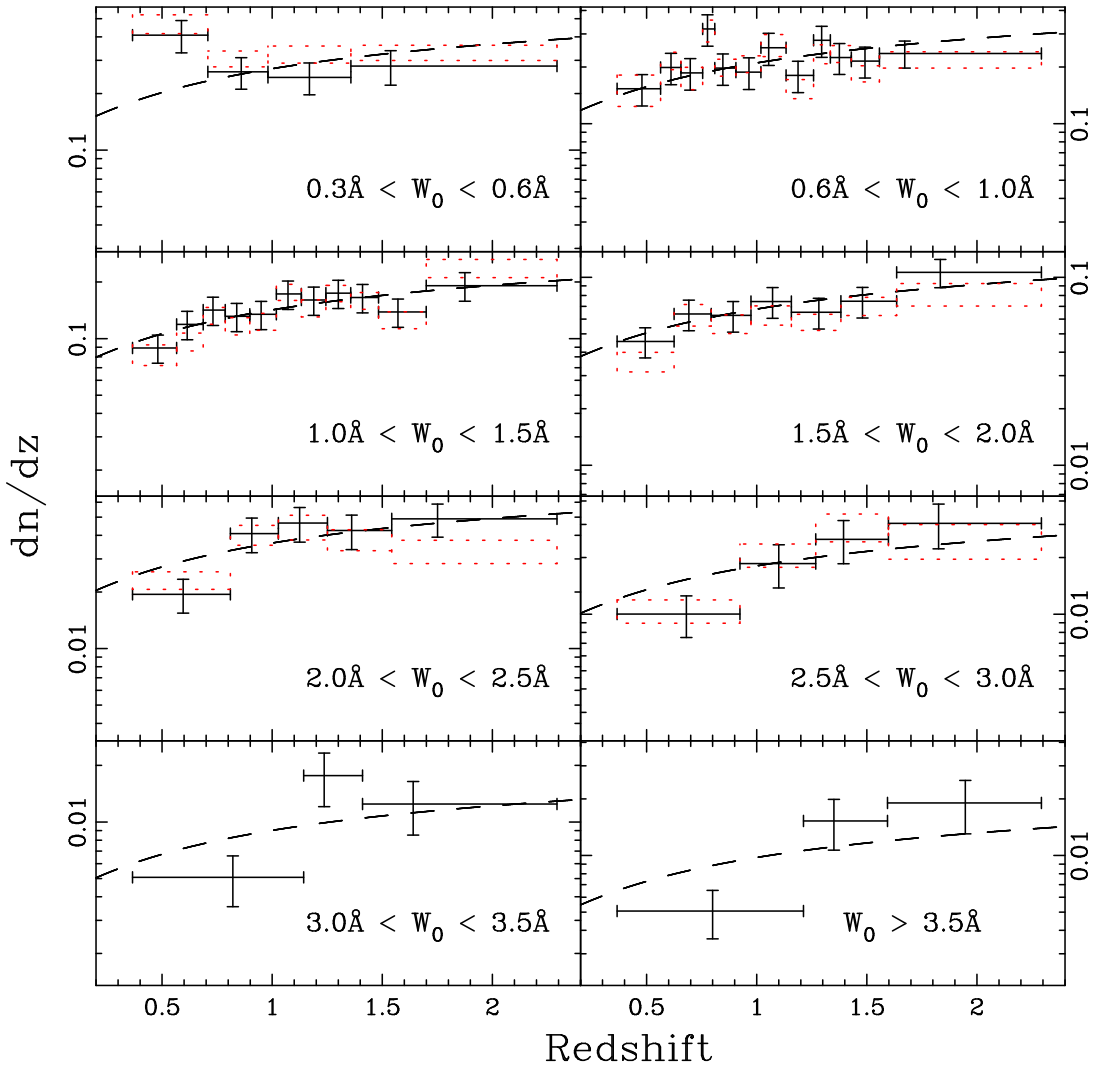

Figure 2.10: Number density evolution of Mg II absorbers for ranges of $W_0^{\lambda 2796}$. The dashed lines are the no-evolution curves for a "WMAP" cosmology, $(\Omega_M, \Omega_\Lambda, h_0) = (0.3, 0.7, 0.7)$. The curves are normalized to minimize the χ^2 to the binned data. The 0.6-1.0 Å, 1.0-1.5 Å, 1.5-2.0 Å, 2.0-2.5 Å and 2.5-3.0 Å samples have χ^2 values that are consistent with no evolution. The no-evolution curve for the 0.3-0.6 Å sample is ruled out at $\simeq 2.5\sigma$ and for the 3.0-3.5 Å and $\geq$ 3.5 Å samples at $\simeq 2.0\sigma$. The dotted boxes represent the results of the Monte Carlo simulation. The widths correspond to the bin sizes and the heights to the $\pm 1\sigma$ values. The 3.0-3.5 Å and greater than 3.5 Å samples were not large enough to permit meaningful Monte Carlo simulations.

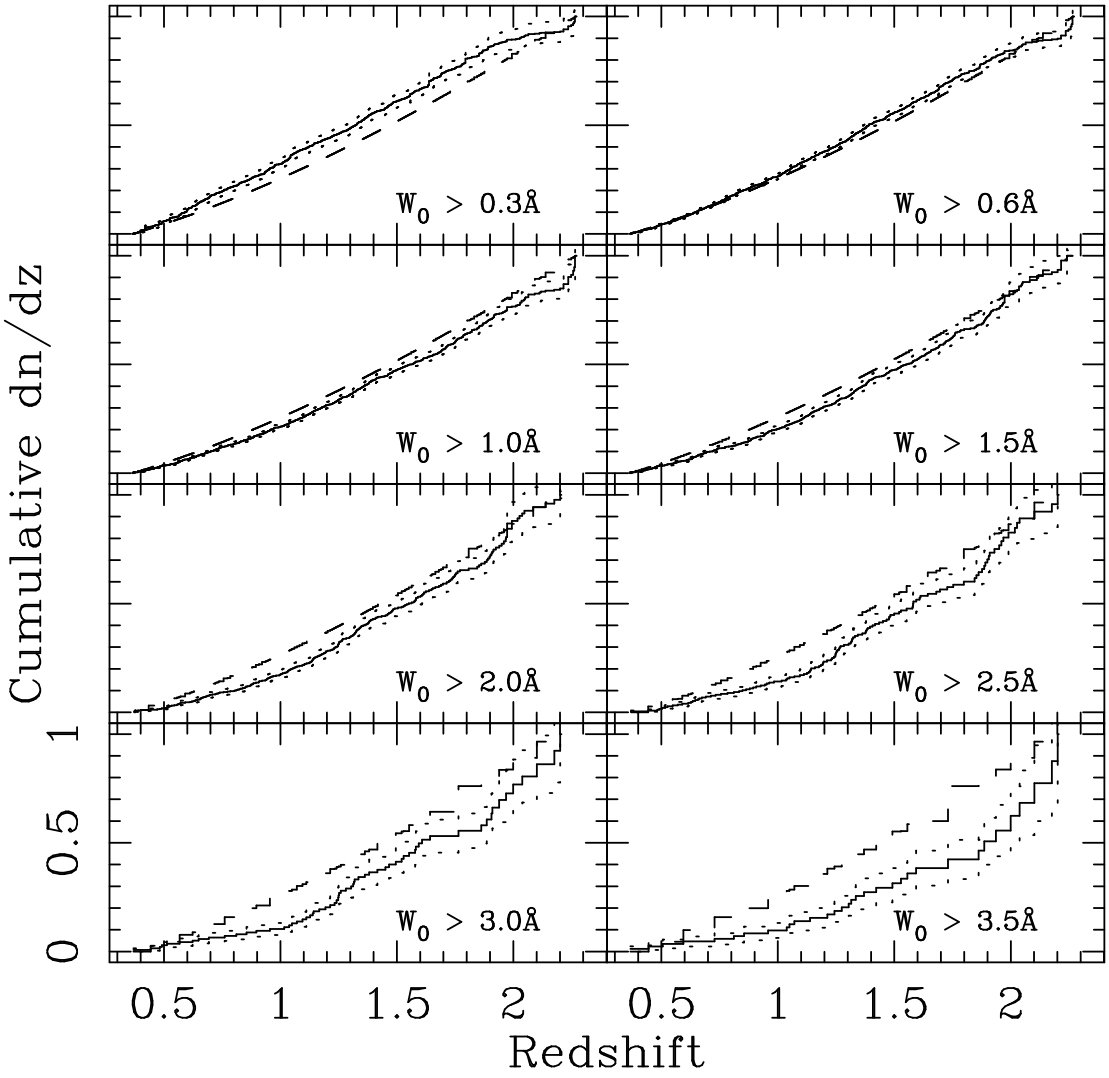

Figure 2.11: The cumulative distribution of dn/dz (solid lines) for the $W_0^{\lambda 2796} \geq W_0^{min}$ samples, compared with the cumulative no-evolution curves (dashed lines) for a "WMAP" cosmology $(\Omega_M, \Omega_\Lambda, h_0) = (0.3, 0.7, 0.7)$. The dotted curves represent the 1σ levels. The no evolution curves under-predict dn/dz at low redshift for the $W_0^{min} = 0.3\,\text{Å}$ sample, and over-predict dn/dz at low redshift for the larger W_0^{min} samples. The data are inconsistent with the NECs at more than 3σ for all but the $W_0^{min} = 0.6\,\text{Å}$ sample.

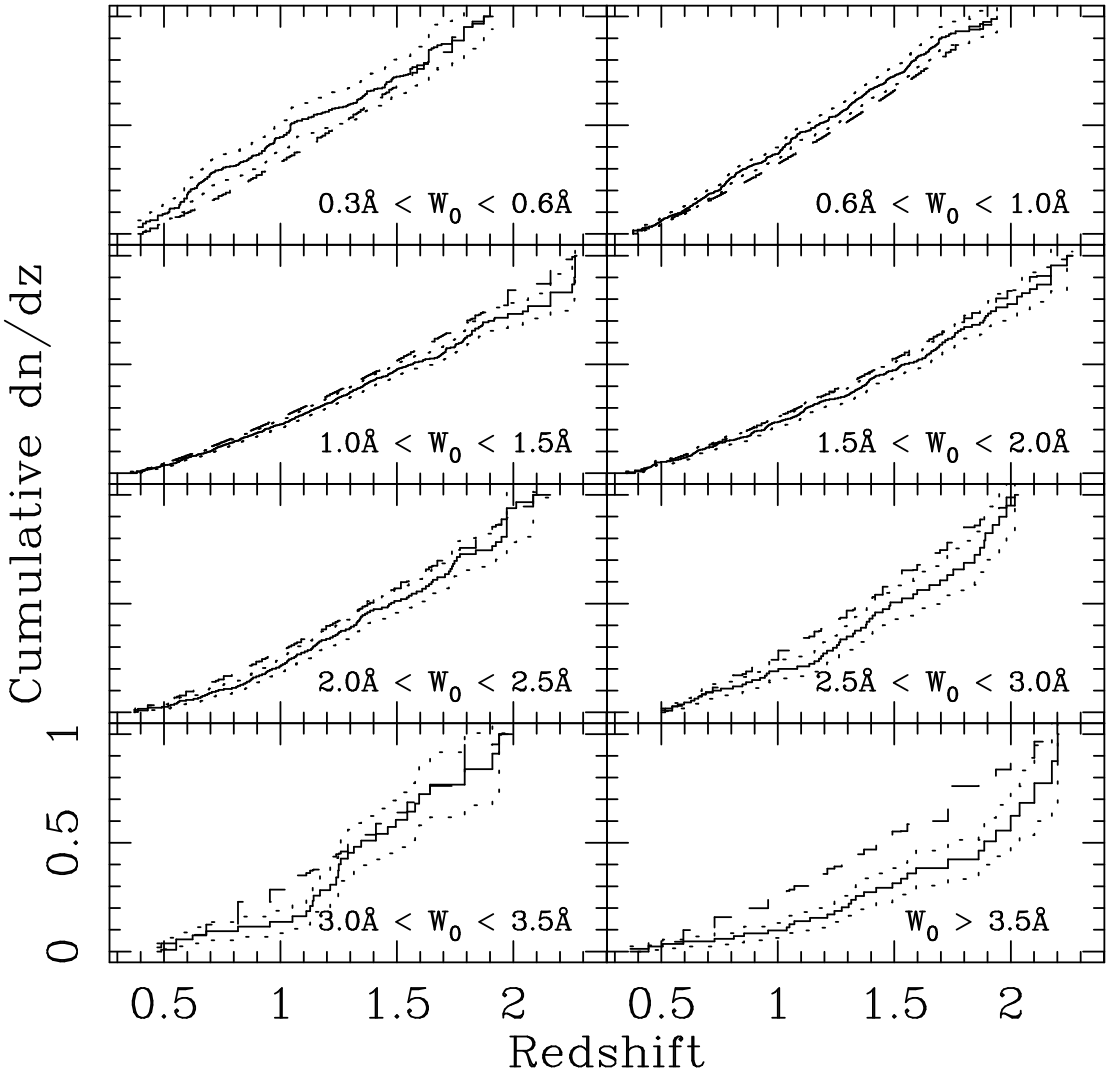

Figure 2.12: The cumulative distribution of dn/dz (solid lines) for the $W_0^{\lambda 2796}$ ranges, compared with the cumulative no-evolution curves (dashed lines) for a "WMAP" cosmology $(\Omega_M, \Omega_\Lambda, h_0) = (0.3, 0.7, 0.7)$. The dotted curves represent the 1σ levels. The no evolution curve under-predicts dn/dz at low redshift for the $W_0^{\lambda 2796} = 0.3$-$0.6\,\text{Å}$ and $W_0^{\lambda 2796} = 0.6$-$1.0\,\text{Å}$ samples, and over-predicts dn/dz at low redshift for the larger $W_0^{\lambda 2796}$ ranges. However, the data rule out the NECs at $\geq 3\sigma$ only for $W_0^{\lambda 2796} \geq 2.0\,\text{Å}$.

and for the $0.3 \leq W_0 < 0.6$ Å sample in Figure 2.10, lie well above the NEC. The increase is greater in magnitude but smaller in significance ($\approx 2\sigma$ versus $\approx 3\sigma$) for the non-cumulative sample. The Monte Carlo results lessen the significance in the cumulative sample, but not in the non-cumulative sample. Thus, the weakest lines in the study show evolution in the sense that their incidence *increases* with decreasing redshift. However, this may be an artifact of the sharp cutoff in the sample at 0.3Å. A sample with $W_0^{\lambda 2796} \geq 0.4$Å is consistent with the NEC, and dn/dz for $0.4 \leq W_0 < 0.6$ Å is within 1σ of the NEC at all redshifts. The possibility that the increase is real cannot be excluded, however.

Values for dn/dz for the entire redshift range are shown in Table 2.1. The $W_0 \geq 0.6$ and 1.0 results are consistent with SS92. However, this survey found a smaller value of dn/dz for $W_0 \geq 0.3$Å (though this difference is confined to $z \gtrsim 1.3$.)

2.3.3 Joint $W_0^{\lambda 2796}$-Redshift Distribution

Conventionally, the W_0-redshift distribution of absorption lines, $d^2n/dz\,dW_0$, has been parameterized by a combination of a power law in redshift and exponential in W_0 (Sargent et al., 1980; Lanzetta et al., 1987; Weymann et al., 1998, etc):

$$n(W_0) = \frac{N^*}{W^*} e^{-\frac{W_0}{W^*}}, \quad N(z) = N_0\,(1+z)^{\gamma}. \tag{2.7}$$

This parameterization is convenient for the determination of best-fit values for the parameters because of the separate W_0 and z dependences. However, this work has shown that W^* depends on redshift. Also, the data reveal that a single power law is not a good fit to dn/dz for any given range of $W_0^{\lambda 2796}$. Furthermore, dn/dz for different ranges of $W_0^{\lambda 2796}$ varies differently with redshift. The exponential form, however, has been shown to be a very good parameterization of the data at all redshifts for the range of $W_0^{\lambda 2796}$ covered by the sample. Therefore, the general form $n(W_0) = \frac{N^*}{W^*}\, e^{-\frac{W_0}{W^*}}$ is retained, but both N^* and W^* are allowed to vary with redshift as a power law in $(1+z)$.

Thus,

$$\frac{d^2n}{dz\,dW_0} = \frac{N^*(z)}{W^*(z)} e^{-\frac{W_0}{W^*(z)}} = \frac{\mathcal{N}^*}{\mathcal{W}^*}\,(1+z)^{\alpha-\beta}\, e^{-\frac{W_0}{W^*}(1+z)^{-\beta}}, \tag{2.8}$$

Table 2.1: dn/dz Comparison

$W_0^{\lambda 2796}$	SDSS		SS92	
Range (Å)	$\langle z_{abs} \rangle$	dn/dz	$\langle z_{abs} \rangle$	dn/dz
≥ 0.3	1.11	0.783 ± 0.033	1.12	0.97 ± 0.10
≥ 0.6	1.12	0.489 ± 0.015	1.17	0.52 ± 0.07
≥ 1.0	1.14	0.278 ± 0.010	1.31	0.27 ± 0.05
≥ 1.5	1.18	0.137 ± 0.006		
≥ 2.0	1.22	0.070 ± 0.005		
≥ 2.5	1.28	0.035 ± 0.003		
$0.3 - 0.8$	1.06	0.428 ± 0.031		
$0.8 - 1.3$	1.07	0.174 ± 0.009		
$1.3 - 1.8$	1.13	0.087 ± 0.005		
$1.8 - 2.3$	1.13	0.048 ± 0.004		
$2.3 - 2.8$	1.24	0.022 ± 0.003		
≥ 2.8	1.28	0.024 ± 0.003		

such that $N^*(z) = \mathcal{N}^*\,(1+z)^\alpha$ and $W^*(z) = \mathcal{W}^*\,(1+z)^\beta$. The likelihood of the data set is then

$$L = \prod_i \frac{(1+z_i)^{\alpha-\beta}\, e^{-\frac{W_0^i}{\mathcal{W}^*}(1+z_i)^{-\beta}}}{\int\int (1+z)^{\alpha-\beta}\, e^{-\frac{W_0}{\mathcal{W}^*}(1+z)^{-\beta}}\, \Delta Z(W_0,z)\, dz\, dW_0}. \tag{2.9}$$

The parameters that maximize the likelihood are $\alpha = 0.226 \pm 0.170$, $\beta = 0.634 \pm 0.097$, and $\mathcal{W}^* = 0.443 \pm 0.032$, which were determined with the aid of the MINUIT[2] minimization software. The resulting normalization is $\mathcal{N}^* = 1.001 \pm 0.132$. Thus, $N^* = 1.001 \pm 0.132\,(1+z)^{0.226\pm0.170}$ and $W^* = 0.443 \pm 0.032\,(1+z)^{0.634\pm0.097}$. The maximum likelihood values are highly correlated, and the errors include the effects of the correlations.

The full covariance matrix is

$$\begin{pmatrix} \sigma^2_{\alpha\alpha} & \sigma^2_{\alpha\beta} & \sigma^2_{\alpha W^*} \\ \sigma^2_{\beta\alpha} & \sigma^2_{\beta\beta} & \sigma^2_{\beta W^*} \\ \sigma^2_{W^*\alpha} & \sigma^2_{W^*\beta} & \sigma^2_{W^*W^*} \end{pmatrix} = \begin{pmatrix} 0.0291 & -0.00990 & 0.00322 \\ -0.00990 & 0.00931 & -0.00292 \\ 0.00322 & -0.00292 & 0.00104 \end{pmatrix}, \tag{2.10}$$

which should be used when calculating the uncertainty in $d^2n/dz\,dW_0$. N^* was determined from the fit so that $\int\int \frac{d^2n}{dz\,dW_0}\, g(W_0,z)\, dz\, dW_0$ equaled the total number of lines in the survey. The full covariance array was used to calculate σ_{N^*}. No contribution from the uncertainty in the number of lines was used, as it was estimated with a jackknife method to be small ($\lesssim 3\%$). Since the uncertainty in N^* is derived from the uncertainty in the other parameters, it should not be considered when using equation 2.8. For example, for $dn/dz = N^*\,(1+z)^\alpha\, e^{-\frac{W_0}{\mathcal{W}^*}(1+z)^{-\beta}}$ the uncertainty is given by

$$\sigma^2_{dn/dz} = \sigma^2_{\alpha\alpha}\left(\frac{\partial\frac{dn}{dz}}{\partial\alpha}\right)^2 + \sigma^2_{\beta\beta}\left(\frac{\partial\frac{dn}{dz}}{\partial\beta}\right)^2 + \sigma^2_{\mathcal{W}^*\mathcal{W}^*}\left(\frac{\partial\frac{dn}{dz}}{\partial\mathcal{W}^*}\right)^2 + \tag{2.11}$$
$$2\sigma^2_{\alpha\beta}\left(\frac{\partial\frac{dn}{dz}}{\partial\alpha}\right)\left(\frac{\partial\frac{dn}{dz}}{\partial\beta}\right) + 2\sigma^2_{\alpha\mathcal{W}^*}\left(\frac{\partial\frac{dn}{dz}}{\partial\alpha}\right)\left(\frac{\partial\frac{dn}{dz}}{\partial\mathcal{W}^*}\right) + 2\sigma^2_{\beta\mathcal{W}^*}\left(\frac{\partial\frac{dn}{dz}}{\partial\beta}\right)\left(\frac{\partial\frac{dn}{dz}}{\partial\mathcal{W}^*}\right),$$

where $\frac{\partial\frac{dn}{dz}}{\partial\alpha} = \frac{dn}{dz}\ln(1+z)$, $\frac{\partial\frac{dn}{dz}}{\partial\beta} = \frac{dn}{dz}\frac{W}{\mathcal{W}^*}(1+z)^{-\beta}\ln(1+z)$, and $\frac{\partial\frac{dn}{dz}}{\partial\mathcal{W}^*} = \frac{dn}{dz}\frac{W_0}{\mathcal{W}^{*\,2}}(1+z)^{-\beta}$. All uncertainties are statistical errors only. Possible systematics are discussed in §2.3.4.

The analyses of §2.3.2 were repeated, comparing the dn/dz curves to those determined using the redshift parameterization of N^* and W^*. The results, shown in Figures 2.13 and 2.14, indicate that the parameterization is indeed a good description of all of the data. The

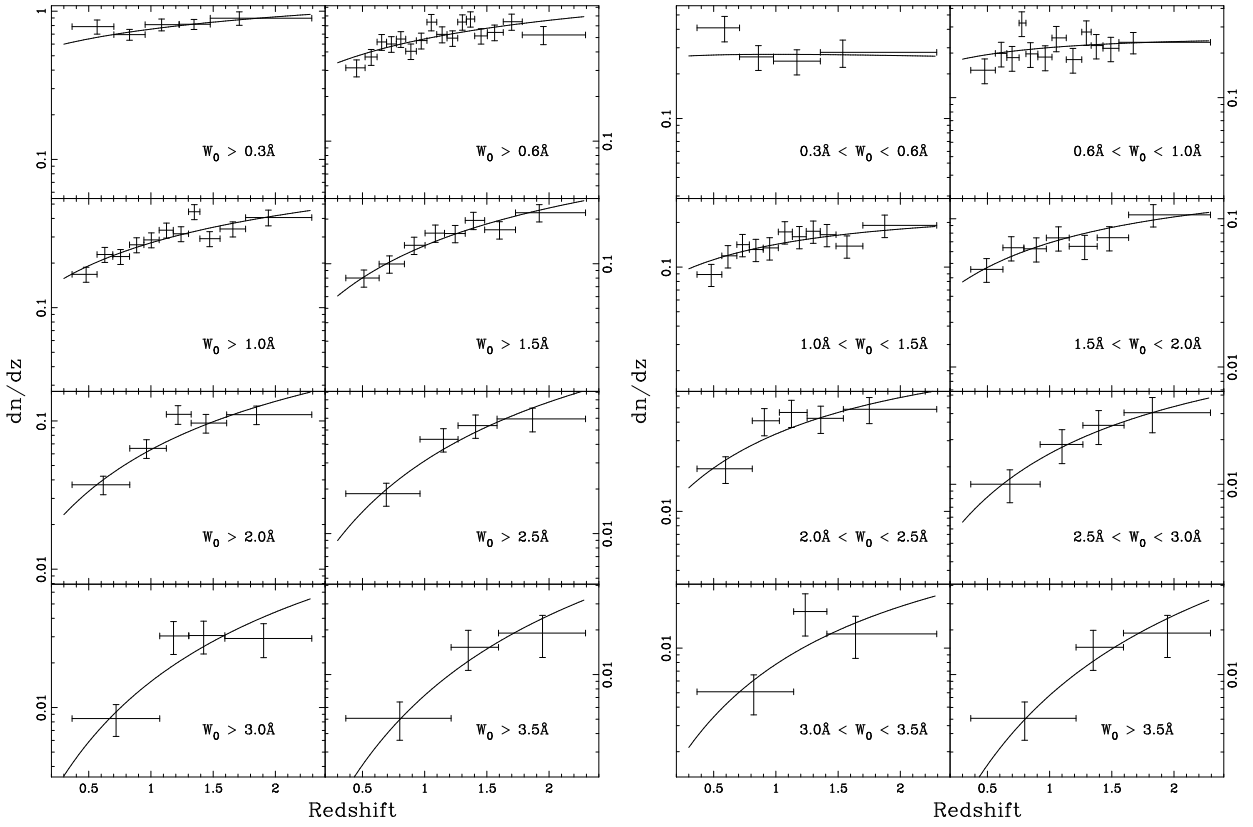

Figure 2.13: dn/dz curves calculated from the parameterization of §2.3.3. The dn/dz data are consistent with the fit for all ranges shown. Left: The cumulative samples. Right: The non-cumulative samples.

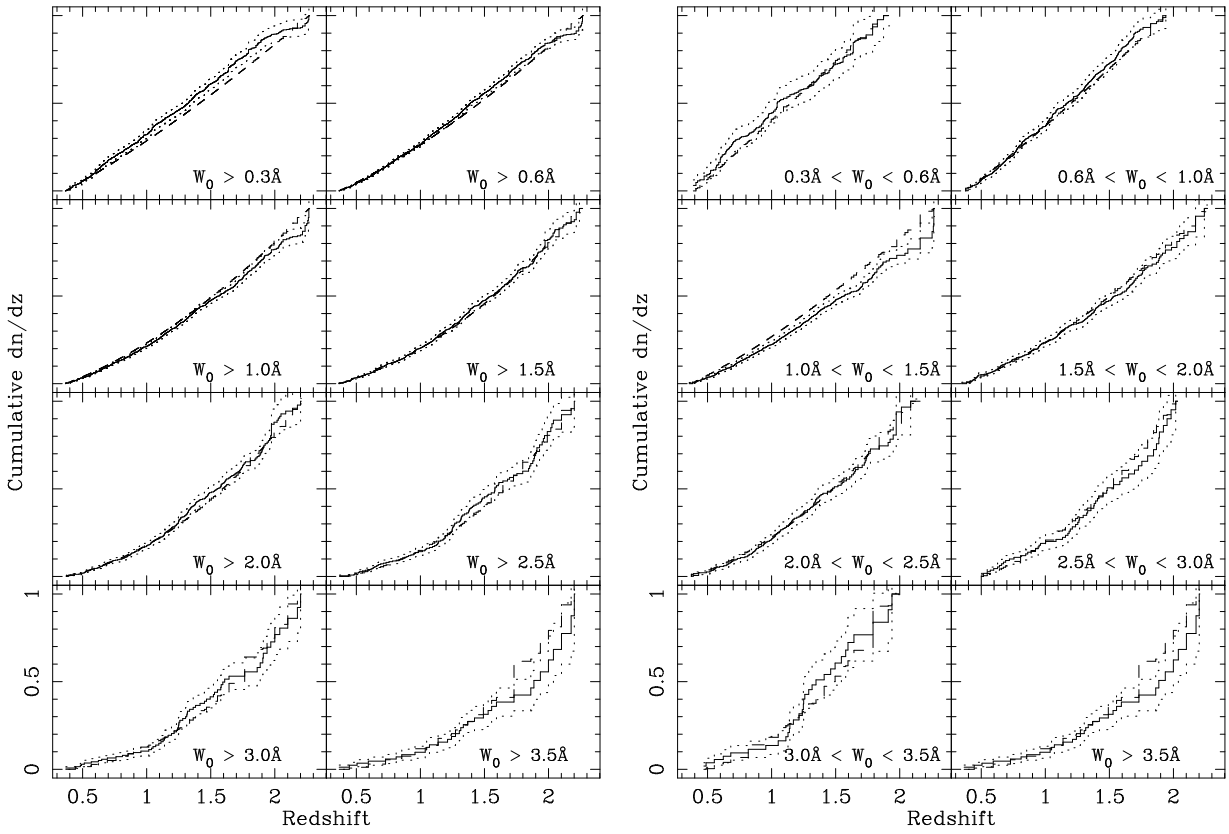

Figure 2.14: The cumulative distribution of dn/dz plotted against the cumulative dn/dz curves calculated from the parameterization of §2.3.3. The dn/dz data are consistent with the fit for all ranges shown.

evolution is well described by a steepening of the $W_0^{\lambda 2796}$ distribution with a normalization that changes such as to keep dn/dz constant for the smaller $W_0^{\lambda 2796}$ values. Extrapolating the parameterization to lower redshift predicts $dn/dz = 0.28 \pm 0.03$ for $W_0^{\lambda 2796} \geq 0.6$Å and $\langle z \rangle = 0.06$, and $dn/dz = 0.11 \pm 0.02$ for $W_0^{\lambda 2796} \geq 1.0$Å and $\langle z \rangle = 0.04$, in comparison to the Churchill (2001) values of $dn/dz = 0.22^{+0.12}_{-0.09}$ and $dn/dz = 0.16^{+0.09}_{-0.05}$, respectively. However, the parameterization is likely inappropriate for describing $W_0^{\lambda 2796} < 0.3$Å lines, since not including the apparently two-component nature of the $W_0^{\lambda 2796}$ distribution leads to underestimates of the number density of weak lines (Figure 2.3).

Table 2.2 summarizes the various parameterizations of the data.

2.3.4 Systematic Errors

The Monte Carlo simulations did not uncover any significant systematic errors. All of the Monte Carlo dn/dz values are consistent with those from the data. However, since the data were used to model the simulated lines, if there are lines with characteristics that make them underrepresented in the data, they would also be underrepresented in the simulated catalogs. Simulations were run to address this issue as the line-finding algorithm was developed. Although it is possible that certain types of lines are missed, such as weak kinematic outliers or lines with abnormally broad or exotic profiles, for example, these effects are likely to be small.

A potentially more serious source of systematic error may arise in the regions of poorly subtracted night sky lines seen in some of the spectra. The error arrays are not always accurate in these regions, and doublets falling between sky lines can be confused with residuals from the poor subtraction. As the errors are larger (though not necessarily accurate) in the night sky regions, the values of W_0^{lim} are large as well. Thus, only the strongest lines would be affected. In principle, the simulations should account for these effects. However, since non-Gaussian profiles are preferentially found among the stronger lines, their simulation is somewhat less reliable. Also, their numbers are much smaller, providing fewer lines to serve as models in the simulation, and less overall significance. The largest $W_0^{\lambda 2796}$ ranges were,

[2] © CERN, Geneva 1994-1998

Table 2.2: Summary of Data Parameterizations

	N^*	W^*
	Data	
Full Sample:	1.134 ± 0.069	0.702 ± 0.017
$0.366 \leq z \leq 0.871$:	1.134 ± 0.124	0.585 ± 0.024
$0.871 \leq z \leq 1.311$:	1.160 ± 0.121	0.741 ± 0.032
$1.311 \leq z \leq 2.269$:	1.243 ± 0.126	0.804 ± 0.034
	Monte Carlo Simulations	
"weak"-phase:	1.71 ± 0.02	0.072 ± 0.001
"strong"-phase:	0.932 ± 0.011	0.771 ± 0.014
	Redshift Dependence	
	$1.001 \pm 0.132\,(1+z)^{0.226 \pm 0.170}$	$0.443 \pm 0.032\,(1+z)^{0.634 \pm 0.097}$

in fact, too sparse for meaningful simulations. Errors of this type would be manifest in the largest $W_0^{\lambda 2796}$ ranges and for redshifts $z \sim 1.6 - 2.0$.

Finally, in quasar absorption-line studies it is of interest to asses if biases due to the presence of the absorber affecting the magnitude and color of the background quasar are present. The most often discussed effect is that of a dimming and reddening of the background quasar due to dust in the absorber. However, the presence of an absorbing galaxy could also have a lensing effect, causing the quasar to appear brighter. These competing effects are investigated, using the absorbers and simulations from this work, in Ménard, Nestor, & Turnshek (in preparation). They find that for $W_0^{\lambda 2796} \lesssim 0.8$, both effects are small. For $0.8 \lesssim W_0^{\lambda 2796} \lesssim 3.0$, the lensing magnification dominates, with the magnitude shift $\delta m \approx 0.1 - 0.2$. For $W_0^{\lambda 2796} \gtrsim 1.2$, the reddening becomes significant, and the extinction effectively cancels the magnification bias for $W_0^{\lambda 2796} \gtrsim 3.0$. As the SDSS EDR quasar catalog selection properties were not necessarily homogeneous, it is difficult to quantify the effect these results may have on the data. For lines with $0.8 \lesssim W_0^{\lambda 2796} \lesssim 1.2$, there may be a slight positive bias in their contribution to the W_0 distribution. For lines with $1.2 \lesssim W_0^{\lambda 2796} \lesssim 3.0$, it is unclear what the effect would be, as the quasars appear brighter, but redder. For the strongest lines, with $W_0^{\lambda 2796} \gtrsim 3.0$, it is probable that there is a slight negative bias in their contribution to $n(W_0^{\lambda 2796})$. If these effects are non-negligible, they could affect the measured $W_0^{\lambda 2796}$ distribution. The biases are likely to be small, however, since it would be peculiar if they conspired to drive $n(W_0^{\lambda 2796})$ to more closely resemble an exponential, and there is no noticeable deviation from an exponential, consistent with the expected biases, seen in Figure 2.3. Since dust increases with decreasing redshift (consistent with the findings of Nestor et al. (2003) and Chapter 3), it is worth considering if the evolution in dn/dz seen for the strongest systems is an effect of increasing dust. However, Ménard et al. find no such increase in bias with decreasing redshift. Also, Ellison et al. (2004) compare Mg II dn/dz determined from radio-selected CORALS survey spectra to values obtained with optical surveys (including this work), and find good agreement. Therefore, the steepening of the $W_0^{\lambda 2796}$ distribution due to a disappearance of the largest $W_0^{\lambda 2796}$ lines at low redshift and the evolution in dn/dz for strong lines appear to be real.

While more recent SDSS quasar spectra offer the opportunity to increase the Mg II

absorber sample by another order of magnitude, systematic errors in line identification and measurement will begin to dominate in the determination of absorber property statistics.

2.3.5 Mg II Doublet Ratio

Mg II doublet ratios span $DR = 2.0$ for completely unsaturated systems to $DR = 1.0$ for completely saturated systems. Figure 2.15 shows the DR distribution for the sample. The doublets are, for the most part, saturated. Ninety percent of doublets with a measured DR are within 3σ of $DR = 2.0$, and 92% have $DR - 1.0 > \sigma_{DR}$. Figure 2.16 shows DR as a function of redshift. There is no detectable evolution in the DR distribution. In fact, the DR distribution is remarkably consistent over the three redshift ranges of Figures 2.5 and 2.6.

2.3.6 Mg II Velocity Dispersions

For absorption lines that are at least partially saturated, such as those that dominate the sample studied here, W_0 is primarily a measure of the number of kinematic subcomponents (clouds) along the line of sight (Petitjean and Bergeron, 1990) and, to a lesser extent, projected velocity dispersion, $\sigma_{vel,p}$ (Churchill et al., 2000). Information about $\sigma_{vel,p}$ of individual systems can be directly extracted by deconvolving the fitted profile and the line spread function. However, as most doublets are at most only mildly resolved, this approach is not sensitive for all but the most resolved systems. Nonetheless, the evolution of the $\sigma_{vel,p}$ distribution over the three redshift bins of Figures 2.5 and 2.6 was investigated. In all three redshift ranges, $\simeq 80\%$ of the systems have measured values of $\sigma_{vel,p} < 90$ km s^{-1}. Comparing just systems with $\sigma_{vel,p} > 90$ km s^{-1}, it was found that $\sigma_{vel,p}$ tends to be smaller in the lowest redshift bin (see Figure 2.17). However, the middle- and lower-redshift bin velocity distributions only differ at the 1σ level.

2.3.7 Fe II λ2600 and Mg I λ2852

Figure 2.18 shows the distribution of Fe II $W_0^{\lambda 2600}$ for the sample. The error-weighted mean

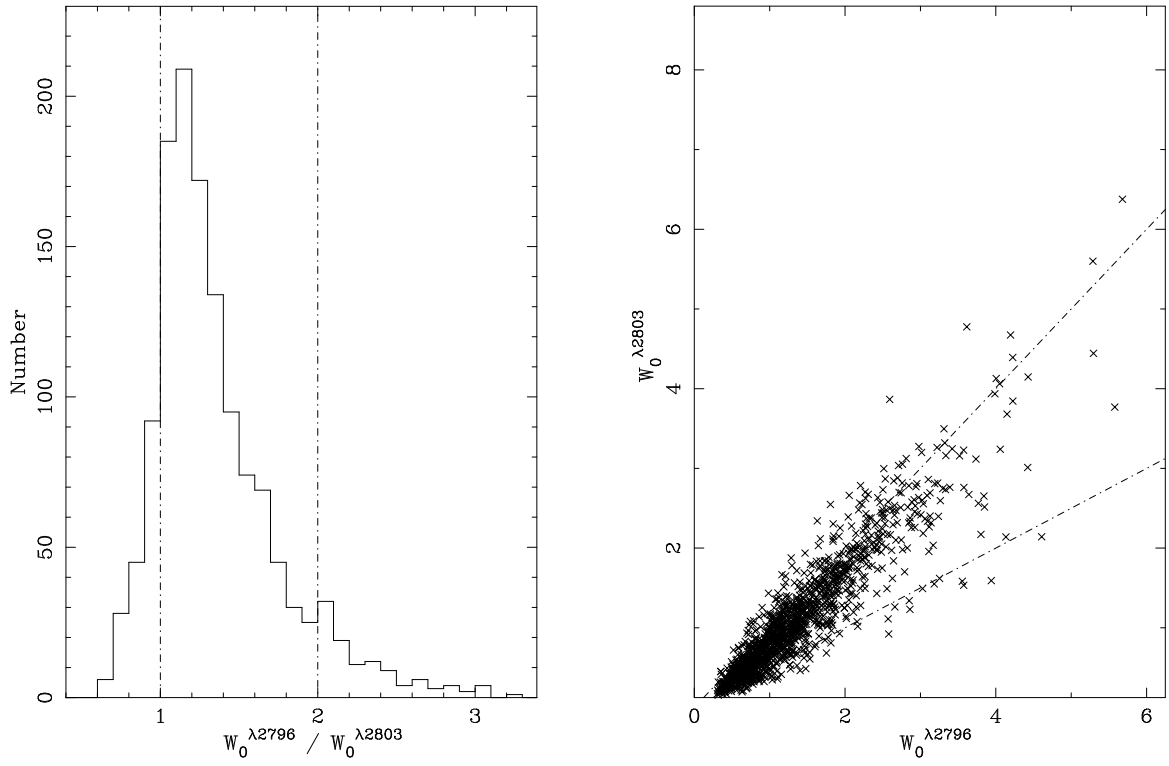

Figure 2.15: Left: the distribution of $W_0^{\lambda 2796}/W_0^{\lambda 2803}$ doublet ratio for Mg II systems with $W_0^{\lambda 2796} \geq 0.3$Å. The dashed lines mark the limits of 1.0 for completely saturated systems and 2.0 for completely unsaturated systems. Values above and below these limits are due to noise. The sample is dominated by saturated systems. Right: $W_0^{\lambda 2803}$ versus $W_0^{\lambda 2796}$.

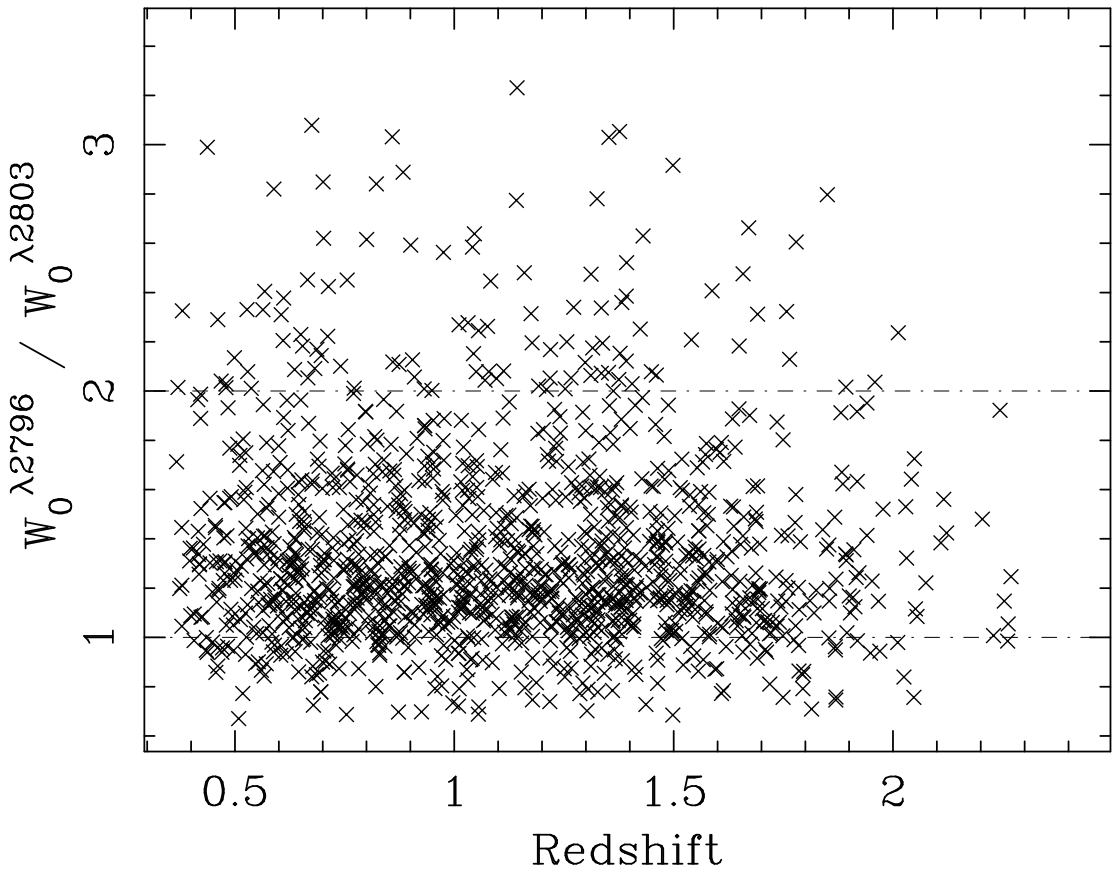

Figure 2.16: $W_0^{\lambda 2796}/W_0^{\lambda 2803}$ doublet ratio as a function of redshift for Mg II systems with $W_0^{\lambda 2796} \geq 0.3$. There is no detected redshift evolution in the doublet ratio.

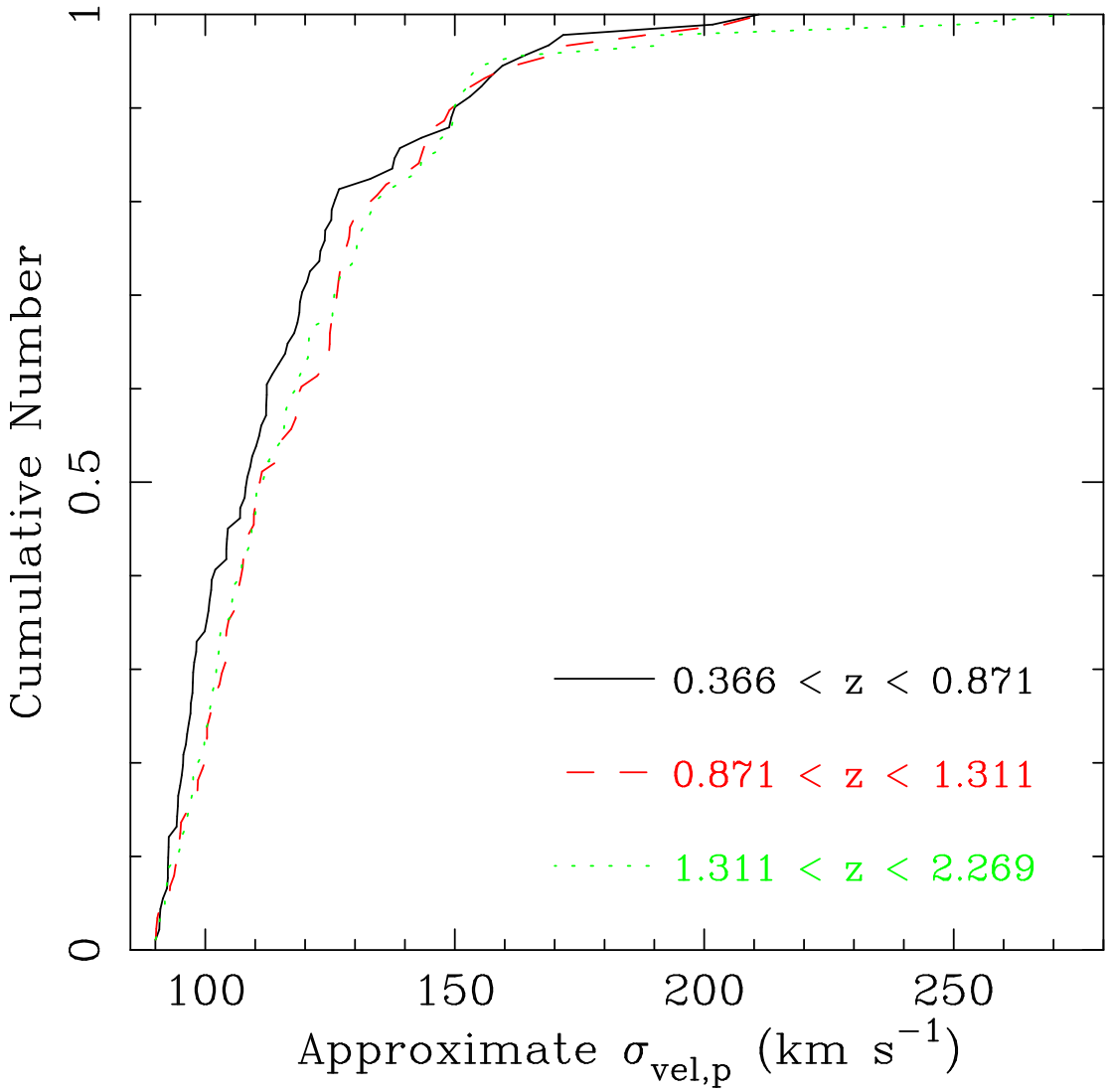

Figure 2.17: Cumulative distribution of approximate velocity dispersions for $\sigma_{vel,p} > 90$ km s^{-1}. The lower and middle redshift bins differ in K-S probability at the $\approx 1\sigma$ level.

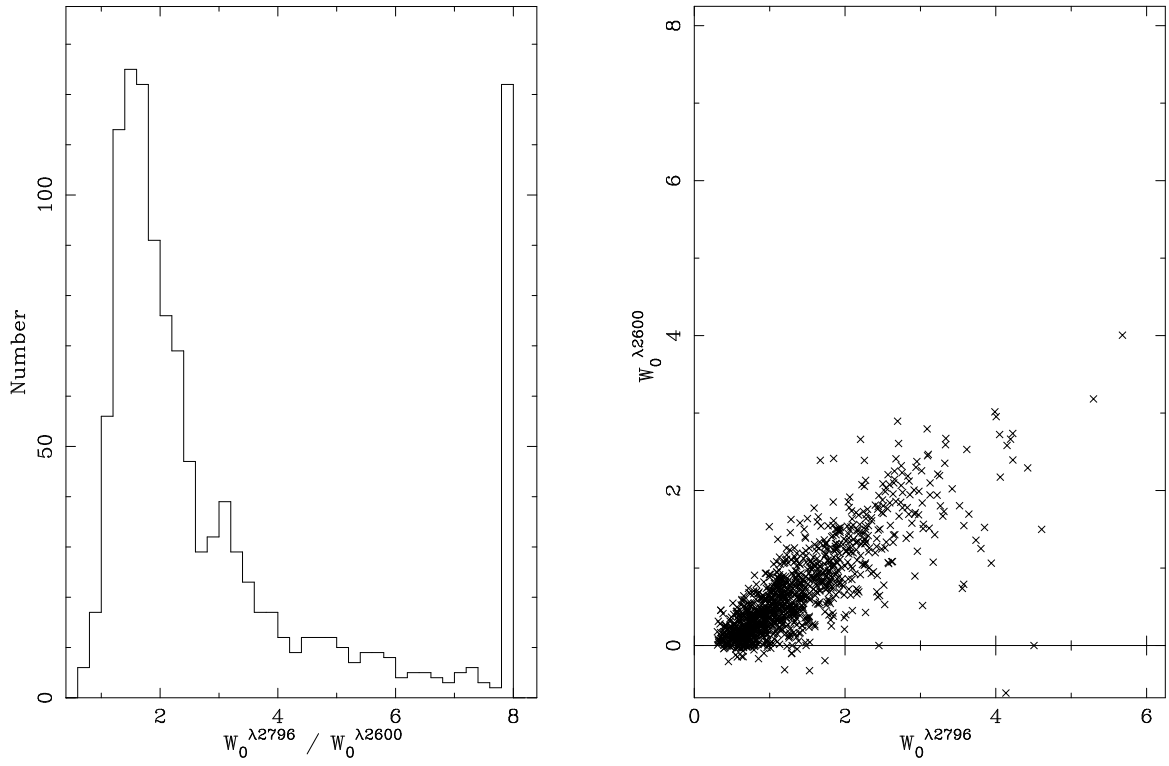

Figure 2.18: Mg II – Fe II ratio. Left: The distribution of Mg II λ2796 – Fe II λ2600 line ratios. The largest bin also contains all systems with ratios greater than 8.0, which includes non-detections of Fe II λ2600. The mean is $\left\langle W_0^{\lambda 2796}/W_0^{\lambda 2600}\right\rangle = 1.42$ and ratios above ≈ 4 are dominated by values with significance less than 3σ. Right: $W_0^{\lambda 2600}$ versus $W_0^{\lambda 2796}$. Negative $W_0^{\lambda 2600}$ values are non-detections with scatter below zero.

is $\left\langle W_0^{\lambda 2796}/W_0^{\lambda 2600}\right\rangle = 1.42$ and the distribution has a smooth tail extending out to large values, though ratios above ≈ 4 are dominated by values with significance less than 3σ. Figure 2.19 shows the distribution of Mg I $W_0^{\lambda 2852}$ for the sample. The error-weighted mean is $\left\langle W_0^{\lambda 2796}/W_0^{\lambda 2852}\right\rangle = 4.14$ and the distribution has a smooth tail extending out to large values, though ratios above ≈ 8 are dominated by values with significance less than 3σ.

2.4 CONCLUSIONS

Over 1,300 Mg II absorption systems have been identified with $W_0^{\lambda 2796} \geq 0.3$Å over the redshift range $0.367 \leq z \leq 2.269$ in the SDSS EDR quasar spectra. The size of the sample is such that statistical errors are comparable to systematic effects and biases. Simulations were used to improve the line-finding algorithm until the systematics could no longer be isolated from the noise at a level where the parameterizations could be further improved. Using the combined redshift and $W_0^{\lambda 2796}$ data, a new redshift parameterization was offered for the distribution of systems. In conclusion, it has been shown that:

1. The rest equivalent width distribution for intervening Mg II $\lambda 2796$ absorption lines detected in the SDSS EDR quasar spectra with $W_0^{\lambda 2796} \geq 0.3$Å is very well described by an exponential, with $N^* = 1.187 \pm 0.052$ and $W^* = 0.702 \pm 0.017$. Power law parameterizations drastically over-predict the number of strong lines, and the exponential under-predicts previously reported values for the number density of weaker lines.
2. The rest equivalent width distribution steepens with decreasing redshift, with W^* decreasing from 0.80 ± 0.04 at $z = 1.6$ to 0.59 ± 0.02 at $z = 0.7$.
3. When compared with the number density of $W_0^{\lambda 2796} < 0.3$Å lines from other studies, the results show that neither an exponential nor a power law accurately represents the full range of $W_0^{\lambda 2796}$. Simulations of the catalog support this finding. A combination of two exponential distributions is proposed, where the weak lines are described by the parameters $N^*_{wk} \approx 1.7$ and $W^*_{wk} \approx 0.1$ and the moderate and strong lines by the parameters $N^*_{str} \approx 0.9$ and $W^*_{str} \approx 0.8$.
4. For lines with $W_0^{\lambda 2796} \lesssim 2$Å, there is no significant evolution detected in dn/dz.

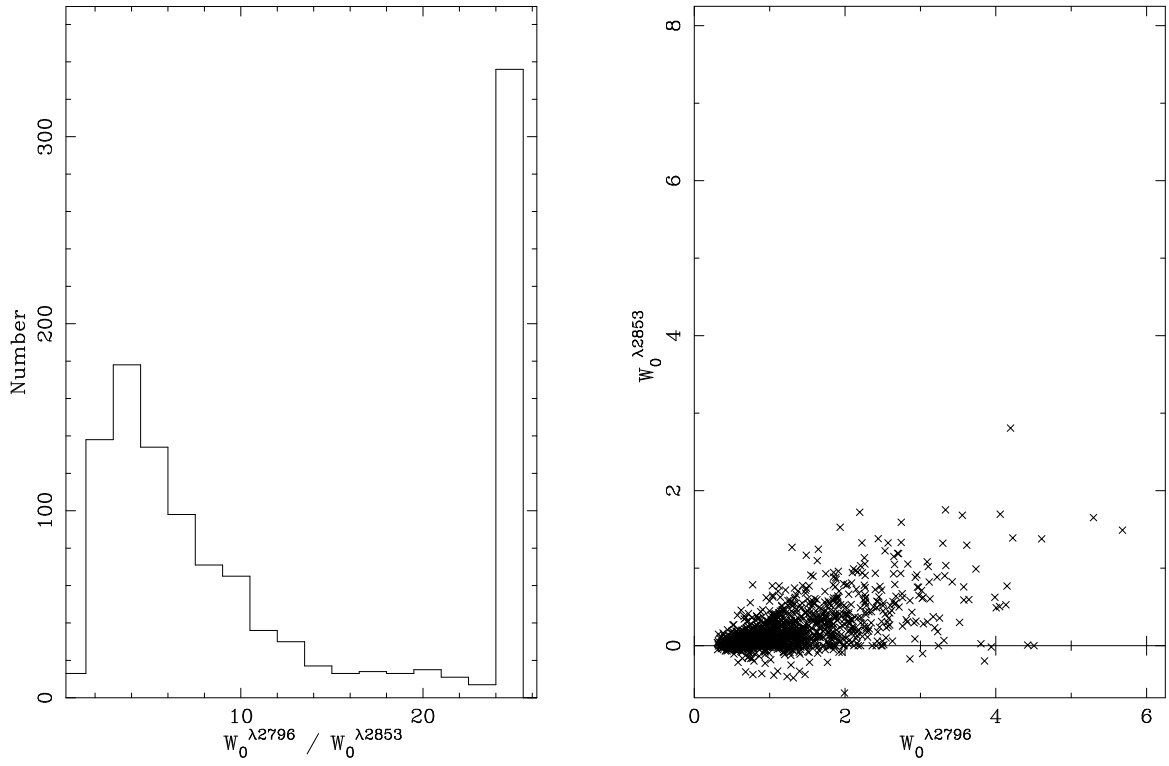

Figure 2.19: Mg II – Mg I ratio. Left: The distribution of Mg II λ2796 – Mg I λ2852 line ratios. The largest bin also contains all systems with ratios greater than 25, which includes non-detections of Mg I λ2852. The mean is $\left\langle W_0^{\lambda 2796}/W_0^{\lambda 2852}\right\rangle = 4.14$ and ratios above ≈ 8 are dominated by values with significance less than 3σ. Right: $W_0^{\lambda 2852}$ versus $\mathrm{W}_0^{\lambda 2796}$. Negative $W_0^{\lambda 2852}$ values are non-detections with scatter below zero.

5. For lines with $W_0^{\lambda 2796} \gtrsim 2$Å, evolution is detected in dn/dz, with a decrease from the no-evolution prediction of $\approx 45\%$ from $z = 1.8$ to 0.6. The evolution is stronger for stronger lines and redshifts $z \lesssim 1$.
6. The number density of Mg II absorption lines with $W_0^{\lambda 2796} \geq 0.3$Å is well parameterized by $\frac{d^2n}{dz\,dW_0} = \frac{N^*(z)}{W^*(z)}\,e^{-\frac{W_0}{W^*(z)}}$, with $N^*(z) = 1.001 \pm 0.132\,(1+z)^{0.226\pm0.170}$ and $W^*(z) = 0.443 \pm 0.032\,(1+z)^{0.634\pm0.097}$.

Further discussion of the physical nature and the evolution of the statistical properties of Mg II absorbers will be presented in Chapter 6.

3.0 MMT SURVEY FOR LOW-Z MG II ABSORPTION SYSTEMS

3.1 INTRODUCTION

With the aim of extending the measurement of Mg II absorber statistics to lower redshift, a spectroscopic quasar absorption line survey was conducted using the Multiple Mirror Telescope (MMT) on Mount Hopkins, AZ. Instrumentation at the MMT allows for optical spectroscopy down to $\lambda \approx 3200$Å, corresponding to an Mg II absorption redshift of $z = 0.14$.

Figure 3.1 demonstrates the dependence of look-back time on redshift. The lines indicate the range of redshift/look-back time covered by the SDSS EDR Mg II absorber survey described in Chapter 2. That catalog is an order of magnitude larger than all previous studies, and covers a broad redshift range that corresponds to roughly half the age of the Universe. However, as Figure 3.1 shows, dt/dz is larger for smaller redshift. Thus, a given δz at low redshift covers more look-back time than an equal δz at higher redshift. Furthermore the low-redshift regime is of particular interest, as the evolution of Mg II systems increases with decreasing redshift, and low-z absorbers can be compared more directly with the local universe. As blind 21cm emission studies are limited to $z \lesssim 0.1$, extending the study of large H I column systems studied via quasar absorption lines to the lowest redshifts possible is necessary for a continuous understanding of the evolution over this important cosmic time interval.

An additional benefit of the MMT survey is that many of the spectra obtained have signal to noise ratios much greater than those typical of the SDSS EDR, enabling the study of $W_0^{\lambda 2796} < 0.3$Å systems, as well as stronger systems, in the same survey. As the transition seen in $n(W_0^{\lambda 2796})$ occurs precisely at the boundary of two different studies, it is a concern that it may arise due to unknown systematic differences in the studies. This concern, which

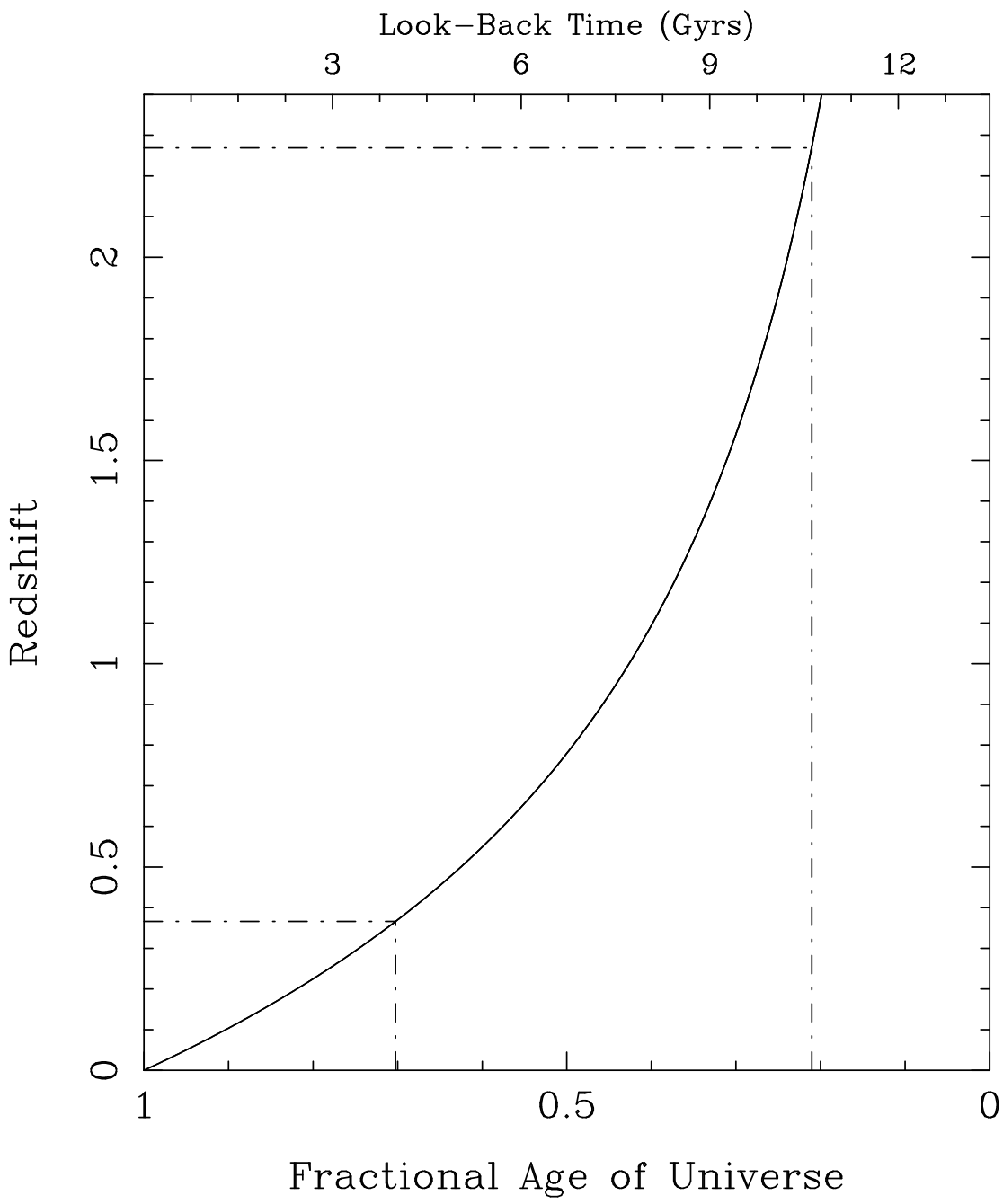

Figure 3.1: Age–redshift relation of the Universe. The lines indicate the range of redshift/look-back time covered by the SDSS EDR Mg II absorber survey described in Chapter 2.

is an important aspect of the understanding of the physical picture of the absorbing clouds, can be addressed with the MMT survey.

3.2 OBSERVATIONS AND DATA REDUCTION

The observations took place over a 42 month period from January of 2001 to May of 2004 at the 6.5m MMT on the summit of Mount Hopkins, AZ. Useful data were collected on 17 nights spread over seven observing runs. The MMT spectrograph was operated using the blue-channel optical layout with the 800 grooves/mm grating, which corresponds to 0.75Å/pixel and a resolution of approximately 2.2Å. Except for a fraction of the first night of observations, the chip was binned 4:1 perpendicular to the dispersion direction. This greatly reduced the CCD read-out time while still preserving a measurable trace profile. Exposure times varied with the quasar magnitude and varying observing conditions, but were typically ten to fifteen minutes per object. Approximately 900 spectra of almost 400 quasars were collected. Quartz lamp exposures were used to correct for pixel to pixel sensitivity variances, and comparison lamp exposures (usually He-Ne-Ar) were used to wavelength calibrate the spectra. As the only interest was in measuring absorption features and the observing conditions were generally non-ideal, spectrophotometric standards were not observed.

The data were reduced in the usual manner using the NOAO Image Reduction and Analysis Facility. Investigation of zero-second exposures did not reveal any systematic structure in the electronic bias and thus only simple fitting of the overscan was preferable for bias subtraction. The quartz spectra were fitted with a high-order spline in the dispersion direction to normalize the flat field by which all object and arc lamp frames were divided. A one-dimensional spectrum was extracted from the arc lamps, emission lines were identified manually with the aid of the maps found on the MMT web site, and a spline was fitted to the dispersion solution. This initial solution was performed for each lamp on a given night. The object spectra were traced and extracted with variance weighting, and identical traces of the appropriate arc lamp exposures performed. The initial dispersion solution was then used as a reference for auto-identification of lines in the newly traced arc spectra, and an individual dispersion solution computed for each extracted object spectrum. Multiple exposures of a

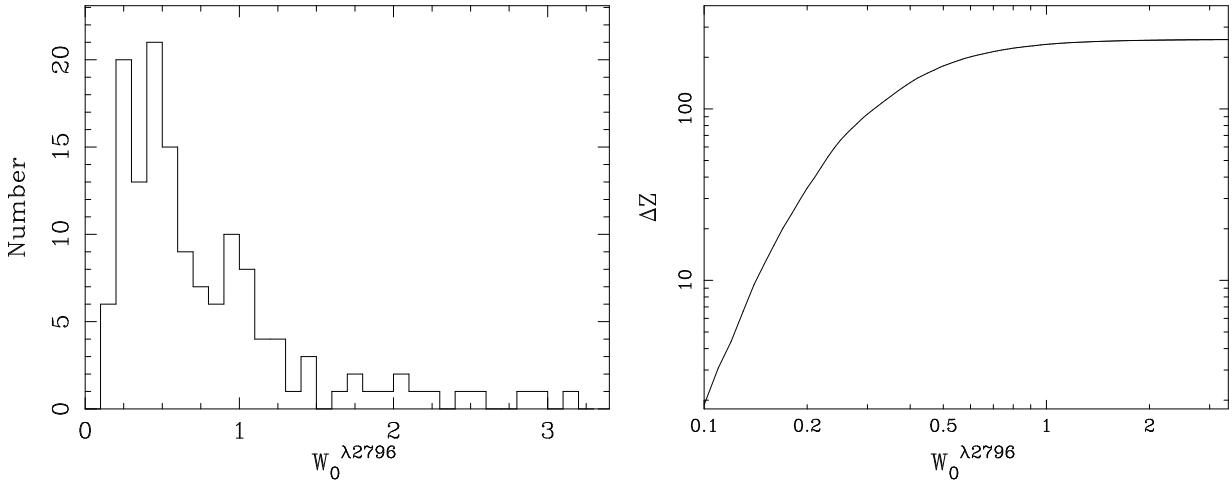

Figure 3.2: Analysis of $W_0^{\lambda 2796}$. Left: The distribution of rest equivalent widths, $W_0^{\lambda 2796}$, for Mg II systems found in the survey. Right: The redshift-path covered by the survey, $\Delta Z\,(W_0^{\lambda 2796}) = \sum_i^{N_{spec}} \int_{z_{min}}^{z_{max}} g(W_0^{\lambda 2796}, z)\, dz$, as a function of $W_0^{\lambda 2796}$.

given quasar were co-added, with the error spectra being added in quadrature. The resulting data set comprised a total of 381 quasars sightlines.

Continua were fitted to the reduced quasar spectra and Mg II doublet candidates found, inspected, and measured in a manner similar to that described in Chapter 2. The same software was used, though with slight modifications for differences in resolution and wavelength coverage between the SDSS and MMT data.

3.3 RESULTS

A total of 141 Mg II doublets were found and measured from the MMT spectra. They cover a redshift range of $0.1973 \leq z \leq 0.6079$ and have $W_0^{\lambda 2796}$ values ranging from 0.12Å to 3.17Å.

Figure 3.2 shows the distribution of $W_0^{\lambda 2796}$ in the MMT survey. The redshift-path coverage as a function of $W_0^{\lambda 2796}$ is also shown. The resulting $n(W_0^{\lambda 2796})$ is shown as the histogram in Figure 3.3. The solid line is a maximum likelihood fit of the form $n(W_0^{\lambda 2796}) = \frac{N^*}{W^*} e^{-\frac{W_0}{W^*}}$ to the data with $W_0^{\lambda 2796} \geq 0.3$Å with $W^* = 0.509 \pm 0.047$ and $N^* = 1.089 \pm 0.121$. The red-dashed line is the low-z result from the SDSS EDR survey, which has a mean redshift

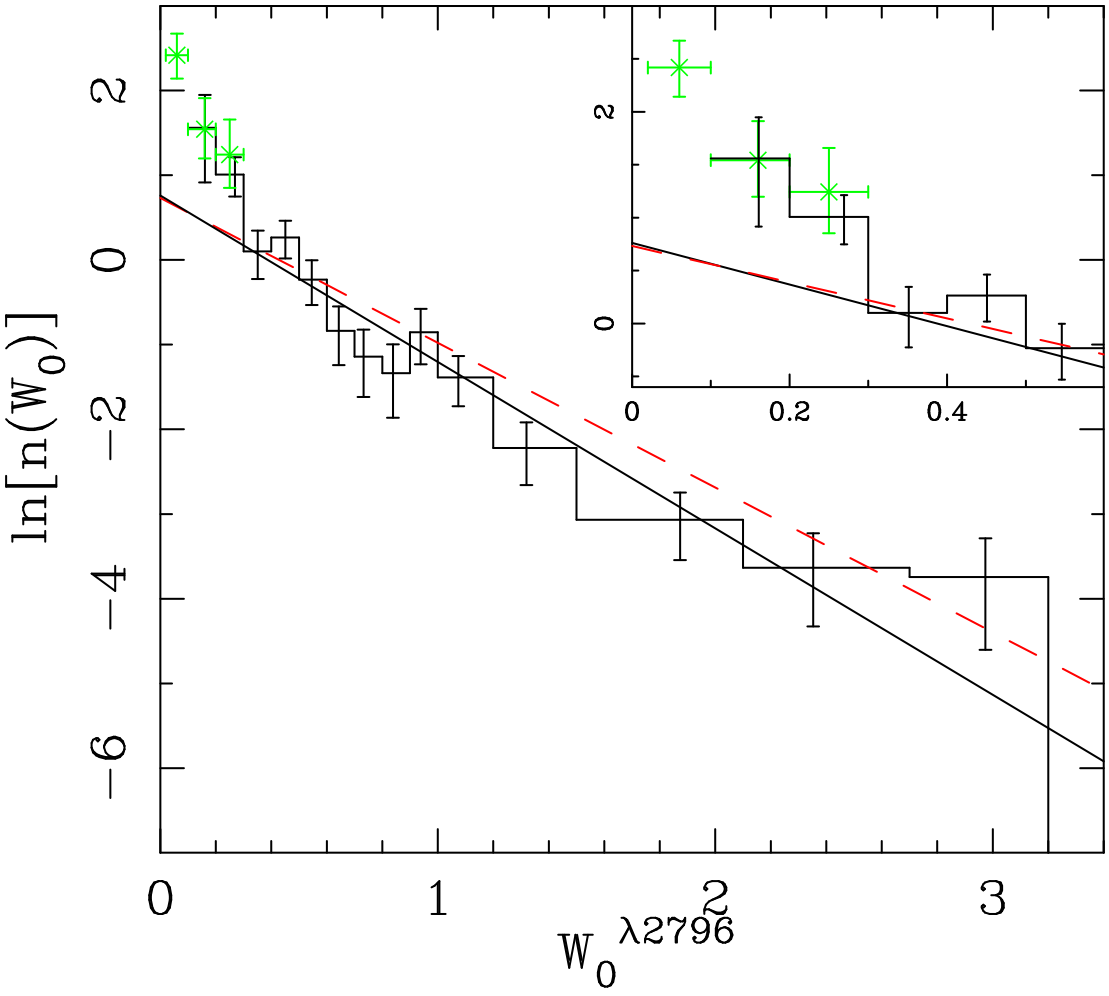

Figure 3.3: Histogram of the $W_0^{\lambda 2796}$ distribution from the MMT data. The solid line is a maximum likelihood fit of the form $n(W_0^{\lambda 2796}) = \frac{N^*}{W^*} e^{-\frac{W_0}{W^*}}$ to data having $W_0^{\lambda 2796} > 0.3$Å, with $W^* = 0.509 \pm 0.047$ and $N^* = 1.089 \pm 0.121$. The red-dashed line is the low-z result from the SDSS EDR survey. The points represent data from CRCV99.

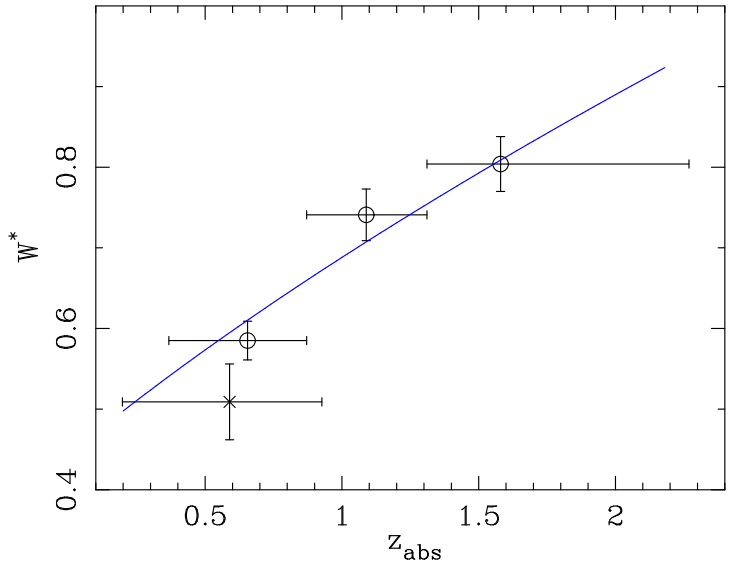

Figure 3.4: Evolution of W^*. The circles are from the SDSS EDR survey. The $\times$ symbol is the MMT result. The curve is the power law prediction described in §2.3.3.

$\langle z_{abs} \rangle = 0.655$. The systems found in the MMT survey have $\langle z_{abs} \rangle = 0.589$. The points represent data from CRCV99. Although there are only 26 systems in the two lowest $W_0^{\lambda 2796}$ bins of the MMT survey, $n(W_0^{\lambda 2796} < 0.3\text{Å})$ is in very good agreement with the CRCV99 results and significantly (1.4σ and 2.4σ) above the extrapolation of the single-exponent fit to $n(W_0^{\lambda 2796})$ for $W_0^{\lambda 2796} \geq 0.3$Å. Thus, the results from the MMT survey confirm the upturn in $n(W_0^{\lambda 2796})$ below 0.3Å that was proposed in Chapter 2.

Figure 3.4 shows $W^*_{\rm MMT}$ along with the values from the SDSS EDR survey. The $W_0^{\lambda 2796}$ distribution determined from the MMT survey is consistent with the SDSS EDR survey results, considering the observed redshift evolution.

The distribution of redshifts for Mg II absorption systems found in the survey is shown in Figure 3.5. Also shown is the sightline coverage for $W_0^{min} = 1.0$Å, 0.6Å, and 0.3Å. The resulting dn/dz values are shown as the black $\times$ symbols in Figure 3.6 for $W_0^{\lambda 2796} \geq 0.1, 0.3, 0.6$ and 1.0Å for $0.126 \leq z < 0.367$ and $0.367 \leq z < 0.956$. The ranges correspond to the redshifts below and overlapping the SDSS EDR survey. Also shown as red circles are the respective data from the EDR survey. The green boxes are from CRCV99. The dashed

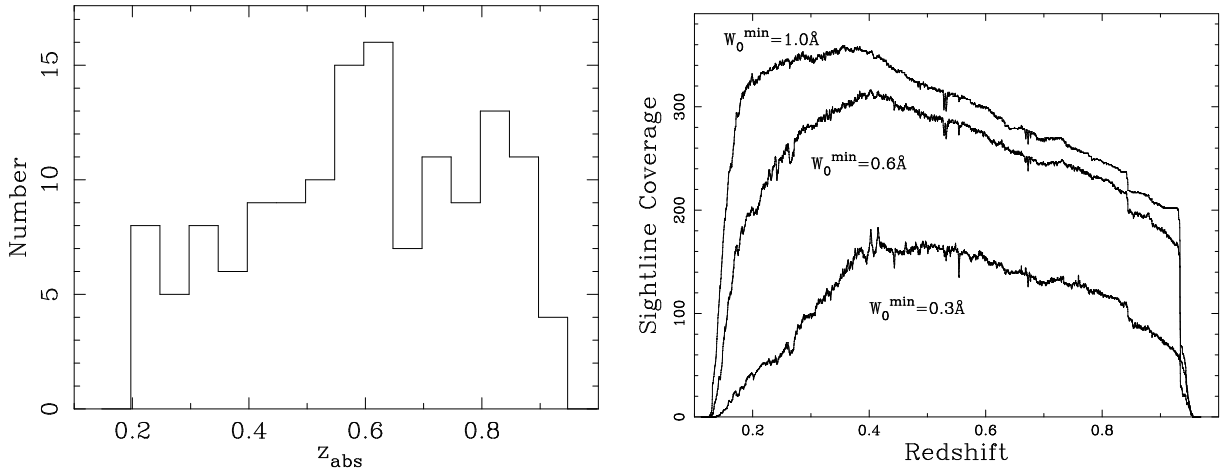

Figure 3.5: Analysis of $n(z)$. Left: The distribution of redshifts for Mg II absorption systems found in the MMT survey. Right: The total number of sightlines with sufficient signal to noise ratio to detect lines with $W_0^{\lambda 2796} \geq W_0^{min}$ as a function of redshift, for $W_0^{min} = 1.0$Å, 0.6Å, and 0.3Å.

lines are the NECs normalized to the binned EDR/CRCV99 data, *excluding* the MMT data. All of the $0.367 \leq z < 0.956$ points are consistent within the errors with the other studies. The $0.126 \leq z < 0.367$ points are approximately 1σ below the NEC for $W_0^{min} = 0.1, 0.3$ and 0.6Å, and $\approx 2.5\sigma$ below the NEC for $W_0^{min} = 1.0$Å.

3.4 CONCLUSIONS

The MMT survey resulted in the identification and measurement of 141 Mg II absorption systems with $W_0^{\lambda 2796} > 0.1$Å over the redshift interval $0.197 \leq z < 0.956$. This extends the Mg II statistics to cover approximately 40% of the look-back time between the present epoch and the lower-limit of the SDSS EDR survey described in Chapter 2. The range of $W_0^{\lambda 2796}$ covered ($0.1\text{Å} < W_0^{\lambda 2796} < 3.2\text{Å}$) allowed for the confirmation of the upturn in $n(W_0^{\lambda 2796})$ below $W_0^{\lambda 2796} \approx 0.3$Å that was suggested in Chapter 2. Unlike the EDR survey, the size of the MMT sample does not allow the study of the strongest systems whose incidence were shown to exhibit strong evolution at redshifts $z \lesssim 1$. However, the MMT survey begins to detect evidence for evolution of the moderate ($W_0^{\lambda 2796} \geq 1.0$Å) systems at redshifts $z \lesssim 0.5$.

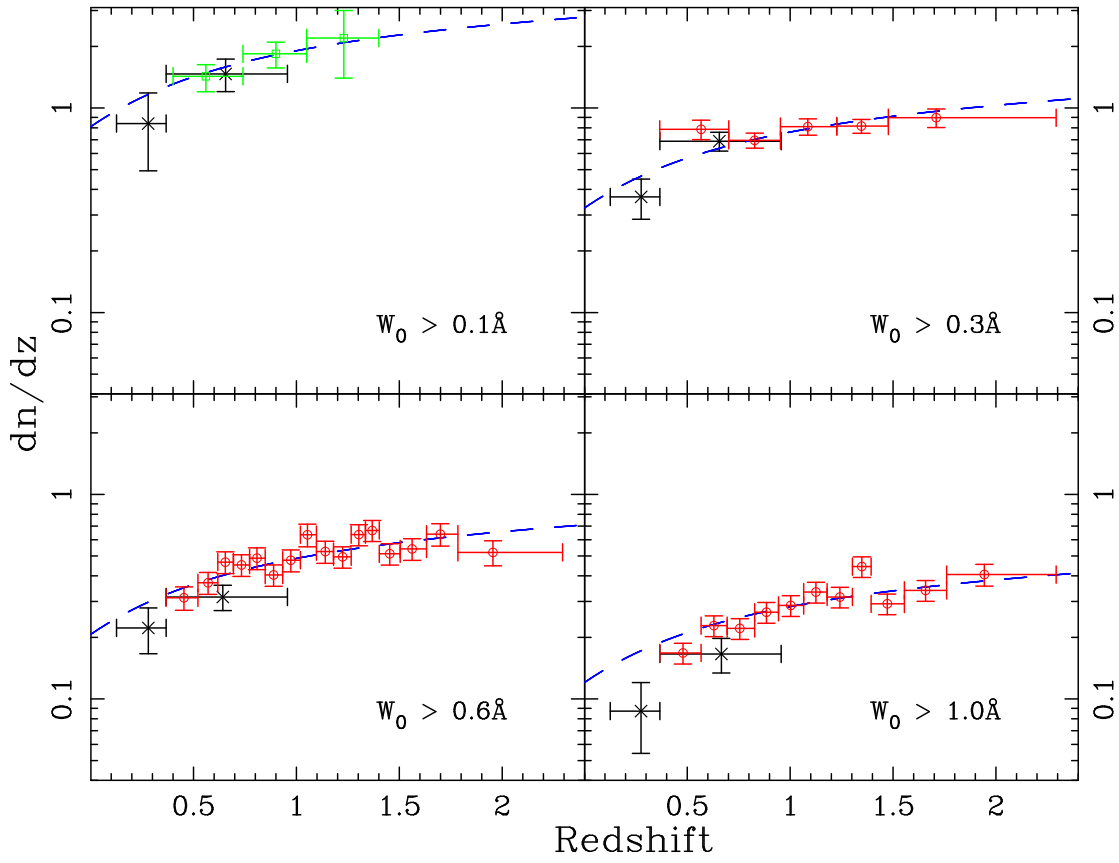

Figure 3.6: dn/dz curves. Black $\times$ symbols represent the MMT results. The ranges correspond to the redshifts below and overlapping the SDSS EDR survey, respectively. Also shown are data from the EDR survey (red circles) and CRCV99 (green boxes). The dashed lines are the NECs normalized to the binned EDR/CRCV99 data, but excluding the MMT data.

RT00 demonstrated that DLA absorbers are drawn almost exclusively from the population of Mg II absorbers that have $W_0^{\lambda 2796} \geq 0.6$Å. Moreover, they claim that half of all absorption systems with both $W_0^{\lambda 2796}$ and Fe II $W_0^{\lambda 2600} \geq 0.5$Å are DLA systems. They use the SS92 parameterization of $W_0^{\lambda 2796} \geq 0.6$Å systems, $dn/dz = 0.24\,(1+z)^{1.02}$, to trace Ω_{DLA} at $z < 1.65$. The SS92 parameterization is very close to the NEC as normalized in Figure 3.6. Therefore, the ($\approx 1\sigma$) detection of evolution seen in Figure 3.6 is of great relevance to the evolution of Ω_{DLA}. At present, Ω_{DLA} at $z < 1.65$ is poorly constrained. The results presented here, however, in combination with the results of an ongoing HST survey for DLAs in known strong Mg II absorption systems will allow a description of the evolution of Ω_{DLA} at low redshift with much greater precision.

Further discussion of these results and their physical implications is presented in Chapter 6.

4.0 DLA GAS METALLICITIES

4.1 INTRODUCTION

All of the metals in the Universe were formed in stars and distributed into the inter-stellar medium (ISM) through mechanisms such as stellar winds and supernovae. Thus, chemical enrichment is intimately tied to star formation history and therefore galaxy evolution. A consistent understanding of the chemical enrichment history of galaxies and the evolution of their star formation rates is a necessary aspect of our understanding of their evolution.

The metallicity of a galaxy is not a uniquely defined attribute. Most galaxies are not enriched with spatial uniformity, often exhibiting region to region variations and/or radial metallicity gradients. Furthermore, the metallicity of the stellar and various gaseous phases are in general not the same. The metallicity of nearby galaxies is typically measured using the fluxes of nebular emission lines from regions that are highly ionized due to star formation activity. These values, however, are not necessarily representative of the chemical abundance of other regions, especially quiescent and/or neutral gaseous regions of the galaxy. Unsaturated absorption lines allow for the determination of ionic column densities in cool gas which, together with the measurement of N_H and, when appropriate, ionization corrections, allow metal abundances to be calculated. This method is limited to situations where a bright source is located behind the gaseous region in question, but has the usual advantage of absorption line studies that it is practical up to the largest quasar redshifts.

Measurements of metals in DLAs are appropriate for studies of the cosmic neutral-gas-phase metallicity because these systems trace the bulk of the neutral hydrogen gas mass of the Universe out to at least redshift $z \approx 3.5$ (see Storrie-Lombardi and Wolfe, 2000; Rao and Turnshek, 2000, and references therein). However, abundance calculations are

complicated by saturation of strong lines. As discussed in Chapter 2, the strong Mg II and Fe II lines that trace large columns of H I are typically saturated. Transitions from elements such as Cr, O, S, Si, and Zn are often unsaturated, and thus allow for measurements of their column densities in spectra with sufficient signal to noise ratios in the appropriate wavelength intervals. Abundance measurements of DLAs at high redshift have found them to be sub-solar, with metallicity values $-3 \lesssim [\mathrm{M/H}] \lesssim -0.5$[1]. There is some evidence for a slight increase with decreasing redshift of the average DLA metallicity, though small number statistics continue to be important concerns in these studies. Specifically, a column-density-weighted determination of the cosmic metallicity is the most relevant measurement that can be made to track the overall chemical evolution of neutral gas in the Universe, but making a column-density-weighted determination leads to a situation where the resultant measurement is mostly dominated by a few of the highest N_{HI} systems (recall $N_{tot} \sim N_{max}^{1/2}$, Chapter 1). Thus, since individual absorbers have a range of metallicities, there is the uncertainty introduced by the small number of very high N_{HI} absorbers so far studied, but which dominate the column-density-weighted determination of metallicity.

Further complications arise from the depletion of refractory elements (elements with high melting temperatures) onto dust grains, leading to an underestimate of the true abundance. Since most metals tend to be present in roughly solar relative abundances[2], especially those with similar nucleosynthetic histories, the amount of dust can be approximated by comparing abundances of elements that rarely show depletion, such as Si and Zn, to abundances of those that do, such as Cr and Fe.

In Chapter 2, a large catalog of absorption systems selected by their Mg II absorption was presented, the strength of which imply high H I column densities. However, few of the spectra have sufficient signal to noise ratios to measure the unsaturated metal transitions. Mean values of the absorption strengths can be obtained, though, by creating composites of the absorption-line spectra shifted to the rest frame of the absorber. By using these composite spectra, the worries related to small number statistics can be mitigated.

Zn II and Cr II exhibit transitions at $\lambda\lambda 2026, 2062$ and $\lambda\lambda\lambda 2056, 2062, 2066$, respectively.

[1] It is customary to quote abundances as logarithmic ratios, relative to solar. Thus [Fe/H]$= -1.0$ indicates a Fe abundance that is $\frac{1}{10}$th the solar value.

[2] However, there are sometimes important exceptions such as O/N.

These are at longer wavelengths than most other unsaturated metal transitions, and their oscillator strengths are relatively large. At the densities and temperatures of DLA systems, both Zn and Cr are believed to be largely in the singly ionized state. Thus, measurements of Zn^+ and Cr^+ are considered to be representative of the total amounts of Zn and Cr. Furthermore, Zn tends not to suffer from depletion onto dust, while Cr does. Their relative abundance is therefore a good estimator of the amount of dust in DLAs.

In §4.2 the method by which the absorber sample is defined, the composite spectra are formed, and the mean N_{HI} of the absorber sample is estimated is explained. Plots and measurements of the composite spectra are also presented in this section. In §4.3 results are presented on the column-density-weighted DLA gas metallicity of the Universe at $z = 0.9 - 2.0$. Conclusions and discussion are presented in §4.4.

4.2 ANALYSIS

4.2.1 Sample Definition

In this study, absorption-line systems from the early results of the SDSS EDR Mg II survey were used to create composite spectra in order to measure mean Zn II and Cr II column densities, and therefore infer their abundances. These consisted of a uniform sample of $W_0^{\lambda 2796} \geq 1.0$Å lines, numbering approximately 640 total systems. While this represents only about half of the total number in the final catalog, the remainder are predominantly weaker and/or noisier. The results from this study suggest that the inclusion of the full catalog would not significantly improve the measurements.

The absorption spectra flux and flux errors were continuum normalized as described in Chapter 2. Systems with $z \lesssim 0.9$ did not allow for the measurement of Zn IIλ2026, and were thus removed from the sample, as were systems for which Zn IIλ2026 fell in the Lyα forest. The Zn II - Cr II absorption region of each spectrum was visually inspected and any system that exhibited absorption from other systems, bad pixels, or otherwise problematic data in these regions was excluded. One of the goals of the analysis was to make an accurate measurement of the Zn II λ2026 absorption line, and in SDSS medium-resolution spectra

this line is potentially blended with the low oscillator strength Mg I λ2026 absorption line. Therefore, the contribution of Mg I 2026 to the blend was estimated by using only spectra that also had data on the higher oscillator strength (but generally unsaturated) Mg I 2852 absorption line. This left a total of 223 systems in the redshift interval $0.9 \leq z \leq 2.0$.

Using HST UV spectroscopy, RT00 showed that strong intervening Mg II−Fe II absorption-line systems identified in quasar spectra characteristically have very high neutral hydrogen column density gas (generally $10^{19} < N_{HI} < 10^{22}$ atoms cm^{-2}). Many are DLAs with $N_{HI} \geq 2 \times 10^{20}$ atoms cm^{-2}. RT00 showed that $\approx 95\%$ of these DLAs can be identified by selecting systems which have a Mg II λ2796 rest equivalent width $W_0^{\lambda 2796} > 0.5$ Å and Fe II λ2600 $W_0^{\lambda 2600} > 0.5$ Å. Although the sample used in this study has $W_0^{\lambda 2796} > 1.0$Å, RT00 find no correlation between $W_0^{\lambda 2796}$ and $N_{H\,I}$. Therefore, $n(W_0^{\lambda 2796})$ from Chapter 2 can be used to estimate the fraction of H I gas missed. Since the results of the full EDR survey indicate that $W_0^{\lambda 2796}$ is ≈ 1.4 times larger than $W_0^{\lambda 2600}$, the criterion that $W_0^{\lambda 2600} > 0.5$ Å is generally, if not completely, consistent with the composite sample.

4.2.2 Forming and Measuring the Composite Spectra

To form composites, the wavelength array of each spectrum was shifted to the absorption rest-frame and re-binned onto a sub-pixel grid, with sub-pixels having one-fifth the size of an original pixel; this minimized data smoothing due to re-binning. Using the 223 systems in the sample, different methods for forming composites were experimented with.

It was found that inverse variance weighting produced the highest signal-to-noise ratio composites, so results produced by this method were adopted, since there is no known correlation between $N_{H\,I}$ and spectrum signal-to-noise ratio. Other methods (e.g., straight averaging) would have produced somewhat lower signal-to-noise ratio composites. It should be noted, however, that if quasar dimming due to the presence of dust and, therefore, high metal content is significant, the mean metallicity would be underestimated, as this weighting method favors brighter quasars.

The composite spectrum in the Zn II – Cr II region derived from the entire sample of 223 absorbers is shown in Figure 4.1. In addition, other composites were formed by roughly

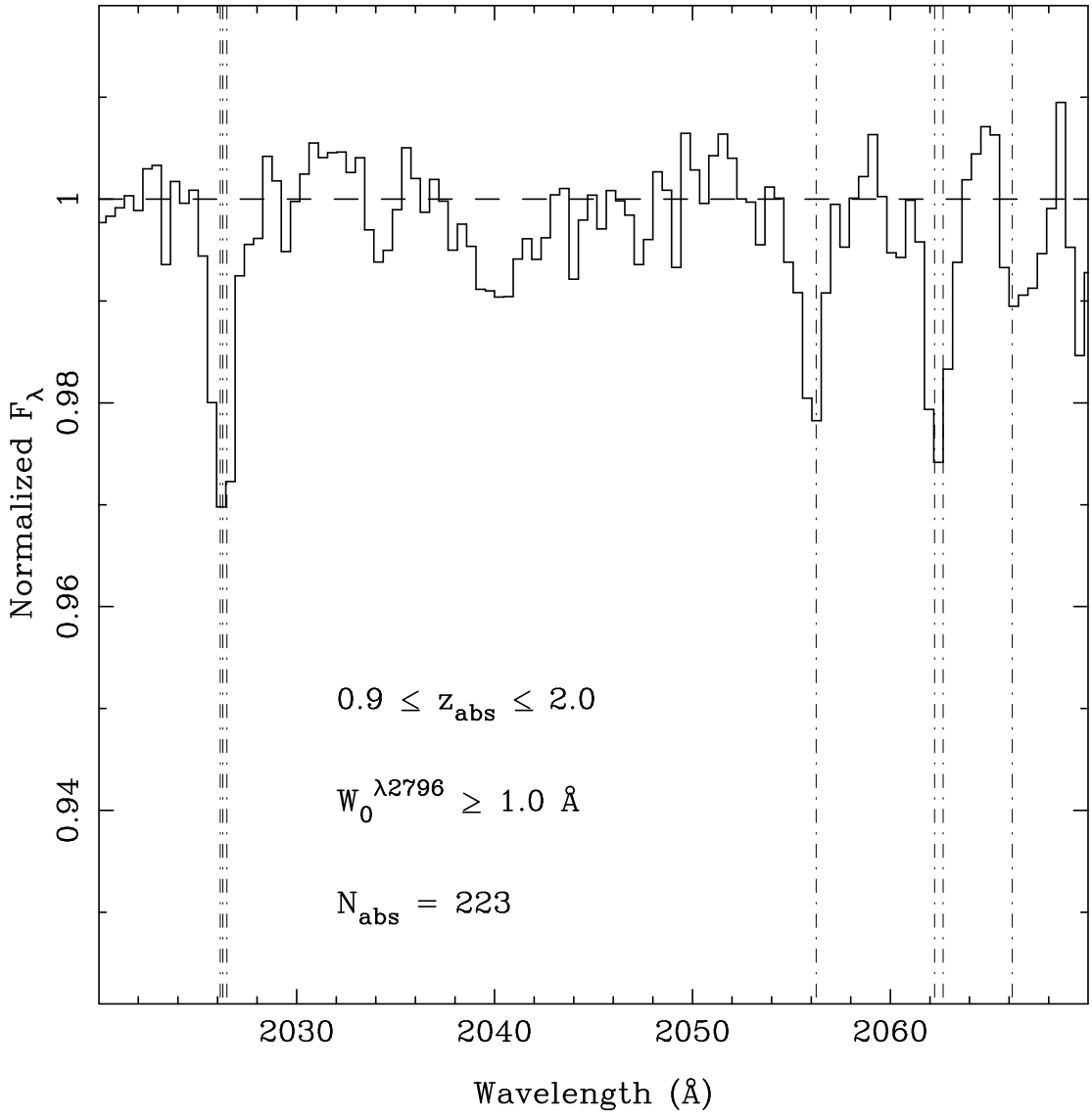

Figure 4.1: Composite spectrum in the rest frame Zn II-Cr II region derived from 223 SDSS quasar spectra. The dashed-dotted lines indicate the rest frame locations of the Zn II, Cr II, and Mg I lines (see Table 4.1).

dividing the sample into quarters while keeping the variance approximately the same in each subsample. Figure 4.2 shows the composites of four subsamples that correspond to Mg II absorbers with moderate ($1.0 \leq W_0^{\lambda 2796} \leq 1.3$ Å) and high ($W_0^{\lambda 2796} > 1.3$ Å) rest equivalent widths, and at lower redshift ($0.9 \leq z < 1.35$) and higher redshift ($1.35 \leq z \leq 2.0$) within the total sample. This subdivision leads to some important results (§4.3 and §4.4). As noted in Chapter 2, the selection of high-N_{HI} systems by identifying large $W_0^{\lambda 2796}$ absorption lines basically amounts to a kinematic criterion. This is because the Mg II λ2796 absorption lines are on the saturated part of the curve of growth, which means that their W_0 values are essentially measures of velocity spread rather than column density.

For optically-thin absorption lines, W_0 is directly proportional to column density (e.g., Petitjean, 1998):

$$N(cm^{-2}) = 1.13 \times 10^{20} \frac{W_0(\text{Å})}{\lambda_0^2(\text{Å}) f}, \tag{4.1}$$

where f is the oscillator strength of the transition. Table 4.1 lists the laboratory wavelengths and oscillator strengths for the transitions considered in this study. The feature at λ2026 is a blend due to Zn II, Mg I, and a very weak Cr II line. The Mg I $W_0^{\lambda 2026}$ was taken to be 32.0 times smaller than the measured value of Mg I $W_0^{\lambda 2852}$ (the ratio of their $\lambda_0^2 f$ values) and Cr II $W_0^{\lambda 2026}$ was taken to be 23.0 times smaller than the measured value of Cr II $W_0^{\lambda 2056}$. The remaining absorption was attributed to be due to Zn II λ2026. The feature at λ2062 is a blend due to Cr II and Zn II. The value of Cr II $W_0^{\lambda 2062}$ was taken to be 0.50 times the measured and summed values of Cr II $W_0^{\lambda 2056}$ and Cr II $W_0^{\lambda 2066}$, or 0.75 times the measured value of Cr II $W_0^{\lambda 2056}$, depending on which resulted in smaller propagated errors. The remaining absorption was then attributed to be due to Zn II λ2062. Measurements of the absorption lines in the Zn II−Cr II region in the five composites shown in Figures 4.1 and 4.2 are reported in Table 4.2, along with the characteristic properties that define the total sample and four subsamples.

4.2.3 The Mean H I of the Sample

To estimate the mean neutral hydrogen column density of the absorber sample, N_{HI} was measured (when available) for every known Mg II system with $W_0^{\lambda 2796} \geq 1$ Å. This includes 24

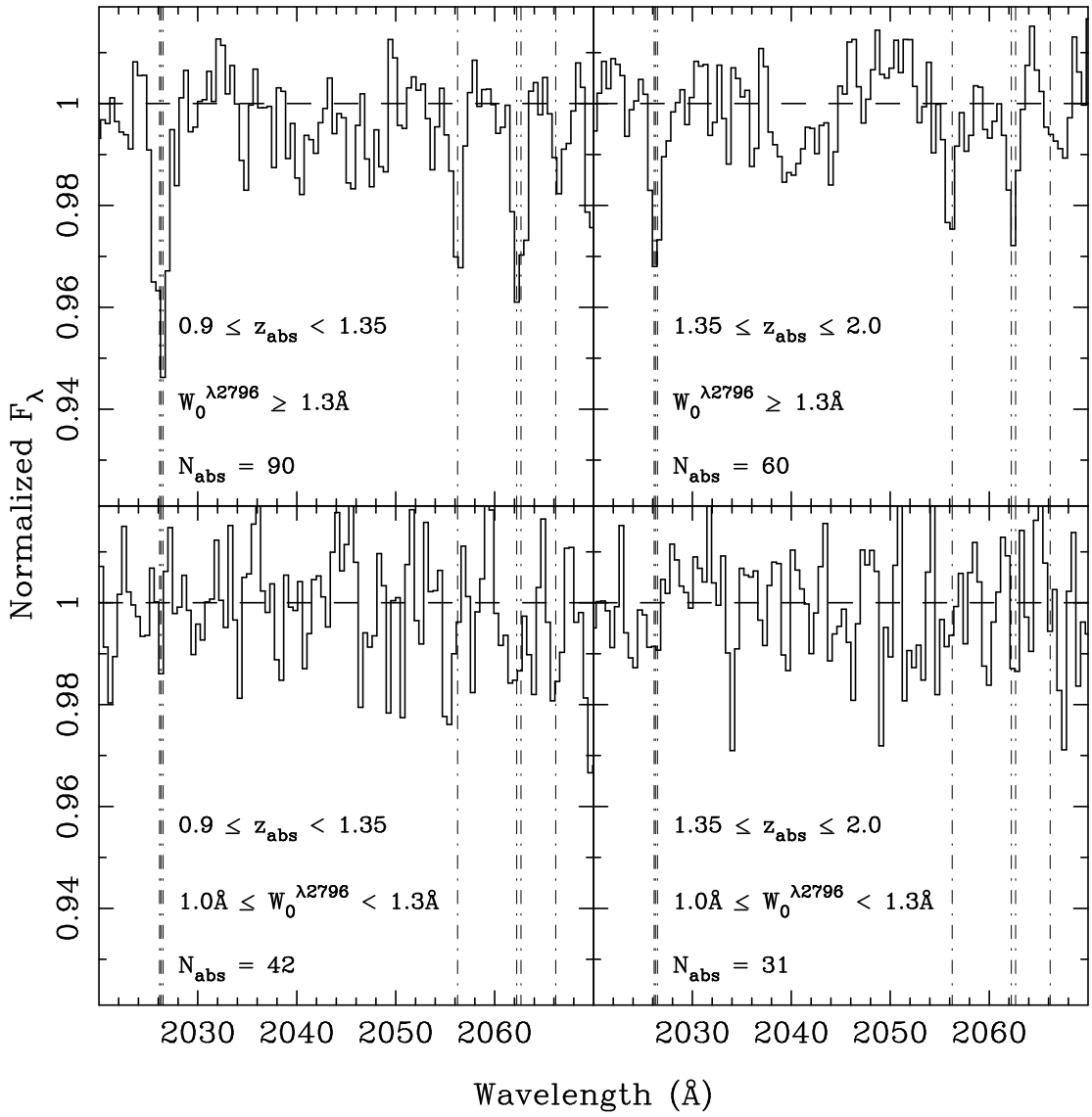

Figure 4.2: Composite spectra for four subsamples of the total sample divided according to redshift and $W_0^{\lambda2796}$ of the Mg II λ2796 absorption line. The dashed-dotted lines continuum indicate the rest frame locations of the Zn II, Cr II, and Mg I lines (see Table 4.1). Notice the presence of stronger metal lines (indicating more chemically evolved structures) in the larger $W_0^{\lambda2796}$ (i.e. larger velocity spread) subsamples, the stronger Zn II (indicating increased metallicity) at lower redshift, and the stronger Cr II relative to Zn II (indicating less dust) at higher redshift.

Table 4.1: Transition Data†

	Zn II		Cr II				Mg I	
λ_0	2026.14	2062.66	2026.27	2056.25	2062.23	2066.16	2026.48	2852.96
f	0.489	0.256	0.00471	0.105	0.0780	0.0515	0.1120	1.8100

† See kingpin.ucsd.edu/~hiresdla/ for details and references.

Table 4.2: W_0 Measurements of Absorber Composite Subsamples*

	Full Sample	Low-z High-W_0	High-z High-W_0	Low-z Low-W_0	High-z Low-W_0
# of Absorbers	223	90	60	42	31
W_0^{2796} Interval	≥ 1.0Å	>1.3Å	>1.3Å	1.0−1.3Å	1.0−1.3Å
z_{abs}-Interval	0.9−2.0	0.9−1.35	1.35−2.0	0.9−1.35	1.35−2.0
Zn II $W_0^{\lambda 2026}$ †	33.6 ± 5.0	70.2 ± 9.3	29.4 ± 7.7	0.1 ± 10.6	6.5 ± 11.3
Mg I $W_0^{\lambda 2026}$ †	10.2 ± 0.2	13.7 ± 0.3	10.9 ± 0.3	5.6 ± 0.4	4.0 ± 0.5
Cr II $W_0^{\lambda 2056}$	31.1 ± 5.1	41.7 ± 7.7	32.2 ± 8.1	6.2 ± 10.3	6.5 ± 11.4
Cr II $W_0^{\lambda 2062}$ †	23.2 ± 3.8	31.2 ± 5.8	24.1 ± 6.0	4.6 ± 7.7	4.8 ± 8.5
Zn II $W_0^{\lambda 2062}$ †	12.3 ± 6.2	26.6 ± 10.3	6.2 ± 9.5	12.4 ± 12.9	6.1 ± 14.3
Cr II $W_0^{\lambda 2066}$	13.0 ± 4.5	19.2 ± 8.3	9.8 ± 16.0	21.5 ± 10.6	2.5 ± 8.0

*All W_0 values are in mÅ, except W_0^{2796}. † Blended feature (see text).

systems studied by RT00 and another 51 systems from ongoing HST UV spectroscopy of the Lyα absorption line in strong Mg II systems (Rao et al. 2004, in preparation). The individual N_{HI} values for these systems were measured by fitting Voigt profiles to the observed Lyα absorption lines. These 75 systems have neutral hydrogen column densities in the range $5 \times 10^{18} < N_{HI} < 7 \times 10^{21}$ atoms cm^{-2}, and their mean neutral hydrogen column density is $\langle N_{HI} \rangle = 3.6 \pm 1.3 \times 10^{20}$ atoms cm^{-2}. This result was taken to represent the mean neutral hydrogen column density of the absorber sample. There is no indication that the $\langle N_{HI} \rangle$ values for the four subsamples defined in Table 4.2 are different from those determined for the entire sample.

The $W_0^{\lambda 2797}$ regime considered ($W_0^{\lambda 2796} \geq 1$ Å) does not represent a census of all H I in the Universe over the studied redshift interval, nor does it even represent all DLAs with $N_{HI} \geq 2 \times 10^{20}$ atoms cm^{-2}. For example, RT00 estimated that 5% of DLAs are missed using their selection criterion (§4.2.1). Moreover, in Chapter 2 it was demonstrated that $n(W^{\lambda 2796}) \propto e^{\frac{-W_0}{0.7}}$, which suggests that about half of the DLAs are missed by excluding $0.5 < W_0^{\lambda 2796} < 1.0$ Å systems from a composite spectrum. HST spectroscopy suggests that Mg II systems in this $W_0^{\lambda 2796}$ range have mean neutral hydrogen column density $<N_{HI}>$ $= 2.7 \pm 1.2 \times 10^{20}$ atoms cm^{-2}. This is 25% smaller than the mean neutral hydrogen column density for higher $W_0^{\lambda 2796}$ Mg II systems, but statistically equivalent given the sizes of the measurement errors. These effects need to be accounted for when deriving the *cosmic* neutral-gas-phase metallicity of DLAs (§4.3.1).

4.3 COLUMN-DENSITY-WEIGHTED COSMIC NEUTRAL-GAS-PHASE METALLICITY OF DLAS

4.3.1 The Zn and Cr Abundances

As noted in §4.1, the basis for using the Zn II and Cr II absorption lines for element abundance determinations stems from the fact that these lines are unsaturated even when the neutral hydrogen column densities are high. This premise was originally put forth by Pettini et al. (1990), and verified in high-resolution studies (e.g., Prochaska and Wolfe, 1999). Al-

though there has been some discussion of the importance of ionization corrections for metal abundance determinations in DLAs (e.g., Howk and Sembach, 1999), this issue needs further study and model-dependent ionization corrections have not been made when reporting results on DLA metal abundances in the literature. However, as mentioned in Section 4.1, it is generally agreed that the bulk of the Zn and Cr is singly ionized in the DLA neutral regions. Hence, in keeping with earlier investigators, it is assumed that a determination of $[Zn^+/H^0]$ is equivalent to [Zn/H] and a determination of $[Cr^+/Zn^+]$ is equivalent to [Cr/Zn].

Given the oscillator strengths and wavelengths of the relevant lines (Table 4.1), the following methods were used to calculate the respective W_0 values for the blended lines. As discussed in §4.2.2, if Mg I λ2852 is unsaturated then Mg I λ2026 will be 32.0 times weaker. Also, Cr II λ2026 is 23.0 times weaker than Cr II λ2056. These results can be used to infer the strength of Zn II λ2026. The strength of Mg I λ2852 in some composites indicates that Mg I will indeed contribute to absorption at λ2026, but Cr II λ2026 makes a very minor contribution. Similarly, Cr II λ2056 and Cr II λ2066 are 1.34 and 0.66 times the strength of Cr II λ2062, respectively; this can be used to infer the strength of Zn II λ2062. Since the λ2062 feature is stronger than Cr II λ2056 in some of the composites, this indicates that Zn II λ2062 does contribute to absorption at λ2062 in these composites.

Thus, there are two approaches for estimating $N_{\rm Zn\,II}$ – using either the inferred value of $W_0^{\lambda 2026}$ or that of $W_0^{\lambda 2062}$. It was found that the approaches give consistent results. In a few individual quasar spectra, comparison of the strength of Mg I λ2852 to that of Mg II $\lambda\lambda$2796, 2803 suggests that Mg I λ2852 may be approaching saturation, which implies that the strength of the Mg I λ2026 line may be more than $\frac{1}{32.0}$ times the strength of Mg I λ2852. If this is the case, it would lead to a systematic error. However, for all of the measured lines the predicted values of W_0 from the determined values of $N_{\rm Zn\,II}$, $N_{\rm Cr\,II}$ and $N_{\rm Mg\,I}$ were consistent with the measured W_0 values. The determinations (with proper error weighting) of [Zn/H] and [Cr/Zn] in the five composites are reported and described in Table 4.3 relative to the solar metallicities of Grevesse and Sauval (1998).

With these results and the results discussed in §4.2.3, it is possible to estimate the cosmic neutral-gas-phase metallicity of DLAs. To do this one must recognize two effects. First, the $W_0^{\lambda 2796} \geq 1.0$ Å composite over the studied redshift interval does not sample all of the DLA

Table 4.3: Abundance Measurements of Absorber Composite Subsamples.

	Full Sample	Low-z High-W_0	High-z High-W_0	Low-z Low-W_0	High-z Low-W_0
[Zn/H]	-0.88 ± 0.19	-0.56 ± 0.19	-0.94 ± 0.21	$< -1.08^{\dagger}$	$< -1.05^{\dagger}$
[Cr/Zn]	-0.45 ± 0.13	-0.64 ± 0.13	-0.38 ± 0.18	$\cdots$	$\cdots$

† Upper limits (2σ) on metallicities represent those that apply for the quoted $W_0^{\lambda 2796}$ interval. Since this does not include 100% of the DLA gas, a correction is made (§4.3.1) to derive results on the cosmic DLA gas metallicity.

gas. By excluding $W_0^{\lambda 2796} < 1.0$ Å systems, $\approx 45\%$ of the DLA gas is likely to be excluded from this composite (§4.2.3). Second, the subsample composites with $1.0 \leq W_0^{\lambda 2796} \leq 1.3$ Å show negligible metallicity (Table 4.3). From this second effect it is inferred that the missed DLA gas has negligible metallicity. Thus, to derive the cosmic DLA gas metallicity, the derived metallicity in the full composite sample must be reduced by a factor of ≈ 1.8. With these consideration taken into account, it is determined that [Zn/H] $= -1.13 \pm 0.19$ in DLAs ($\approx 0.074 \pm 0.011$ times solar, see §4.3.2 for a discussion of the error). The corresponding result for Cr, which should not have much dependence on the missed DLAs, is [Cr/Zn] $= -0.45 \pm 0.13$. This indicates that $\approx 65\%$ of the Cr is depleted onto grains. For comparison, [Cr/Zn] values are typically ≈ -1 to -2 for sighlines through the Milky Way disk (Savage and Sembach, 1996), and ≈ 0.2 to -0.8 in individual DLAs (Prochaska et al., 2003, also `kingpin.ucsd.edu/~hiresdla/`).

In addition, the following trends are present (Table 4.3). The derived metallicities are highest in the composites which have the largest $W_0^{\lambda 2796}$, which in turn correspond to those with the largest velocity spreads. Also, within the high-$W_0^{\lambda 2796}$ regime, the Zn abundance is larger and [Cr/Zn] is smaller in the lower redshift composite. Since these results are based on measurements of unsaturated Zn II and Cr II absorption lines in composite spectra, with corrections made for missed DLAs, they are equivalent to column-density-weighted deter-

minations of cosmic neutral-gas-phase metallicities in DLAs. These findings are consistent with and directly comparable to the results of Pettini et al. (1999) and, more recently, the results summarized by Turnshek et al. (2003).

4.3.2 Statistical and Systematic Errors

As discussed in §4.2.3, the statistical error on $<N_{HI}>$ is 36% (0.16 dex). Thus, since the measured errors on W_0 in the total sample and in the two high-$W_0^{\lambda 2796}$ subsamples are smaller, this error dominates the uncertainties in [Zn/H] determinations. With the aide of future HST UV spectroscopy of high-N_{HI} systems, this error may be reduced. The statistical errors in [Cr/Zn] determinations are smaller since $<N_{HI}>$ does not enter into the determinations. Recall that, within the redshift and $W_0^{\lambda 2796}$ intervals under study (§4.2.1), there is at present no evidence that $<N_{HI}>$ is correlated with redshift or $W_0^{\lambda 2796}$. However, if such a correlation were present, it would give rise to a systematic error. Additional analysis would be needed to remove any systematic error. In all cases the errors quoted are statistical errors propagated from W_0 and/or $<N_{HI}>$ measurement errors.

4.4 CONCLUSIONS

In this chapter, a new method for measuring cosmic DLA metal abundance using composite spectra selected via the Mg II λ2796 absorption signature was presented. The cosmic DLA gas Zn and Cr abundances were derived in two Mg II $W_0^{\lambda 2796}$ intervals which correspond to high and moderate velocity dispersion regimes. Within each of these kinematic regimes low-redshift ($0.9 \leq z < 1.35$) and high-redshift ($1.35 \leq z \leq 2.0$) intervals were considered. It was demonstrated that at redshifts $0.9 \leq z \leq 2.0$, after correction for missed DLAs, the overall [Zn/H] $= -1.13 \pm 0.19$ ($= 0.074 \pm 0.011$ times solar), which is consistant with the average of values determined from individual DLAs, and [Cr/Zn] $= -0.45 \pm 0.13$, which indicates that $\approx 65\%$ of the Cr is depleted onto grains. This is comparable to results from previous studies, and less than typical values for sightlines through the Milky Way disk.

There are clear trends in the composite spectra which indicate that metallicities are

higher in absorption systems which exhibit larger velocity spreads (i.e., in the high-$W_0^{\lambda 2796}$ absorbers). Moreover, among the high-$W_0^{\lambda 2796}$ absorbers, both the metallicity and dust content increase with decreasing redshift. [Zn/H] is larger and [Cr/Zn] is smaller at lower redshift, with [Zn/H]= -0.56 (28% solar) and [Cr/Zn]= -0.64 at $<z>= 1.15$, and [Zn/H]= -0.94 (11% solar) and [Cr/Zn]= -0.38 at $<z>= 1.53$.

The implications of these results and physical interpretations will be discussed in Chapter 6.

5.0 IMAGING AND SPECTRAL ENERGY DISTRIBUTIONS OF ABSORBER GALAXIES

5.1 INTRODUCTION

The most direct way in which to study the physical nature of galactic structures associated with intervening quasar absorption features is to image the galaxy associated with the absorption. However, a plethora of complications has, until recently, prevented the successful identification and study of such galaxies. Concerning DLAs, the foremost complication is the dearth of known systems at $z < 1.65$. Due to the $(1 + z)^4$ surface-brightness dimming, even bright galaxies are difficult to image at high redshift and small angular separations to a bright quasar. At relatively low redshift, the task is non trivial as well. Proper subtraction of the quasar point-spread function (PSF) must be done to investigate small impact parameters, and even when a bright galaxy is found at reasonable angular separation to the sightline, faint limiting magnitudes must be reached in order to rule out dwarf or low surface brightness (LSB) galaxies at smaller impact parameters. Furthermore, absorber identification remains highly speculative unless the galaxy redshift can be shown to be equal to that of the absorption.

At high redshift, ground-based imaging of DLA galaxies has had little success, either because the quasar PSF prevents the detection of objects very close to the quasar sight line, or because the DLA galaxy is simply too faint, or both. In addition, the faintness of any candidates close to the quasar sight line makes it difficult to obtain confirming redshifts. Imaging of high-redshift DLA galaxies with HST has been more successful at identifying faint candidates close to the quasar sight lines, but only a few of these have confirmed redshifts (see Warren et al., 2001, and references therein). The main conclusion of these studies has

been that most high-redshift DLA galaxies are under-luminous in comparison to the Lyman break galaxy population.

Primarily, the study of high-redshift DLA galaxy types has been limited to theory. In a series of papers, Wolfe, Prochaska and collaborators argue, based on kinematics and comparison to local gas-rich galaxies, that high-z DLAs are rotationally supported disks that are the progenitors of present-day spirals (Prochaska and Wolfe, 1998; Wolfe and Prochaska, 2000; Maller et al., 2001, etc.). Haehnelt et al. (1998), however, model DLA absorption with irregular protogalactic clumps with some success, and claim that the disk picture is not a unique explanation for DLA galaxies.

Morphologies, colors, and stellar populations of low-redshift DLA galaxies can be more easily studied, but progress has been slow mainly due to their rarity. Burbidge et al. (1996) obtained HST images along the sight line towards the BL Lac object AO 0235+165 which contains a $z = 0.524$ DLA system selected on the basis of 21 cm absorption; they found a significant number of galaxies near the sight line, including an AGN which has broad absorption line (BAL) features and a fainter, late-type galaxy. Both of these objects are at the DLA redshift but the late-type galaxy has a smaller impact parameter. Le Brun et al. (1997) presented HST images of six low-redshift DLA galaxies that included spirals, low surface brightness (LSB) galaxies, and compact objects, with luminosities ranging from $0.07L^*$ to $1.4L^*$. Three of these six were selected on the basis of 21 cm absorption. In another case, no evidence for a galaxy at the $z = 0.656$ DLA redshift toward the quasar 3C 336 was found, despite very deep ground-based and HST imaging (Steidel et al., 1997; Bouché et al., 2001).

Steidel et al. (1994) conducted an imaging survey of $0.2 \leq z \leq 1.0$ Mg II absorbers. Unfortunately, they have not published their images or results for individual systems. However, they claim that the Mg II absorber galaxy population appears similar to normal galaxies at the present epoch, ranging from late-type spirals to galaxies with colors similar to $z = 0$ ellipticals. They describe the "average" Mg II galaxy as a $0.7L^*$ Sb galaxy.

Despite the evidence for a mix of morphological types contributing to the population of galaxies selected via their large H I column absorption signature, the paradigm that DLAs are comprised primarily of disk galaxies has lingered. Further imaging studies, particularly

of low-redshift DLAs, are necessary to settle this issue. In this Chapter, results from imaging projects involving six DLA galaxies toward five sightlines are presented. The corresponding DLA absorption lines were discovered in HST spectroscopic surveys for DLA lines in known strong Mg II absorption-line systems. The first study involves detailed observations of the sight line toward the quasar OI 363 (0738+313). Excluding quasars selectively observed because they were known to be located behind gas-rich galaxies and systems which lack confirming UV spectroscopic observations of the actual Ly line, this sight line contains the two lowest redshift classical damped Lyα quasar absorption-line systems found in survey mode (i.e., with $N_{H\,I} = 2 \times 10^{20}$ atoms cm^{-2}), one at $z_{abs} = 0.0912$ and the other at $z_{abs} = 0.2212$. The second study involves optical and near-infrared ground-based imaging results on four low-redshift DLA galaxies toward the quasars B2 0827+243 ($z_{DLA} = 0.525$), PKS 0952+179 ($z_{DLA} = 0.239$), PKS 1127-145 ($z_{DLA} = 0.313$), and PKS 1629+120 ($z_{DLA} = 0.532$).

Cosmology-dependent calculations in this Chapter were performed using $(\Omega_M, \Omega_\lambda, h) = (1, 0, 0.65)$. This was the cosmology used in the original publications (Turnshek et al., 2001; Rao et al., 2003), and was used more extensively in the prior literature; thus it is more convenient for comparisons to previous works. The different cosmologies do lead to non-negligible differences in determination of impact parameters and luminosities. However, the differences are not substantial enough to affect any of the conclusions. See Appendix A for comparisons to the "WMAP" cosmology.

5.2 PREVIOUS RESULTS

5.2.1 OI 363

Rao and Turnshek (1998) presented the HST-FOS UV spectrum of OI 363 (0738+313) which led to the identification of the two absorbing systems at $z_{abs} = 0.0912$ and $z_{abs} = 0.2212$ with H I column densities of $N_{HI} = (1.5 \pm 0.2) \times 10^{21}$ atoms cm^{-2} and $N_{HI} = (7.9 \pm 1.4) \times 10^{20}$ atoms cm^{-2}, respectively. They also presented a 45 min R-band WIYN image of the OI 363 field in seeing of 0.55 arcsec. Analysis of this image resulted in a list of 15 resolved objects

and 11 point sources brighter than R = 24 mag within 40 arcsec of the quasar sight-line. The closest resolved object was found to be a galaxy (R = 20.8 mag, labeled G1, hereafter 0738 G1) 5.7 arcsec to the south-southeast of the quasar and the closest unresolved object is presumably a star (labeled S1, R = 20.8 mag) 2.5 arcsec to the northeast of the quasar. Fainter objects were visible in the R-band WIYN image but they were not tabulated since such a list would have suffered from incompleteness. However, the existence of a marginally significant fainter extended feature a few arcsec to the west-southwest of the quasar sight-line was noted (marked with a cross on Figure 4 of Rao and Turnshek (1998)). It appears to be the brightest part of a "fuzz" near the quasar, and was reported to have an R-band surface brightness of ≈ 25.3 mag arcsec^{-2}. Notably, the brightest galaxy in the field is a luminous spiral (named G11, R = 17.1 mag) ≈ 31 arcsec to the east of the quasar with a redshift of $z \approx 0.06$. A similarly luminous spiral at a somewhat larger redshift of $z = 0.09$, i.e., the redshift of the lowest redshift DLA absorber, could have easily been detected in this field if it was present, but the observations ruled this out. Note that there is an absorption line at ≈ 1290 Å in the original FOS low-resolution spectrum of the quasar, which can be identified as Lyα with a rest equivalent width of W≈ 0.7 Å and a redshift of $z_{abs} \approx 0.06$. The existence of a Lyα line at $z = 0.06$ is consistent with the results of Guillemin and Bergeron (1997).

Both of the DLA absorbers along this sight-line have been shown to have associated H I 21cm absorption (Lane et al., 1998a,b; Chengalur and Kanekar, 1999). Currently, the $z_{abs} = 0.2212$ system shows only a single narrow 21 cm absorption feature, while the $z_{abs} = 0.0912$ system is best fit by multiple Gaussian components: two narrow cold components with thermal kinetic widths of $T_k \approx 300$ and 100 K, and a third broad component with $T_k \approx 5000$ K (Lane et al., 2000). This suggests the presence of two temperature phases for the neutral medium, similar to those found in the Galaxy. For this lower redshift system, excluding the velocity interval where absorption is detected (a region covering ≈ 55 km s^{-1}), an upper limit has been placed on the H I gas mass. Sensitive WSRT 21 cm emission measurements of the $z_{abs} = 0.0912$ absorber place the upper limit at $M_{HI} \leq 3.7 \times 10^9 h_{65}^{-2}$ M$_\odot$ for an assumed velocity spread of 100 km s^{-1} (Lane, 2000). This requires the H I mass of the absorber to be somewhat less than that of a normal spiral galaxy. In principal, since the velocity spread would be lower for a more face-on spiral, the formal H I mass limit for

this special case could be even lower. However, if the 21 cm emission is confined to a very narrow velocity interval, a significant amount of the 21 cm emission could be missed because it falls in the same velocity intervals as the absorption.

5.2.2 B2 0827+243

The 0827+243 DLA system at $z = 0.525$ with column density $N_{HI} = (2.0 \pm 0.2) \times 10^{20}$ atoms cm^{-2} was confirmed in the RT00 survey for DLA systems in known strong Mg II absorbers. Steidel et al. (2002) presented complimentary imaging and spectroscopic results for this field, identifying the DLA galaxy (hereafter called 0827 G1) 5.8″ (32 kpc at $z = z_{abs}$) from the line of sight. They report a spectroscopic redshift of $z = 0.5258$ for 0827 G1. They also present an HST-WFPC2 F702W image of this field and note the possible presence of a satellite galaxy $\approx 2''$ West-Northwest of the center of 0827 G1. Steidel et al. (2002) also present Keck spectra showing the kinematic properties of 0827 G1 and of the $z = 0.525$ Mg II absorption-line system. They note that the satellite galaxy might be responsible for the apparent reversal in the direction of the radial velocity profile of 0827 G1 seen at the West end. This interaction might also be dispersing the gas out to large galactocentric radii, leading to the high H I column density of the absorbing gas and to the ≈ 270 km s^{-1} wide, four-component, Mg II absorption line. The unsaturated Mg I λ2852 line shows similar structure with the central two components that are ≈ 50 km s^{-1} apart being the strongest. The 21 cm absorption line has been measured at moderate spectral resolution and covers ≈ 50 km s^{-1}, though it is uncertain how many absorbing components might be contributing to the profile (Kanekar and Chengalur, 2001). Based on a comparison of redshift and velocity spread, it is likely that the H I absorption arises in gas associated with the two main Mg I absorbing clouds. Indeed, there is compelling evidence that strong Mg II absorbers which show 21 cm absorption are also associated with strong Mg I absorption (Lane, 2000). Moreover, systems with larger Mg I λ2852 rest equivalent width (or velocity spread when observed at high resolution) also have larger 21 cm line velocity spreads (Lane, 2000).

5.2.3 PKS 0952+179

The DLA system towards 0952+179 at redshift $z = 0.239$ with column density $N_{HI} = (2.1 \pm 0.3) \times 10^{21}$ atoms cm^{-2} was also confirmed in the RT00 survey. Bergeron and Boisse (1991) imaged this field and found no absorber galaxy down to $m_R \sim 23.2$ ($M_R = -17.1$). Drinkwater et al. (1993) also studied this field and, despite reaching $m_R \sim 21.82$ ($M_R = -18.51$), find no resolved object at the DLA redshift.

5.2.4 PKS 1127-145

The 1127−145 DLA system at $z = 0.313$ has a column density $N_{HI} = (5.1 \pm 0.9) \times 10^{21}$ atoms cm^{-2}. It was confirmed in the RT00 survey. Bergeron and Boisse (1991) found two bright elongated objects at the DLA redshift. The closer object has an impact parameter of $b = 77$ kpc and m$_R = 19.5$ (M$_R = -21.4$). The other object has $b = 41$ kpc and m$_R = 19.6$ (M$_R = -21.3$). They also report faint structure within $6''$ of the sightline and speculate that it may be a galaxy(s) clustered about the $z = 1.19$ quasar. Lane et al. (1998a) find two faint objects close to the sightline. Optical spectroscopy revealed one of the galaxies to be at $z = 0.312$, but the other did not exhibit emission lines and therefore does not have a determined redshift.

5.2.5 PKS 1629+120

The sight line towards the quasar PKS 1629+120 ($V = 18.4$, $z_{em} = 1.795$) contains a DLA system at $z = 0.532$ with column density $N_{HI} = (5.0 \pm 1.0) \times 10^{20}$ atoms cm^{-2}. It was discovered in an HST Cycle 9 survey for DLAs in strong Mg II-Fe II absorption-line systems (Rao et al., 2003) This system had not previously been imaged.

5.3 OPTICAL AND NEAR-IR IMAGING OBSERVATIONS

The five quasar fields were observed during the period between November 1997 and June 2001. Optical images were obtained with the MDM Observatory 2.4m Hiltner Telescope on

Kitt Peak using the 1024×1024 Templeton CCD ($0.285''$ pixel^{-1}) and with the 3.5m WIYN telescope on Kitt Peak. Observations with the WIYN telescope were made in both classical-scheduling mode using the Mini-Mosaic 4096×2048 SITe CCD pair ($0.141''$ pixel^{-1}) as well as queue-mode by the WIYN queue observing team using a 1024×1024 Tektronix CCD ($0.195''$ pixel^{-1}). The near-infrared images were obtained at the 3.0m NASA IRTF on Mauna Kea using NSFCAM in combination with a 256×256 InSb detector array ($0.30''$ pixel^{-1}) and the 3.6m ESO NTT on La Silla using SOFI, which uses a 1024×1024 HgCdTe detector array ($0.292''$ pixel^{-1}). The near-IR images were obtained using using several different short-exposure dither patterns, flat-fielded with sky frames that were obtained from the dithered object frames, and then shifted before addition to obtain a "final" image. All images were processed using the recommended procedures and standard star observations were used to calibrate the photometry. The observations are summarized in Table 5.1. Some of the observations listed in Table 5.1 were taken under less than ideal conditions, but were still useful for confirmation of some of the derived results. Some of the images shown in §5.5.1 are smoothed to enhance low surface brightness features. The smoothed images were used to delineate the low surface brightness features and set the aperture for doing the photometry, but photometric measurements were made on the unsmoothed images, unless otherwise noted. Limiting 3σ surface brightnesses and seeing measurements for the final combined (unsmoothed) images used in the analysis of the B2 0827+243, PKS 0952+179, PKS 1127-145, and PKS 1629+120 fields are given in Table 5.2. Limiting 2σ aperture magnitudes for the final combined (unsmoothed) images used in the analysis of the OI 363 field are given in Table 5.3.

5.4 STELLAR POPULATION TEMPLATE FITS

Galaxy colors obtained with multi-band photometric data can be used to infer information about the stellar populations that contribute to the observed flux. For the galaxy 0738 G1 in the field of OI 363, the publicly available spectral synthesis code *hyperz* (Bolzonella et al., 2000) was used to model a galaxy near redshift $z = 0.22$. The details of the procedure are discussed in §5.5.1.2. For the study involving the B2 0827+243, PKS 0952+179, PKS

Table 5.1: Journal of Imaging Observations

Telescope	Filter	Date	Min.
	OI 363		
MDM	U	1999 Feb 20	60
		1999 Nov 13	90
		1999 Nov 14	60
WIYN	B	1997 Nov 5	30
		1998 Nov 25	15
	R	1997 Nov 5	45
		1999 Jan 18	15
	I	1997 Dec 5	50
IRTF	J	1998 Dec 13	30
		1999 Apr 29	63
	H	1998 Dec 13	30
		2000 Mar 8	63
	K	1998 Dec 12	130
		1998 Dec 14	132
		1999 Apr 28	63
		2000 Mar 6	126
	B2 0827+243		
MDM	U	1999 Nov 13,14	100
WIYN	B	1999 Jan 18	54
	R	1999 Jan 18	15
MDM	I	1999 Nov 14	28
IRTF	K	1999 Apr 27	62

Telescope	Filter	Date	Min.
	PKS 0952+179		
MDM	U	1999 Feb 17−20	180
	B	1999 Feb 18,20	60
	R	1999 Feb 19,20	75
WIYN	R	1999 Mar 20	27
NTT	J	1999 Jan 02	60
	K_s	1999 Jan 02	60
IRTF	K	1998 Dec 12	20
		2000 Mar 06	63
	PKS 1127−145		
MDM	U	1999 Feb 18,19	120
	B	1999 Feb 19,20	60
	R	1999 Feb 18−20	80
	I	1999 Nov 13	14
		2001 Feb 26	30
NTT	J	1999 Jan 02	80
IRTF	K	1998 Dec 13	60
		1999 Apr 28	63
	PKS 1629+120		
WIYN	U	2001 Jun 25,27	60
MDM	B	2000 Sep 29	45
	R	2000 Sep 29,30	45
IRTF	J	2000 Sep 30	50
	K	2000 Sep 29	60

Table 5.2: 3σ Surface Brightness Limits (μ) and Seeing Measurements (Θ)

	μ (mags/arcsec^2)						Θ (arcsec)					
Field	μ_U	μ_B	μ_R	μ_I	μ_J	μ_K	Θ_U	Θ_B	Θ_R	Θ_I	Θ_J	Θ_K
0827+243	24.0	25.1	24.1	22.9	$\cdots$	19.6	1.3	1.0	0.8	1.1	$\cdots$	0.7
0952+179	24.2	24.8	24.9	$\cdots$	22.2	20.8	1.2	1.1	0.7	$\cdots$	0.7	0.9
1127−145	24.0	25.0	24.5	$\cdots$	22.8	20.4	0.9	1.2	0.9	$\cdots$	0.7	0.8
1629+120	23.6	24.6	24.2	$\cdots$	21.1	20.4	1.3	1.3	1.2	$\cdots$	1.0	1.0

1127-145, and PKS 1629+120 fields, a new procedure was developed which is described below.

Stellar population synthesis models were used to fit the photometry for objects with sufficient multi-band data in order to investigate the stellar populations present in the DLA galaxies. This included object(s) in the 0827+243, 1127-145, and 1629+120 fields. However, multiple stellar populations typically contribute to an observed spectral energy distribution (SED). Therefore, a fitting method which allows for contributions from multiple stellar populations attenuated by a variable amount of wavelength-dependent extinction due to dust was used. Galaxy colors are known to be degenerate in age–metallicity–redshift space, so further assumptions and an interpretation of what the fits mean is generally required.

First, when performing fits, the redshift of the galaxy was set to the DLA redshift. In all three cases there was reasonable justification for this. The adopted redshift was either confirmed spectroscopically or verified to be a likely photometric redshift. Second, the metallicities of all the template spectra were fixed to be solar. This is useful, since solar metallicity is an often-used benchmark. However, it is well-known that the measured neutral-gas-phase metallicities of DLA gas at moderate to high redshift are closer to one-tenth solar. If lower metallicities (e.g. $\approx 0.2 - 0.02$ solar) hold for the stellar component of the DLA galaxies studied here, the nature of the age–metallicity degeneracy means that the age of the stellar population(s) in the DLA galaxy would generally be underestimated. If the stellar metallicity were ≈ 0.2 solar, the effect would be quite small, but at metallicities as low as

≈ 0.02 solar, the effect is substantial. Thus, even with the advantage of fixing redshift, the age–metallicity degeneracy gives rise to some interpretive limitations. Another limitation is the degree to which any adopted set of template spectra (see below) are applicable to fit the observed SEDs. In each case, when the qualitative results of the SED fitting is taken in combination with morphological information, a consistent conclusion which provides useful information on the evolutionary history of a DLA galaxy as presented in §5.5 is generally able to be drawn.

For the template spectra, the galaxy isochrone synthesis spectral evolution library (GISSEL99) of Bruzual and Charlot (see Bruzual A. and Charlot, 1993) was used. Templates with a Scalo IMF corresponding to instantaneous bursts observed at eleven different ages: 10^{-3}, 10^{-2}, 0.05, 0.1, 0.2, 0.3, 0.6, 1.0, 1.5, 4, and 12 Gyrs were chosen. From these original eleven, an additional 110 templates were generated by applying a Calzetti reddening law (Calzetti et al., 2000) with ten different dust extinction values, corresponding to $E(B-V)$ of 0.05, 0.1, 0.2, 0.3, 0.4, 0.5, 0.6, 0.7, 0.8, and 0.9. The convolution of each of these 121 redshifted templates with the UBRJK filter set (UBRIK for 0827 G1) was converted to flux units, resulting in a flux five-vector for each template. Models were then built to minimize the χ^2 fit to the observed photometric SEDs for each of the $121!/(121-N)!N!$ combinations of N five-vectors, where N was the number of component templates used in the fit. Cases where the value of N was 1, 2, or 3 were investigated. The model that gave the most reasonable value for reduced χ^2 was then reported as the most likely (combination of) stellar population(s) in a galaxy. Although three-burst models were explored, the resulting reduced χ^2 values did not justify their use.

The standard interpretation of reduced χ^2 fitting results holds for the best fits presented in §5.5. That is, if the adopted template spectra are representative of the observed SEDs and if the derived observational errors are valid, model fits which have a reduced χ^2 between ≈ 0.8 and 2 (which correspond to reduced χ^2 probabilities between ≈ 0.5 and 0.2) are taken to be acceptable fits. A reduced χ^2 value much larger than this should formally be rejected. There are two possible reasons for this. Either (1) the errors have been underestimated, which might be the case if some unknown systematic error in some of the photometry exists, or (2) the set of template spectra used to fit the observed SEDs are inappropriate. In cases

where a larger reduced χ^2 was found, the quoted fits still provide qualitative information on the nature of the DLA galaxy's stellar population. It might be that the χ^2 could be reduced further by assuming some specific form for time-variable star formation, and/or by using different metallicities, and/or by tracking down an unknown systematic error in the photometry. Another possibility is finding a reduced χ^2 value much less than one (resulting in a probability greater than 0.5). This may be indicative of over-fitting the data or error estimates that are too large.

The specifics of the various fits to DLA galaxy SEDs are discussed in §5.5. Models that included a negative population were rejected as unphysical. Quoted stellar population fractions are by burst mass, though it should be kept in mind that any such method is sensitive only to the light output of the galaxy, and as younger populations will have smaller mass to light ratios, large old populations may not be resolved by this technique when a significant young burst is present. As noted above, instantaneous bursts may, in many cases, be unreliable approximations for star formation histories of real galaxies. By building the best-fit model from multiple templates, however, a non-parametric star formation history was, effectively, mimicked. Nonetheless, the process was repeated with sets of exponentially decreasing star formation rates. The results from the two methods were consistent. For example, a galaxy that showed an equal combination of old and young stellar populations from the first method would show a long e-folding time in the second method, while a galaxy with a predominately young population would show a very short e-folding time.

5.5 DLA GALAXY IDENTIFICATIONS

As detailed below, two of the six DLA galaxies in the fields of OI 363, B2 0827+243, PKS 0952+179, PKS 1127-145, and PKS 1629+120 have confirmed slit redshifts, two have a photometric redshift consistent with the DLA absorption redshift, and two are identified based on their proximity to the quasar sight line. It should be kept in mind that the degree of confidence for any "identification" of a DLA galaxy is variable, with the confidence being highest when the candidate DLA galaxy has a low impact parameter to the quasar sight line *and* there is a confirming slit spectrum showing it is at the DLA system redshift. However,

even when the confidence is relatively high, it is possible that a fainter galaxy or a galaxy with a smaller impact parameter, might be the actual DLA absorber. Here, the assumption is made that a neutral gas cloud (or clouds along the line of sight) associated with the galaxy identified as the DLA galaxy is the site of the DLA absorption.

Where possible, bright stars in the field were used to model the PSF, which was then subtracted before any photometric measurements were made. This was sometimes not possible in the IRTF images since there were often no bright stars in the small field of view (77″) and no PSF star was observed separately.

5.5.1 OI 363

The IRTF K-band image (Figure 5.1) shows 0738 G1 (≈ 5.7 arcsec southeast of the quasar) and reveals the presence of luminous features in the fuzz surrounding the quasar that were not very significant in the Rao and Turnshek (1998) WIYN R-band image. The fuzz is seen to consist of features of low, but not uniform, surface brightness. The imaging is suggestive that, within the fuzz, the elongated feature to the east-southeast of the quasar could be part of a (spiral) "arm" since it is approximately concentric with respect to the somewhat off-centered light surrounding the quasar; a similar "arm" is not apparent on the opposite side of the quasar. To the west-southwest there is a feature elongated from east to west that appears like a "jet" since it runs nearly perpendicular to the otherwise concentric-looking extended light. This jet-like feature appears to have structure. It is coincident with the cross marked on the original Rao and Turnshek (1998) WIYN R-band image, but it does not emanate from the quasar nucleus. In the discussion below, the terms "arm-like feature" and "jet-like feature" are used to describe the appearance of these regions, but there is certainly no *strong* evidence that these terms describe their actual physical nature.

Table 5.3 lists the UBRIJHK photometric measurements of 0738 G1, the arm-like feature, and the jet-like feature. Details of how these measurements were made and how they have been used to infer the properties of the two DLA galaxies at $z = 0.22$ and $z = 0.09$ are given below.

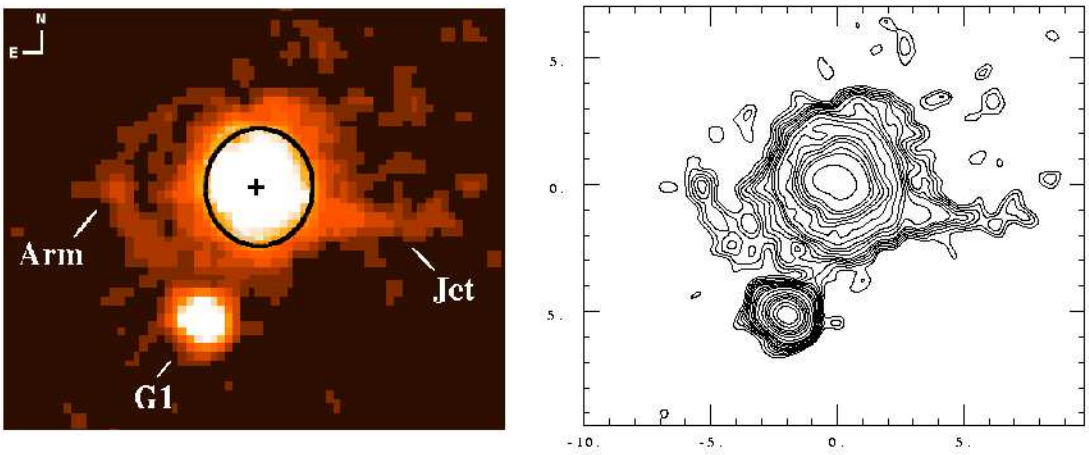

Figure 5.1: The left panel shows an IRTF K-band image of the OI 363 quasar field after smoothing with a Gaussian having a FWHM equivalent to the seeing (0.75 arcsec) and then subtracting the quasar's nuclear PSF. The center of the subtracted nuclear PSF is marked with a "+." The image is 20×17 arcsec. In the central region, enclosed in the ellipse drawn on the figure, the light appears to be dominated by an elliptical host ($M_K \approx -25.8$ or $L_K \approx 3.3L_K^*$ at $z_{Q,host} = 0.63$) to the quasar ($M_K \approx -28.6$ or $L_K \approx 44L_K^*$ at $z_{Q,nuc} = 0.63$). One or more of the low surface brightness features labeled "arm" and "jet" (i.e. the arm-like and jet-like features described in the text), and the light between them, presumably correspond to the DLA galaxy at $z = 0.09$, which gives rise to the DLA absorption-line system at $z = 0.0912$ with $N_{HI} = 1.5 \times 10^{21}$ atoms cm^{-2}. The dwarf galaxy labeled 0738 G1 is at $z = 0.22$, which gives rise to the DLA absorption-line system at $z = 0.2212$ with $N_{HI} = 7.9 \times 10^{20}$ atoms cm^{-2}. The right panel shows an isophotal plot of the same region where the faintest isophote corresponds to 3σ above the background.

Table 5.3: Photometry for the OI 363 Field

	Limiting	G1			Jet	Arm
Filter	mag	Aperture mag	Total mag	μ_0	μ	μ
U	24.7	23.67 ± 0.15	22.8 ± 0.15	23.8 ± 0.3	···	···
B	25.7	23.46 ± 0.05	22.7 ± 0.05	23.4 ± 0.2	···	···
R	27.0	21.49 ± 0.07	20.8 ± 0.05	21.5 ± 0.1	25.1 ± 0.2	···
I	24.1	21.07 ± 0.12	20.4 ± 0.1	21.0 ± 0.1	···	···
J	22.8	19.82 ± 0.12	18.9 ± 0.1	19.9 ± 0.1	22.1 ± 0.5	···
H	21.0	19.38 ± 0.12	18.7 ± 0.1	19.6 ± 0.1	···	···
K	22.5	18.52 ± 0.12	17.8 ± 0.1	18.3 ± 0.1	21.9 ± 0.2	21.5 ± 0.2

5.5.1.1 0738 G1 Spectrum Much of the evidence concerning the redshift and nature of 0738 G1 comes from an optical spectrum of 0738 G1 presented and discussed in Rao et al. (2003). They compare the 0738 G1 spectrum with a spectrum of an early-type galaxy (the type E3 elliptical galaxy NGC 4648, Kennicutt 1992a) redshifted to $z = 0.22$, and suggest that 0738 G1 is probably best classified as a dwarf elliptical, or possibly E/S0. Features in the 0738 G1 spectrum such as the 4000 Å break, the G band at rest wavelength 4304 Å, the MgI + MgH ("Mg b") band at 5175 Å, the NaD lines at 5893 Å, and a TiO band at 6260 Å give strong evidence that 0738 G1 is indeed at $z = 0.22$.

5.5.1.2 0738 G1 Spectral Energy Distribution Since the imaging data were taken with three different telescopes in various conditions and with widely varying limiting magnitudes, an appropriate procedure had to be used to accurately determine 0738 G1's colors. The worst seeing conditions ($\approx$ 1.0 arcsec) were in the U and H bands. Therefore, all of the other images (BRIJK) were degraded to this resolution by convolution with a Gaussian before the photometric measurements were made. An aperture size of 1.4 arcsec ($\approx$ 4.9 kpc at $z = 0.22$) was then determined to be a good choice to include most of the galactic light detectable above the sky background in the faintest image and still yield minimal errors.

However, it should be noted that nearly half of 0738 G1's light in the WIYN R-band was not included in the 1.4 arcsec aperture. Comparison of the WIYN B-band and R-band images, which represents the best two-color data, showed no *significant* evidence for a color gradient in 0738 G1. The estimated errors in 0738 G1's magnitudes (Table 5.3) include both the statistical errors and zero-point calibration errors.

0738 G1 is a neutral-colored dwarf galaxy (B−K= 4.9) with $L_K = 0.10L_K^*$, $L_R = 0.12L_R^*$ and $L_B = 0.10L_B^*$, where an L^* galaxy corresponds to $M_K^* = -24.5$, $M_R^* = -21.9$ and $M_B^* = -20.9$. See Loveday (2000) for M_K^*, Marinoni et al. (1999) for M_B^*, and Poggianti (1997) and Cowie et al. (1994) for K corrections.

Given the UBRIJHK colors of 0738 G1, further evidence of its redshift comes from a derivation of its photometric redshift. As Figure 5.2 shows, $z = 0.2$ is the most probable redshift based on fitting 1996 Bruzual and Charlot galaxy model templates to the colors (see more discussion below). In particular, it was possible to obtain an excellent match to the spectral energy distribution of 0738 G1 using *hyperz* (§5.4) to model a galaxy near redshift $z = 0.22$. While a variety of metal abundances were considered, the fits were not very sensitive to metallicity for these colors. However, slightly higher and lower redshifts could not be ruled out definitively based on the photometry alone (Figure 5.2) and, in the end, the best evidence for the $z = 0.22$ redshift of 0738 G1 comes from its slit spectrum (Rao et al., 2003) and the circumstantial evidence provided by the existence of the $z = 0.2212$ absorber in the field. Therefore, while the derivation of photometric redshifts for intrinsically faint DLA galaxies would seem to be a promising method when used with the expectation that there will be a galaxy in the field at the absorption redshift, the technique should be used with caution since most photometric redshift techniques have been tested by comparing photometric and spectroscopic redshifts of intrinsically luminous galaxies, and evidence suggests that DLA galaxies are often not very luminous.

In order to consider how well the observed colors of 0738 G1 at $z = 0.22$ match different types of galaxies, and what this might tell us about the present nature of 0738 G1 and its progenitor, *hyperz* was also used to determine a range of spectral synthesis models. First the colors of 0738 G1 were dereddened using a Galactic extinction law and $A_B = 0.18$ (Cardelli, Clayton, & Mathis 1989). *Hyperz* was then used to investigate the range of models and

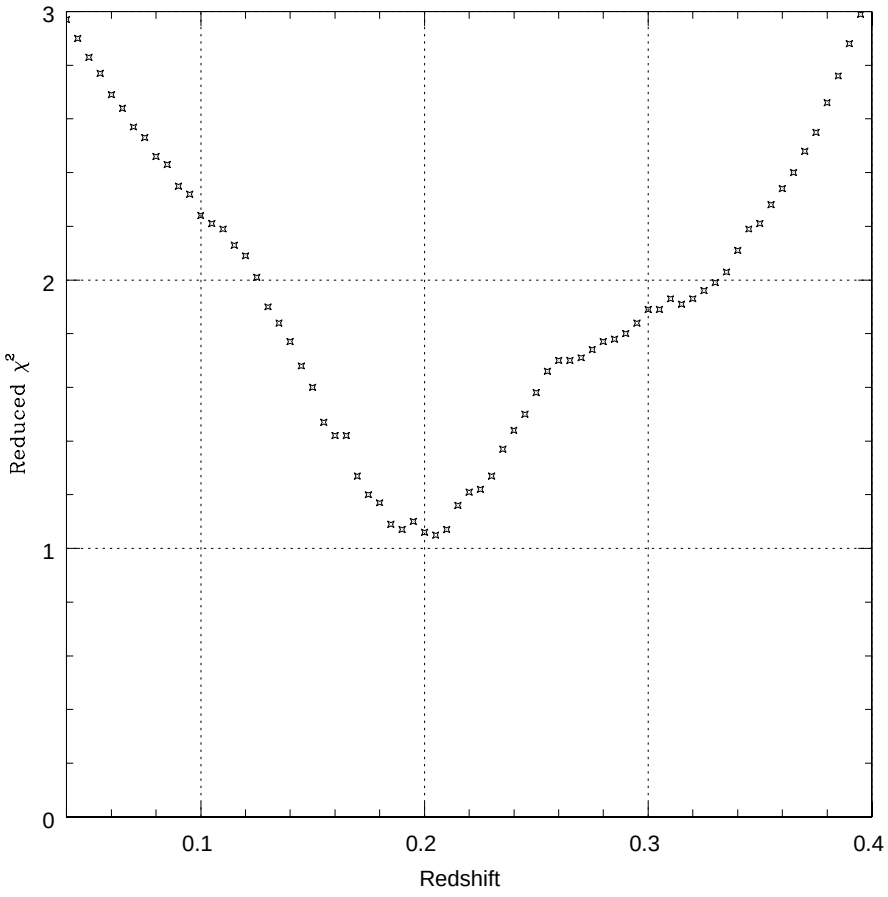

Figure 5.2: χ^2 plot showing the reliability of the photometric redshift determination for 0738 G1. The most probable photometric redshift is $z \approx 0.2$, which matches the slit redshift.

ages that produced acceptable fits to the observed colors of 0738 G1. For the analysis the metallicity was set to 20% of the solar value. The amount of intrinsic visual extinction, A_V, was allowed to be a free parameter, assuming that the Calzetti et al. (2000) reddening law holds. The available GISSEL96 template sets were for an instantaneous single-burst model, plus models with exponentially decreasing star formation rates with e-folding times in Gyrs of $\tau = 1$, 2, 3, 5, 15, 30, and infinity (i.e. constant star formation rate). Models with $\tau < 3$ are generally taken to correspond to early type galaxies (e.g. type E or S0). Of these models, the burst models at ages between $0.36 - 3.5$ Gyrs, and with A_V ranging between $1.3 - 0.1$, respectively, were found to give acceptable fits to the color data. Also, a $\tau = 1$ model with $A_V = 0.5$ fits the color data reasonably well at an age of 3.5 Gyrs. A 0.72 Gyr old burst model with $A_V = 1.0$ mag gave the best overall fit. [Note that for the Cardelli et al. (1989) Galactic extinction law, $A_V = 1$ corresponds to $N_{HI} = 1.9 \times 10^{21}$ atoms cm^{-2}; while for the Calzetti et al. (2000) extinction law which was used in the *hyperz* simulations, $A_V = 1$ might lie in the range $N_{HI} = 0.4 - 2.0 \times 10^{21}$ atoms cm^{-2}, but a good estimate is hindered by the absence of a metallicity measurement for 0738 G1. This should be compared to the value observed in the $z = 0.22$ absorber at impact parameter $b = 20$ kpc, $N_{HI} = 7.9 \times 10^{20}$ atoms cm^{-2}.] Figure 5.3 shows the color data with the models over-plotted. The best-fitting model is in panel (a) and three reasonable alternative models are shown in panels (b), (c), and (d). These galaxy templates are generally consistent with the observed spectrum of 0738 G1 (Rao et al., 2003). A comparison of the model fits shown in Figure 5.3 indicates that far-UV observations could break some of the UBRIJHK color degeneracy which makes it hard to distinguish age and extinction in burst models. Thus, lacking far-UV photometry of 0738 G1, it can only be inferred that the progenitor population originated at a formation epoch between $z_f \approx 0.26$ (corresponding to the 0.36 Gyr old burst model) and $z_f \approx 0.84$ (corresponding to the 3.5 Gyr old models). For the four models illustrated in Figure 5.3, Figure 5.4 shows the corresponding inferred color (B−K) evolutionary history of 0738 G1's progenitor prior to its current state at $z = 0.22$, including effects due to the K-correction but assuming that no change in intrinsic dust extinction occurred. As would be expected, in all cases the color evolution suggests that the progenitor of 0738 G1, with B−K= 4.9 at $z = 0.22$, would have been considerably bluer close to its formation epoch, i.e., B−K<4

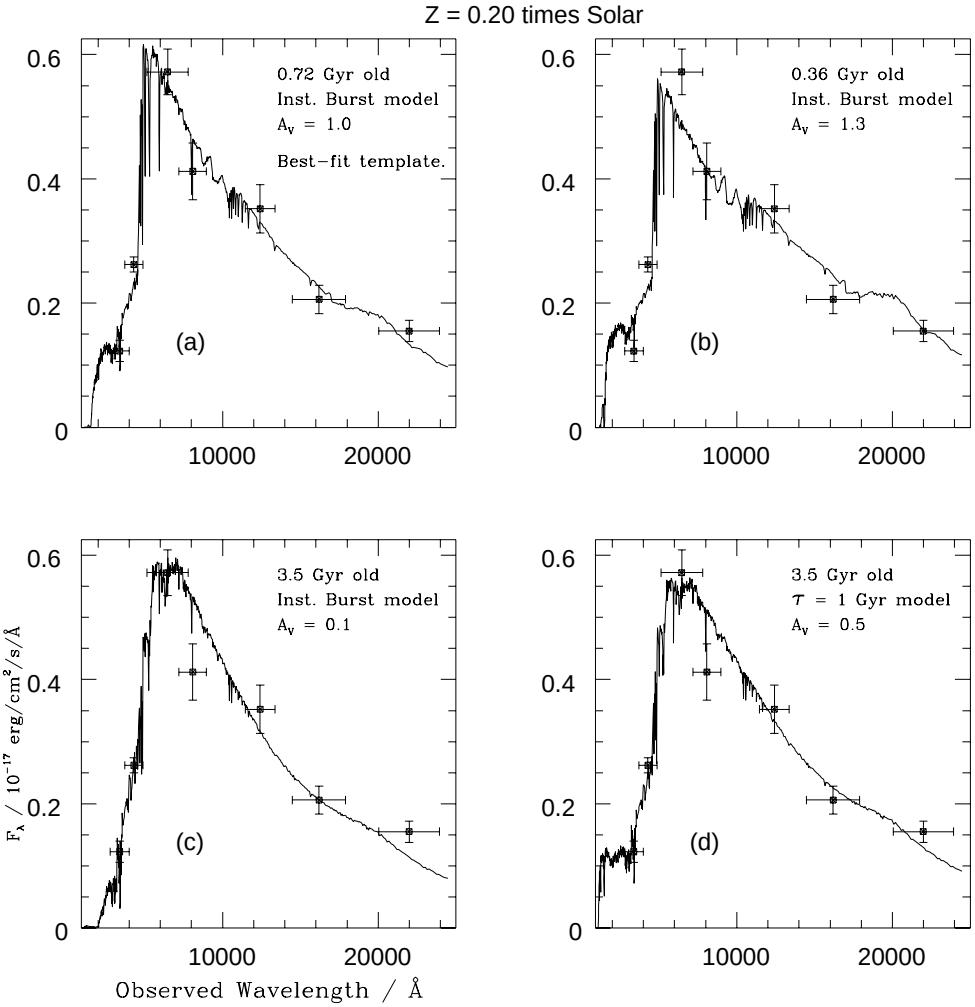

Figure 5.3: Photometry of 0738 G1 ($z = 0.22$) corrected for Galactic reddening ($A_B = 0.18$) and converted to an f_λ scale showing the agreement between the colors (U, B, R, I, J, H, K) and the 1996 models of Bruzual and Charlot (see Bruzual A. and Charlot, 1993). The four panels are as follows: (a) a 0.72 Gyr old instantaneous-burst model with $A_V = 1.0$, (b) a 0.36 Gyr old instantaneous-burst model with $A_V = 1.3$, (c) a 3.5 Gyr old instantaneous-burst model with $A_V = 0.1$, and (d) a 3.5 Gyr old model with an exponentially decreasing star formation rate ($\tau = 1$ Gyr and $A_V = 0.5$). All models use 20% solar metallicity and use a Scalo (1986) initial mass function. Panel (a) is the best-fitting model, while the others are acceptable alternatives.

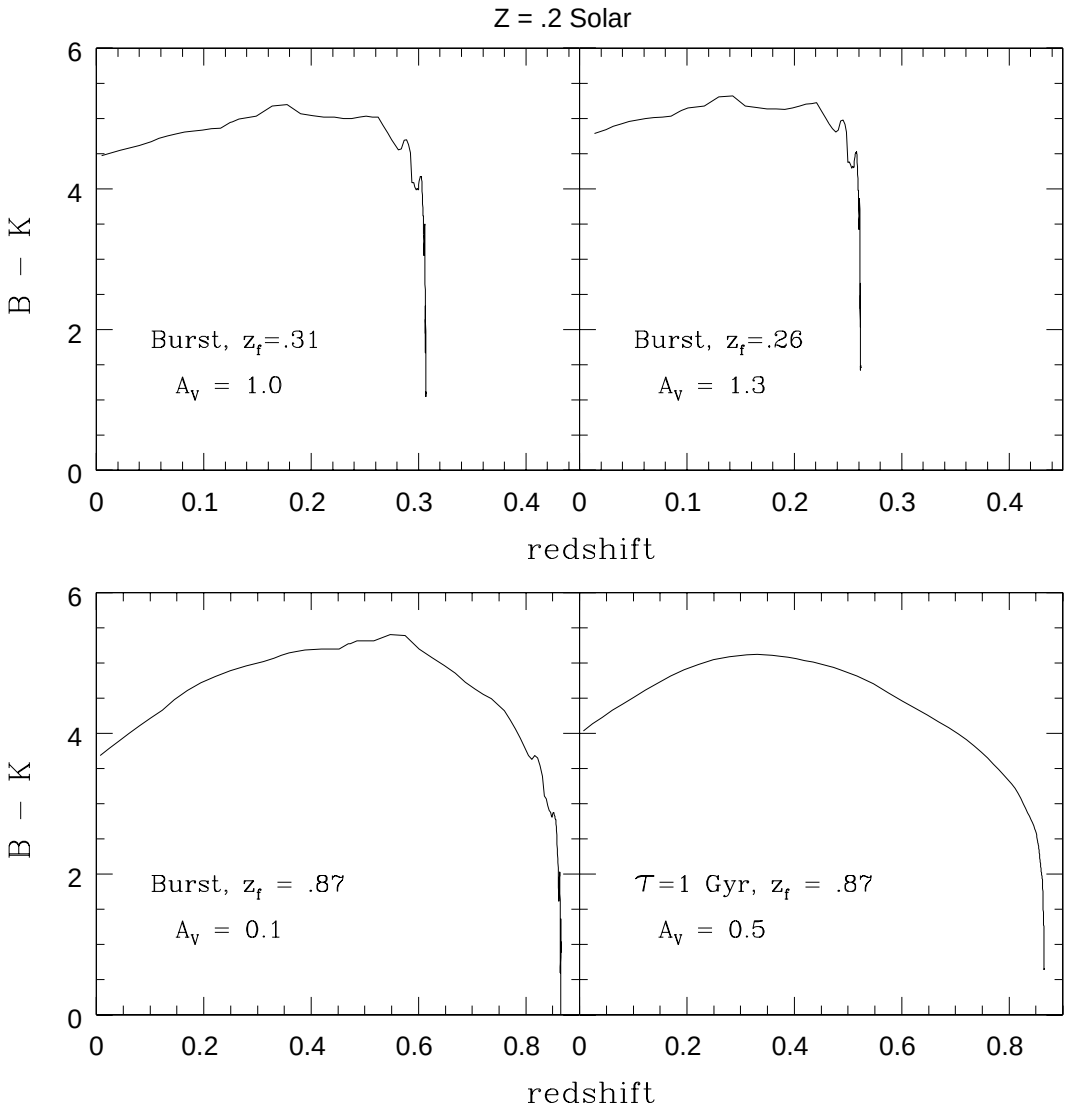

Figure 5.4: Calculated B−K color evolution of 0738 G1 ($z = 0.22$) from its formation epoch to the present. Panels a-d correspond to panels a-d in Figure 5.3, respectively. Dust extinction was assumed constant in the calculation.

at $z \approx z_f$. Therefore, 0738 G1 might be a faded, low-redshift counterpart originating from the population of moderate-redshift ($z \approx 0.3 - 0.9$) "faint blue galaxies" that have been identified in surveys (e.g., Ellis, 1997, and references therein). Further details are given in the next section.

5.5.1.3 0738 G1 Star Formation Rate A 4σ upper limit to the Hα flux of $f_{H\alpha} < 2.5 \times 10^{-16}$ ergs cm^{-2} s^{-1} was derived by Rao et al. (2003). At $z = 0.22$ this translates to an Hα luminosity of $L_{H\alpha} < 3.4 \times 10^{40}$ ergs s^{-1} and a corresponding star formation rate < 0.3 M$_\odot$ yr^{-1} (Kennicutt, 1992b). This limit is not unexpected for the bulge-dominated region of a galaxy.

The details of the star formation process that correspond to the spectral synthesis models which were discussed in the previous section and illustrated in Figures 5.3 and 5.4 can also be specified. Using the total magnitudes given in Table 5.3 it is found that: (a) for the best-fitting 0.72 Gyr old burst model there is (of course) no current star formation and the total stellar mass involved is 5.8×10^9 M$_\odot$, (b) for the 0.36 Gyr old burst model the total mass is 5.3×10^9 M$_\odot$, (c) for the 3.5 Gyr old burst model the total mass is 7.1×10^9 M$_\odot$, and (d) for the 3.5 Gyr old $\tau = 1$ model the total mass is 7.6×10^9 M$_\odot$, where the initial star formation rate is 7.8 M$_\odot$ yr^{-1} and the star formation rate at $z = 0.22$ is 0.24 M$_\odot$ yr^{-1}. This is consistent with the upper limit on the star formation of 0.3 M$_\odot$ yr^{-1} from Hα. Note that using total magnitudes (Table 5.3) results in stellar masses and star formation rates that are about a factor of two larger than when aperture magnitudes are used.

5.5.1.4 0738 G1 Radial Brightness Profile The radial brightness profile of 0738 G1 is also of interest. Using the WIYN R-band data with the best seeing (≈ 0.55 arcsec), the radial brightness profile of 0738 G1 was analyzed. The observed light profile is the convolution of the true, two-dimensional light profile and the image PSF. If the true profile is symmetric and the PSF is well approximated by a Gaussian, the convolution reduces to a simple one-dimensional integral (see Binney & Tremaine 1987) that makes it possible to compare a model radial brightness profile to the data in a straightforward manner. The observed light profile of 0738 G1 is very close to symmetric, so this method was used. Elliptical isophotes

were fitted to the brightness profile of 0738 G1. The resulting radial brightness profile along the semi-major axis is shown in Figure 5.5. Three models were fitted to the data: (a) a pure $r^{1/4}$ (bulge) profile, (b) a pure exponential (disk) profile, and (c) a combination bulge-disk profile. As shown in the corresponding panels (a-c) of Figure 5.5, a pure-disk model is a poor fit, while a pure-bulge model gives better results. The bulge-disk combination is clearly the best fit and is the preferred model, but it includes an extra free parameter. This simple model and the small angular extent of 0738 G1 compared to the seeing make it difficult to pin down the bulge-to-total light ratio, the bulge half-light radius or the disk scale-length with accuracy, but the fits suggest that a moderate amount of each is necessary to fit the light profile well.

Owing to the need for some disk light, this result therefore seems reasonably consistent with the interpretation that 0738 G1 is an early-type "dwarf spiral," which has been discussed as a recently-recognized new class of galaxy (Schombert et al., 1995). In many respects these galaxies resemble the H I-rich dwarf Es, E/S0s, and S0s mentioned in §5.5.1.1. According to Schombert et al. (1995), the dwarf spirals are found only in the field and have total luminosities $M_B > -17.6$, diameters $R_{26} < 6.5$ kpc, low central surface brightnesses $\mu_0 > 24$ B mag arcsec^{-2}, and low H I masses $M_{HI} \leq 1.7 \times 10^9$ $M_\odot$ (converting the Schombert et al. (1995) values to the assumed cosmology with $H_0 = 65$ km s^{-1} Mpc^{-1}). This represents a class of objects which are currently rich in neutral gas, relative to their low surface brightness, and small in angular size. The central surface brightness of 0738 G1 ($\mu_0 \approx 23.4$ m_B arcsec^{-2}) is somewhat brighter than the parameters given by Schombert et al. (1995).

5.5.1.5 0738 G1 H I Mass Estimate 0738 G1 is displaced 5.7 arcsec from the quasar sight-line, corresponding to an impact parameter of $b = 20$ kpc. This is a relatively large impact parameter in relation to the apparent optical size of 0738 G1 (Figure 5.1). It is not unusual to find evidence for a relatively large impact parameter when trying to identify galaxies giving rise to quasar absorption-line systems, but it is somewhat surprising for a DLA system and so it leaves open the possibility that the site of the absorption is an H I cloud in a galaxy that is a companion to 0738 G1. However, consideration of this is beyond the scope of the available data, so only the description of 0738 G1 is presented here. If the

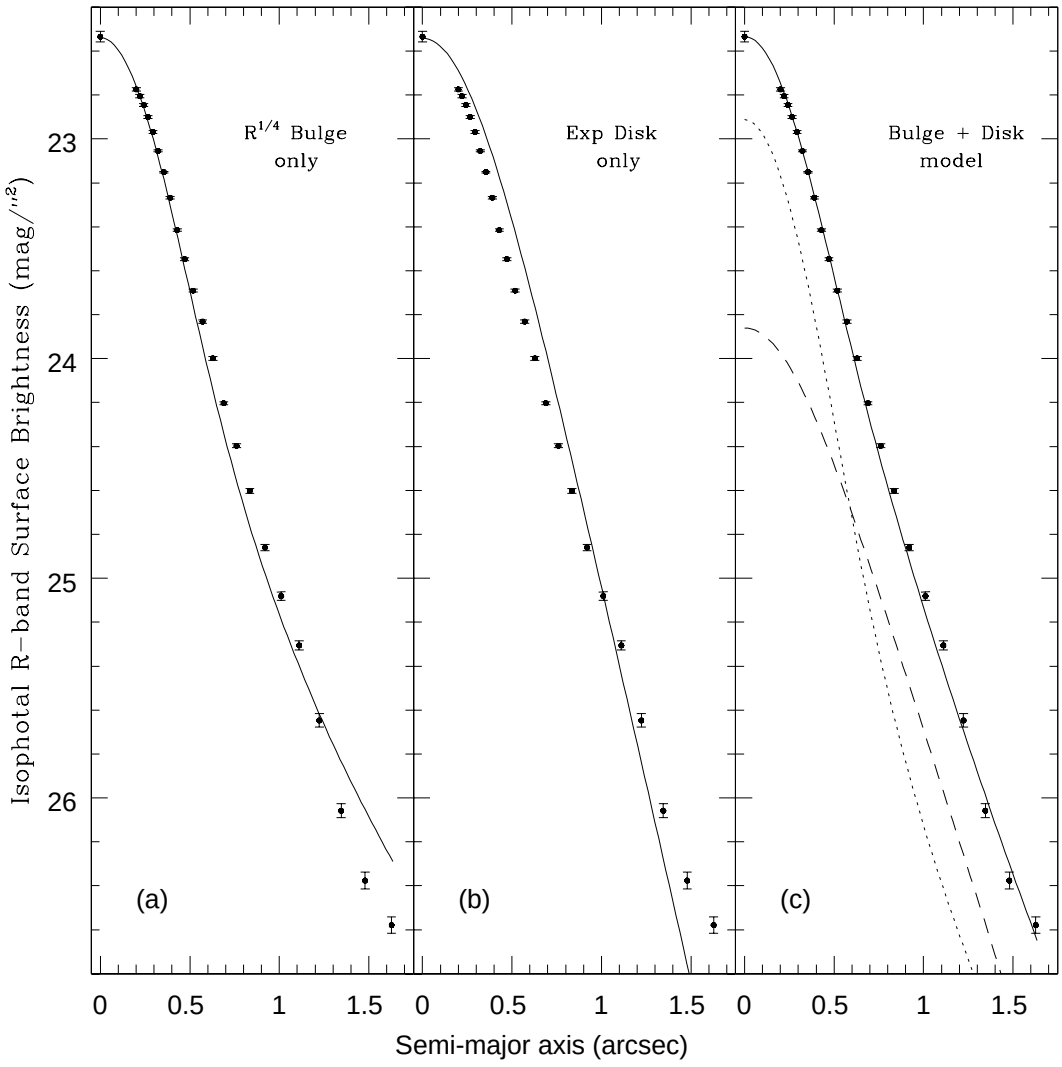

Figure 5.5: Model fits to the R-band radial light profile of 0738 G1: (a) an $r^{1/4}$ (bulge) profile alone, (b) an exponential (disk) profile alone, and (c) the best-fitting model where the interior isophotes are dominated by an $r^{1/4}$ law and the outer isophotes are dominated by an exponential.

$z = 0.2212$ absorber is assumed to have a uniform H I column density of $\approx 8 \times 10^{20}$ atoms cm^{-2} extended over a radius equal to the impact parameter, then its deduced H I mass is $M_{HI} \approx 3 \times 10^{10}$ M$_\odot$. This H I mass estimate is about an order of magnitude greater than quoted above for H I-rich dwarf Es, E/S0s, S0s, or spirals, though it would be much smaller if the covering fraction is significantly less than unity.

5.5.1.6 The "Fuzz" Near the Quasar (z=0.09) The arm-like and jet-like features are the two brightest patches of low surface brightness extended light near the quasar (i.e. the "fuzz"). Since there is no useful spectrum of any part of the fuzz or data that can be used to derive a photometric redshift for these features, their redshifts cannot be known with certainty. In principal, the light could be from a combination of: (1) unrelated foreground or background objects at neither of the two damped redshifts, (2) the quasar host galaxy at $z = 0.63$, (3) the "true" DLA galaxy at $z = 0.22$ (assuming that 0738 G1 at redshift $z = 0.22$ does not have a sufficient H I extent), and (4) the DLA galaxy at $z = 0.09$. Examination of the infrared images do suggest a combination of objects or perhaps a single disturbed object (see Figure 5.1). Therefore, each of these four possibilities will be discussed.

(1) Contamination from unrelated objects is possible. However, examination of the infrared images suggests that $< 1\%$ of the frame contains detectable infrared sources at the sensitivity of the K-band images. Therefore, if an unrelated object or objects are present near the quasar sight-line, this is an unlucky configuration, so this possibility will not be considered further.

(2) There is a reasonable chance that some of the quasar's host galaxy light at $z = 0.63$ is present in the infrared light surrounding the quasar. The quasar, OI 363, is optically luminous (V$\approx$16.1, M$_V \approx -26.1$) and radio loud. Infrared studies of optically luminous, radio loud quasars in the H-band (McLeod and Rieke, 1994) show that it is not unusual for these types of quasars to have luminous host galaxies, e.g., $> 2L^*_H$, and HST-WFPC2 studies at $z < 0.46$ show that the host galaxies of radio loud quasars are almost exclusively ellipticals (McLure et al., 2000; Hamilton et al., 2002, references therein). Examination of the infrared OI 363 images after subtraction of the unresolved nuclear quasar light (Figure 5.1) indicates that the remaining light is not exclusively from an elliptical host centered

on the quasar. A reasonable deconvolution of the image suggests that the nuclear quasar component has $M_K \approx -28.6$ ($L_K \approx 44L_K^*$) while its host has an $r^{1/4}$ profile and $M_K \approx -25.8$ ($L_K \approx 3.3L_K^*$), which is completely consistent with previous findings on radio loud quasar hosts. Nevertheless, after subtraction of the nuclear and host components some light remains between the arm-like and the jet-like features. In any case, the mere presence of the arm-like and jet-like features indicates that the surrounding light is not exclusively associated with an elliptical host. An illustration of the light that is believed to be dominated by the quasar elliptical host is contained within the ellipse drawn ixn Figure 5.1. However, there are uncertainties with this deconvolution and better spatial resolution would be needed to accurately separate out the various components.

(3) The possibility that some of the extended, low surface brightness light surrounding the quasar is due to the DLA galaxy at $z = 0.22$ is dismissed since 0738 G1 is identified as the DLA galaxy. However, recall that the impact parameter of 0738 G1 is 5.7 arcsec or $b = 20$ kpc, which may be large for a dwarf galaxy giving rise to DLA absorption (§5.5.1.5).

(4) From the arguments presented above (1-3), it is concluded that *some* of the light surrounding the quasar is from the DLA galaxy at $z = 0.09$.

Owing to the approximately circular nature of the resolved light, regardless of whether a contribution from an elliptical host is removed, and the possibility of an actual spiral arm, it may be that this DLA galaxy is a nearly face-on spiral. The considerable morphological structure surrounding the quasar does leave open the possibility that the $z = 0.09$ DLA galaxy is an irregular or an interacting system. However, the 21 cm HI absorption might be expected to be complex if an interaction occurred, and there is no evidence for this in the present 21 cm data (see 5.2.1). In either case, to place a conservative *upper limit* on the light from the $z = 0.09$ DLA galaxy it is appropriate to assume that *all* of the light surrounding the unresolved part of the quasar image (including what is believed to be the quasar host) belongs to it. With this assumption an upper limit on the K-band luminosity of the DLA galaxy at $z = 0.09$ of $L_K \approx 0.13L_K^*$ is obtained. Assuming the arm-like and jet-like features are both at $z = 0.09$, the arm-like feature has $L_K \approx 0.0007L_K^*$ with color R−K>5.5 (i.e. it is red and not detected in the R-band WIYN data) and the jet-like feature has $L_K \approx 0.0005L_K^*$ with a blue color of R−K≈3.2. This would imply that the jet-like feature is

a site of relatively recent star formation, while the arm-like feature is an older population. The diameter of the measurable light distribution was estimated to be $\approx 7 - 9$ arcsec, or $\approx 12 - 16$ kpc, and the separation from the quasar sight-line to be < 2 arcsec, or impact parameter $b < 3.6$ kpc. As noted above, light contributed by an elliptical quasar host galaxy (i.e. some light inside the ellipse shown in Figure 5.1) might have to be subtracted from the measured upper limit on the DLA galaxy's light in order to determine its true luminosity. In fact, a reasonable deconvolution suggests that the quasar host contributes $\approx 50\%$ of the total measured light, in which case the luminosity of the $z = 0.09$ DLA galaxy is $L_K \approx 0.08 L_K^*$. Regardless of the amount of contribution from the host galaxy, the resulting interpretation is that the $z = 0.09$ DLA galaxy is a low surface brightness galaxy with a diameter of ≈ 14 kpc at low impact parameter from the quasar sight-line. The details cannot be sorted out definitively without better data. Thus, the morphology of this low surface brightness dwarf galaxy remains uncertain – (another?) dwarf (possibly face-on) spiral, or an irregular, or an interacting system.

Given the above indication of the putative $z = 0.09$ DLA galaxy's diameter, it is useful to estimate its H I gas mass using some reasonable assumptions. If it simply is assumed that the circular H I gas radius is the same as the extent of the galaxy seen in the K-band image (i.e. radius r ≈ 7 kpc) and that the H I column density is uniformly $N_{HI} \approx 1.5 \times 10^{21}$ atoms cm^{-2} over that extent, the deduced H I mass is $M_{HI} \approx 6.5 \times 10^9$ M$_\odot$. This is a factor of 2 larger than the upper limit of Lane (2000) but, as discussed in §5.2.1, some of the H I 21 cm emission searched for by Lane (2000) may have been missed since velocity intervals which included absorption had to be excluded in their analysis. At the same time, the assumptions used above may over-estimate the H I mass since the impact parameter is evidently small and the H I gas distribution may be patchy or fall off exponentially with impact parameter. Nevertheless, the order of magnitude of this estimate is of interest; the total H I mass is smaller than the estimate for the $z = 0.2212$ DLA system (§5.5.1.5).

5.5.2 B2 0827+243

This quasar sight line contains a DLA system at $z = 0.525$ with column density $N_{HI} = (2.0 \pm 0.2) \times 10^{20}$ atoms cm^{-2} (RT00). Figure 5.6 shows $\approx 30'' \times 30''$ B, R, I, and K images of this field. The quasar PSFs have been subtracted and the residuals masked out. The galaxy $6''$ to the east of the sight line, labeled G1, was identified as the DLA galaxy (Steidel et al., 2002) *A posteriori*, a hint of a Southwest extension to 0827 G1 was found in the smoothed I-band image (see inset in Figure 5.6) consistent with the possible satellite galaxy reported by Steidel et al. (2002) The I-band image was obtained in $1.1''$ seeing compared to the $\approx 0.1''$ seeing of the HST image. Thus, the satellite noted by Steidel et al. (2002) is unresolved and is not distinct from 0827 G1 in the ground-based image. It is possible that the Southwest extension detected here is a low surface brightness feature of the interacting system and was not detected in the HST image. In either case, the imaging data are consistent with 0827 G1 being a disturbed spiral galaxy.

Although the impact parameter of 0827 G1 is large ($b = 34$ kpc), its high inclination angle should increase the likelihood that DLA column densities could be observed at large galactocentric distances. But it is also possible that an object hidden under the quasar PSF might be the actual absorber. To explore this possibility, the quasar PSF was subtracted in the WFPC2 image using the procedure described in Hamilton et al. (2002), but no convincing evidence for a galaxy hidden under the quasar PSF was found.

Photometric measurements of 0827 G1 along with 1σ uncertainties are given in Table 5.4. Results from stellar population spectral evolutionary synthesis model fits redshifted to $z = 0.525$ are shown in Figure 5.7. Details of the models and fitting procedures are described in §5.4. The best-fit single-burst model, a 0.05 Gyr old burst with $E(B-V) = 0.6$, results in a reduced χ^2 of 5.5. A family of two-burst models having approximately equal combinations by mass of (1) a dusty [$0.6 \lesssim E(B-V) \lesssim 0.9$], young (0.01 Gyr) burst and (2) a nearly dust free [$0.0 \lesssim E(B-V) \lesssim 0.2$], 0.2 to 0.6 Gyr old burst have the smallest reduced χ^2 values, but these are also statistically poor fits with reduced χ^2 values between 4.8 and 5.2. The fit with the smallest reduced χ^2 is shown in Figure 5.7. Apparent magnitudes from Table 5.4 along with K-corrections derived from this best-fit model give absolute magnitudes for

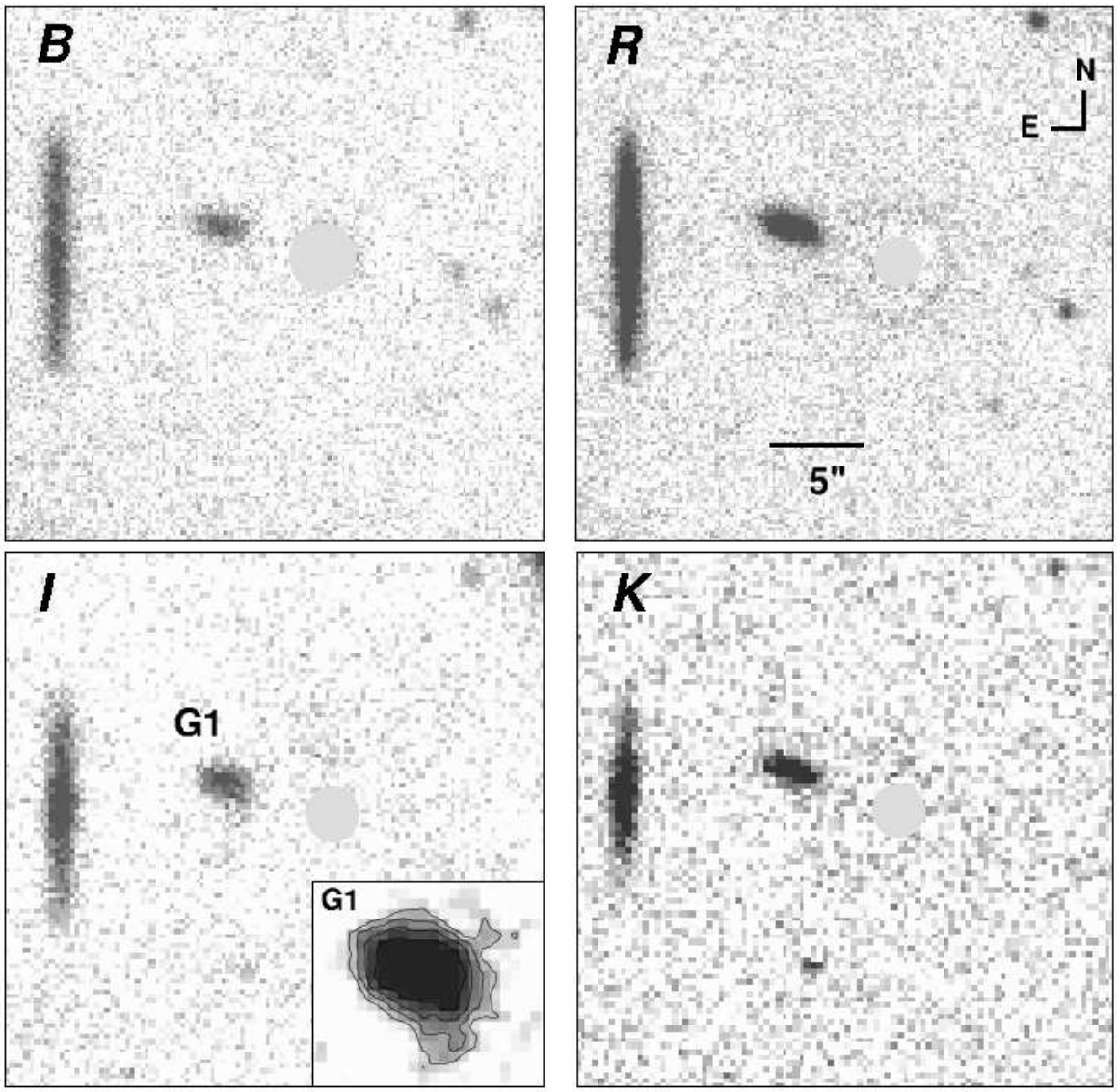

Figure 5.6: B, R, I, and K images of the B2 0827+243 field that contains a DLA system at $z = 0.525$. The quasar PSFs have been subtracted and the residuals have been masked. 0827 G1 has a measured redshift of $z = 0.5258$ (Steidel et al., 2002) and is identified as the DLA galaxy. The inset is a smoothed image of 0827 G1 in I, where a gaussian smoothing with $\sigma = 0.8$ pixels has been applied. The outermost contour is 1σ above the sky background. Note that the N-S oriented edge-on galaxy $\approx 15''$ East of the quasar is at $z = 0.199$ (Steidel et al., 2002).

Table 5.4: Photometry of 0827 G1

m_U	m_B	m_R	m_I	m_K
22.61 ± 0.16	22.76 ± 0.04	20.82 ± 0.05	20.34 ± 0.05	17.07 ± 0.05

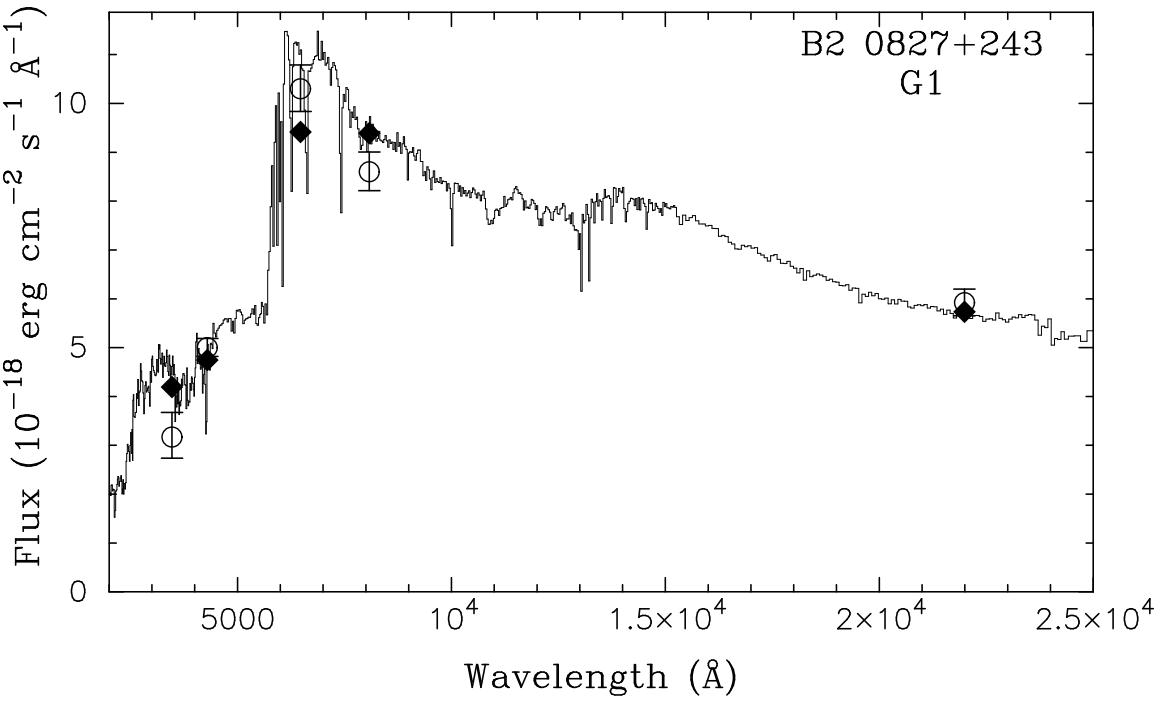

Figure 5.7: Best-fit two-burst model of a galaxy at $z = 0.525$ overlaid on the photometry of 0827 G1 in the B2 0827+243 field. The open circles with 1σ error bars are photometric measurements. For comparison, the filled diamonds are model flux values determined at the effective wavelength of the filter by convolving the filter response function with the model spectral energy distribution. The model is a two-burst combination of (1) a 48% by mass burst that is young (0.01 Gyr) and dusty with $E(B-V) = 0.6$ and (2) a 52% by mass burst that is older (0.6 Gyr) and dust free with $E(B-V) = 0.0$.

0827 G1 of $M_U = -20.3$, $M_B = -20.6$, $M_R = -21.7$, $M_I = -22.1$ and $M_K = -24.7$ at $z = 0.525$.

5.5.3 PKS 0952+179

The DLA system towards this quasar is at redshift $z = 0.239$ with column density $N_{HI} = (2.1 \pm 0.3) \times 10^{21}$ atoms cm^{-2} (RT00). Figure 5.8 shows $20'' \times 20''$ images of this field through the B, R, J, and K filters. The quasar PSF has been subtracted in the B, R, and J images and the residuals have been masked out. The quasar has simply been masked out in the K band image because there were no suitable bright stars in the IRTF-NSFCAM field of view that could be used to perform a good PSF subtraction of the quasar light. All four images have been smoothed to enhance low surface brightness features. Objects identified in the J image that are detected in at least one of the B, R, and K images have been numbered sequentially in order of increasing radial distance from the quasar. The objects labeled 1 and 2 are detected in both J and K and, due to their proximity to the quasar sight line, are the best candidates for the DLA galaxy. Their morphology suggests that they might be two nearly edge-on galaxies. While the J image, with a seeing of $0.7''$ and limiting surface brightness of 24 mag/arcsec^2, is exceptionally good by ground-based imaging standards, higher resolution imaging, for example with *NICMOS* on HST, is required to be better able to resolve these features and, perhaps, comment on the nature of the $z = 1.478$ quasar host galaxy as well (Kukula et al., 2001, cf). Table 5.5 gives the positions of the labeled objects relative to the quasar along with apparent magnitudes and 1σ uncertainties.

5.5.3.1 An ERO at z=0.239? The brightest of these in K, object 7, is an extremely red object (ERO) with $R - K = 6.5$ (see Table 5.5). EROs are generally thought to be either ellipticals at $z \gtrsim 1$ whose red colors are due to large K-corrections or star forming galaxies whose red colors are due to heavily obscured stellar or AGN emission (e.g. Cimatti et al., 1999; Dey et al., 1999; Daddi et al., 2000; Smith et al., 2001). The lowest redshift ERO known is the $z = 0.65$ galaxy, PDFJ011423 (Afonso et al., 2001), whose red colors and spectral energy distribution are consistent with it being a dusty starburst with 5 to

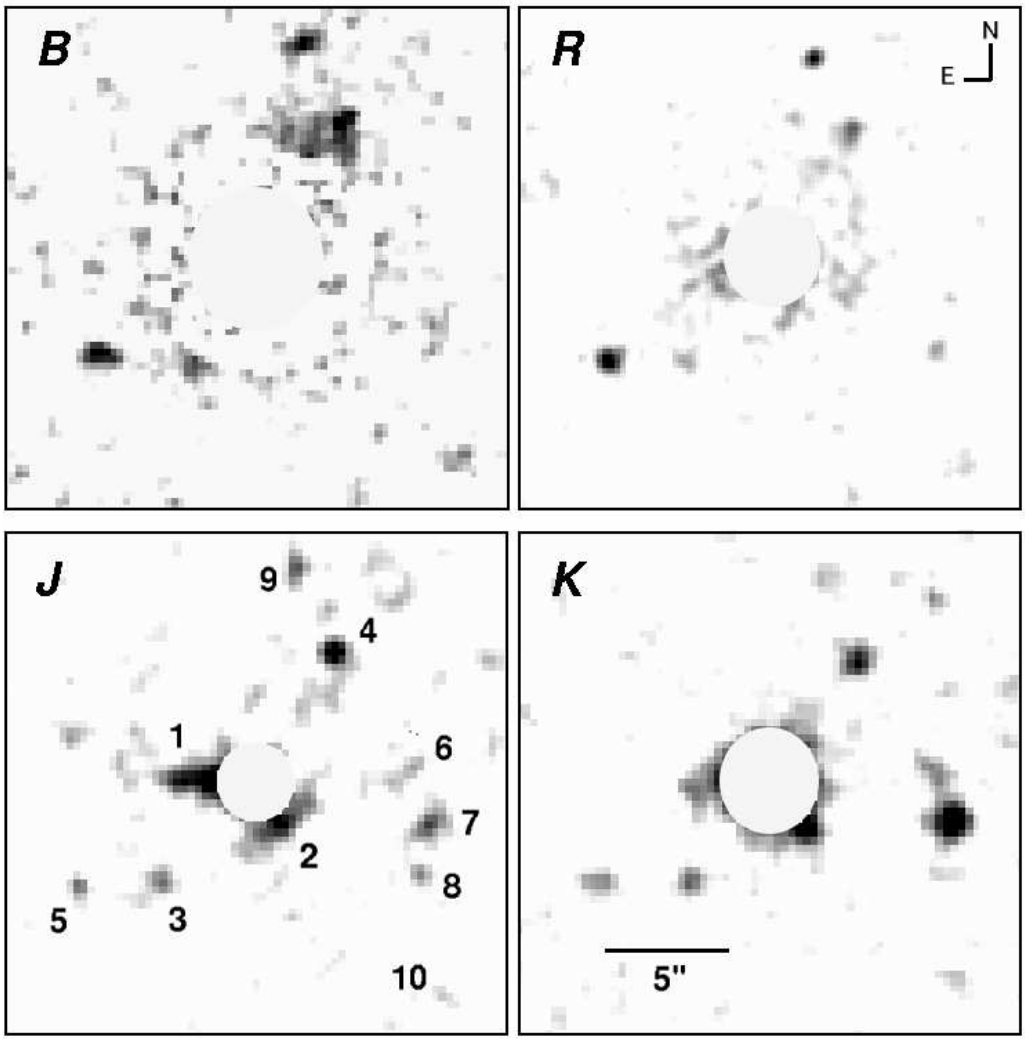

Figure 5.8: Smoothed B, R, J, and K images of the PKS 0952+179 field that contains a DLA system at $z = 0.239$. The PSF of the quasar has been subtracted in the B, R, and J images, but not in the K image as there was no suitable PSF star in the field. The residuals in B, R, and J, and the quasar in K have been masked. Objects are labeled only on the J image for clarity. All ten of these are detected in K. Features in the B and R images that lie at the edges of the mask are artifacts of the PSF subtraction process; only objects labeled 3, 4, 5, 8, 9, and 10 are detected in B, while those labeled 3, 4, 5, 7, 8, 9, and 10 are detected in R. Objects 1 and 2 are the best candidates for the DLA galaxy. Object 7 is an ERO with $R - K = 6.5$. See §5.5.3.1 for more details.

Table 5.5: Photometry of Objects in the PKS 0952+179 Field

Object	$\Delta\alpha$ $''$	$\Delta\delta$ $''$	m_B	m_R	m_J	m_K
1	-2.9	-0.1	$\cdots$	$\cdots$	22.3 ± 0.2	21.2 ± 0.3
2	$+1.4$	-1.8	$\cdots$	$\cdots$	23.1 ± 0.4	20.8 ± 0.1
3	-3.7	-4.3	25.9 ± 0.3	25.2 ± 0.2	22.5 ± 0.3	20.7 ± 0.2
4	$+3.5$	$+5.1$	25.0 ± 0.2	24.5 ± 0.2	22.1 ± 0.2	20.1 ± 0.2
5	-6.7	-4.4	24.8 ± 0.2	24.0 ± 0.1	23.2 ± 0.4	20.4 ± 0.2
6	$+6.8$	$+0.5$	27.1 ± 0.7	27.1 ± 0.8	22.3 ± 0.3	20.6 ± 0.2
7	$+7.5$	-2.0	$\cdots$	25.9 ± 0.3	22.0 ± 0.3	19.4 ± 0.1
8	$+7.0$	-3.9	27.9 ± 1.6	25.1 ± 0.2	23.0 ± 0.4	21.8 ± 0.4
9	$+1.9$	$+8.4$	24.9 ± 0.2	24.5 ± 0.1	22.4 ± 0.3	21.0 ± 0.2
10	$+7.8$	-8.7	25.0 ± 0.2	24.5 ± 0.2	22.5 ± 0.3	21.2 ± 0.3

6 magnitudes of optical extinction. Other EROs classified as starbursts have similar dust extinctions (Afonso et al., 2001). PDFJ011423 is bright in K ($m_K = 15.3$) and has extremely red colors with $R-K = 5.8$ and $J-K = 3.1$. In comparison, object 7 is relatively faint with $K = 19.4$ and is also extremely red with $R-K = 6.5$ and $J-K = 2.6$. The redshift of object 7 is not known, but if it is at the DLA redshift, it would have to be a star forming region that is heavily obscured by dust. At $z = 0.239$, $K = 19.4$ corresponds to $M_K = -20.7$, where a K band K-correction of -0.2 magnitudes has been applied (Cowie et al., 1994). This implies an absolute luminosity of $L_K = 0.03L_K^*$, comparable to the luminosity of a single star-forming region within a galaxy. It is found that, based on GISSEL99 galaxy spectral evolutionary synthesis models, its colors can be attributed to a region of star formation with age $\lesssim 0.6$ Gyr at $z = 0.239$ if the extinction is $A_V \gtrsim 4.8$. Thus, the luminosity, colors, and implied extinction are consistent with object 7 being at $z = 0.239$. If confirmed, it would be the lowest redshift ERO known.

However, the observational constraints are not tight enough to rule out the possibility that object 7 is a higher redshift elliptical galaxy. Its colors fall on the "starburst" side, but near the edge, of the $R-K$ versus $J-K$ plane used to classify EROs (Pozzetti & Mannucci 2000). Uncertainties in the photometry as well as in the definition of the plane do not preclude object 7 from crossing the plane and being classified as a passively-evolving elliptical at $z \approx 1.5$ (Cimatti et al., 1999). In this case, object 7 might be part of a cluster of galaxies that also includes the quasar PKS 0952+179 ($z_{em} = 1.478$); it would be $\sim L^*$ at this redshift. A significant number of EROs are detected in the extended $5' \times 5'$ field surrounding this quasar, and this might be supporting evidence for the over-density of EROs found by Cimatti et al. (2000) around radio loud quasars. Thus, the proximity of object 7 to the DLA galaxy might just be a coincidence.

5.5.3.2 The DLA Galaxy While the nature of none of the objects labeled in Figure 5.8 is known for certain, it is of interest to examine the possibility that they are star-forming regions associated with the DLA galaxy. The colors of all the labeled features are consistent with them being at $z = 0.239$, but with varying degrees of obscuration. The implications might be that the DLA galaxy is either a patchy LSB galaxy or a disturbed system in which

object 7 is a recently-triggered star-forming region. The galaxy would extend anywhere from $\approx$ 45 kpc (objects 1 to 7) to $\approx$ 55 kpc (objects 5 to 7). The total luminosity of the PKS 0952+179 DLA galaxy cannot be measured since some of it is likely to be hidden by the quasar PSF. The total luminosity of all the objects labeled in Figure 5.8 is $m_K = 18.1$. If this is considered a lower limit to the luminosity of the DLA galaxy, then $M_K < -22.0$ or $L_K > 0.1L_K^*$. If only objects 1 and 2 were part of the DLA galaxy, it would extend $\approx$ 24 kpc with $m_K < 20.2$, $M_K < -19.5$, and $L_K > 0.01L_K^*$. If objects 1 and 2 were two edge-on galaxies, as their J-band morphologies might suggest, then possibly half of the galaxy that is object 1 is obscured by the quasar PSF. In this case, each of the edge-on galaxies would be a dwarf with a luminosity on the order of $0.01L_K^*$.

However, in the absence of higher-resolution imaging, objects 1 and 2 are tentatively identified as the DLA galaxy since these have the smallest impact parameters, and since there is no observable emission between these and objects 3 – 10. Given the assumption that half of object 1 is obscured by the quasar PSF, objects 1 and 2 have a total luminosity of $L_K = 0.02L_K^*$. Since these objects extend into the quasar PSF, their impact parameter cannot be determined to better than the radius of the circle that encloses all residuals left over from subtracting the quasar PSF in the unsmoothed J-band image. This is because subtracting the PSF resulted in noisy residuals near the PSF core and no useful information could be extracted within this radius. The radius was measured to be $1.2''$ which, at $z = 0.239$, implies $b < 4.5$ kpc.

Note that luminous galaxies in the extended field surrounding this quasar have spectroscopic redshifts different from the DLA absorption redshift (Bergeron and Boisse, 1991), and that the $z = 0.239$ system is the only known absorption-line system in the spectrum of this quasar. High resolution observations of the $z = 0.239$ Mg II absorption line do not exist, and so the kinematic structure of the Mg II-absorbing gas has not been studied in detail. However, the 21 cm absorption line is narrow with a FWHM of only 7.7 km s^{-1} (Kanekar & Chengalur 2001a), indicative of simple kinematic structure.

5.5.4 PKS 1127-145

This DLA system is at $z = 0.313$ with column density $N_{HI} = (5.1 \pm 0.9) \times 10^{21}$ atoms cm^{-2} (RT00). Figure 5.9 shows $\approx 50'' \times 50''$ images of this field in U, B, R and J. The quasar PSF has been subtracted in each of the four images and the residuals have been masked out. Furthermore, the images have been smoothed to enhance low surface brightness features. The two large spiral galaxies, labeled "a" and "b", are at the DLA redshift (Bergeron and Boisse, 1991). Galaxy "a" is clearly warped and has a dwarf companion $\approx 2''$ to the Southwest. Galaxy "b" has a faint extension towards the East that is visible in R and J. The object $3''$ West of the quasar, labeled 1, is an emission-line object with a confirmed redshift of $z = 0.3121 \pm 0.0003$ (Lane et al., 1998a). No emission lines were detected in the spectrum of object 3, and so its redshift is not known. However, the J band image in Figure 5.9 suggests that there may be LSB features to the East of the quasar that extend out to the position of object 3. Thus, the "DLA galaxy" is identified as the patchy/irregular LSB structure visible primarily in J that extends $\approx 10''$ (44 kpc) in the N-S as well as E-W directions and encompasses objects 1, 2, 3, and 4.

Since the DLA galaxy as defined above overlaps with the quasar PSF, its impact parameter cannot be determined to better than the radius of the circle that encloses all residuals left over from subtracting the quasar PSF in the unsmoothed J-band image. This radius, which is assumed to be an upper limit to the DLA galaxy's impact parameter, was measured to be $1.5''$ which, at $z = 0.313$, implies $b < 6.5$ kpc. No useful information could be extracted within this radius. The DLA galaxy is quite possibly the remains of a dwarf galaxy that is being tidally disrupted by the more massive spirals, and in which these four objects represent regions of recent star formation.

5.5.4.1 Photometry Photometric measurements of objects 1, 2, 3, and 4 are given in Table 5.6 along with their 1σ uncertainties. Object 2 is below the detection limit in R and has $R - J > 2.3$. Lower limits to the U, B, R, and K magnitudes of object 2 were measured with the same aperture size used to measure its magnitude in J.

Objects 1, 3, and 4 have blue colors. Stellar population synthesis model fits to the

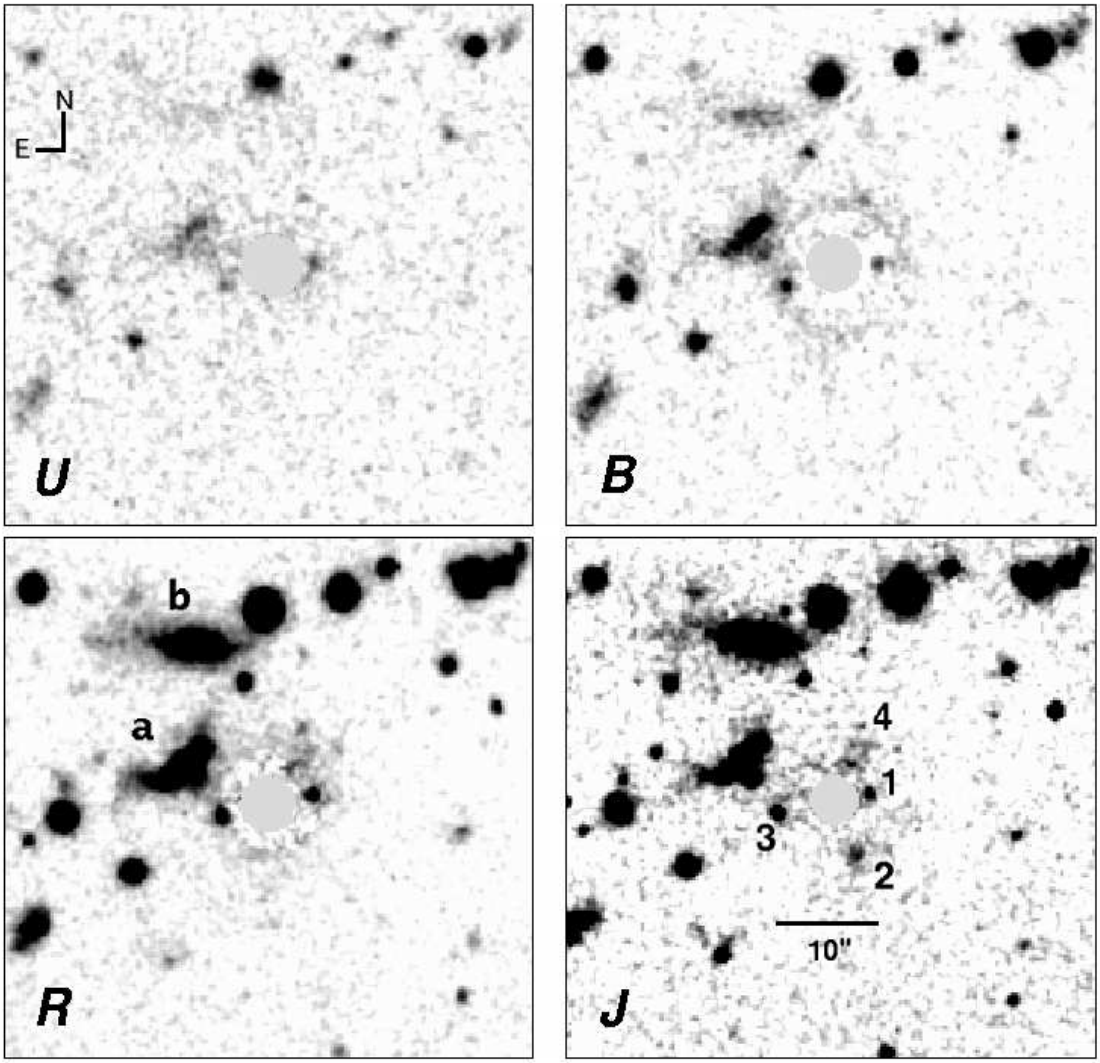

Figure 5.9: Smoothed U, B, R, and J images of the PKS 1127−145 field that contains a DLA system at $z = 0.313$. The PSFs of the quasar have been subtracted and the residuals masked. The DLA galaxy is assumed to be the patchy/LSB structure that extends between objects 3 and 1 in the E-W direction and between objects 4 and 2 in the N-S direction. Object 1 has a measured slit redshift of $z = 0.3121$. The two large spirals in the field, labeled "a" and "b" are also at the DLA redshift. Note the presence of several EROs that are visible in J but are faint or below the detection limit in R. The ring-like structures around the quasar in B and R, left over from the quasar PSF subtraction process, appear enhanced due to the smoothing and are not real.

Table 5.6: Photometry of Objects in the PKS 1127−145 Field

Obj	$\Delta\alpha$	$\Delta\delta$	m_U	m_B	m_R	m_J	m_K
	$''$	$''$					
1	+3.8	+0.3	23.00 ± 0.19	24.09 ± 0.15	22.58 ± 0.08	21.87 ± 0.13	20.64 ± 0.15
2	+2.5	−5.8	>23.9	>24.8	>24.5	22.02 ± 0.13	>20.3
3	−5.4	−1.6	23.55 ± 0.21	23.68 ± 0.09	22.40 ± 0.07	20.94 ± 0.07	20.23 ± 0.20
4	+3.2	+7.2	23.93 ± 0.25	24.94 ± 0.17	24.11 ± 0.19	22.93 ± 0.22	20.96 ± 0.30

photometry of these star-forming regions are shown in Figure 5.10. Details of the models are given in §5.4. For object 1, a family of single bursts fit the data well. These have burst ages ranging from 0.1 to 0.3 Gyr and $0.0 \lesssim E(B-V) \lesssim 0.10$. The top panel of Figure 5.10 shows the best-fit model, which is a 0.2 Gyr old burst with no extinction. This fit resulted in a reduced χ^2 of 1.37.

Single burst models are not a good fit to the photometry of object 3. The best fit has a high reduced χ^2 of 3.80. For two-burst models the best fit, with a reduced χ^2 of 1.77, is obtained when the populations are (1) an $\approx 70\%$ by mass burst that is young (0.001 Gyr) and dusty with $E(B-V) \approx 0.7$, and (2) an $\approx 30\%$ by mass burst that is 1.0 Gyr old with no dust. This two-burst model is shown in the middle panel of Figure 5.10.

Object 4 is well fit by a family of single bursts having ages in the range of 0.01 to 0.05 Gyrs and $0.05 \lesssim E(B-V) \lesssim 0.2$. Of these, the best-fit model is a 0.01 Gyr burst with $E(B-V) = 0.2$ and results in a reduced χ^2 of 1.01. This single-burst model is shown in the lower panel of Figure 5.10.

The absolute magnitudes of the three objects were determined using the apparent magnitudes given in Table 5.6 along with K-corrections derived from their best-fit SED. In the R band, these are −18.1, −18.6, and −16.6 for objects 1, 3, and 4 giving a total R band luminosity for the galaxy of $M_R = -19.2$ or $L_R = 0.16 L_R^*$. Here, the luminosities of the three features have been added and the result reported as the luminosity of the DLA galaxy. In the K band, absolute magnitudes −19.7, −20.2, and −19.6 are found with a total K band

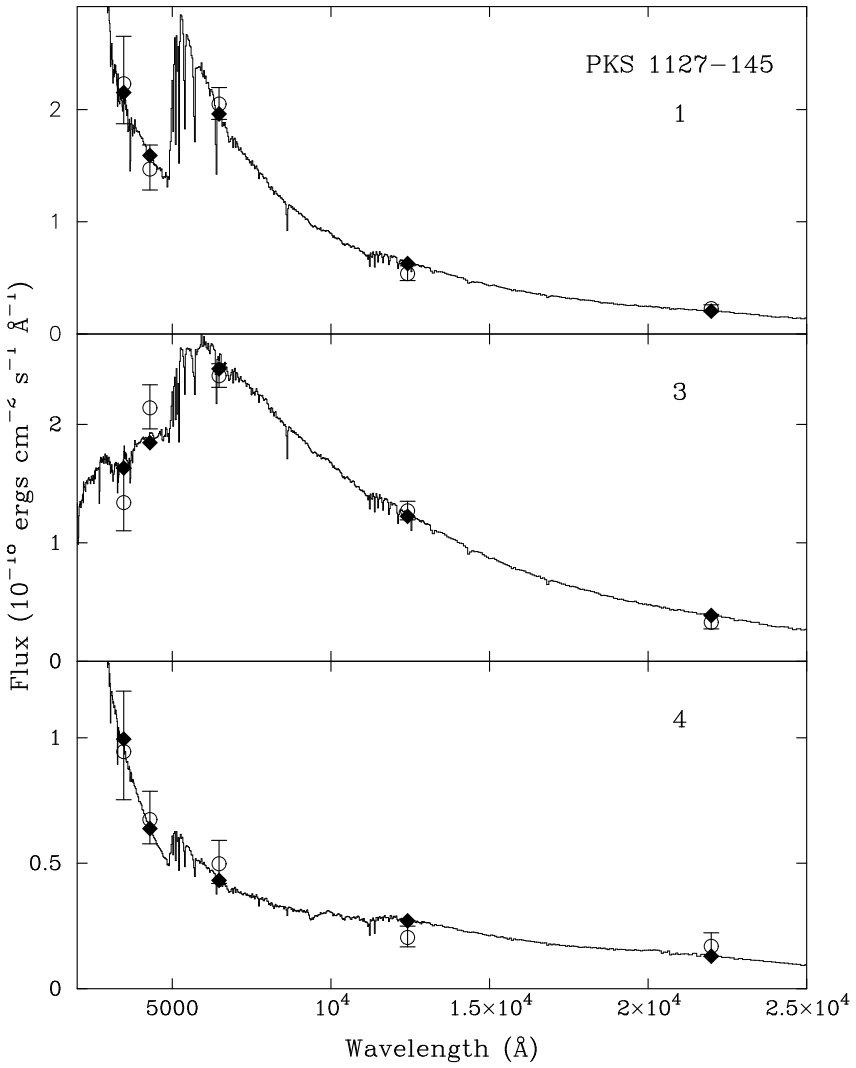

Figure 5.10: Stellar population spectral synthesis model fits at $z = 0.313$ for objects 1, 3, and 4 in the PKS 1127−145 field. The open circles with 1σ error bars are photometric measurements. For comparison, the filled diamonds are model flux values determined at the effective wavelength of the filter by convolving the filter response function with the model spectral energy distribution. The best-fit model for object 1 is a single 0.2 Gyr old burst with no extinction. Object 3 is best fit by a two-burst model with (1) an $\approx 70\%$ by mass burst that is young (0.001 Gyr) and dusty with $E(B-V) \approx 0.7$, and (2) an $\approx 30\%$ by mass burst that is 1.0 Gyr old with no dust. Object 4 is best-fit by a single 0.01 Gyr burst with $E(B-V) = 0.2$.

luminosity of $M_K^* = -21.0$ or $L_K = 0.04 L_K^*$.

5.5.4.2 More EROs Closer inspection of Figure 5.9 reveals many objects in this $50'' \times 50''$ field that are relatively bright in J, but are below the detection limits or are very faint in R. Several of these are in the vicinity of galaxy "b" and could well be dusty regions in which star formation is being triggered by the interaction between galaxies "a" and "b". Their location is compelling evidence for their association with the $z = 0.313$ galaxies, though the possibility that they are associated with the radio-loud, $z_{em} = 1.187$, quasar cannot be ruled out.

5.5.4.3 Kinematics High resolution observations of the Mg II absorption line have not been published but the high rest equivalent width of the 2796 Å line, $W_0^{\lambda 2796} = 2.21$ Å, implies a velocity width of $\gtrsim 240$ km s^{-1}. The 21 cm absorption line profile of this DLA system is also complex (Lane, 2000), and has been shown to vary on time scales of a few days (Kanekar & Chengalur 2001b). The 21 cm absorption line extends over 85 km s^{-1} and is resolved into 5 components. The deepest component, with optical depth $\tau \approx 0.11$, is at the low-velocity end of the profile. Prochaska and Wolfe (1997, 1998) have used simulations to show that this type of leading-edge profile is produced along a line of sight that passes through a rotating disk. On the other hand, Haehnelt et al. (1998), who consider gas infall due to merging, and McDonald and Miralda-Escudé (1999) who consider moving clouds in a spherical halo, have also reproduced leading-edge line profiles. In the case of the PKS 1127−145 DLA system, both the image and kinematics are more consistent with the latter interpretations. However, this DLA system appears to be even more complex in its structure and kinematics since it is not an isolated system and probably owes its morphology to the nature of its environment.

5.5.5 PKS 1629+120

The sight line towards the quasar PKS 1629+120 ($V = 18.4$, $z_{em} = 1.795$) contains a DLA system at $z = 0.532$ with column density $N_{HI} = (5.0 \pm 1.0) \times 10^{20}$ atoms cm^{-2}. This system

was discovered in an HST Cycle 9 survey for DLAs in strong Mg II-Fe II absorption-line systems (see Rao et al., 2003). This line of sight has two Mg II systems, one at $z = 0.5313$ with Mg II $W_0^{\lambda 2796} = 1.40$ Å and Fe II $W_0^{\lambda 2600} = 0.70$ Å (Aldcroft et al., 1994), and one at $z = 0.9005$ with Mg II $W_0^{\lambda 2796} = 1.06$ Å and Fe II $W_0^{\lambda 2600} = 0.63$ Å (Barthel et al., 1990). The $z = 0.9005$ system is sub-DLA with $N_{HI} = (5.0 \pm 0.4) \times 10^{19}$ atoms cm^{-1} (Rao et al., 2003).

5.5.5.1 Imaging Results Figure 5.11 shows $\approx 40'' \times 40''$ U, B, R and K images of this field. All four quasar PSFs have been subtracted, resulting in residuals that are comparable to the background in each image. The position of the quasar is marked with a "+". Unresolved objects are labeled with an "S" and are presumed to be stars while resolved objects are galaxies labeled with a "G". They are numbered in order of increasing distance from the quasar. 1629 G1 appears patchy in U, possibly indicating regions of recent star formation. An edge-on, disk-like structure can be seen in B. It appears bulge-like in K, and shows signs of both bulge and disk structure in R. These morphological features are consistent with 1629 G1 being a mid-type spiral galaxy. As is shown below, the photometry of 1629 G1 is consistent with it being the DLA galaxy at $z = 0.532$. In this case, its impact parameter, i.e., the projected distance from the center of 1629 G1 to the center of the PSF of the quasar, is $b = 17$ kpc.

5.5.5.2 Photometry of 1629 G1 Photometric measurements and 1σ uncertainties of 1629 G1 are given in Table 5.7. These magnitudes were used to determine a photometric redshift for 1629 G1 by using the galaxy spectral templates of Bruzual & Charlot (2003, in preparation) in a principal component analysis (A. Conti, private communication). The best-fit template was determined at redshifts $0 < z < 2$ in steps of 0.001. The resulting reduced χ^2, which was determined at each step, has a minimum equal to 0.7 at $z \approx 0.59$ and redshifts in the range $0.50 < z < 0.65$ are good fits with reduced $\chi^2 \leq 1$. The reduced χ^2 at $z = 0.90$ is ≈ 4, making $z = 0.90 \approx 30$ times less probable than $z = 0.59$. Therefore, the possibility that 1629 G1 is the sub-DLA galaxy at $z = 0.901$ can be ruled out, and that 1629 G1 is the DLA galaxy at $z = 0.532$ is assumed. However, a slit redshift is required to

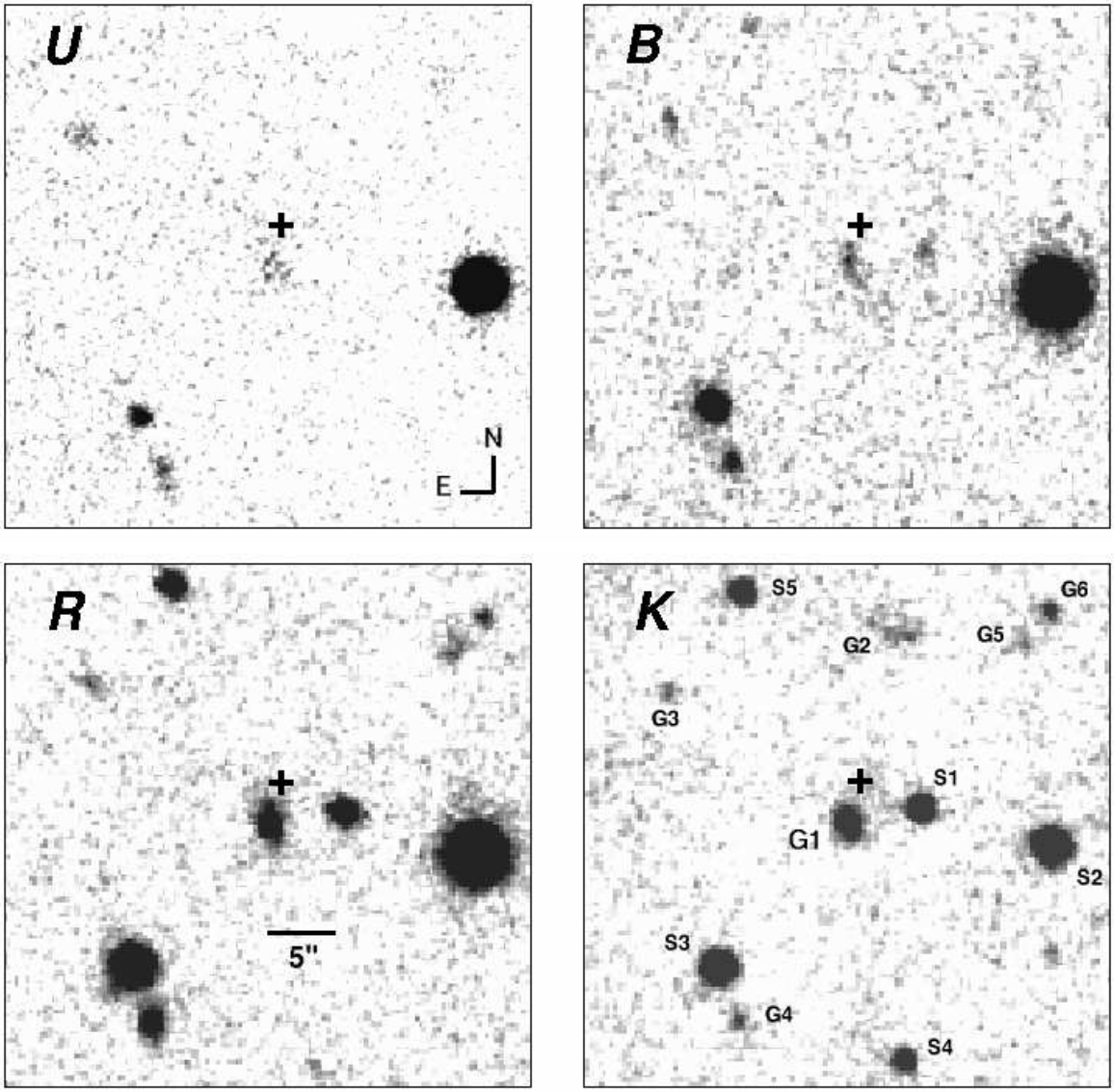

Figure 5.11: U, B, R, and K images of the PKS 1629+120 field that contains a DLA system at $z = 0.532$. The PSF of the quasar, whose position is marked with a "+", has been subtracted in all four images. The PSF subtraction here is cleaner than in the other three DLA fields since PKS 1629+120 is relatively faint. Resolved objects are labeled with a "G" and unresolved objects are labeled with an "S". 1629 G1 is identified as the DLA galaxy.

Table 5.7: Photometry of 1629 G1

m_U	m_B	m_R	m_J	m_K
22.61 ± 0.09	23.15 ± 0.11	21.37 ± 0.04	19.20 ± 0.07	17.65 ± 0.06

unambiguously determine the redshift of 1629 G1.

Stellar population synthesis models were also fit to the photometry as described in §5.4. The best-fit model, which results in a reduced $\chi^2 = 0.82$, is shown in Figure 5.12. It is a single 0.05 Gyr old burst and has $E(B-V) = 0.5$. The apparent magnitudes from Table 5.7 in combination with K-corrections derived from this model give absolute magnitudes of $M_U = -20.3$, $M_B = -20.3$, $M_R = -21.3$, $M_J = -23.0$, and $M_K = -23.9$ at $z = 0.532$.

5.5.5.3 The z=0.901 Sub-DLA Galaxy 1629 G1 is the only galaxy detected near the quasar sight line, and it was shown that its photometry is consistent with it being the $z = 0.532$ DLA galaxy. Having assumed that 1629 G1 is at $z = 0.532$, the whereabouts of the $z = 0.901$ sub-DLA galaxy must now be considered. One possibility is that it is below the detection limit of all the images. A second possibility is that it lies directly along the line of sight to the quasar and was subtracted along with the quasar PSF. Third, it might be one of the galaxies detected at large impact parameter. Each of these is considered in turn.

If the first possibility is true, then the $z = 0.901$ galaxy must have a surface brightness of $\mu_K > 21.6$ mag arcsec^{-2} and $\mu_R > 25.4$ mag arcsec^{-2} at the 3σ level (see Table 5.2). Assuming that it is a face-on galaxy with an extent of 20 kpc, it is found that $m_R > 23.2$ and $M_R > -21.5$, where a K-correction for an Sb-type galaxy has been applied (Poggianti, 1997), or $L_R < 1.3L_R^*$. Similarly, in the K band it is found that $m_K > 19.4$ and $M_K > -24.4$, or $L_K < 0.4L_K^*$.

The quasar PSF was subtracted reasonably cleanly since the PSF was well sampled by several stars brighter than the quasar in each frame. If there is a galaxy coincident on the sky with the quasar, then it would have to mimic a point source and be centered exactly on the quasar PSF. Although this is a possibility, it is highly unlikely.

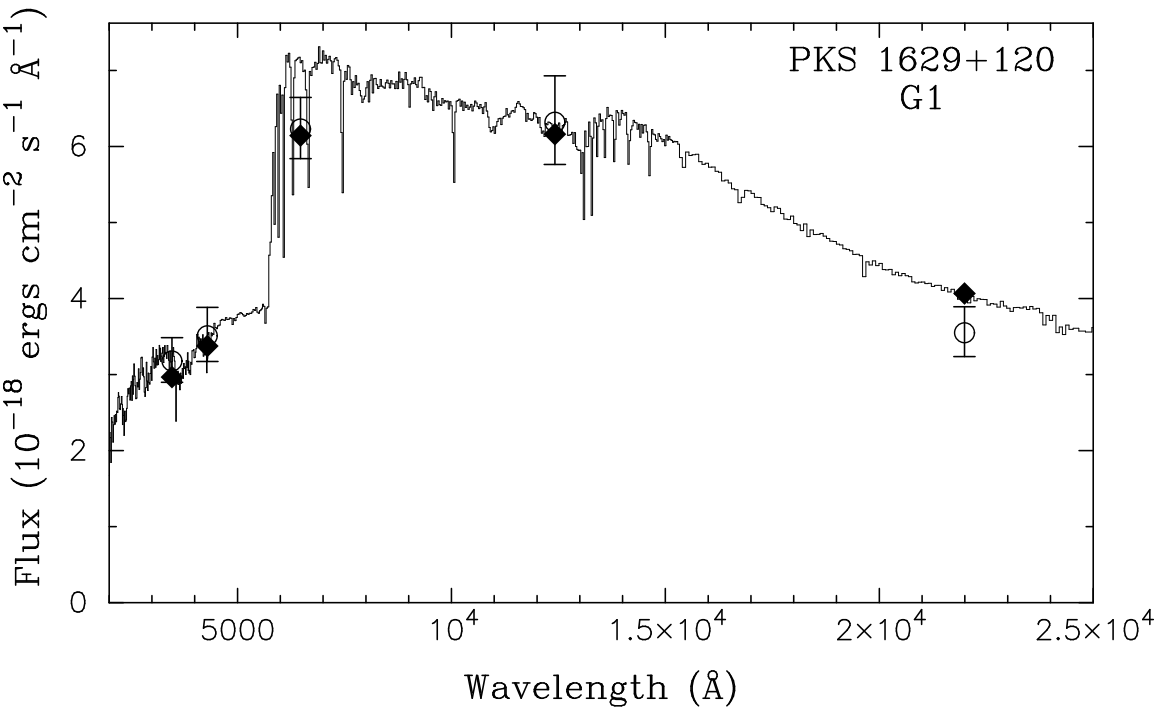

Figure 5.12: Best-fit single-burst model at $z = 0.532$ overlaid on the photometry for 1629 G1 in the PKS 1629+120 field. The open circles with 1σ error bars are photometric measurements. For comparison, the filled diamonds are model flux values determined at the effective wavelength of the filter by convolving the filter response function with the model spectral energy distribution. The model is a 0.05 Gyr old single burst with $E(B-V) = 0.5$.

Except for 1629 G1, all detected galaxies lie between 11 and 19 arcseconds from the quasar and have impact parameters between 72 and 124 kpc at $z = 0.901$, i.e., larger than what is typical for Mg II absorbers of this strength (Steidel, 1993, Chapter 6). The implied impact parameters at $z = 0.532$ are also large, ranging between 62 and 107 kpc. Therefore, from impact parameter considerations, these are not likely to be either of the two absorbing galaxies.

Finally, note that if 1629 G1 was at $z = 0.901$, then the DLA galaxy, which would have gone undetected, would have to have $L_R < 0.3L_R^*$ and $L_K < 0.2L_K^*$. Moreover 1629 G1 would have $L_R = 2.1L_R^*$ and $L_K = 4.5L_K^*$, and it would be an unusually luminous low-redshift sub-DLA galaxy. Thus, it is more reasonable to conclude that 1629 G1 is at $z = 0.532$ and that the $z = 0.902$ sub-DLA galaxy is not detected in the images.

5.6 CONCLUSIONS

The OI 363 findings represent some of the first results on the *detailed properties* of DLA galaxies. Perhaps fittingly, these results were determined from the two lowest redshift ($z = 0.09$ and 0.22) confirmed classical DLA systems discovered in a quasar absorption-line survey program.

The $z = 0.22$ DLA galaxy is a faint (B= 22.7, K= 17.8) neutral-colored (B−K= 4.9) galaxy with dwarf-galaxy-like K- and B-band luminosities of $L_K = 0.10L_K^*$ and $L_B = 0.10L_B^*$, respectively. Its spectrum is that of an early type galaxy (S0 or even E). Analysis of the 7-color (UBRIJHK) data suggests that 0738 G1's spectral energy distribution is well-fitted by an instantaneous single-burst model with the burst taking place 0.36 ($A_V = 1.3$) to 3.5 ($A_V = 0.1$) Gyrs ago, or a 3.5 Gyr old model with an exponentially decreasing star formation rate ($\tau = 1$ Gyr) and $A_V = 0.5$. Its current rate of star formation is low, < 0.3 $M_\odot$ yr^{-1}. Examination of the evolutionary history of these models implies that the progenitor population of 0738 G1, if seen near the population's formation epoch at $z_f \approx 0.3 - 0.9$, would have properties similar to the population of "faint blue galaxies" presently observed at moderate redshift. Analysis of the extended radial light profile from the WIYN R-band image of 0738 G1 indicates that its outer isophotes are better fit by an exponential than an $r^{1/4}$ law, which offers some evidence for an early-type dwarf S0 or spiral interpretation.

The putative $z = 0.09$ DLA galaxy is likely to be all or part of the resolved light surrounding the quasar. In terms of its luminosity, it is also a dwarf galaxy, inferred to have $L_K \leq (0.08 - 0.13)L_K^*$, with the higher value holding for the case where the quasar host galaxy at $z = 0.63$ does not contribute to the detected resolved light. There is considerable morphological structure in the light surrounding the quasar, including the arm-like and jet-like features. The arm-like feature is red in color and, if it is an *actual* arm, this suggests that the DLA galaxy might be a low surface brightness dwarf spiral. However, the presence of the other structure (i.e. the blue colored jet-like feature) leaves open the possibility that the DLA galaxy is an irregular or an interacting system. For these galaxies the H I gas masses deduced from the observed impact parameters and H I column densities lie in the range $M_{HI} \approx (6 - 23) \times 10^9$ $M_\odot$. These estimates are approximate because it is not

known if the observed H I is distributed like a face-on circular slab around the center of the identified DLA galaxy (as the calculation of the H I mass assumed) or whether the H I gas is exponentially distributed or clumped in giant clouds associated with the identified galaxy.

The other four new low-redshift DLA galaxies have an interesting mix of morphologies. The two higher redshift galaxies, G1 PKS 0827+243 ($z = 0.525$) and G1 PKS 1629+120 ($z = 0.532$) are $\approx L^*$ spirals. Higher resolution HST observations of the former reveal that an interaction between the luminous spiral and a satellite dwarf galaxy might be responsible for the presence of DLA gas at larger galactocentric distances. An extension to 0827 G1 has, *a posteriori*, been detected in the ground-based images that might indicate the presence of a satellite. In the absence of high resolution images of the PKS 1629+120 field, a more detailed description of that DLA galaxy's morphology cannot be offered. Images of the two lower redshift DLA systems are more complex. Lacking higher resolution images, there are two possible identifications for the $z = 0.239$ PKS 0952+197 DLA galaxy. Either it is the object(s) that overlaps with the quasar PSF in the J-band image, or it is a larger, irregular dwarf galaxy with patchy structure. In the former case, it is unlikely that the luminosity of this DLA galaxy exceeds a few hundredths of L^*. Faint patchy morphology is also present in the $z = 0.313$ DLA galaxy in the PKS 1127−145 field. However, in this case numerous star-forming regions are clearly visible. These regions are blue and displaced enough from the quasar sight line that a confirming slit redshift has been obtained for one of them. Because of the appearance of this patchy irregular structure, it is likely that the nearby $\approx L^*$ spiral galaxies, the closer one of which was once thought to be the DLA galaxy, are responsible for tidally disrupting the actual DLA galaxy that lies along the line of sight to the quasar. Thus, the DLA galaxy takes the form of an extended irregular structure with star-forming regions. However, the possibility that these star-forming regions are individual interacting or merging galaxies cannot be ruled out. Again, higher resolution images would be needed to clarify the situation. Whichever is the case, the total light from the DLA galaxy does not exceed $0.16L^*$.

Additional discussion concerning the results presented in this chapter appears in Chapter 6.

6.0 SUMMARY AND DISCUSSION

In Chapters 2 through 5, many new results of concern to the study of the nature and evolution of galaxies and galactic structures selected via gas cross section have been presented.

In Chapters 2 and 3, the results of two surveys for intervening Mg II absorbers in the spectra of background quasars were described. Their incidence, dn/dz, and distribution of rest equivalent widths, $n(W_0^{\lambda 2796})$, as well as their evolution in redshift, was investigated. It was found that a single component distribution was insufficient to describe $n(W_0^{\lambda 2796})$, though a two-exponential fit provided a satisfactory fit to the data. It was further shown that the distribution of systems with $W_0^{\lambda 2796} \geq 0.3$Å steepens with redshift. The evolution is consistent with the total co-moving cross section for absorption decreasing with decreasing redshift in a sense that the strongest lines evolve the fastest. Systems with $W_0^{\lambda 2796} \gtrsim 2$Å show strong evidence for evolution at redshifts $z \lesssim 1$, and evolution is detected for lines with $W_0^{\lambda 2796} \gtrsim 1$Å at redshifts $z \lesssim 0.5$.

Measurements of the cosmic neutral hydrogen gas-phase metallicity and dust content were presented in Chapter 4. Composites of spectra selected due to the presence of Mg II absorption were formed, in the rest frame of the absorber, and used to measure the average Zn II and Cr II column densities. Abundances calculated with approximated H I columns were found to be consistent with the column density-weighted average of abundances calculated from direct determinations. It was shown that metallicity strongly correlates with velocity dispersion as measured by $W_0^{\lambda 2796}$. It was also shown that both metallicity and dust content increase with decreasing redshift over the range $2.0 > z > 0.9$.

In Chapter 5, detailed observations of six DLA galaxies were presented. Two of the identified galaxies were shown to be $\approx L^*$ spirals. The other DLA galaxies were identified as an LSB, a dwarf LSB, a dwarf spiral, and a patchy/irregular/LSB. These and other studies

have effectively settled the DLA morphology issue in favor of the mixed-morphology scenario over a primarily rotationally-supported disk paradigm.

In this Chapter, discussion and implications of the results presented above are discussed in detail.

6.1 MG II ABSORBERS

The determination of $n(W_0^{\lambda 2796})$ and dn/dz provide insight into the nature of the systems comprising the population of Mg II absorbers. Specifically, the inability of a single functional form to describe $n(W_0^{\lambda 2796})$ suggests that multiple physical populations contribute to the absorption. Additionally, $n(W_0^{\lambda 2796})$ can be used to infer average absorption cross sections for a given $W_0^{\lambda 2796}$ regime. The $W_0^{\lambda 2796}$-dependent evolution of dn/dz holds further clues related to the nature of Mg II absorbers. Also note that a significant fraction ($\approx 36\%$) of Mg II systems with $W_0^{\lambda 2796} \geq 0.5$Å and $W_0^{\lambda 2600} \geq 0.5$Å are DLAs. The implications of the evolution in Mg II dn/dz to Ω_{DLA} will be investigated in a future publication, once the analysis of a large HST study of $N_{H\,I}$ in known Mg II absorbers (consisting mainly of systems from this dissertation) is completed (Rao, Turnshek, & Nestor, in preparation).

6.1.1 The Nature of the Absorbers

The distribution of $W_0^{\lambda 2796}$ for absorbers with $W_0^{\lambda 2796} \geq 0.3$Å is fit very well by a single exponential. However, extrapolating this exponential to smaller values of $W_0^{\lambda 2796}$ underpredicts the incidence of lines (Figure 2.3), motivating a two-component description of the form of Equation 2.5. This is the first clear indication of such a transition and raises the question of whether the ensemble of clouds comprising Mg II absorbers are the result of two physically distinct populations.

In a series of papers utilizing HIRES/Keck data (Charlton and Churchill, 1998; Churchill et al., 2000; Churchill and Vogt, 2001; Churchill et al., 2003), Churchill and collaborators have investigated the kinematic structure of Mg II absorbers at $0.4 < z \lesssim 1.2$. For intermediate/strong absorbers ($W_0^{\lambda 2796} \geq 0.3$Å), they show that the absorption systems are composed

of multiple kinematic subsystems, usually containing a dominant subsystem (ensemble of clouds) with a velocity width $\approx 10 - 15\,\mathrm{km\,s^{-1}}$ and a corresponding H I column density which is optically thick at the Lyman limit (i.e., $N_{H\,I} \gtrsim 3 \times 10^{17}$ atoms cm^{-2}). Additionally, a number of weaker, often unresolved (at ≈6 km s^{-1} resolution) subsystems (clouds) with a large spread of velocity separations (up to $\approx 400\,\mathrm{km\,s^{-1}}$) from the systemic velocity of the absorber are usually present (see Churchill and Vogt, 2001, Figure 7.) These weaker subsystems typically contribute only 10%-20% of the rest equivalent width. The strongest Mg II absorbers ($W_0^{\lambda 2796} \gtrsim 2$Å) often contain more than one of the dominant subsystems and have equivalent widths dominated by saturated features.

CRCV99 presented a HIRES/Keck study of weak ($W_0^{\lambda 2796} < 0.3$Å) Mg II absorption systems. The properties of the kinematic subsystems comprising weak Mg II absorbers are similar to the weak subsystems of intermediate/strong Mg II absorbers. The individual clouds have $W_0^{\lambda 2796} \lesssim 0.15$Å and sub-Lyman limit H I columns.

Although most of the Mg II λ2796 lines in the EDR survey are at least partially saturated, the *degree* of saturation is correlated with $W_0^{\lambda 2796}$. For example, the DR values for systems with $0.3\text{Å} \lesssim W_0^{\lambda 2796} \lesssim 1\text{Å}$ indicate a mix in degree of saturation. For lines in this regime, $n(W_0^{\lambda 2796})$ is sensitive to the distribution of Mg II column densities, $n(N_{Mg\,II})$. In fact, Churchill and Vogt (2001) and Churchill et al. (2003) find almost identical power law slopes for $n(W_0^{\lambda 2796})$ and $n(N_{Mg\,II})$ in their $0.3\text{Å} \leq W_0^{\lambda 2796} \leq 1.5\text{Å}$ sample. Systems with $W_0^{\lambda 2796} \gtrsim 2$Å, however, are almost always highly saturated. Also, a *general* distinction between weak ($W_0^{\lambda 2796} < 0.3$Å) and intermediate/strong ($W_0^{\lambda 2796} \geq 0.3$Å) Mg II absorbers is the absence or presence of a "dominant" subsystem, though the differences are neither discrete nor without exception. Therefore, given the form of $n(W_0^{\lambda 2796})$, it is appropriate to consider a picture in which the *sum* of the weaker kinematic subsystems (clouds) in an absorber are described by N^*_{wk} and W^*_{wk}, and the stronger (dominant ensembles) plus weaker subsystems by N^*_{str} and W^*_{str}. If this multi-population explanation is indeed correct, the nature of these populations needs to be explained. First, the weak subsystems are considered.

It has been demonstrated that absorption line systems can be associated with galaxies out to large galactocentric distances ($\approx 100h^{-1}$ kpc for C IV and $\approx 200h^{-1}$ kpc for Lyα absorbers, for example; Chen et al. (2001a); Chen et al. (2001b)). Although there is evidence

for Lyα absorbers in voids (Penton et al., 2002), these appear to be limited to the weakest systems. Also, Rigby et al. (2002) conclude that a significant fraction of relatively strong Lyα forest lines ($10^{15.8}$ cm$^{-2} \lesssim N_{H\,I} \lesssim 10^{16.8}$ cm^{-2}) are associated with single-cloud weak Mg II absorbers.

Therefore, it is considered whether single-cloud/Lyα forest absorbers can contribute significantly to the "weak" component of $n(W_0^{\lambda 2796})$. C2000 claim to be 93% complete to $W_0^{\lambda 2796} = 0.03$Å. Thus, using the measurements of single-cloud systems from C2000 with $W_0^{\lambda 2796} \geq 0.03$Å, it is found that $W_{sc}^* = 0.098 \pm 0.027$[1]. Rigby et al. (2002) give a dn/dz value for the single-cloud systems, which can be used to normalize $n_{sc}(W_0^{\lambda 2796})$. While this comparison is approximate in that the redshift range covered by the C2000 sample, $0.4 < z < 1.4$, is different than that of the EDR sample, the result shown in Figure 6.1 demonstrates that the single-cloud/Lyα forest systems (which constitute only a portion of the weak subsystem population) should contribute significantly to the upturn in $n(W_0^{\lambda 2796})$.

Although the Mg II absorber galaxy population has been shown to span a range of galaxy colors and types, Steidel et al. (1994) describe the "average" galaxy associated with an intermediate/strong Mg II absorber galaxy as one which is consistent with a typical $0.7L^*$ Sb galaxy. Furthermore, Steidel et al. (2002, also see Ellison et al. (2003)) compare the galaxy rotation curves to the absorption kinematics for a sample of high inclination spiral Mg II absorption galaxies. They find extended-disk rotation dominant for the absorption kinematics, though a simple disk is unable to explain the range of velocities, consistent with a disk plus halo-cloud picture. However, there are several counter evidences to a rotating disk description for the dominant subsystems. The most important is that imaging often fails to reveal a disk galaxy in proximity to the absorption line of sight. DLA galaxies, which are a subset of strong Mg II absorbing galaxies, are not dominated by classic spirals. Of the 14 identified DLA galaxies summarized below (§6.3), only six are spirals. Furthermore, systems that have been studied without the discovery of the absorbing galaxy despite deep imaging rule out at least bright spirals (though disky-LSBs may still contribute). Thus, though

[1]Since only the $W_0^{\lambda 2796} < 0.3$Å systems are considered here, the abnormally strong $W_0^{\lambda 2796} = 0.681$Å single-cloud system in C2000 was excluded from the calculation of W_{sc}^*.

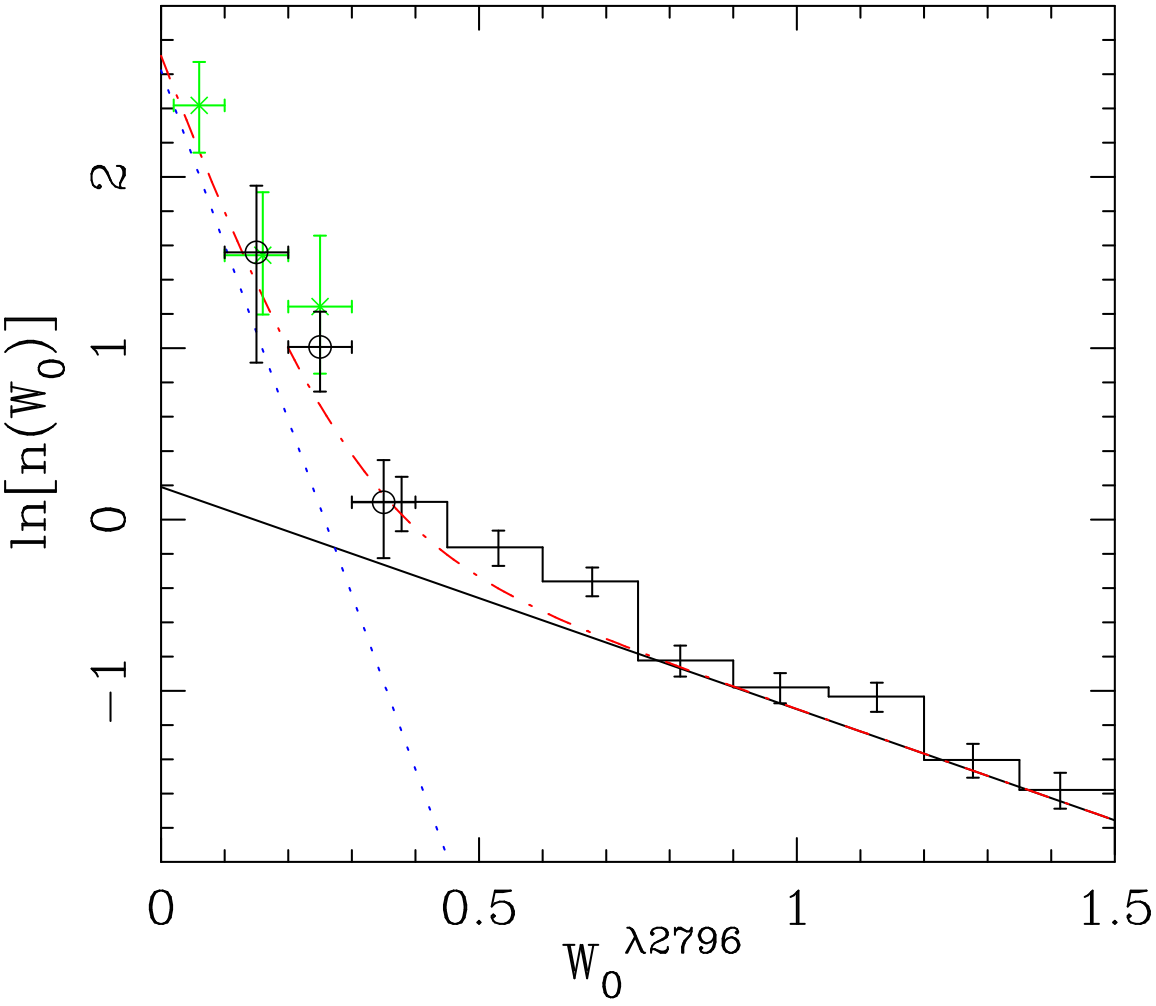

Figure 6.1: Predicted $n(W_0^{\lambda 2796})$ for Lyα forest/single-cloud Mg II. The solid line is the maximum likelihood fit to the the EDR data (shown as the histogram) with $W_0^{\lambda 2796} \geq 0.5$Å. The dotted line is the approximation for single-cloud Mg II $n(W_0^{\lambda 2796})$ using data from Churchill et al. (2000) and a normalization from Rigby et al. (2002). The dot-dash curve is the sum of the two distributions. The circles are from the MMT survey and the $\times$ symbols are from CRCV99.

it is likely that rotating disks do contribute to the population comprising the dominant kinematic subsystem(s) of $W_0^{\lambda 2796} \geq 0.3$Å absorbers, they can only account for a (perhaps small) fraction of the total population. The detailed nature of the remaining contribution is yet unclear.

Thus, though a two-component description is sufficient to describe $n(W_0^{\lambda 2796})$ within the current data, it is likely that more than two physically distinct populations contribute significantly to the phases comprising the absorbing clouds. By observing a large number of galaxy types that sample a range of $W_0^{\lambda 2796}$ and impact parameter, it would be possible to ascertain what populations contribute most directly to the absorber population.

6.1.2 The Absorber Cross sections

The relative mean absorber cross section, $\sigma(z)$, for ranges of $W_0^{\lambda 2796}$ can be determined directly from $n(W_0^{\lambda 2796})$. Additionally, knowledge of dn/dz and the galaxy luminosity function (LF) allows the approximation of the normalization of the mean absorber cross section, under the assumption that the absorbers arise in galaxies, since dn/dz is the product of $\sigma(z)$ and the number density of absorbers, $n(z)$. However, the process is inherently uncertain since: (a) the redshift dependence of the galaxy LF is not well determined; (b) though a scaling relation $\sigma(L) \propto (L/L^*)^\beta$ has traditionally been assumed, the determination of β is uncertain and likely not universal for all morphological types or redshifts, if it is even appropriate; and (c) depending on the value of β and the LF faint-end slope, the minimum absorber galaxy luminosity (which also is likely to be dependent on morphology and redshift) can have large effects in the statistically-determined cross sections.

Nonetheless, an approximate normalization is of physical interest. Thus, R_{eff} is defined to be the effective projected radius for absorption such that $\sigma(L) \equiv \pi R_{eff}^2(L)$. Note that the galactocentric radius within which the absorption may occur (i.e., the range of impact parameter) may be very different than R_{eff}. Steidel et al. (1994) find absorbing galaxies as faint as $L \sim 0.05\, L^*$, and a scaling law for the gaseous cross section $R_{eff}(L)/R_{eff}^* = (L/L^*)^{0.2}$ for both optical (B-band) and near-IR (K-band) luminosity. They claim the relation is much tighter for the near-IR. Thus, the redshift parameterization of the K-band LF from the

MUNICS data set (Drory et al., 2003) and $L_{min} = 0.05\,L^*$ are used, though $L_{min} = 0.25\,L^*$ and $L_{min} = 0.001\,L^*$ are also tested to investigate the effects of using high/low values of L_{min}. The Dickinson and Steidel (1996) revised scaling law for Mg II systems with $W_0^{\lambda 2796} \geq 0.3$Å is adopted, namely $R_{eff}(L_K)/R^*_{eff} = (L_K/L^*_K)^{0.15}$.

The results for the different W_0^{min} values from Chapter 2 are shown in Figure 6.2. Despite the limitations of this approach, approximate values for R^*_{eff} are apparent: $\approx 60-100\,h_{70}^{-1}$ kpc for $W_0^{\lambda 2796} \geq 0.3$Å, $\approx 40-60\,h_{70}^{-1}$ kpc for $W_0^{\lambda 2796} \geq 1.0$Å, $\approx 10-30\,h_{70}^{-1}$ kpc for $W_0^{\lambda 2796} \geq 2.0$Å and $\lesssim 10\,h_{70}^{-1}$ kpc for $W_0^{\lambda 2796} \geq 3.5$Å. Guillemin and Bergeron (1997) find $R^*_{eff} = 65\,h_{70}^{-1}$ kpc using the upper envelope of the distribution of observed impact parameters for a sample with $0.3 \leq W_0^{\lambda 2796} \leq 4.7$Å and $\langle W_0^{\lambda 2796} \rangle = 1.3$Å. CRCV99 find $R^*_{eff} = 110\,h_{70}^{-1}$ kpc for their $W_0^{\lambda 2796} \geq 0.02$Å sample, but use a LF normalization that is ~ 3.5 times the values adopted here. Chen et al. (2001a) find $R^*_{eff} = 137\,h_{70}^{-1}$ kpc for C IV absorbers, which may sample larger galactocentric radii. The R^*_{eff} values are averages; it is expected that there are large galaxy to galaxy variations. Direct comparison of R^*_{eff} to the distribution of impact parameters would require knowledge of the gas geometry and the (likely $W_0^{\lambda 2796}$-dependent) covering factor. For example, small regions that allow large $W_0^{\lambda 2796}$ absorption may be found at galactocentric radii $r \gg R_{eff}$ if the covering factor for such absorption is $f \ll 1$.

Also note that for the single-cloud Mg II systems (see §6.1.1), Rigby et al. (2002) derive $dn/dz = 1.1 \pm 0.06$, which is similar to the EDR dn/dz result for systems with $W_0^{\lambda 2796} \geq 0.3$Å. If their claim that the single-cloud systems are 25%-100% of the Lyα forest with $10^{15.8}$ cm^{-2} $< N$(H I) $< 10^{16.8}$ cm^{-2} is accurate, then R^*_{eff} for this range of Lyα forest lines (if they can be associated with galaxies) would be $\approx 100 - 400\,h_{70}^{-1}$ kpc. This can be compared to the claim of Chen et al. (2001) that all N(H I) $\gtrsim 10^{14}$ cm^{-2} Lyα forest lines arise within the characteristic radius $R^* \approx 250\,h_{70}^{-1}$ kpc of luminous galaxies.

6.1.3 Nature of the Evolution

6.1.3.1 $W_0^{\lambda 2796} < 0.3$Å Systems The Lyα forest dn/dz is known to decrease strongly over the redshift interval $4 \gtrsim z \gtrsim 1.6$, but little evolution is present at lower redshifts (see Weymann et al., 1998, and references therein). In §6.1.1, it was speculated that a portion

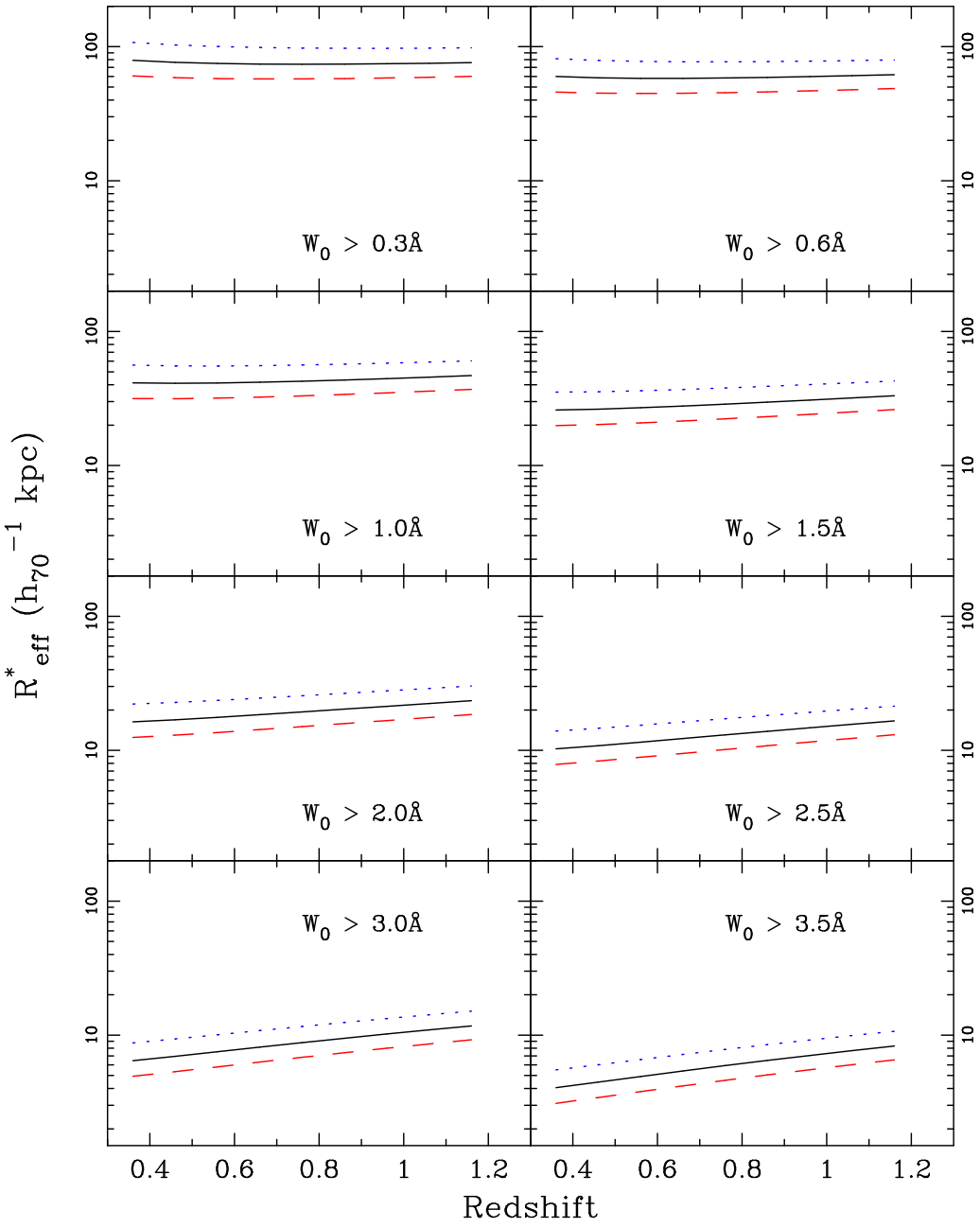

Figure 6.2: Cross section estimates $\sigma(L^*) = \pi\, R^{*2}_{eff}$. The solid lines represent the $L_{min} = 0.05\, L^*$ result. The dashed-lines are for a small value of $L_{min} = 0.001\, L^*$ and the dotted-lines a large value $L_{min} = 0.25\, L^*$. The redshift parameterization of the K-band LF from the MUNICS data set, a scaling relation $R_{eff}/R^*_{eff} = (L/L^*)^{0.15}$, and dn/dz from the parameterization of Chapter 2 are used.

of the enriched Lyα forest contributes to the weak subsystems found in Mg II absorbers. If this is indeed the case, then this evolution may manifest itself in dn/dz for the weakest ($W_0^{\lambda 2796} < 0.3$Å) Mg II systems. No data exist on dn/dz at $z > 1.6$ for the weakest systems, but CRCV99 detect no evolution in dn/dz for $W_0^{\lambda 2796} > 0.1$Å systems over $1.4 < z < 0.4$ (e.g., see Figure 3.6). Below $z = 0.36$, the MMT data show weak ($\approx 1\sigma$) evidence for a decrease from the no-evolution prediction.

6.1.3.2 The Lack of Measured Evolution in Intermediate-strength ($0.3 \leq W_0^{\lambda 2796} \lesssim 2$Å) Systems

The EDR sample covers the redshift interval $z = 2.267$ to $z = 0.366$ which corresponds to 6.6 Gyrs, or about half the age of the universe. As long assumed and recently demonstrated with the Hubble deep fields (see Ferguson et al., 2000, for a review), galaxies were quite different at $z = 2.3$ than at $z = 0.4$. It is therefore noteworthy that, even with the large absorber sample presented here, relatively little evolution is detected in the bulk of Mg II absorption systems. For example, it is believed that the global star formation rate peaked near $z = 1$ and has declined by a factor of ≈ 2 by $z = 0.5$ and by a factor of ≈ 10 by $z = 0$ (Hopkins, 2004, and references therein). Contrastingly, the total cross section for absorption $n(z)\,\sigma(z)$ of the $W_0^{min} = 0.6$Å and 1.0Å samples evolves $\lesssim 10\%$ from $z = 1.9$ to $z = 0.5$ (corresponding to an interval of 5 Gyrs). The corresponding R_{eff} values do, however, indicate that much of this cross section is at large galactocentric radius, extending well beyond stellar galactic radii.

Two immediate conclusions can be drawn from the lack of evolution in the total cross sections. First, a large majority of the structures responsible for the bulk of the absorption cross section were in place by $z \approx 2$. Second, either the time scales governing the dynamics of the structures is greater than several Gyrs, or some process(es) regulate the production/destruction of the structures such that a nearly steady state is reached.

Mo and Miralda-Escude (1996) explore two-phase models for gaseous galactic halos in which "cold phase" clouds condense from the extended "hot phase" ionized halo at a cooling radius r_c, and undergo infall at $v \simeq V_{cir}$. Setting $r_c = R^*_{eff}$ (appropriate for a spherical geometry and a covering factor of unity), and using $R^*_{eff} \simeq 100$ kpc, their model results give $V_{cir} \simeq 250{-}400\,\mathrm{km\,s^{-1}}$ over $2 \leq z \leq 1$, which is consistent with the observed kinematic ranges

over $1.2 \leq z \leq 0.4$ from Churchill and Vogt (2001). Using these values $t_{infall} \approx 0.25 - 0.4$ Gyr is obtained. Thus, it would appear that a large degree of regulation is necessary, in this picture, to explain the lack of evolution in $n(z)\,\sigma(z)$. Ionization from star formation and the disruption from instabilities and evaporation of smaller clouds should at least partially regulate the cooling. The result of these and/or other regulatory mechanisms must ensure that the minimum time span over which condensation occurs be equal to at least several times t_{infall}.

The evolutionary situation for disks may be more complex. Simulations suggest that, to overcome "angular momentum catastrophe", local disks were not formed until $z \leq 1$ (Mo et al., 1998; Weil et al., 1998) and have since undergone much evolution (Mao et al., 1998). Disks were likely plentiful at higher z, but smaller in size for a given V_{cir}, and largely dissipated or destroyed in mergers. Driver et al. (1998) find a deficit of $z > 2$ spirals in the HDF suggesting that this marks the onset of their formation. Disks certainly contribute at least partially to the absorber population. However, if their contribution to $0.3 \leq W_0^{\lambda 2796} \lesssim 2.0$Å Mg II absorption systems is significant, then the lack of evolution becomes difficult to explain.

6.1.3.3 Evolution of Strong Systems ($W_0^{\lambda 2796} \gtrsim 2$Å) Evolution is detected in the strongest $W_0^{\lambda 2796}$ Mg II systems, in the sense that the strongest lines evolve away, with the evolution being stronger for increasingly stronger lines and at redshifts $z \lesssim 1$. For example, it is found that the total cross section for absorption of Mg II systems with $W_0^{\lambda 2796} \geq 2.0$Å ($\approx 10\%$ of all systems with $W_0^{\lambda 2796} \geq 0.3$Å) decreases by $45^{+14}_{-17}\%$ from $z = 1.8$ to 0.6 and with $W_0^{\lambda 2796} \geq 3.5$Å ($\approx 1\%$ of all systems with $W_0^{\lambda 2796} \geq 0.3$Å) by $60^{+19}_{-34}\%$ from $z = 1.9$ to 0.8. Note that for the $W_0^{\lambda 2796}$ values considered in this work, $W_0^{\lambda 2796}$ is correlated with the number of kinematic subsystems (clouds) comprising the absorber and thus velocity dispersion.

A speciously simple picture for the evolution of Mg II λ2796 lines considers that velocity dispersions scale with halo mass, and halo masses grow with decreasing redshift. In this picture, with the approximation that the cross section for a given dispersion scales with mass and the mass spectrum evolves according to the formalism of Sheth and Tormen (Sheth and Tormen, 1999), the cross sections should *increase* with decreasing redshift by approximately

an order of magnitude per unit redshift for $2 > z > 0$. This is clearly ruled out by the data. This can be understood on physical grounds if the low-ionization gas giving rise to Mg II absorption is in clouds bound in galaxy halos, since the individual clouds are not expected to be virialized on group scales. A single Mg II system sampling a group dispersion would require the chance alignment of several virialized member galaxy halos along the line of sight.

However, Churchill et al. (2000) show kinematic profiles of four $z > 1$ and one $z \approx 0$ system with $W_0^{\lambda 2796} \geq 2$Å, each of which exhibit two strong "dominant subsystem" components, and suggest the possibility that the strongest systems have a connection to galaxy pairs. For example, they find a 25% chance that a random sightline through the Galaxy would also intercept the LMC, and a 5% chance that it would intercept the SMC. This possible connection can be investigated by imaging $W_0^{\lambda 2796} \geq 2$Å systems: the EDR sample contains 77 such lines with $z < 1$ and 20 with $z < 0.6$.

Absorption dn/dz is the product of the number density of absorbers times the average individual cross section for absorption. Most galactic halos are already in place by $z > 1$, so except for mergers of galaxies separated by $v > 500\,\mathrm{km\,s^{-1}}$, the evolution in dn/dz is primarily an evolution of the gas absorption cross section in individual halos. Evolution in metallicity or metagalactic ionization cannot explain the cross section evolution, since they would tend to increase the number of individual enriched, low ionization clouds along a line of sight through a galaxy. The $W_0^{\lambda 2796}$-dependent decrease in cross section must therefore be indicative of an evolution in the kinematic properties of a subset of the galaxy population, from intermediate to low redshift. Although the issues discussed in §6.1.3.2 likely hold clues to the nature of this evolution, a precise description will require knowledge of the physical nature of the clouds that comprise the different ranges of $W_0^{\lambda 2796}$ in Mg II absorption systems.

6.2 DLA GAS METALLICITY

In Chapter 4, the cosmic neutral-gas-phase metallicity of DLAs was calculated using composite spectra. It was found that $[\mathrm{Zn/H}] = -1.13 \pm 0.19$ for DLA gas. Furthermore, [Zn/H] was shown to increase for $W_0^{\lambda 2796} > 1.3$Å systems by 0.38 ± 0.28 dex, or approximately 140^{+220}_{-110}%, from the redshift bin $0.9 \leq z < 1.35$ ($\langle z \rangle = 1.15$) to $1.35 \leq z \leq 2.0$ ($\langle z \rangle = 1.55$).

These values are consistent with the H I column density-weighted values from direct measurements. Figure 6.3 shows the [Zn/H] values (corrected for missing DLAs, see Chapter 4) from Chapter 4 plotted over metallicity ([M/H]) measurements in individual DLAs from Prochaska et al. (2003). Their [M/H] values are derived from abundance measurements of α-elements or Zn, with decreasing priority: Si, S, O, Zn. The relative area of the boxes represent the relative $N_{H\,I}$ values of the DLAs. Notice that there are few measurements at $z < 1.65$, and thus the determination of [M/H] in this regime has been dominated by the strongest few systems, resulting in large small-number-statistic errors.

Additionally, it was determined that [Cr/Zn] $= -0.45 \pm 0.13$ indicating that $\approx 65\%$ of the Cr is depleted onto dust grains. For $W_0^{\lambda 2796} > 1.3$Å systems, dust was shown to increase by 0.26 ± 0.22 dex, or approximately $80^{+120}_{-70}\%$, over the same redshift bins. According to Savage and Sembach (1996), [Cr/Zn] values in the Milky Way Galaxy are typically -0.5 (halo), -0.8 (disk+halo), -1.1 (warm disk), and -2.1 (cool disk). Thus, while the measured value of [Cr/Zn] provides evidence for significant depletion of Cr on to dust grains in the sample, the effect is not nearly as large as in the Galactic ISM. It is of interest to assess the affect of this dust in the high-$W_0^{\lambda 2796}$ subsamples at low and high redshift since they exhibit the highest metallicities. For the adopted $<N_{HI}>$ of the sample ($\approx 3.6 \times 10^{20}$ atoms cm^{-2}), this amount of dust in the absorber rest frame would give rise to mean values of $<\mathrm{A}_V^{absorber}>=$ 0.07 mag for the low-redshift subsample ($<z>$=1.15, [Zn/H]$= -0.56$, [Cr/Zn]$= -0.64$) and $<\mathrm{A}_V^{absorber}>=$ 0.02 mag for the high-redshift subsample ($<z>$=1.53, [Zn/H]$= -0.94$, [Cr/Zn]$= -0.38$). This is largely independent of the nature of the dust, i.e., Galactic-like, LMC-like, or SMC-like. Individual high-$W_0^{\lambda 2796}$ absorbers would undoubtedly exhibit a reasonable spread of $\mathrm{A}_V^{absorber}$ values around these mean values, and typically the low-$W_0^{\lambda 2796}$ absorbers would give rise to little extinction. For an absorber at the mean redshift of the low-redshift subsample, the mean V-band extinction in the observer frame would be $<\mathrm{A}_V^{observed}>=$ 0.16 mag for both Galactic-like and SMC-like dust; while for an absorber at the mean redshift of the high-redshift subsample, the mean V-band extinction in the observer frame would be $<\mathrm{A}_V^{observed}>=$ 0.06 mag for both Galactic-like and SMC-like dust. These results, which are consistent with the (slightly lower $\langle z \rangle$) results of Ménard, Nestor and Turnshek (in preparation), may provide some indication of the importance of selection

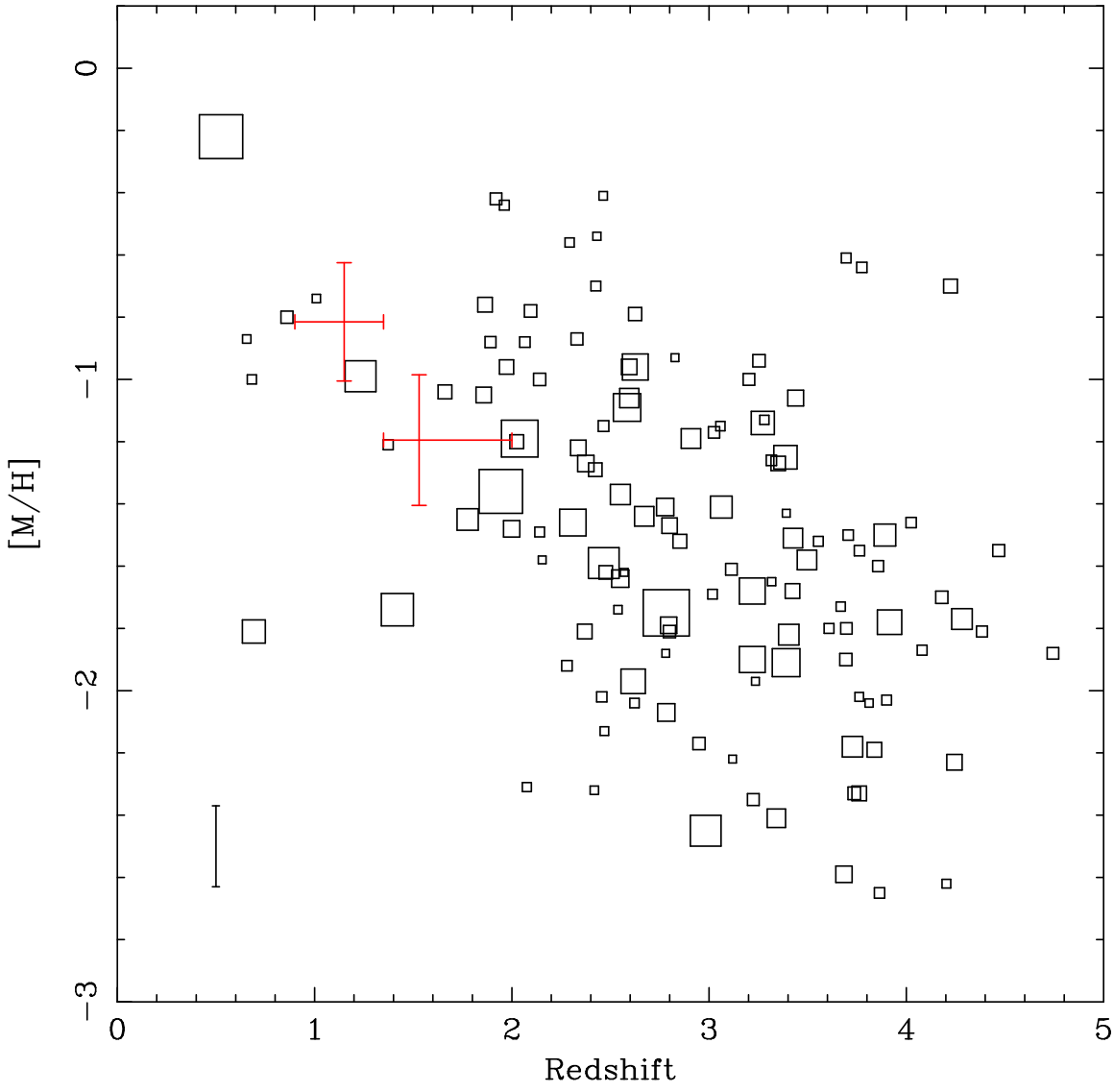

Figure 6.3: DLA Redshift – Metallicity Relation. The red bars are the [Zn/H] values (corrected for missing DLAs, see Chapter 4) from Chapter 4. Boxes represent [M/H] measurements in individual DLAs from Prochaska et al. (2003). The box sizes are scaled with the $N_{H\,I}$ value of the DLA. The average error in the individual measurements is shown in the lower left.

effects caused by dust. However, the possibility of a significant number of extremely dusty absorbers being excluded from the sample due to dimming of background quasars is still an open issue.

A strong correlation between [Zn/H] (metallicity) and $W_0^{\lambda 2796}$ (velocity dispersion) was discovered. Although this was not previously expected, it is consistent with the fact that DLAs are almost exclusively sub-solar in metal abundances. Metals produced in regions of star formation are more likely to enrich neutral-gas regions of the galaxy when velocity dispersions are large. It is possible that larger velocity spreads correspond to deeper gravitational potential wells. These more massive regions would lead to more chemically evolved structures. Alternatively, larger velocity spreads could correspond to regions in relatively close proximity to intense bursts of star formation, which would also lead to kinematically broad structures of chemically enriched gas. However, lacking a detailed physical picture of the clouds comprising Mg II absorption, the precise nature of this correlation remains speculative.

6.3 DLA GALAXY IMAGING

The observations described in Chapter 5 add to the small but growing list of DLA galaxies at low redshifts. Table 6.1 lists the status and properties (luminosity relative to L^*, L/L^*, neutral hydrogen column density, N_{HI}, and impact parameter, b) of galaxy identifications for 14 DLA systems with $z_{DLA} \lesssim 1$ and $N_{HI} \geq 2 \times 10^{20}$ atoms cm^{-2} (but not including local galaxies). The distributions of DLA galaxy properties for these 14 cases are shown in Figure 6.4. B-band luminosities are plotted when available. K-band luminosities are plotted for galaxies that are not detected in B, but this substitution should not grossly affect any trends in the data. For the case of the DLA galaxy in the 3C 336 field (see 5.1), only an upper limit to its luminosity can be determined since the galaxy is not detected. For the same reason, the impact parameter is unknown. This case is clearly representative of another dwarf DLA galaxy if stars are present in the H I gas at all. Although the data set contains only 14 systems, some important trends emerge.

The b vs. L/L^* plot shows that low-luminosity dwarf galaxies with small impact pa-

Table 6.1: Low-Redshift DLA Galaxy Properties

QSO	$z_{\rm DLA}$	$N_{\rm HI}/10^{20}$ cm^{-2}	Luminosity	b kpc	Morphology	Ref.
			This work			
0738+313	0.091	15	$0.08L_K^*$	< 3.6	LSB	1
	0.221	7.9	$0.1L_B^*$	20	Dwarf spiral	1
0827+243	0.525	2.0	$0.8L_B^*$,$1.6L_R^*$, $1.2L_K^*$	34	Disturbed spiral	1
0952+179	0.239	21	$0.02L_K^*$	< 4.5	Dwarf LSB	1
1127−145	0.313	51	$0.12L_B^*$, $0.16L_R^*$, $0.04L_K^*$	< 6.5	Patchy/irr/LSB	1
1629+120	0.532	5.0	$0.6L_B^*$,$1.1L_R^*$, $0.6L_K^*$	17	Spiral	1
			Other work			
0235+164	0.524	4.5	$0.8L_B^*$	6.0	Late-type spiral	2,3
0302−223	1.010	2.3	$0.2L_B^*$	9.2	Semi-compact	4
0454+039	0.859	4.7	$0.4L_B^*$	6.4	Compact	4
0809+483	0.437	6.3	$1.7L_B^*$	9.6	Giant Sbc	4
1209+107	0.633	2.0	$1.6L_B^*$	11.2	Spiral	4
1229−021	0.395	5.6	$0.1L_B^*$	7.6	LSB	4,5
1328+307	0.692	15	$0.4L_B^*$	6.5	LSB	4,5
1622+239	0.656	2.3	$< 0.05L_K^*$	$\cdots$	LSB? compact?	6

(1) This dissertation. (2) Burbidge et al. (1996). (3) Yanny et al. (1989). (4) Le Brun et al. (1997). (5) Steidel et al. (1994). (6) Steidel et al. (1997).

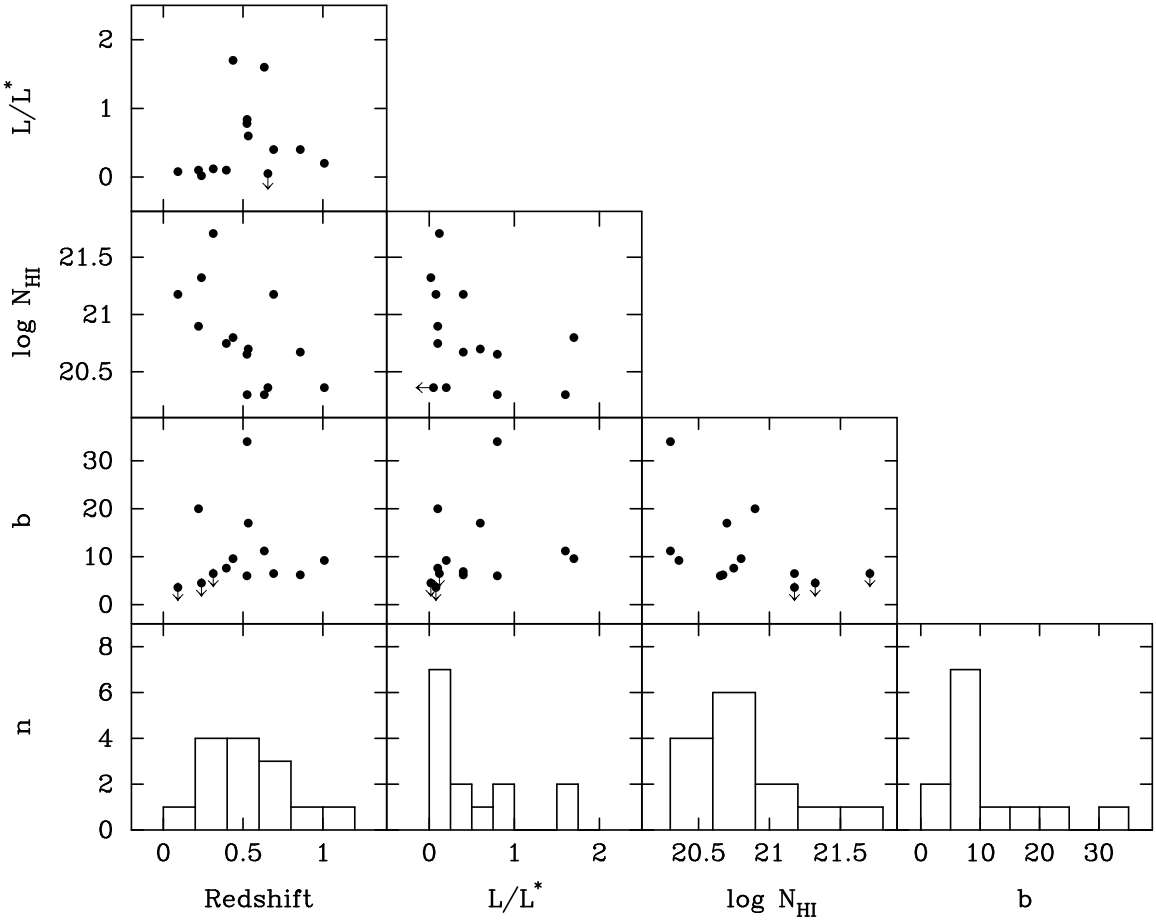

Figure 6.4: Distribution of properties for the DLA galaxies listed in Table 6.1. An upper limit for the luminosity of the DLA galaxy in the 3C 336 field is plotted but an impact parameter is not since no DLA galaxy has been detected. B-band luminosities are plotted in all cases except the two for which only K-band measurements exist. The impact parameter b has units of kpc. Upper limits in b are indicated by the arrows. The b histogram has upper limits included as measurements.

rameters dominate this small sample. Since DLA galaxies are H I cross section selected, this means that sub-L^* dwarf galaxies dominate the H I cross section at $z \approx 0.5$. This is also indicated by the luminosity histogram, n vs. L/L^*, which implies that it is ≈ 3 times more likely for a quasar sight line to intercept an $\approx 0.1L^*$ galaxy than an $\approx L^*$ galaxy. For galaxies at the present epoch, Zwaan et al. (2002, see their figure 1) show that the probability of intercepting DLA gas, i.e., the cross sectional area of DLA gas per unit volume, as a function of galaxy magnitude is flat for a steeply rising optical luminosity function with $\alpha = -1.5$, and decreases at faint magnitudes for $\alpha = -1.2$ or $\alpha = -1.0$. Expressed as a function of luminosity, this probability would rise as $\sim L^{-1}$ towards the faint end for the case where $\alpha = -1.5$ and, based on the data points in their figure 1, would increase as $\sim L^{-0.5}$ towards the faint end for $\alpha = -1.0$. For the latter case, the trends at $z = 0$ and $z \approx 0.5$ are similar. Turnshek et al. (2002) arrived at much the same conclusion (see their figure 4). They compared the optical diameter-limited ($>7'$) complete sample of $z = 0$ galaxies from Rao and Briggs (1993) to a $z \approx 0.5$ sample similar to the one in Table 6.1. They found that the relative absolute magnitude distributions of the two samples are comparable within the large uncertainties associated with the low-redshift sample.[2]. Note that Table 6.1 has the final measurements for the four DLA galaxies discussed in this paper as opposed to the preliminary measurements used in Turnshek et al. (2002). Also, the galaxy towards AO 0235+164 was not included in their analysis.

The trend that higher column densities tend to be observed at low impact parameters (b vs. $\log N_{HI}$) is not unexpected. However, what is unexpected is that the highest column densities are observed in galaxies with the lowest luminosities ($\log N_{HI}$ vs. L/L^*). This latter trend might be explained if a selection bias exists such that bright galaxies with high column densities at small impact parameters are missing from the sample. This might be caused by dimming of the background quasar due to reddening from the foreground DLA gas, excluding such quasars from the magnitude-limited sample. While a study by Ellison et al. (2001) on the occurrence of DLAs at $z \approx 2$ in a radio-selected quasar sample did not show a significant excess in the DLA number density as compared to DLAs found in

[2]This statement is based on a relative comparison at the two epochs, independent of any evolution in dn/dz (which measures evolution in galaxy number density times galaxy cross section) for DLAs (RT00)

optically-selected quasar samples, this might not hold true at lower redshift.

Two specific oddities of the sample are worth mentioning here: (1) The four DLA galaxies with $N_{HI} > 1 \times 10^{21}$ atoms cm^{-2} are all LSB galaxies. This may have significant implications for the whereabouts of the bulk of the H I gas, since the cosmological determination of Ω_{HI} from DLA systems is dominated by the highest N_{HI} systems. These four DLAs contain over two-thirds of the total column density in Table 6.1. Zwaan et al. (2003) have shown that only 15% of the neutral gas at the present epoch is contained in low surface brightness galaxies. Thus, if the low-redshift DLA galaxy trends hold up with larger samples, it would indicate that a different population of objects is responsible for the bulk of the neutral hydrogen gas in the universe at $z \approx 0.5$. (2) The three galaxies that have the largest impact parameters (17, 20, and 34 kpc) are spirals. G1 in the B2 0827+243 field is an $\approx L^*$ spiral and has the largest impact parameter and, as discussed earlier, it shows signs of an interaction that might be responsible for distributing the gas to larger galactocentric distances. It was only possible to see evidence for this in the high-resolution HST image that exists for the field. Similar high-resolution HST images do not exist for the other two large-impact-parameter fields, i.e., the dwarf spiral in the OI 363 field and the $\approx L^*$ spiral in the PKS 1629+120 field. Study of these two fields at higher resolution would be highly desirable in order to understand the reality and nature of this DLA gas at unusually large galactocentric distance.

It would clearly have been much more difficult to deduce these properties from similar observations if these same objects were at moderate to high redshift. However, a collection of such detailed results, used in conjunction with statistical results on the incidence, cosmological H I gas mass density and column density distribution of DLA absorption systems (RT00), will eventually be needed to accurately reveal the evolution of the bulk of the neutral gas in the Universe (as tracked by DLA quasar absorption systems) and the corresponding evolutionary relationship to DLA galaxies (i.e. the associated stellar light). One qualitative question presently of interest is to determine if the DLA population shows little evolution from $z \approx 4.0$ to $z \approx 0.5$, as has been recently suggested by Pettini et al. (1999) and RT00 on the basis of their metallicities and statistics, respectively. It would seem that there has to be some significant evolution in the DLA population from $z > 0.5$ to the present epoch if the results of Rao and Briggs (1993) at $z = 0$ are correct (also see Zwaan et al., 2003).

The Rao and Briggs (1993) study places almost all of the local H I gas in luminous spirals. In particular, it should be emphasized that DLA surveys are a probe of the integrated H I gas cross section, and the results suggest that this may be quite a separate issue from CCD imaging surveys which probe the luminous components of galaxies. A better knowledge of the properties of all galaxy populations at low redshifts (including luminous galaxies, dwarfs, and those with low surface brightnesses) is required to secure a better understanding of the integrated relative H I cross sections of the various galaxy types. Present evidence suggests that luminous galaxies were approximately in place by $z \approx 1$, with less luminous galaxies showing more evolution at lower redshift (e.g., Im et al., 1996, 1999). Therefore, one could envisage a scenario where luminous galaxies contribute little to the DLA detections, except locally at $z \approx 0$, while an evolving population of dwarfs and low surface brightness galaxies cause the bulk of the detections at $z > 0$. Indeed, the present congeries of identified low-redshift DLA galaxies suggest that a significant fraction of them are dwarf and low surface brightness galaxies, and the possible connection to the evolving moderate redshift "faint blue galaxy" population (§5.6) is intriguing. At the same time, with regard to current DLA surveys based on magnitude limited samples, it is possible that dust extinction may cause a substantial fraction of the H I gas cross section associated with luminous spirals to be missed. Luminous spirals would be expected to have higher metallicities and thus dust content. This is not expected to be a problem for dwarfs. Clearly the statistical survey results and the low-redshift follow-up studies of DLA systems need to be extended and improved to address these evolutionary issues properly. It is also of interest to consider selection effects more carefully as well as design experiments which will reach to lower H I masses in searches for large quantities of H I gas not associated with luminous spirals. The current 21 cm emission surveys are sensitive to $M_{HI} \approx 10^7$ $M_\odot$ locally.

Regardless of the outcome of such new programs, the results reported here and in other works have effectively settled the low-z morphology issue in favor of the mixed-morphology scenario: DLAs are drawn from a wide variety of types of gas-rich galaxies.

6.4 SUMMARY

6.4.1 Achievements

The SDSS EDR survey presented in Chapter 2 represents an order of magnitude increase in the number of Mg II systems thus far studied. I developed an original continuum fitting algorithm and doublet identification and analysis software. My analyses have allowed the measurement of the statistics of Mg II absorbers and their evolution in redshift with unprecedented significance. Furthermore, my new redshift and $W_0^{\lambda 2796}$ parameterization proposed in this dissertation accurately allows the first parameterized description of the evolving nature of $n(z, W_0^{\lambda 2796})$ due to the steepening of $n(W_0^{\lambda 2796})$ with decreasing redshift. My MMT survey, presented in Chapter 3, provides the first accurate measurement of Mg II dn/dz at low redshift. In addition, it is the first study with both sufficient sensitivity to detect weak Mg II systems and sufficient size to detect significant numbers of strong systems in an individual survey. This allowed the confirmation of the upturn in $n(W_0^{\lambda 2796})$ below $W_0^{\lambda 2796} = 0.3$Å that was speculated in Chapter 2.

I developed an original method for studying metal abundances in large H I column absorption systems, which was described in Chapter 4. I used this method to calculate the cosmic neutral hydrogen gas-phase metallicity and dust content at redshifts $0.9 < z < 2$. A weak correlation for both [Zn/H] and dust content with redshift was detected, and, for the first time, a strong correlation between [Zn/H] and projected line-of-sight velocity dispersion as measured by $W_0^{\lambda 2796}$ was discovered.

The imaging results described in Chapter 5 represent much of the current evidence confirming that a variety of galaxy types contribute to the DLA galaxy population. Classic techniques such as deep-imaging, optical spectroscopy of absorber candidates, and isophotal-profile analysis were used to study the absorbing galaxies. Additionally, I designed new techniques to take advantage of multi-band photometric data, developing algorithms to match stellar populations and dust contents to the galaxy SEDs.

6.4.2 Implications

Several lines of evidence suggest that the clouds giving rise to Mg II absorption comprise multiple physically-distinct populations. The results from high resolution work and the transition in $n(W_0^{\lambda 2796})$ are perhaps the strongest evidences, but the apparent contribution of enriched Lyα forest lines, the inability of simple physical models to reproduce in full the kinematic data and the menagerie of galaxy types, luminosities, and impact parameters that contribute to the absorber galaxy population are also consistent with this picture.

The incidence of Mg II systems does not show significant evidence for evolution at $z \gtrsim 1$, though evolution is detected at $1 \gtrsim z \gtrsim 0.2$. The population of lines with $W_0^{\lambda 2796} \geq 0.3$Å exhibit a steepening of the distribution of $W_0^{\lambda 2796}$ with decreasing redshift, such that the total co-moving absorption cross section decreases at a rate proportional to $W_0^{\lambda 2796}$. This is interpreted as an evolution in the kinematic properties of the absorbing galaxy population. Metallicity of high-$N_{H\,I}$ gas (as selected by Mg II absorption) was also shown to be highly correlated with kinematic properties as measured by $W_0^{\lambda 2796}$, and both metallicity and dust content for these systems increase with decreasing redshift, though measurements at $z < 0.9$ were not possible.

DLAs comprise a subset of intermediate/strong Mg II systems. They are shown to be drawn from a variety of morphological types with a range of luminosities, environments, and impact parameters. The results of RT00 show that approximately 18±6% of Mg II absorption systems with $W_0^{\lambda 2796} \geq 0.6$Å are DLAs. Amongst the identified DLA galaxies summarized above, all but one has $b < 20$kpc (0827 G1, with $b = 38\,h_{70}^{-1}$ kpc). This can be compared to $R_{eff}^{*} \approx 60$ kpc for Mg II systems with $W_0^{\lambda 2796} \geq 0.6$Å (§6.1.2). Direct comparison of DLA impact parameters and estimated values of R_{eff}^{*} are suspect for several reasons, including the different redshift ranges and the possibility of non-unity covering factors. Nonetheless, comparisons of the magnitudes indicate consistency: $b = 20-30$kpc corresponds to $10-25\%$ of the projected area within 60 kpc, which is consistent with the fraction of $W_0^{\lambda 2796} \geq 0.6$Å Mg II systems that are also DLAs.

A picture of galactic structures selected via gas cross section is beginning to emerge. Gaseous halos of bright galaxies extend out to large galactocentric radii ($\gtrsim$ 100kpc). In-

dividual halo sizes certainly vary, and there is likely to be dependence on luminosity and morphology. Various cloud or cloud-ensemble types contribute to Mg II absorption, and likely to DLA absorption as well. The structures responsible for DLA and Mg II absorption were in place by $z \approx 2 - 4$. For redshifts $z \gtrsim 1$, unknown physical processes regulate the incidence of Mg II and DLA systems, such that there is little evolution. For redshifts $z \lesssim 1$, the strongest Mg II systems begin to evolve away. By $z = 0$, Ω_{DLA} has decreased by a factor of $\approx 4 - 5$ from the high-redshift value. However, the degree of evolution of DLA systems throughout the redshift interval $1.65 > z > 0$ is poorly known. Continued work, utilizing results from this dissertation, will improve our knowledge of the redshift dependence of Ω_{DLA} at low z. Although DLAs are a subset of intermediate/strong Mg II systems, the details of the relationship are not yet clear. DLAs have sub-solar metal abundances, and their metallicity correlates with the velocity dispersion of Mg II absorption features, which suggests that mixing is an important variable in determining [M/H] in DLAs. Continuing study of low-redshift absorption systems will begin to bridge the gap between our knowledge of the local Universe and the evolving nature of gas-cross-section-selected galactic structures at earlier epochs.

The nature of gas-cross-section-selected galactic structures has important relevance to the study of galaxy evolution as a whole. Simulations are reaching a level of sophistication whereby they are able to make predictions concerning quasar absorption line statistics. Large (e.g., SDSS) and deep (e.g., HDFs) optical surveys are expanding the redshift range for which we can compare the galactic stellar- and gaseous-component statistics. It is perhaps too early to tell if these systems can be related directly to the faint blue galaxy population and/or the missing small-scale halo structures, for example, but continued progress in quasar absorption-line studies and follow up imaging, combined with ever-improving theory and simulations, should ameliorate the consistency of the various fields of study concerning galaxy evolution.

APPENDIX A

COSMOLOGY-DEPENDENT CALCULATIONS

This dissertation contains several physical attributes of galaxies and galactic structures such as distances and look-back times that are not directly observable, but are determined for a given cosmology from observables such as angular separation and redshift. Most were calculated by writing algorithms in C to numerically compute the necessary integrals. Although the programs were original to this dissertation, the theoretical formalisms were taken from published sources, mostly Peebles (1993) and Hogg (2000). For completeness, the derivation of the relevant formulae is described in this appendix.

The proper physical distance between two objects in the expanding Universe can be written in term of a time-dependent scale factor $a(t)$:

$$l(t) = l_0\, a(t). \tag{A.1}$$

Using the familiar inverse square law solution to Poisson's equation for the Newtonian gravitational acceleration, $\nabla \cdot \mathbf{g} = -4\pi\, G\, (\rho + 3\, \frac{p}{c})$, one obtains

$$\frac{\ddot{a}}{a} = -\frac{4}{3}\pi G(\rho + 3\,\frac{p}{c}) + \frac{c^2\Lambda}{3}, \tag{A.2}$$

where the density ρ and pressure p account only for "ordinary" material. The $c^2\Lambda = 8\pi G\rho_\Lambda$ term accounts for "dark" energy/pressure, if it exists. Energy conservation requires

$$\dot{\rho} = -3(\rho + \frac{p}{c})\frac{\dot{a}}{a}. \tag{A.3}$$

Equation A.3 can be used to eliminate pressure from Equation A.2, which can then be multiplied by $\dot{a}$ to form a perfect differential with the solution

$$\left(\frac{\dot{a}}{a}\right)^2 = \frac{8}{3}\pi G\rho + \frac{c^2\Lambda}{3} + \frac{c^2 k}{a^2}, \tag{A.4}$$

where k is a constant of integration. The Hubble constant H is defined by

$$H \equiv \frac{v}{l} = \frac{\dot{a}}{a}, \tag{A.5}$$

the redshift is

$$1 + z \equiv \frac{\lambda_0}{\lambda} = \frac{a_0}{a}, \tag{A.6}$$

and

$$\left(\frac{\dot{a}}{a}\right)^2 = \left(\frac{\dot{z}}{1+z}\right)^2. \tag{A.7}$$

If the mean mass density is dominated by nonrelativistic matter, $p \ll \rho \propto a^{-3}$, and one may write

$$\frac{\ddot{a}}{a} = H_0^2\left[-\Omega_M(1+z)^3/2 + \Omega_\Lambda\right], \tag{A.8}$$

and

$$\frac{\dot{a}}{a} = H_0 E(z) \equiv H_0\left[\Omega_M(1+z)^3 + \Omega_\Lambda + \Omega_k(1+z)^2\right]^{1/2}, \tag{A.9}$$

where

$$\Omega_M = \frac{8\pi G\rho_0}{3H_0^2}, \quad \Omega_\Lambda = \frac{c^2\Lambda}{3H_0^2} \quad \text{and} \quad \Omega_k = \frac{c^2 k}{(H_0 a_0)^2}. \tag{A.10}$$

From Equations A.4, A.5 and A.10, one can see that

$$1 = \Omega_M + \Omega_\Lambda + \Omega_k. \tag{A.11}$$

It is traditional to write $\Omega = \Omega_M + \Omega_\Lambda = 1 - \Omega_k$. Then Ω is the mass-energy density of the Universe expressed as a fraction of the closure density. The constant k (and therefore Ω_k) is related to the curvature of space. For $k = 0$, $\Omega = 1$ and the Universe is flat. For $k > 0$, $\Omega < 1$ and the Universe is open, and for $k < 0$, $\Omega > 1$ and the Universe is closed. It is also traditional to express the Hubble constant as $H_0 = h \times 100\,\mathrm{km\,s^{-1}\,Mpc^{-1}}$. In Chapters 2 through 4, calculations were done assuming a flat Universe with $\Omega_M = 0.3$, $\Omega_\Lambda = 0.7$ and a present day value of the Hubble constant $H_0 = 70\,\mathrm{km\,s^{-1}\,Mpc^{-1}}$ (i.e., $h = 0.7$), and in

Chapter 5 with $\Omega_M = 1$, $\Omega_\Lambda = 0$ and $h = 0.65$, though expressions will be derived here with full generality.

The relevant derived parameters in this dissertation are look-back time, line-of-sight intersection probability, impact parameter for a given angular separation and the comoving volume element, all as a function of redshift. To calculate the look-back time as a function of redshift, one may write $\dot{a} = da/dt$, or $dt = da/\dot{a}$ and therefore

$$t(z) = \int_0^a \frac{da}{\dot{a}} = \int_0^a \frac{da}{a\, H_0 E(z)} = \frac{1}{H_0} \int_z^\infty \frac{dz}{(1+z)E(z)}, \tag{A.12}$$

which is integrated numerically to give $t(z)$. The look-back time is then $t(0) - t(z)$, or

$$t_L(z) = \frac{1}{H_0} \int_0^z \frac{dz}{(1+z)E(z)}. \tag{A.13}$$

The proper displacement of a light ray with a redshift z is determined by setting $ds^2 = c^2dt^2 - dl^2 = 0$. Thus

$$dl = c\, dt = c\, \dot{a}^{-1}\, da = \left(\frac{\dot{a}}{a}\right)^{-1} \frac{c\, dz}{(1+z)}. \tag{A.14}$$

Using Equation A.9, the proper displacement can be written

$$\frac{dl}{dz} = \frac{c}{H_0\, E(z)\, (1+z)}. \tag{A.15}$$

Note that the look-back time is just the $1/c$ times the integral of the proper displacement, as it must be. The proper displacement also determines the interception probability, $dP = \sigma(z)\, n(z)\, dl$, where $\sigma(z)$ represents the cross section and $n(z)$ the number density. For a population that does not evolve, $\sigma(z) = \sigma_0$ and $n(z) = n_0(1+z)^3$. One may write:

$$\frac{dP}{dz} = \sigma(z)\, n(z)\, \frac{dl}{dz} = \sigma_0\, n_0\, \frac{c\,(1+z)^2}{H_0\, E(z)}. \tag{A.16}$$

The spatial part of the time-dependent line element $ds^2 = c^2dt^2 - (a(t)\, dl)^2$ can be written $dl^2 = dx^2 + dy^2 + dz^2 + dw^2$, where curvature has been allowed for by embedding the three-sphere in a flat four-dimensional space with orthogonal position coordinates x, y, z and w. Changing to spherical coordinates, one finds:

$$ds^2 = c^2dt^2 - a(t)^2 \left[\frac{dr^2}{1 + k\, r^2} + r^2\, (d\theta^2 + \sin^2\theta\, d\phi^2)\right], \tag{A.17}$$

where $r^2 = x^2 + y^2 + z^2$ and $R^2 = r^2 + w^2$ has been identified with the constant of integration k in equation A.4 such that $k = R^{-2}$ and is a constant of the cosmology. In the $r \ll R$ limit, ds^2 becomes the familiar Minkowski metric. It is useful to make the coordinate change

$$r = R \sin \chi = k^{-1/2} \sin \chi. \tag{A.18}$$

The line element then simplifies to

$$ds^2 = c^2 dt^2 - \frac{a(t)^2}{k} \left[d\chi^2 + \sin^2 \chi \, d\Omega \right]. \tag{A.19}$$

Setting $ds^2 = 0$ and $d\Omega = 0$, the coordinate distance to an event at t_e is

$$\chi = k^{1/2} \int_{t_e}^{0} \frac{c \, dt}{a} = c \, k^{1/2} \int_{a_e}^{a_0} \frac{da}{a\dot{a}} = \frac{c \, k^{1/2}}{H_0} \int_{a_e}^{a_0} \frac{da}{a^2 E(z)} = \frac{c \, k^{1/2}}{H_0 a_0} \int_0^z \frac{dz}{E(z)}, \tag{A.20}$$

and thus

$$r = k^{-1/2} \sin \left[\sqrt{\Omega_k} \int_0^z \frac{dz}{E(z)} \right]. \tag{A.21}$$

The impact parameter b at coordinate distance r for a given observed angle θ to a line of sight is

$$b = \theta \, a \, r = \frac{\theta \, a_0 r}{(1+z)} = \frac{\theta \, H_0 a_0 r}{H_0 (1+z)} = \frac{\theta \, c \, r_A}{H_0 (1+z)}, \tag{A.22}$$

where the "angular-size" distance r_A is given by

$$r_A = \frac{1}{\sqrt{\Omega_k}} \sin \left[\sqrt{\Omega_k} \int_0^z \frac{dz}{E(z)} \right]. \tag{A.23}$$

Note that r_A is well defined even for a negative Ω_k value, since $i \sin(i \, z) = -\sinh(z)$. Furthermore, the area subtended by solid angle $d\Omega$ is $dA = a^2 r^2 d\Omega$. Thus, the proper volume element is

$$dV = \frac{dl}{dz} \, dz \, a^2 r^2 \int d\Omega = \frac{4\pi \, r_A^2 \, c^3 \, dz}{E(z) \, H_0^3 \, (1+z)^3}. \tag{A.24}$$

The comoving volume element is just the proper volume element times three factors of the relative scale factor:

$$\frac{dV_C}{dz} = \frac{4\pi \, r_A^2 \, c^3}{E(z) \, H_0^3}. \tag{A.25}$$

Figure A.1 shows the interception probability for a non-evolving population (i.e., NECs), look-back times, impact parameters (b) and relative luminosity for a given magnitude for three different $(\Omega_M, \Omega_\Lambda, h)$ cosmologies: the "WMAP" cosmology used throughout most

of this dissertation, $(0.3, 0.7, 0.7)$, shown as the solid black curve; the no-Λ flat cosmology used in Chapter 5, $(1.0, 0.0, 0.65)$, shown as the red dashed curve; and a no-Λ low-density cosmology $(0.2, 0.0, 0.7)$, shown as the green dotted curve. The relative luminosity curves are simply the ratio of the $r_A(z)$ distances, and are shown relative to the no-Λ flat cosmology (i.e., the luminosity of an object at $z = 0.9$ is underestimated by 50% in the no-Λ flat cosmology if the true cosmology corresponds to the WMAP values.)

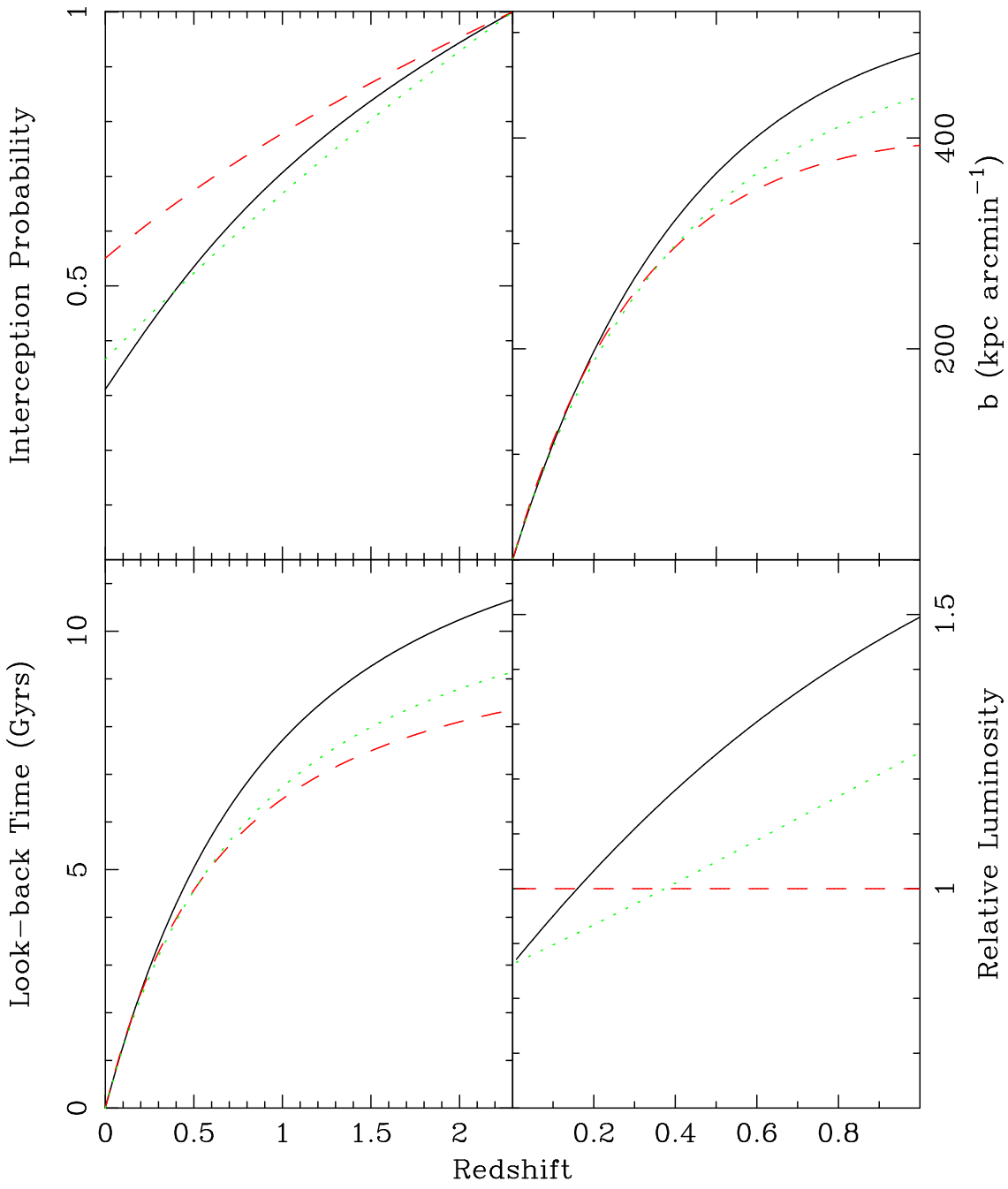

Figure A.1: Comparison of $(\Omega_M, \Omega_\Lambda, h)$ cosmology-dependent calculations. Shown are the $(0.3, 0.7, 0.7)$ "WMAP" cosmology (solid black curve), the $(1.0, 0.0, 0.65)$ no-Λ flat cosmology (red dashed curve), and a $(0.2, 0.0, 0.7)$ no-Λ low-density cosmology (green dotted curve). The relative luminosity curves are shown relative to the no-Λ flat cosmology (see text.)

APPENDIX B

THE Mg II ABSORBER CATALOGS

In this appendix, the 1331 Mg II absorber from the SDSS EDR survey and the 141 Mg II absorbers from the MMT survey are shown. The SDSS EDR systems are presented first, ordered by increasing redshift, followed by those from the MMT survey. The redshift and $W_0^{\lambda 2796}$ is listed on top of each frame, and the vertical lines mark the central position of λ2796 and λ2803.

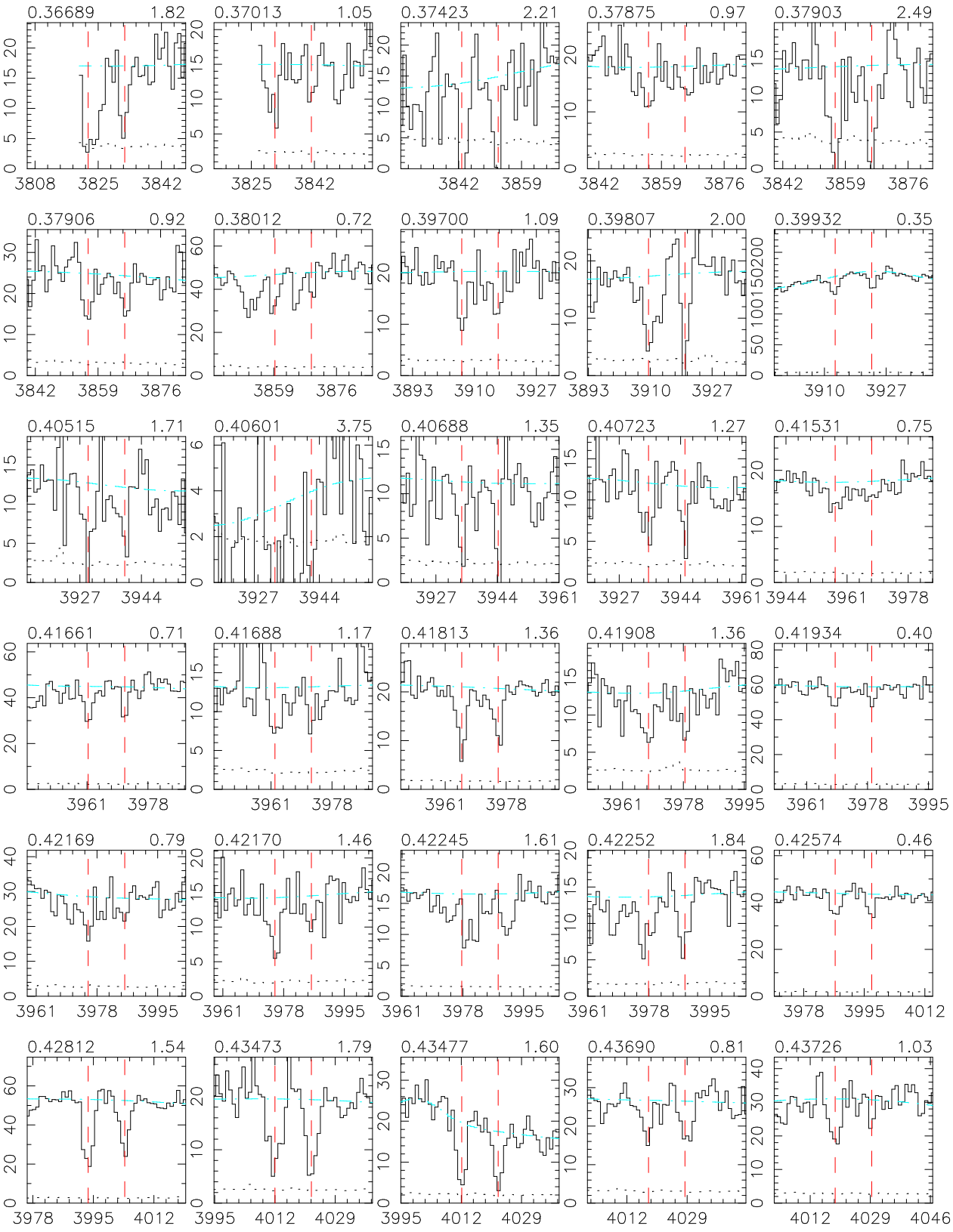
SDSS EDR
0.36689 1.82
0.37013 1.05
0.37423 2.21
0.37875 0.97
0.37903 2.49
0.37906 0.92
0.38012 0.72
0.39700 1.09
0.39807 2.00
0.39932 0.35
0.40515 1.71
0.40601 3.75
0.40688 1.35
0.40723 1.27
0.41531 0.75
0.41661 0.71
0.41688 1.17
0.41813 1.36
0.41908 1.36
0.41934 0.40
0.42169 0.79
0.42170 1.46
0.42245 1.61
0.42252 1.84
0.42574 0.46
0.42812 1.54
0.43473 1.79
0.43477 1.60
0.43690 0.81
0.43726 1.03

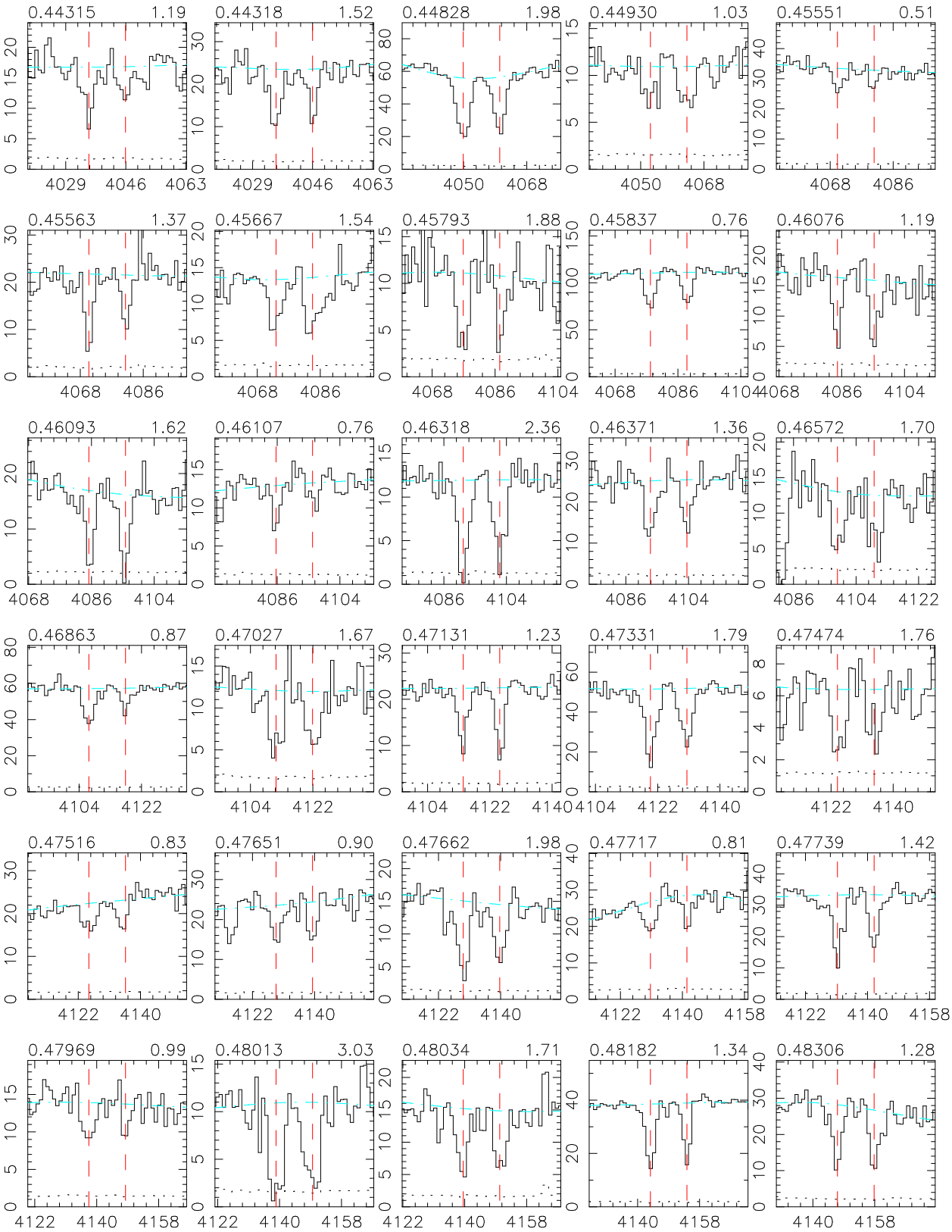
SDSS EDR
0.44315 1.19
0.44318 1.52
0.44828 1.98
0.44930 1.03
0.45551 0.51
0.45563 1.37
0.45667 1.54
0.45793 1.88
0.45837 0.76
0.46076 1.19
0.46093 1.62
0.46107 0.76
0.46318 2.36
0.46371 1.36
0.46572 1.70
0.46863 0.87
0.47027 1.67
0.47131 1.23
0.47331 1.79
0.47474 1.76
0.47516 0.83
0.47651 0.90
0.47662 1.98
0.47717 0.81
0.47739 1.42
0.47969 0.99
0.48013 3.03
0.48034 1.71
0.48182 1.34
0.48306 1.28

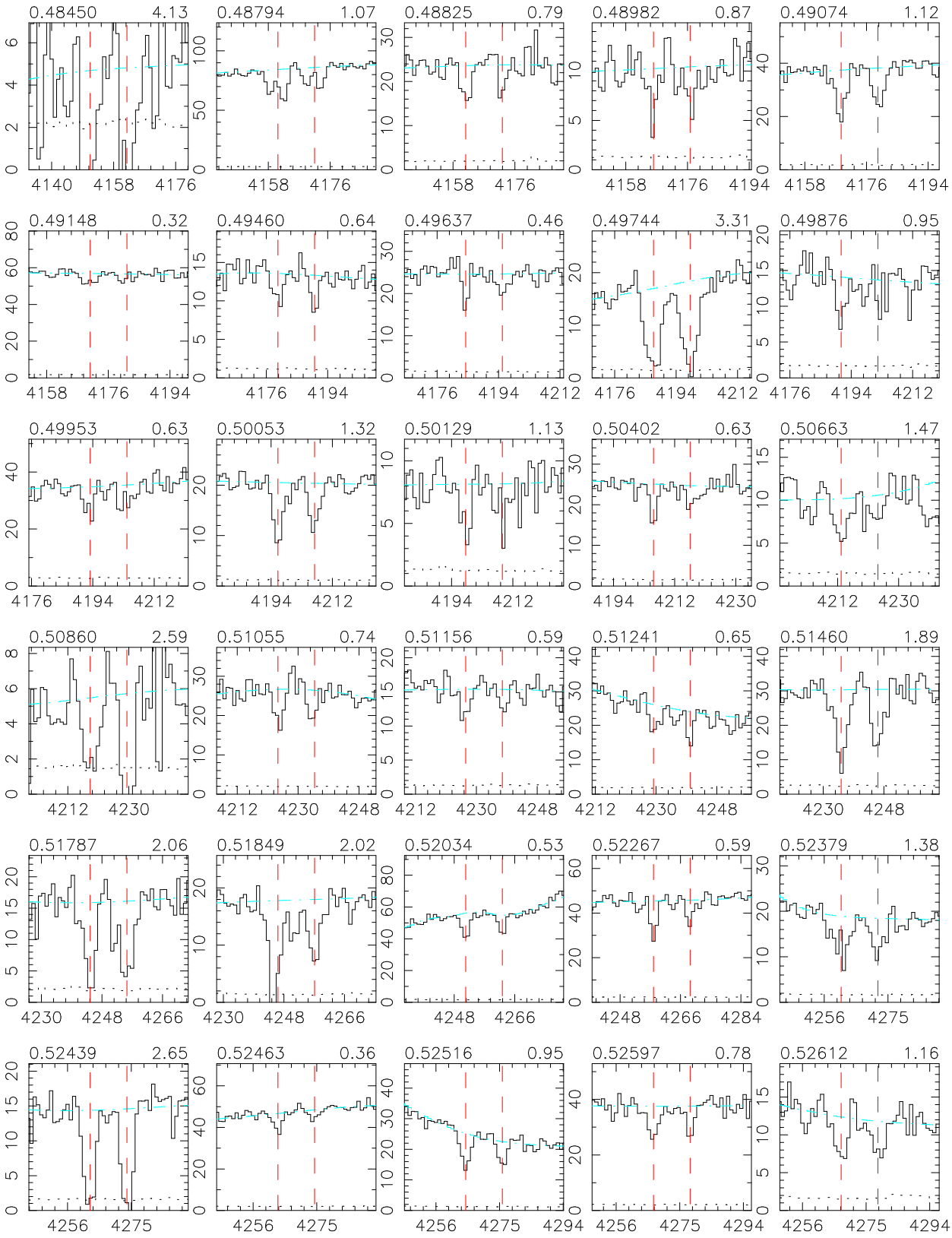
SDSS EDR
0.48450 4.13
0.48794 1.07
0.48825 0.79
0.48982 0.87
0.49074 1.12
0.49148 0.32
0.49460 0.64
0.49637 0.46
0.49744 3.31
0.49876 0.95
0.49953 0.63
0.50053 1.32
0.50129 1.13
0.50402 0.63
0.50663 1.47
0.50860 2.59
0.51055 0.74
0.51156 0.59
0.51241 0.65
0.51460 1.89
0.51787 2.06
0.51849 2.02
0.52034 0.53
0.52267 0.59
0.52379 1.38
0.52439 2.65
0.52463 0.36
0.52516 0.95
0.52597 0.78
0.52612 1.16

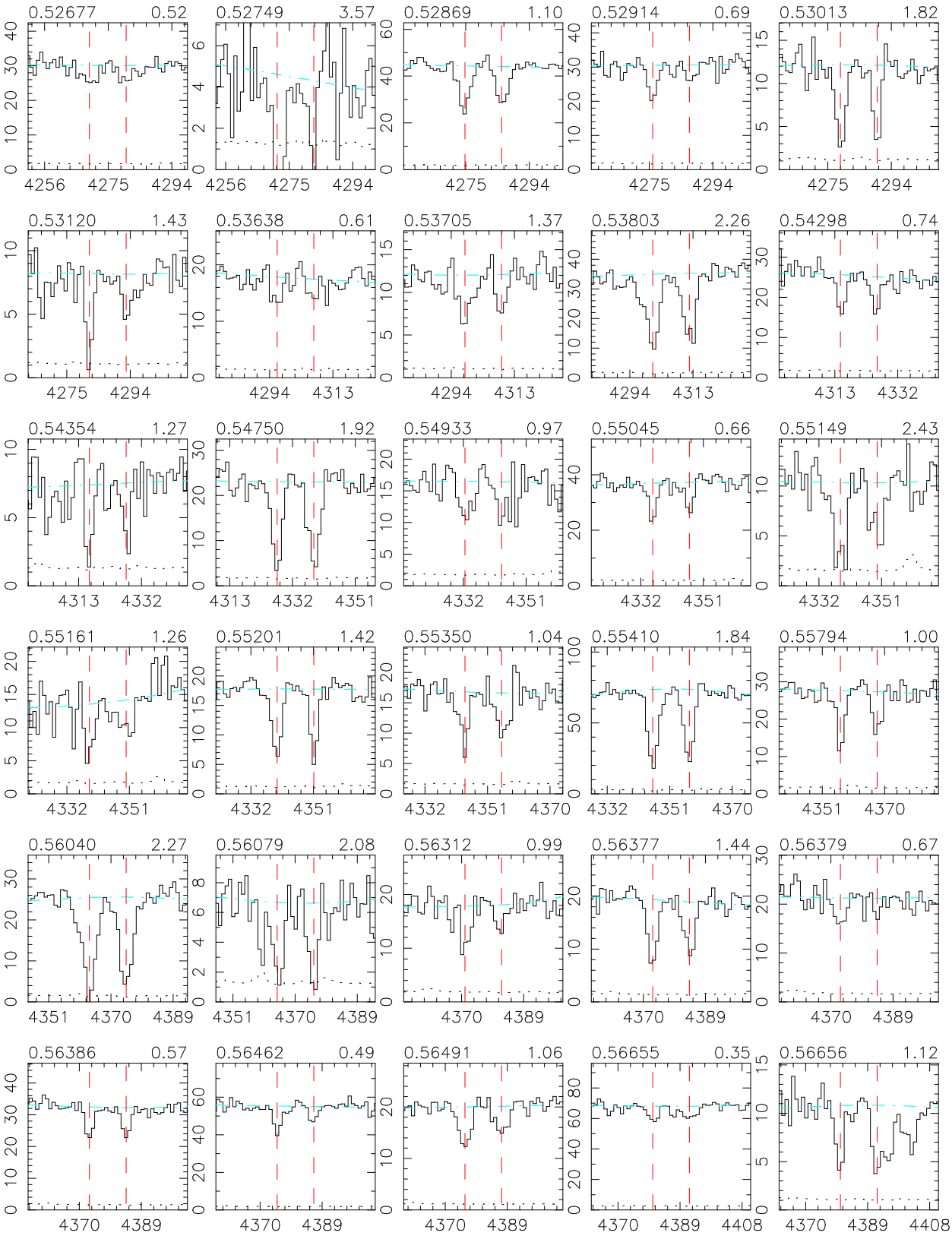
SDSS EDR
0.52677 0.52
0.52749 3.57
0.52869 1.10
0.52914 0.69
0.53013 1.82
0.53120 1.43
0.53638 0.61
0.53705 1.37
0.53803 2.26
0.54298 0.74
0.54354 1.27
0.54750 1.92
0.54933 0.97
0.55045 0.66
0.55149 2.43
0.55161 1.26
0.55201 1.42
0.55350 1.04
0.55410 1.84
0.55794 1.00
0.56040 2.27
0.56079 2.08
0.56312 0.99
0.56377 1.44
0.56379 0.67
0.56386 0.57
0.56462 0.49
0.56491 1.06
0.56655 0.35
0.56656 1.12

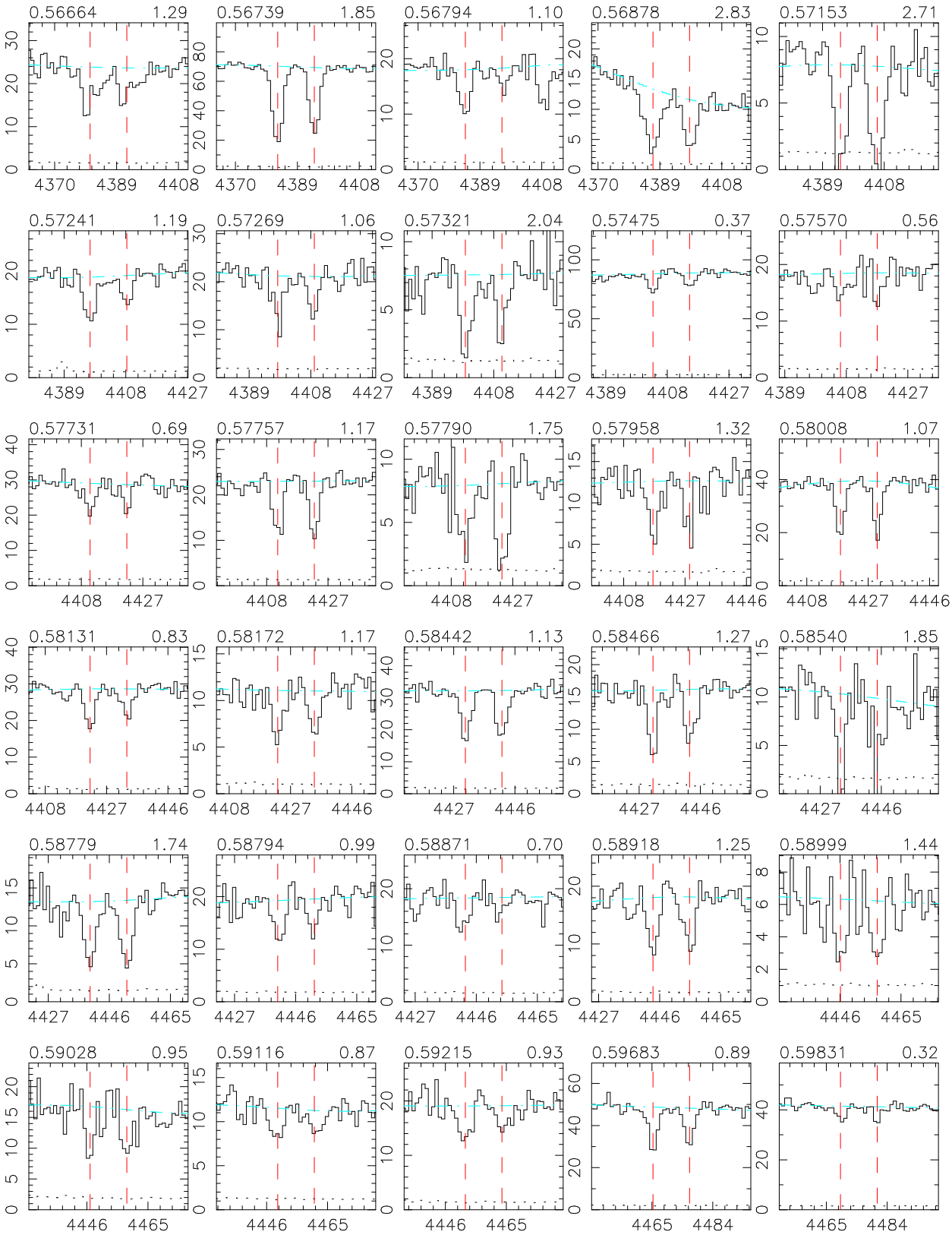
SDSS EDR
0.56664 1.29
0.56739 1.85
0.56794 1.10
0.56878 2.83
0.57153 2.71
0.57241 1.19
0.57269 1.06
0.57321 2.04
0.57475 0.37
0.57570 0.56
0.57731 0.69
0.57757 1.17
0.57790 1.75
0.57958 1.32
0.58008 1.07
0.58131 0.83
0.58172 1.17
0.58442 1.13
0.58466 1.27
0.58540 1.85
0.58779 1.74
0.58794 0.99
0.58871 0.70
0.58918 1.25
0.58999 1.44
0.59028 0.95
0.59116 0.87
0.59215 0.93
0.59683 0.89
0.59831 0.32

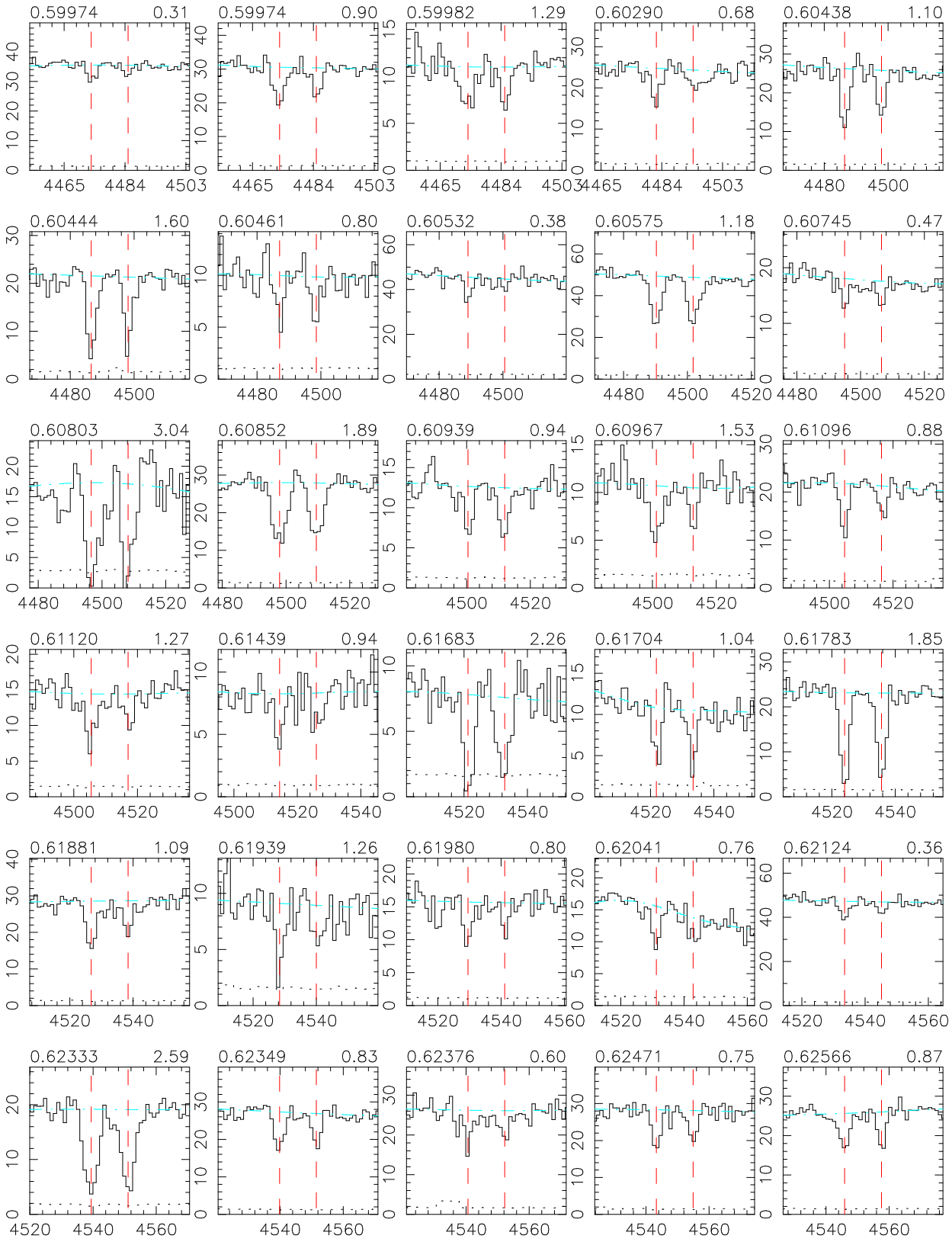
SDSS EDR
0.59974 0.31
0.59974 0.90
0.59982 1.29
0.60290 0.68
0.60438 1.10
0.60444 1.60
0.60461 0.80
0.60532 0.38
0.60575 1.18
0.60745 0.47
0.60803 3.04
0.60852 1.89
0.60939 0.94
0.60967 1.53
0.61096 0.88
0.61120 1.27
0.61439 0.94
0.61683 2.26
0.61704 1.04
0.61783 1.85
0.61881 1.09
0.61939 1.26
0.61980 0.80
0.62041 0.76
0.62124 0.36
0.62333 2.59
0.62349 0.83
0.62376 0.60
0.62471 0.75
0.62566 0.87

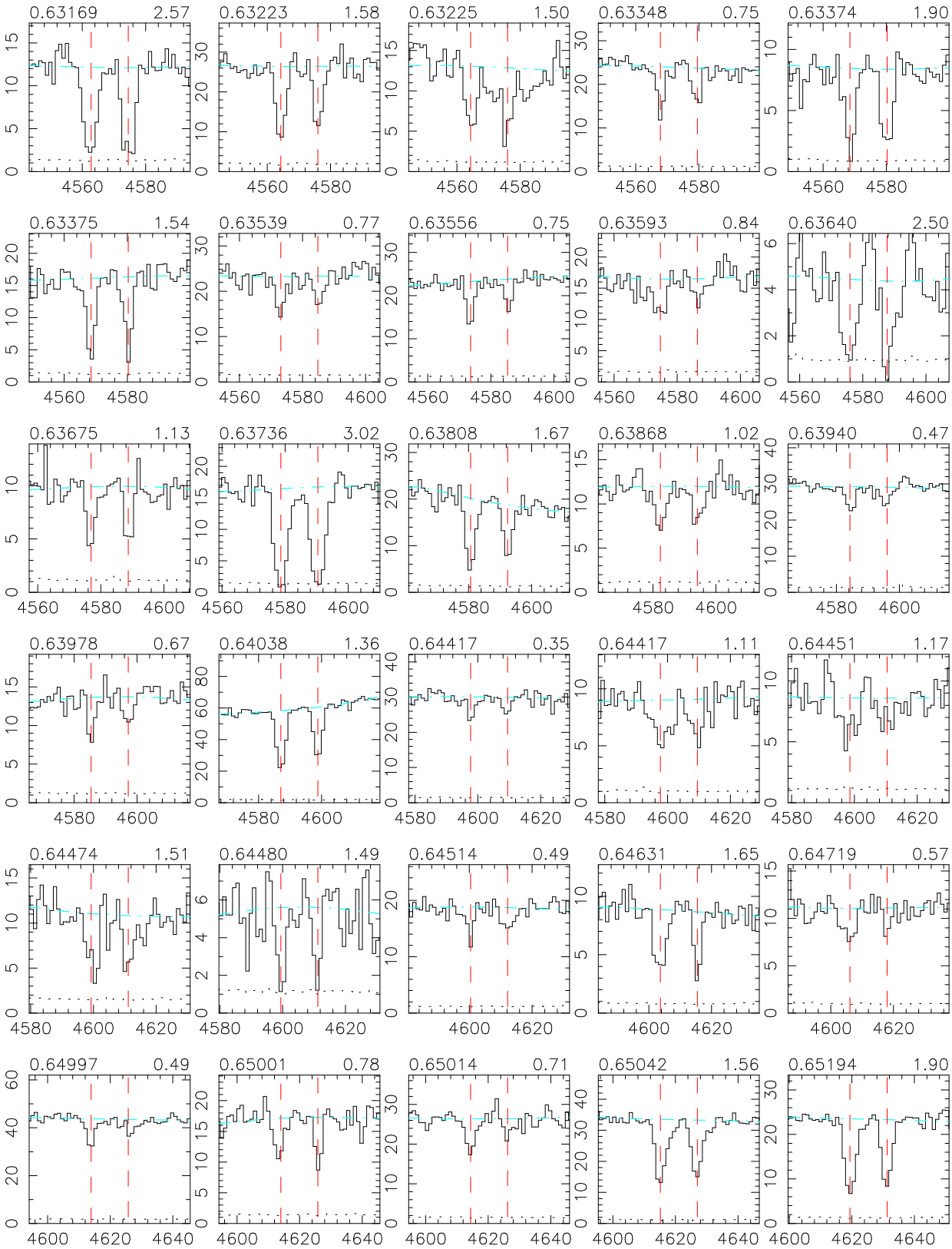
SDSS EDR
0.63169 2.57
0.63223 1.58
0.63225 1.50
0.63348 0.75
0.63374 1.90
0.63375 1.54
0.63539 0.77
0.63556 0.75
0.63593 0.84
0.63640 2.50
0.63675 1.13
0.63736 3.02
0.63808 1.67
0.63868 1.02
0.63940 0.47
0.63978 0.67
0.64038 1.36
0.64417 0.35
0.64417 1.11
0.64451 1.17
0.64474 1.51
0.64480 1.49
0.64514 0.49
0.64631 1.65
0.64719 0.57
0.64997 0.49
0.65001 0.78
0.65014 0.71
0.65042 1.56
0.65194 1.90

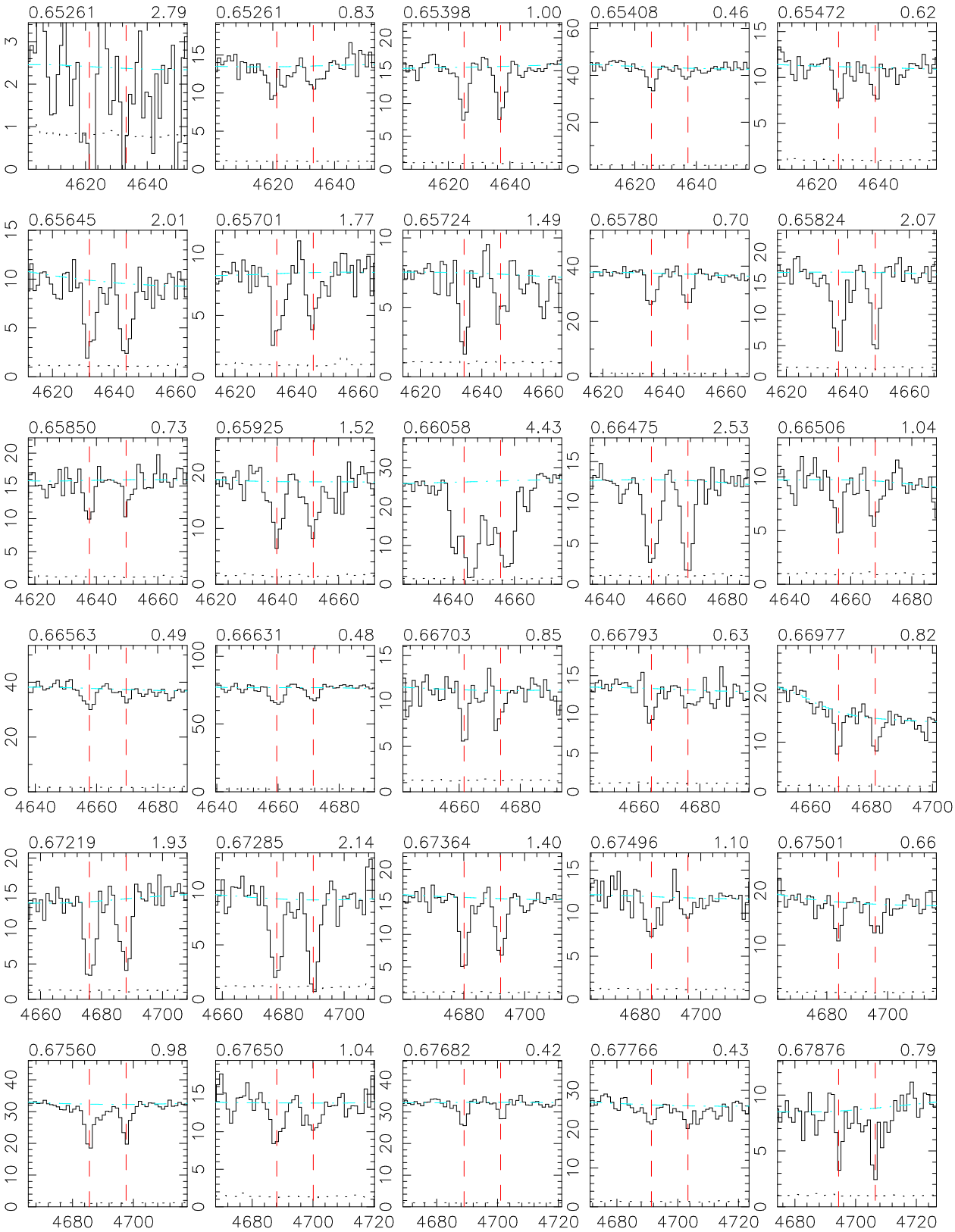
SDSS EDR
0.65261 2.79
0.65261 0.83
0.65398 1.00
0.65408 0.46
0.65472 0.62
0.65645 2.01
0.65701 1.77
0.65724 1.49
0.65780 0.70
0.65824 2.07
0.65850 0.73
0.65925 1.52
0.66058 4.43
0.66475 2.53
0.66506 1.04
0.66563 0.49
0.66631 0.48
0.66703 0.85
0.66793 0.63
0.66977 0.82
0.67219 1.93
0.67285 2.14
0.67364 1.40
0.67496 1.10
0.67501 0.66
0.67560 0.98
0.67650 1.04
0.67682 0.42
0.67766 0.43
0.67876 0.79

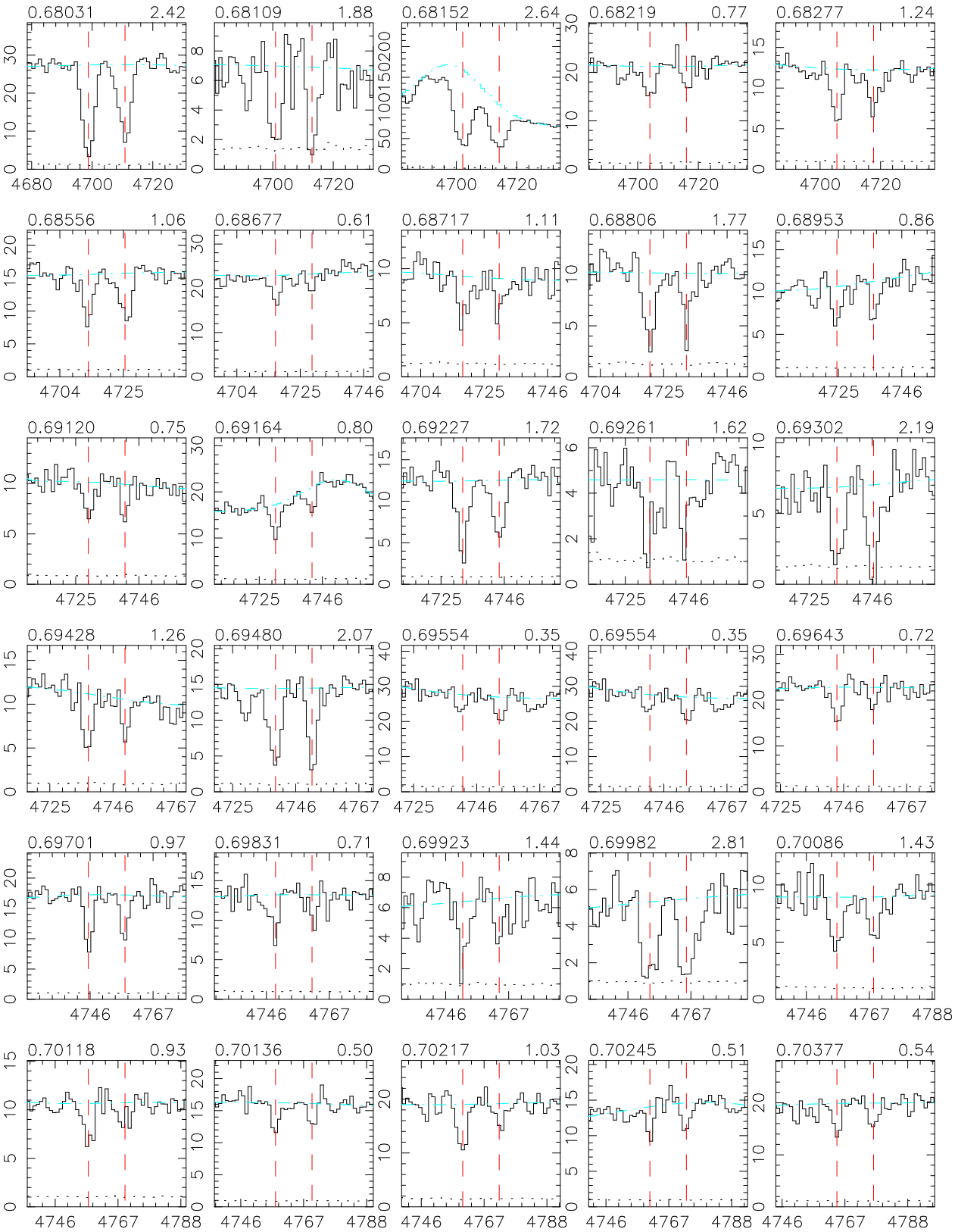
SDSS EDR
0.68031 2.42
0.68109 1.88
0.68152 2.64
0.68219 0.77
0.68277 1.24
0.68556 1.06
0.68677 0.61
0.68717 1.11
0.68806 1.77
0.68953 0.86
0.69120 0.75
0.69164 0.80
0.69227 1.72
0.69261 1.62
0.69302 2.19
0.69428 1.26
0.69480 2.07
0.69554 0.35
0.69554 0.35
0.69643 0.72
0.69701 0.97
0.69831 0.71
0.69923 1.44
0.69982 2.81
0.70086 1.43
0.70118 0.93
0.70136 0.50
0.70217 1.03
0.70245 0.51
0.70377 0.54

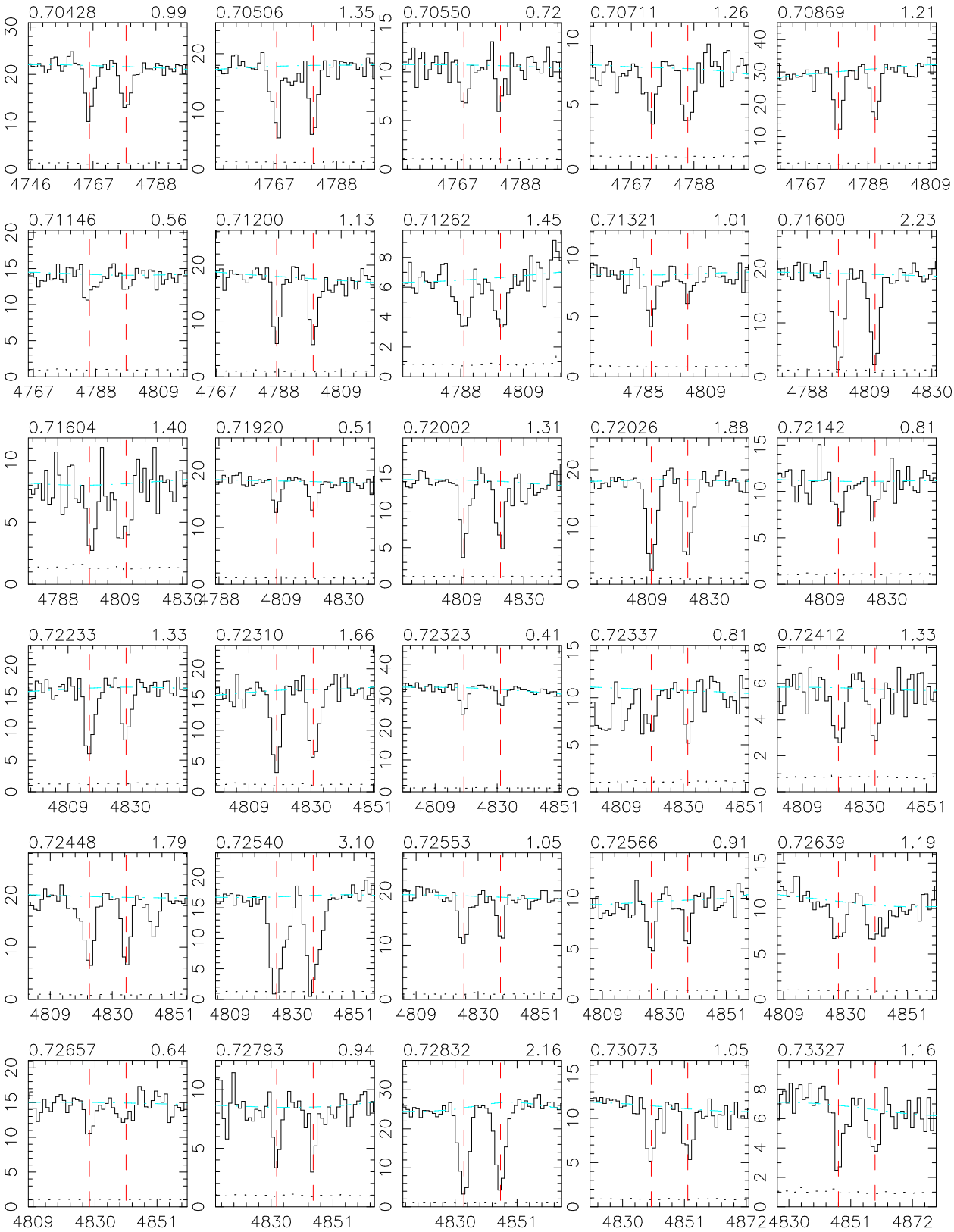
SDSS EDR
0.70428 0.99
0.70506 1.35
0.70550 0.72
0.70711 1.26
0.70869 1.21
0.71146 0.56
0.71200 1.13
0.71262 1.45
0.71321 1.01
0.71600 2.23
0.71604 1.40
0.71920 0.51
0.72002 1.31
0.72026 1.88
0.72142 0.81
0.72233 1.33
0.72310 1.66
0.72323 0.41
0.72337 0.81
0.72412 1.33
0.72448 1.79
0.72540 3.10
0.72553 1.05
0.72566 0.91
0.72639 1.19
0.72657 0.64
0.72793 0.94
0.72832 2.16
0.73073 1.05
0.73327 1.16

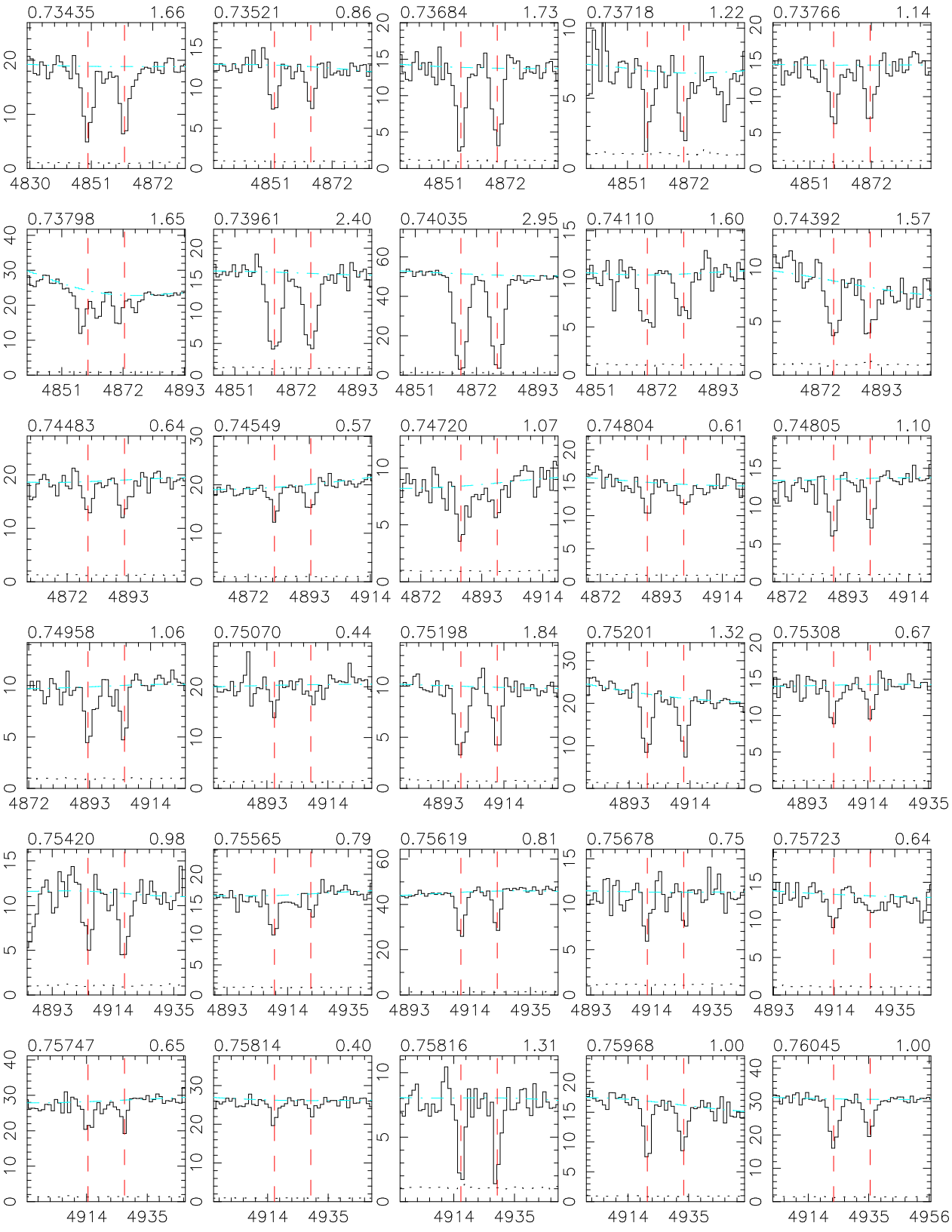
SDSS EDR
0.73435 1.66
0.73521 0.86
0.73684 1.73
0.73718 1.22
0.73766 1.14
0.73798 1.65
0.73961 2.40
0.74035 2.95
0.74110 1.60
0.74392 1.57
0.74483 0.64
0.74549 0.57
0.74720 1.07
0.74804 0.61
0.74805 1.10
0.74958 1.06
0.75070 0.44
0.75198 1.84
0.75201 1.32
0.75308 0.67
0.75420 0.98
0.75565 0.79
0.75619 0.81
0.75678 0.75
0.75723 0.64
0.75747 0.65
0.75814 0.40
0.75816 1.31
0.75968 1.00
0.76045 1.00

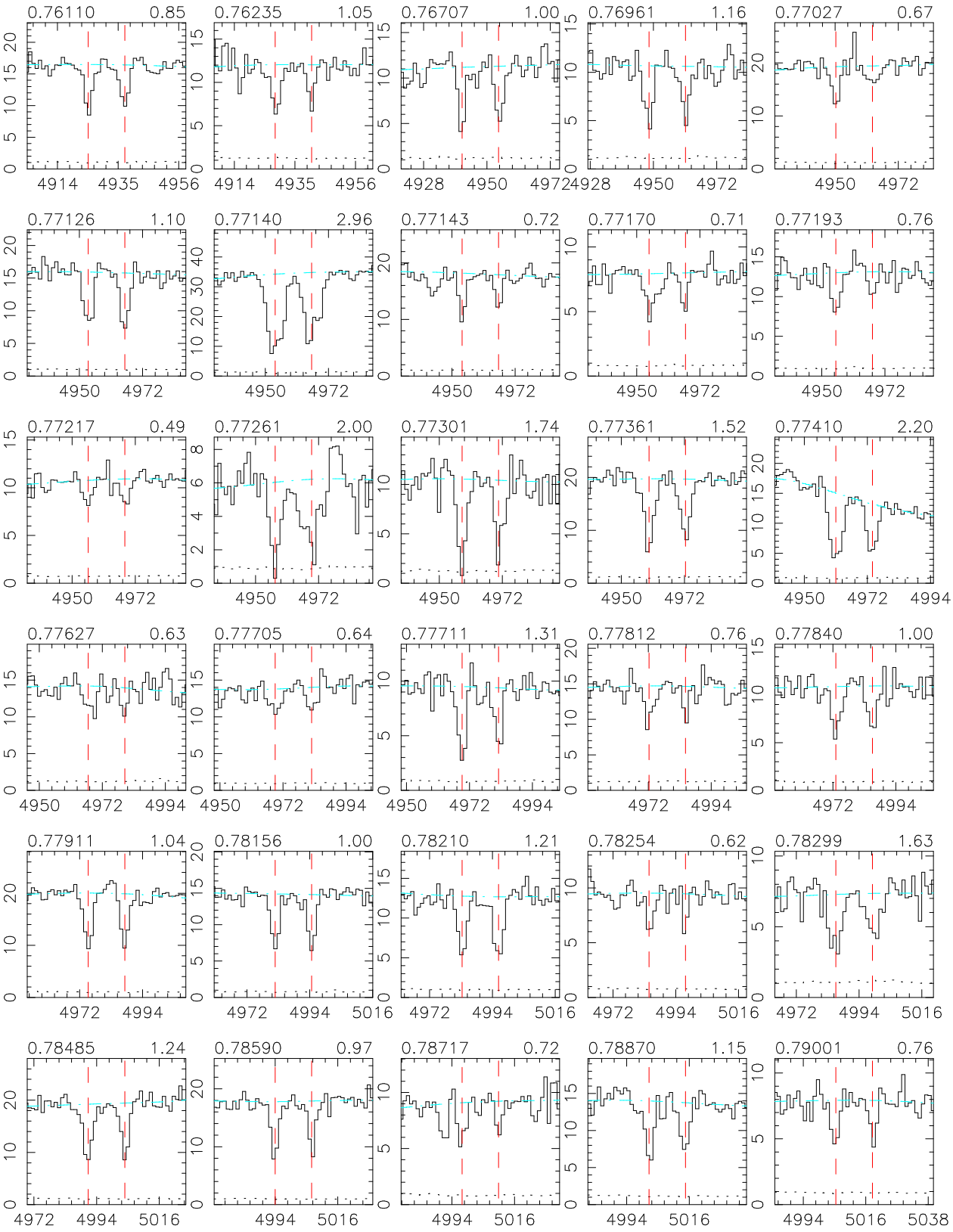
SDSS EDR
0.76110 0.85
0.76235 1.05
0.76707 1.00
0.76961 1.16
0.77027 0.67
0.77126 1.10
0.77140 2.96
0.77143 0.72
0.77170 0.71
0.77193 0.76
0.77217 0.49
0.77261 2.00
0.77301 1.74
0.77361 1.52
0.77410 2.20
0.77627 0.63
0.77705 0.64
0.77711 1.31
0.77812 0.76
0.77840 1.00
0.77911 1.04
0.78156 1.00
0.78210 1.21
0.78254 0.62
0.78299 1.63
0.78485 1.24
0.78590 0.97
0.78717 0.72
0.78870 1.15
0.79001 0.76

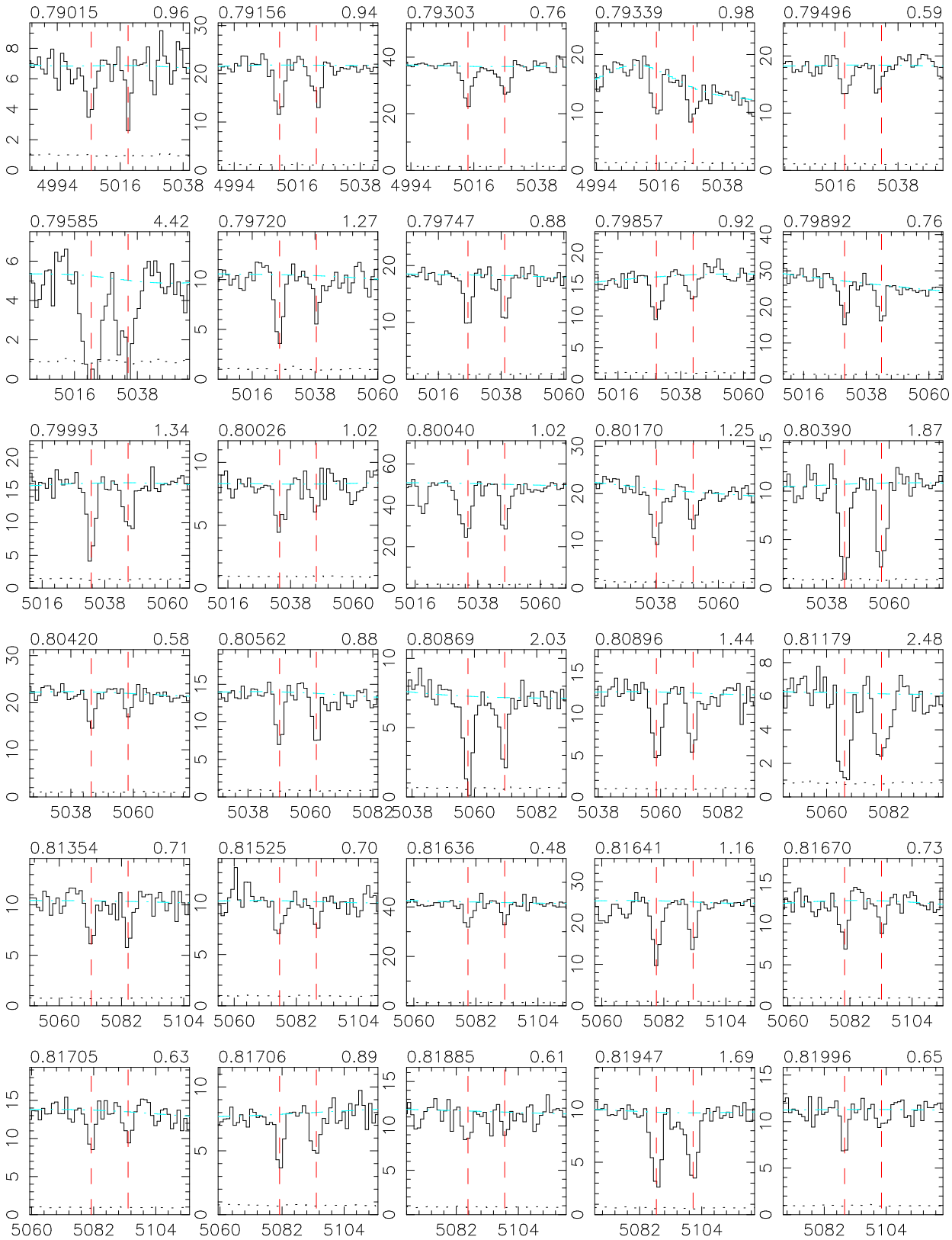
SDSS EDR
0.79015 0.96
0.79156 0.94
0.79303 0.76
0.79339 0.98
0.79496 0.59
0.79585 4.42
0.79720 1.27
0.79747 0.88
0.79857 0.92
0.79892 0.76
0.79993 1.34
0.80026 1.02
0.80040 1.02
0.80170 1.25
0.80390 1.87
0.80420 0.58
0.80562 0.88
0.80869 2.03
0.80896 1.44
0.81179 2.48
0.81354 0.71
0.81525 0.70
0.81636 0.48
0.81641 1.16
0.81670 0.73
0.81705 0.63
0.81706 0.89
0.81885 0.61
0.81947 1.69
0.81996 0.65

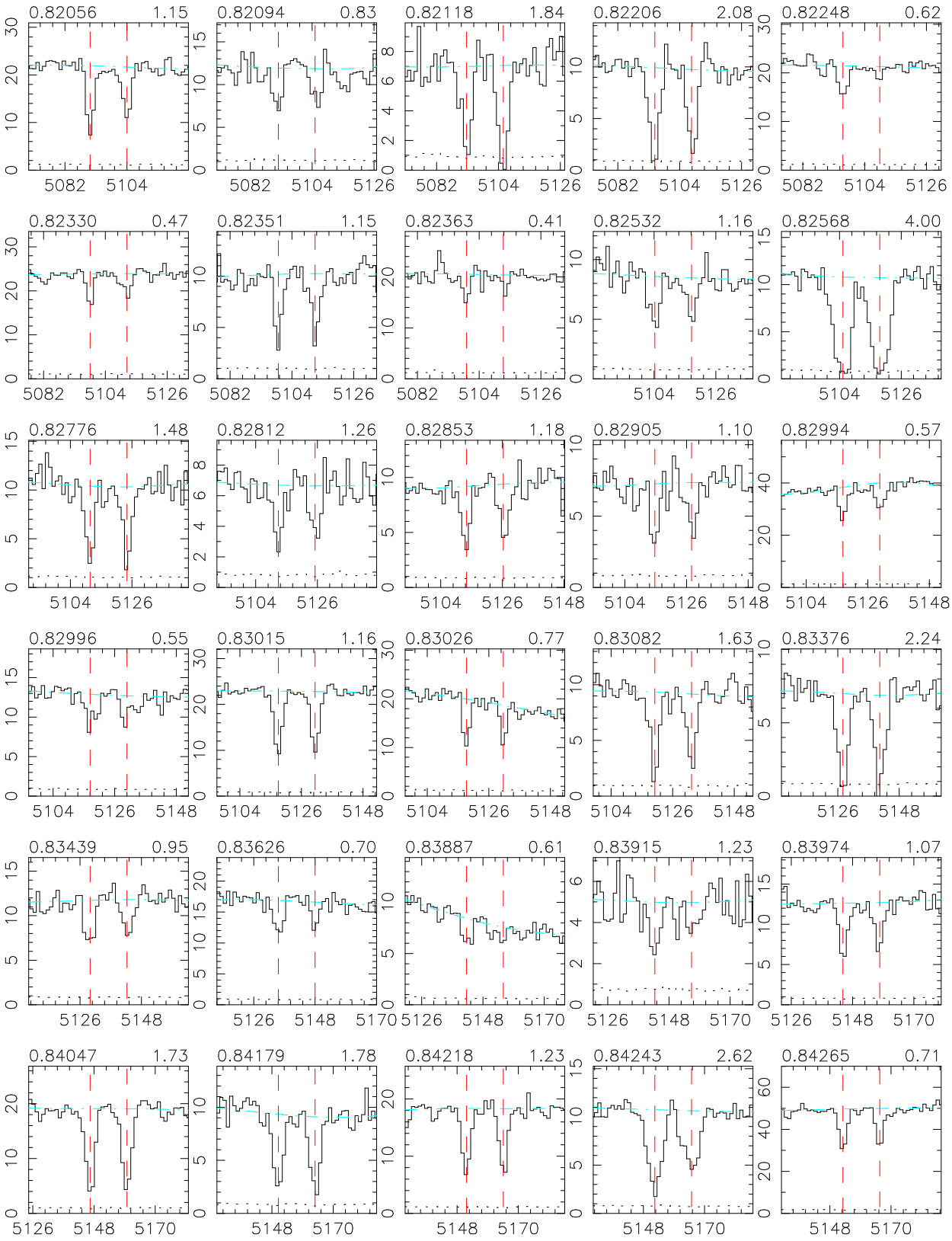
SDSS EDR
0.82056 1.15
0.82094 0.83
0.82118 1.84
0.82206 2.08
0.82248 0.62
0.82330 0.47
0.82351 1.15
0.82363 0.41
0.82532 1.16
0.82568 4.00
0.82776 1.48
0.82812 1.26
0.82853 1.18
0.82905 1.10
0.82994 0.57
0.82996 0.55
0.83015 1.16
0.83026 0.77
0.83082 1.63
0.83376 2.24
0.83439 0.95
0.83626 0.70
0.83887 0.61
0.83915 1.23
0.83974 1.07
0.84047 1.73
0.84179 1.78
0.84218 1.23
0.84243 2.62
0.84265 0.71

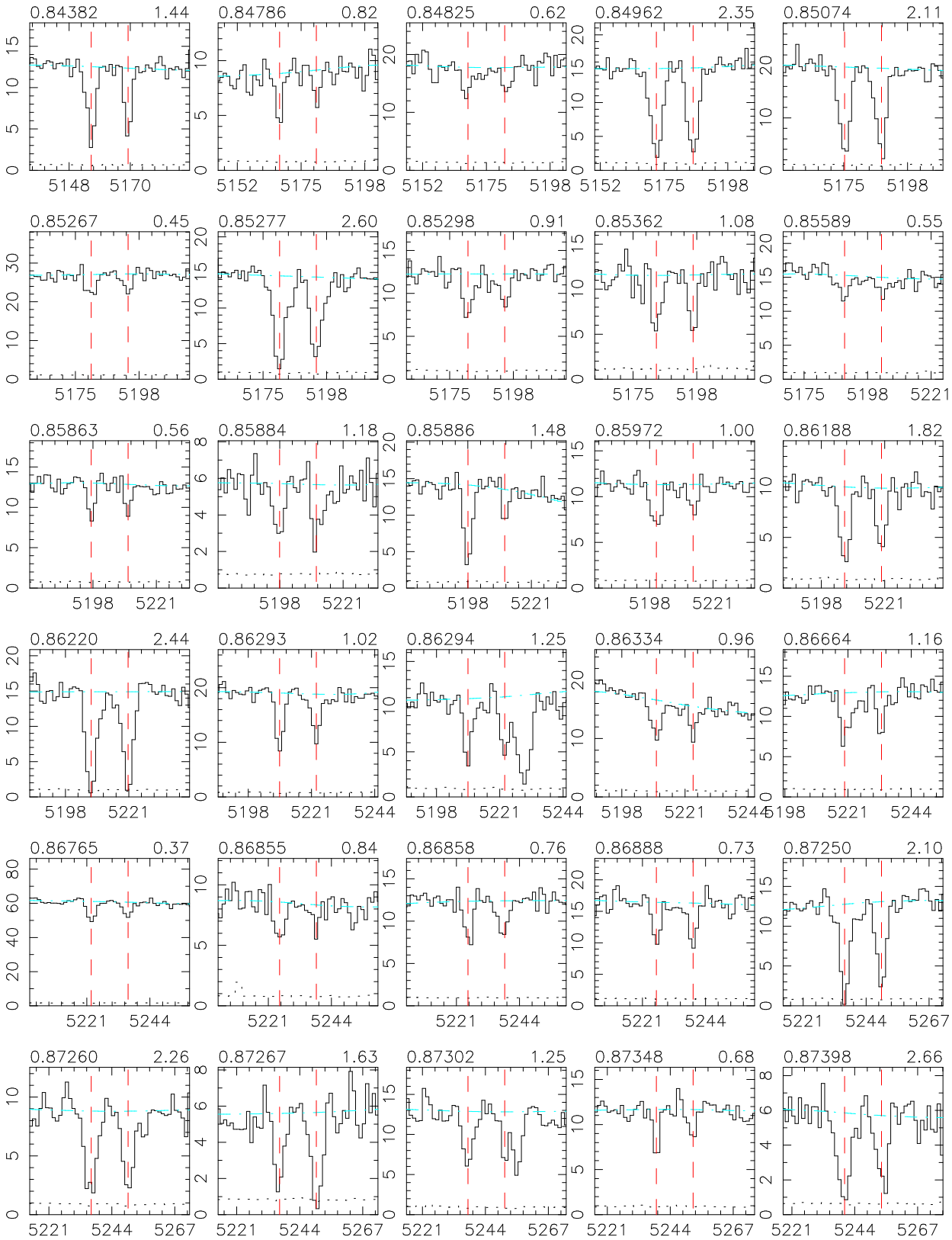
SDSS EDR
0.84382 1.44
0.84786 0.82
0.84825 0.62
0.84962 2.35
0.85074 2.11
0.85267 0.45
0.85277 2.60
0.85298 0.91
0.85362 1.08
0.85589 0.55
0.85863 0.56
0.85884 1.18
0.85886 1.48
0.85972 1.00
0.86188 1.82
0.86220 2.44
0.86293 1.02
0.86294 1.25
0.86334 0.96
0.86664 1.16
0.86765 0.37
0.86855 0.84
0.86858 0.76
0.86888 0.73
0.87250 2.10
0.87260 2.26
0.87267 1.63
0.87302 1.25
0.87348 0.68
0.87398 2.66

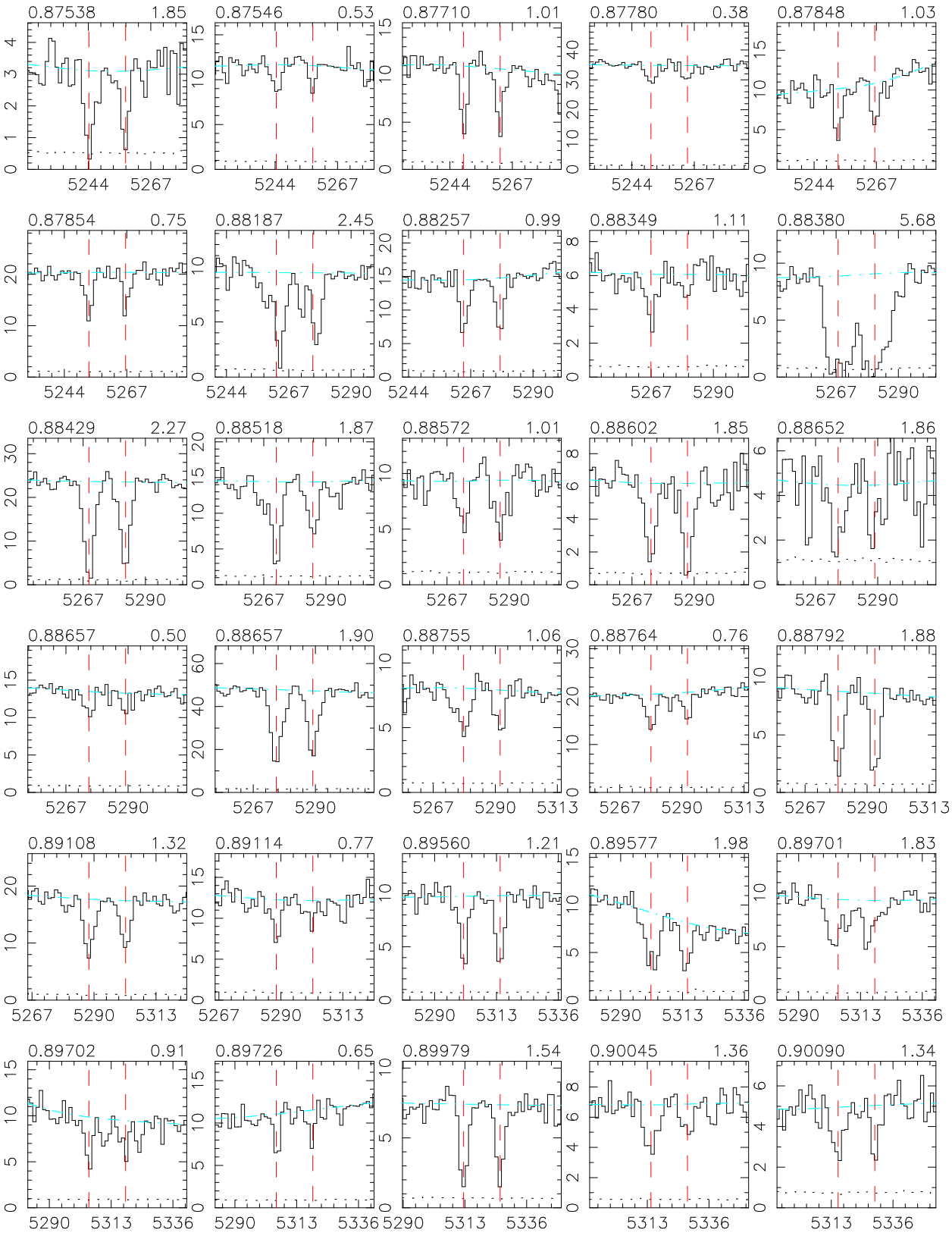
SDSS EDR
0.87538 1.85
0.87546 0.53
0.87710 1.01
0.87780 0.38
0.87848 1.03
0.87854 0.75
0.88187 2.45
0.88257 0.99
0.88349 1.11
0.88380 5.68
0.88429 2.27
0.88518 1.87
0.88572 1.01
0.88602 1.85
0.88652 1.86
0.88657 0.50
0.88657 1.90
0.88755 1.06
0.88764 0.76
0.88792 1.88
0.89108 1.32
0.89114 0.77
0.89560 1.21
0.89577 1.98
0.89701 1.83
0.89702 0.91
0.89726 0.65
0.89979 1.54
0.90045 1.36
0.90090 1.34

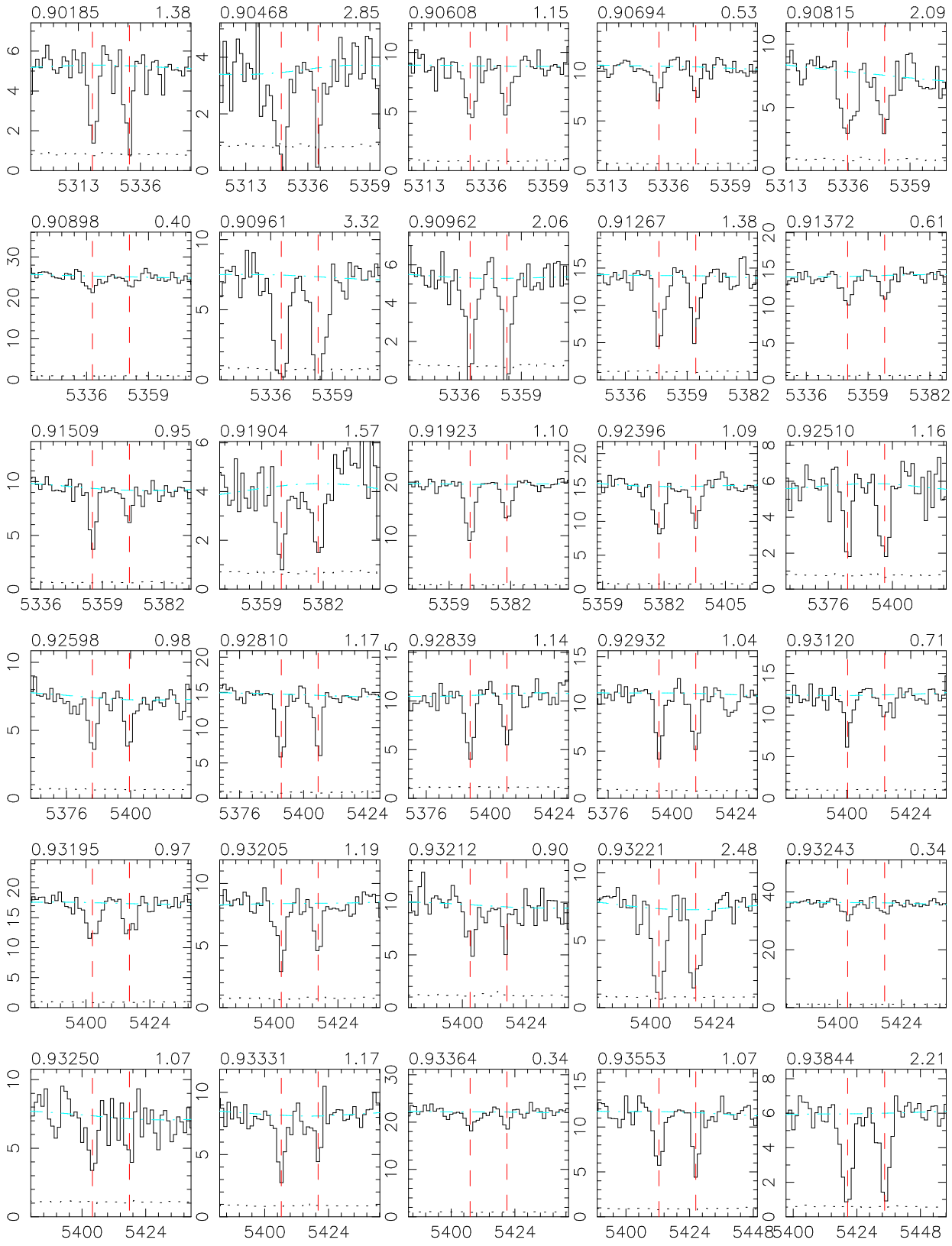
SDSS EDR
0.90185 1.38
0.90468 2.85
0.90608 1.15
0.90694 0.53
0.90815 2.09
0.90898 0.40
0.90961 3.32
0.90962 2.06
0.91267 1.38
0.91372 0.61
0.91509 0.95
0.91904 1.57
0.91923 1.10
0.92396 1.09
0.92510 1.16
0.92598 0.98
0.92810 1.17
0.92839 1.14
0.92932 1.04
0.93120 0.71
0.93195 0.97
0.93205 1.19
0.93212 0.90
0.93221 2.48
0.93243 0.34
0.93250 1.07
0.93331 1.17
0.93364 0.34
0.93553 1.07
0.93844 2.21

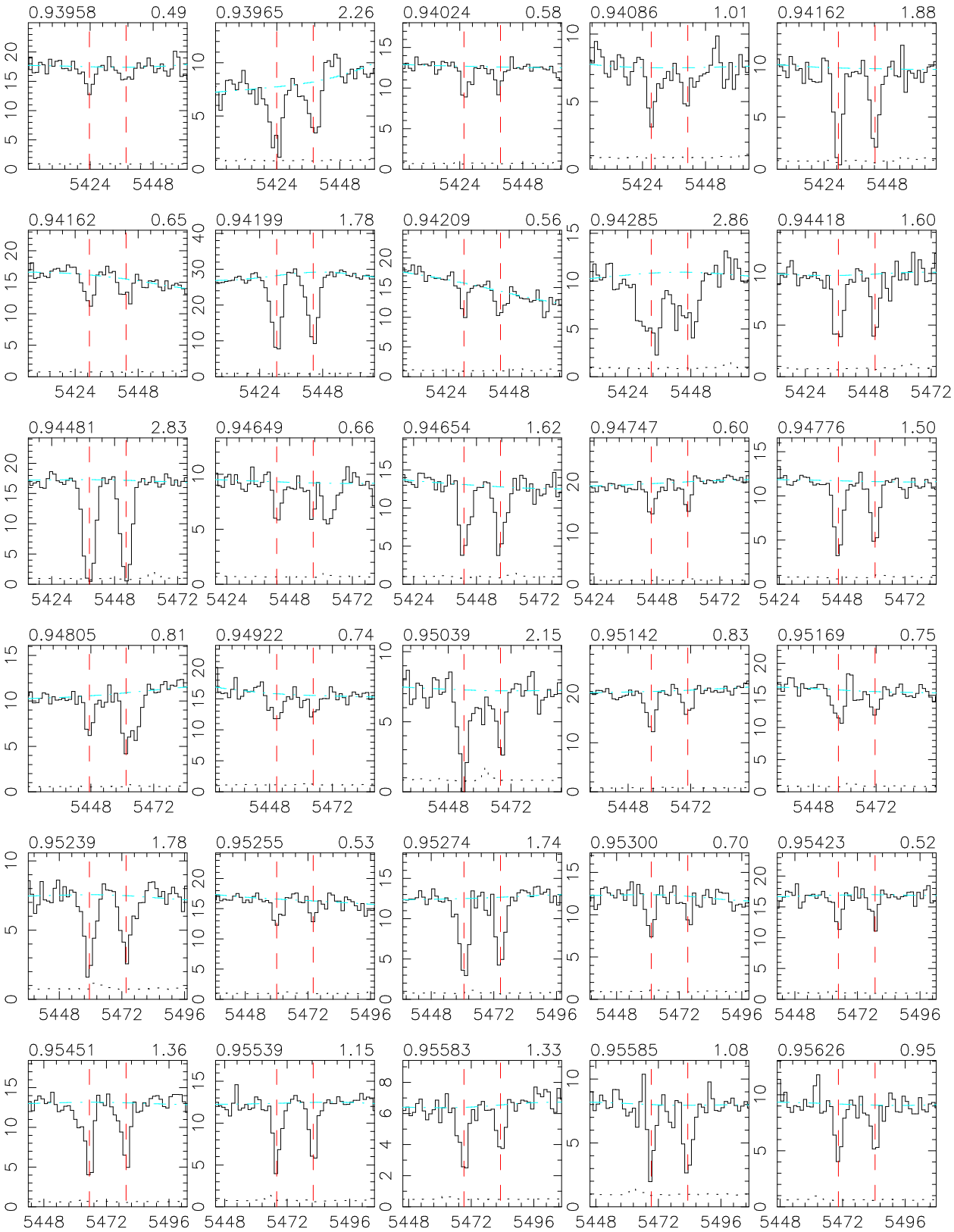
SDSS EDR
0.93958 0.49
0.93965 2.26
0.94024 0.58
0.94086 1.01
0.94162 1.88
0.94162 0.65
0.94199 1.78
0.94209 0.56
0.94285 2.86
0.94418 1.60
0.94481 2.83
0.94649 0.66
0.94654 1.62
0.94747 0.60
0.94776 1.50
0.94805 0.81
0.94922 0.74
0.95039 2.15
0.95142 0.83
0.95169 0.75
0.95239 1.78
0.95255 0.53
0.95274 1.74
0.95300 0.70
0.95423 0.52
0.95451 1.36
0.95539 1.15
0.95583 1.33
0.95585 1.08
0.95626 0.95

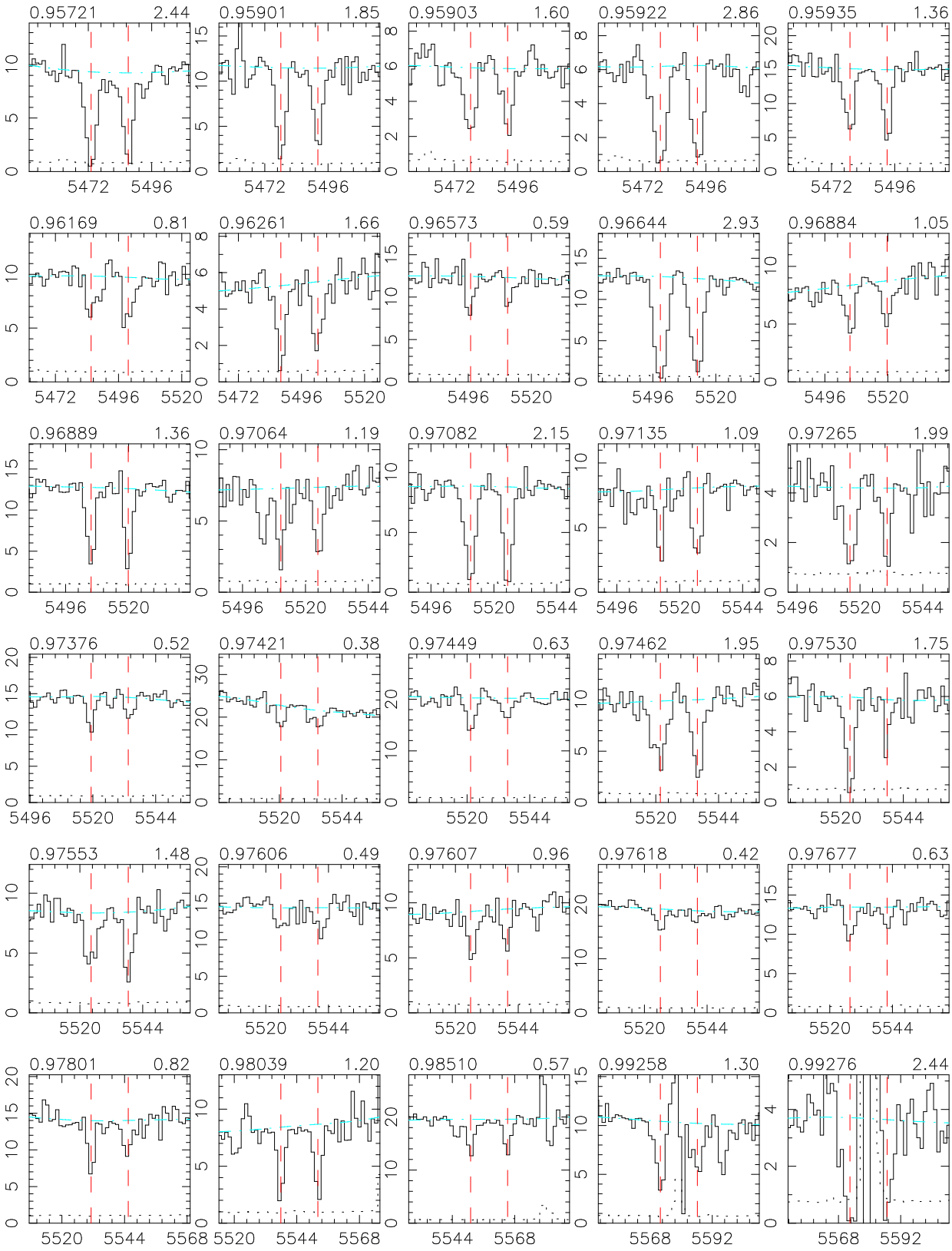
SDSS EDR
0.95721 2.44
0.95901 1.85
0.95903 1.60
0.95922 2.86
0.95935 1.36
0.96169 0.81
0.96261 1.66
0.96573 0.59
0.96644 2.93
0.96884 1.05
0.96889 1.36
0.97064 1.19
0.97082 2.15
0.97135 1.09
0.97265 1.99
0.97376 0.52
0.97421 0.38
0.97449 0.63
0.97462 1.95
0.97530 1.75
0.97553 1.48
0.97606 0.49
0.97607 0.96
0.97618 0.42
0.97677 0.63
0.97801 0.82
0.98039 1.20
0.98510 0.57
0.99258 1.30
0.99276 2.44

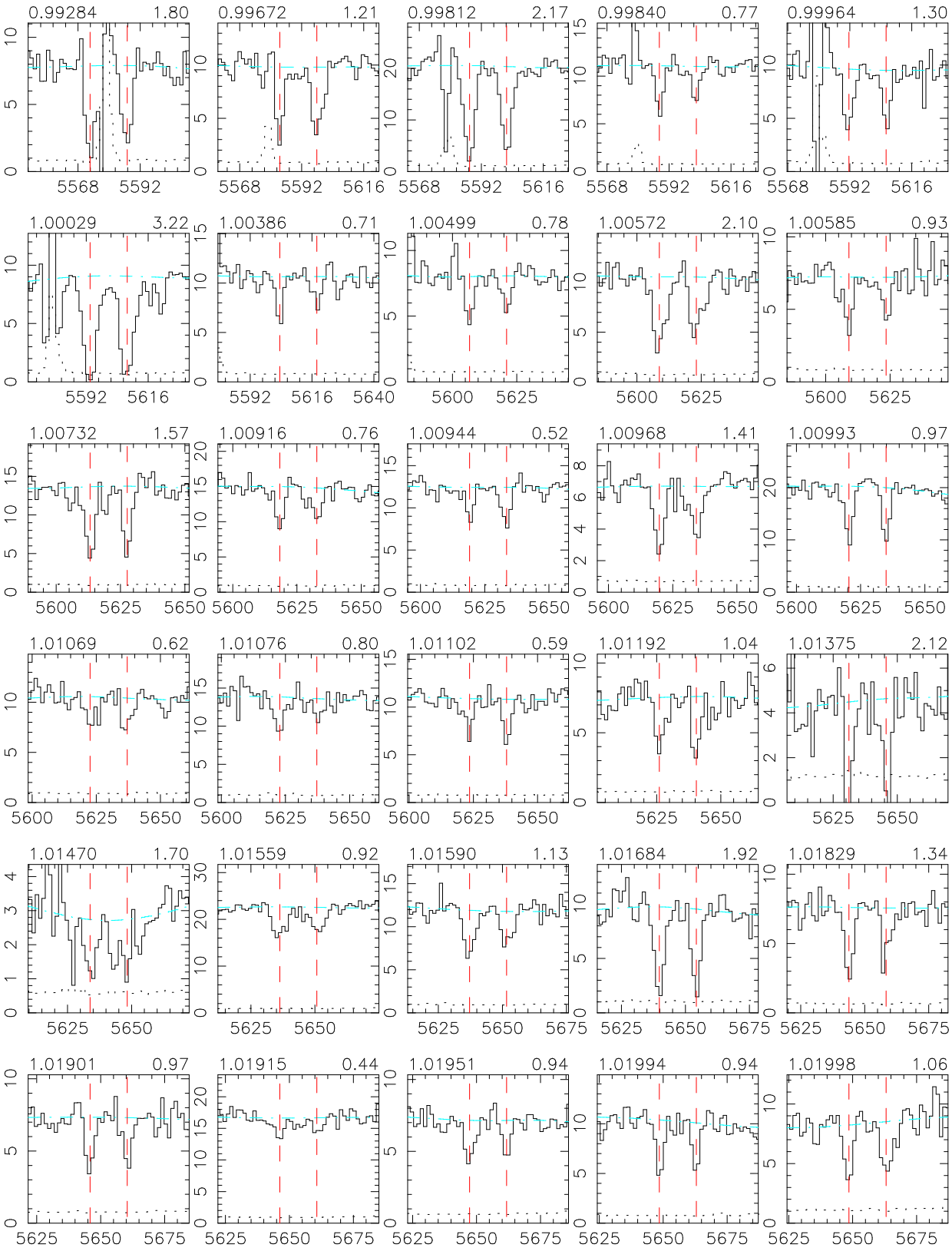
SDSS EDR
0.99284 1.80
0.99672 1.21
0.99812 2.17
0.99840 0.77
0.99964 1.30
1.00029 3.22
1.00386 0.71
1.00499 0.78
1.00572 2.10
1.00585 0.93
1.00732 1.57
1.00916 0.76
1.00944 0.52
1.00968 1.41
1.00993 0.97
1.01069 0.62
1.01076 0.80
1.01102 0.59
1.01192 1.04
1.01375 2.12
1.01470 1.70
1.01559 0.92
1.01590 1.13
1.01684 1.92
1.01829 1.34
1.01901 0.97
1.01915 0.44
1.01951 0.94
1.01994 0.94
1.01998 1.06

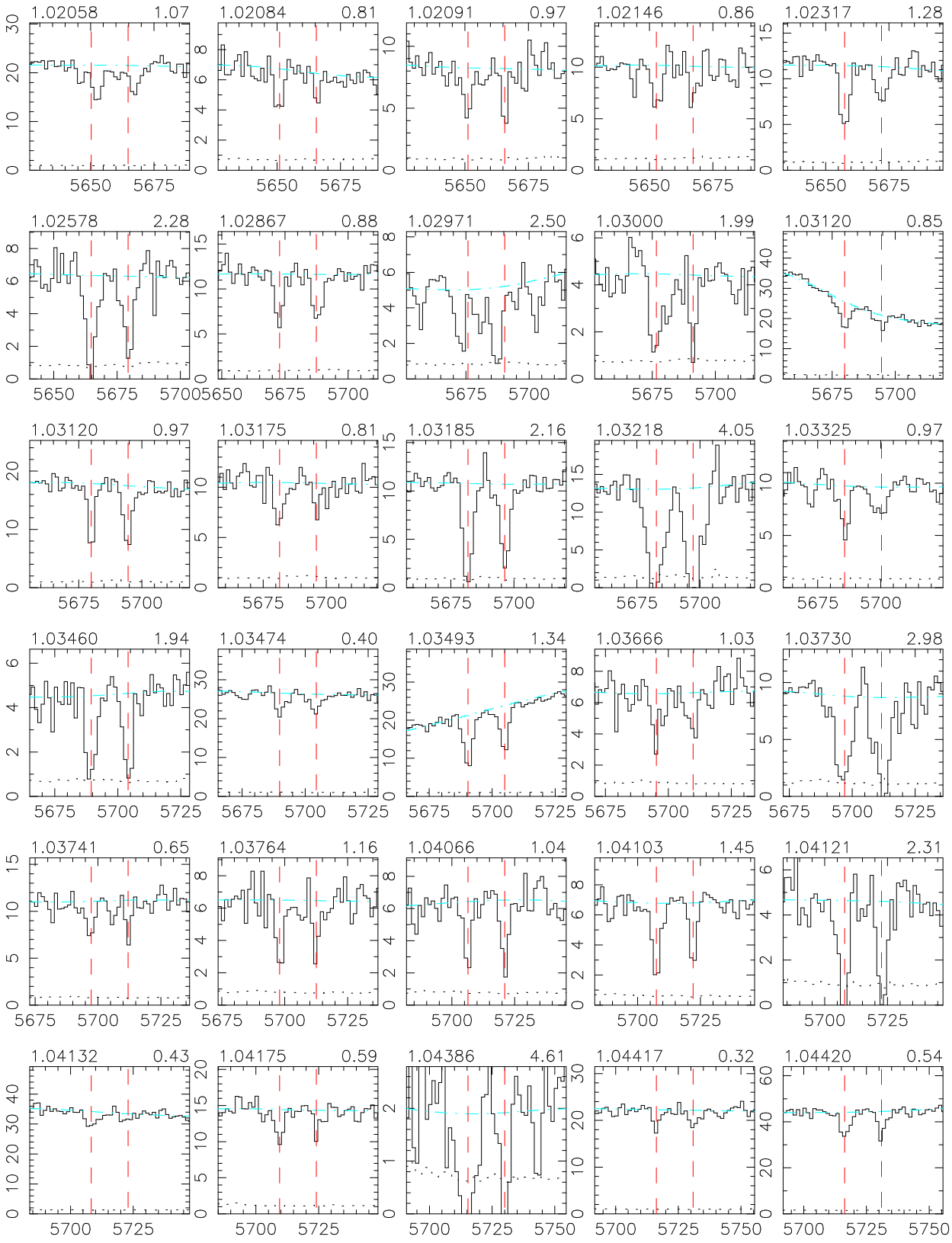
SDSS EDR
1.02058 1.07
1.02084 0.81
1.02091 0.97
1.02146 0.86
1.02317 1.28
1.02578 2.28
1.02867 0.88
1.02971 2.50
1.03000 1.99
1.03120 0.85
1.03120 0.97
1.03175 0.81
1.03185 2.16
1.03218 4.05
1.03325 0.97
1.03460 1.94
1.03474 0.40
1.03493 1.34
1.03666 1.03
1.03730 2.98
1.03741 0.65
1.03764 1.16
1.04066 1.04
1.04103 1.45
1.04121 2.31
1.04132 0.43
1.04175 0.59
1.04386 4.61
1.04417 0.32
1.04420 0.54

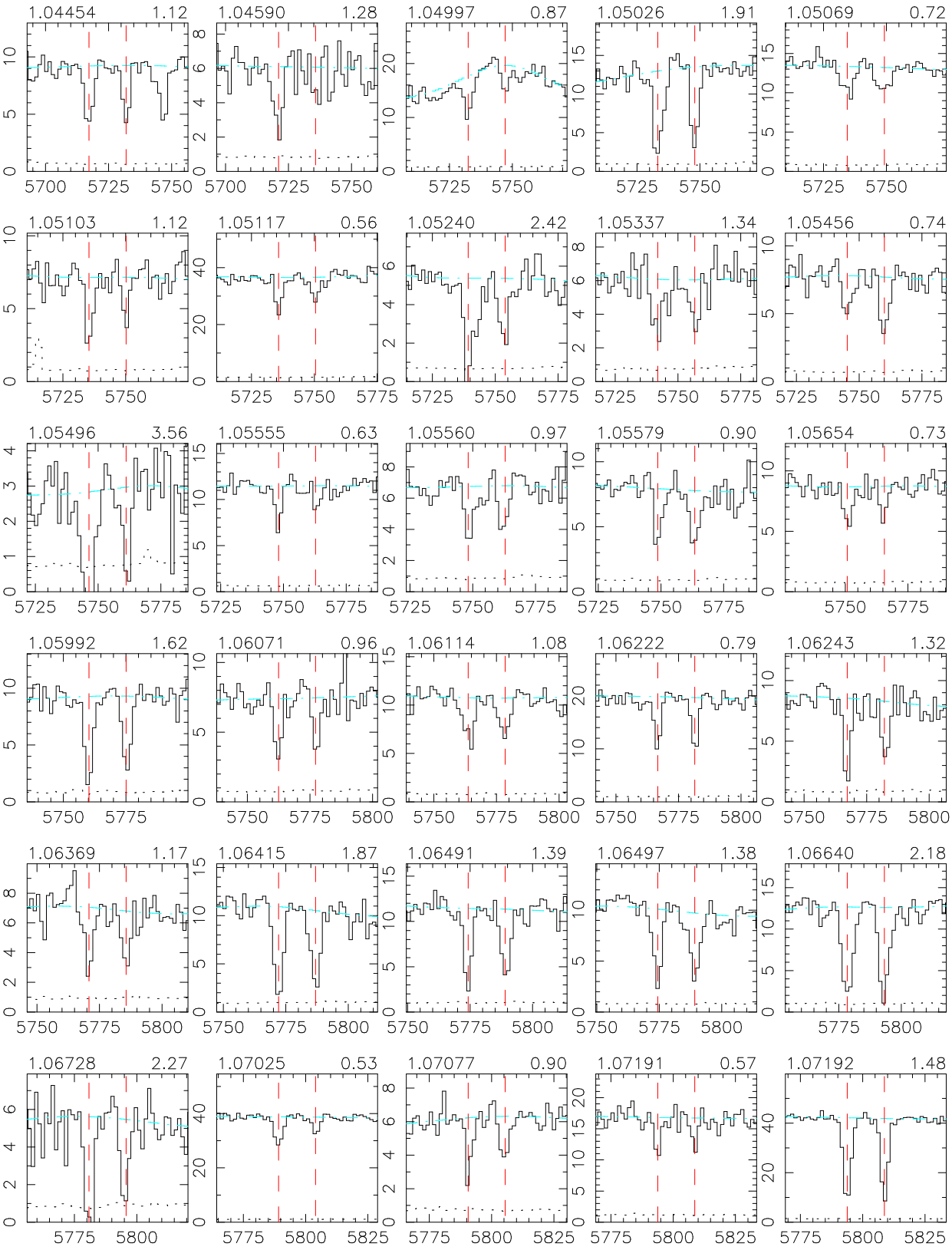
SDSS EDR
1.04454 1.12
1.04590 1.28
1.04997 0.87
1.05026 1.91
1.05069 0.72
1.05103 1.12
1.05117 0.56
1.05240 2.42
1.05337 1.34
1.05456 0.74
1.05496 3.56
1.05555 0.63
1.05560 0.97
1.05579 0.90
1.05654 0.73
1.05992 1.62
1.06071 0.96
1.06114 1.08
1.06222 0.79
1.06243 1.32
1.06369 1.17
1.06415 1.87
1.06491 1.39
1.06497 1.38
1.06640 2.18
1.06728 2.27
1.07025 0.53
1.07077 0.90
1.07191 0.57
1.07192 1.48

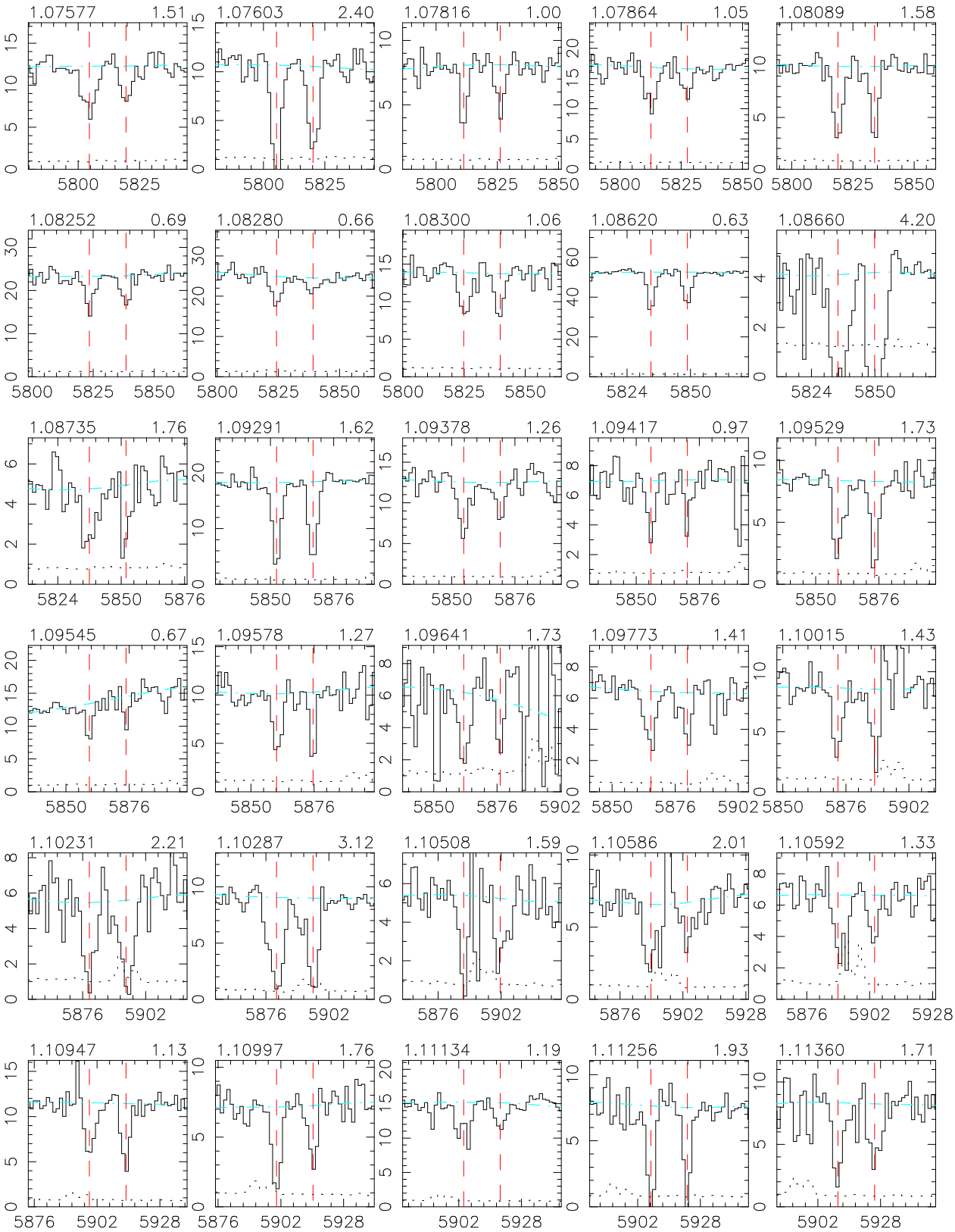
SDSS EDR
1.07577 1.51
1.07603 2.40
1.07816 1.00
1.07864 1.05
1.08089 1.58
1.08252 0.69
1.08280 0.66
1.08300 1.06
1.08620 0.63
1.08660 4.20
1.08735 1.76
1.09291 1.62
1.09378 1.26
1.09417 0.97
1.09529 1.73
1.09545 0.67
1.09578 1.27
1.09641 1.73
1.09773 1.41
1.10015 1.43
1.10231 2.21
1.10287 3.12
1.10508 1.59
1.10586 2.01
1.10592 1.33
1.10947 1.13
1.10997 1.76
1.11134 1.19
1.11256 1.93
1.11360 1.71

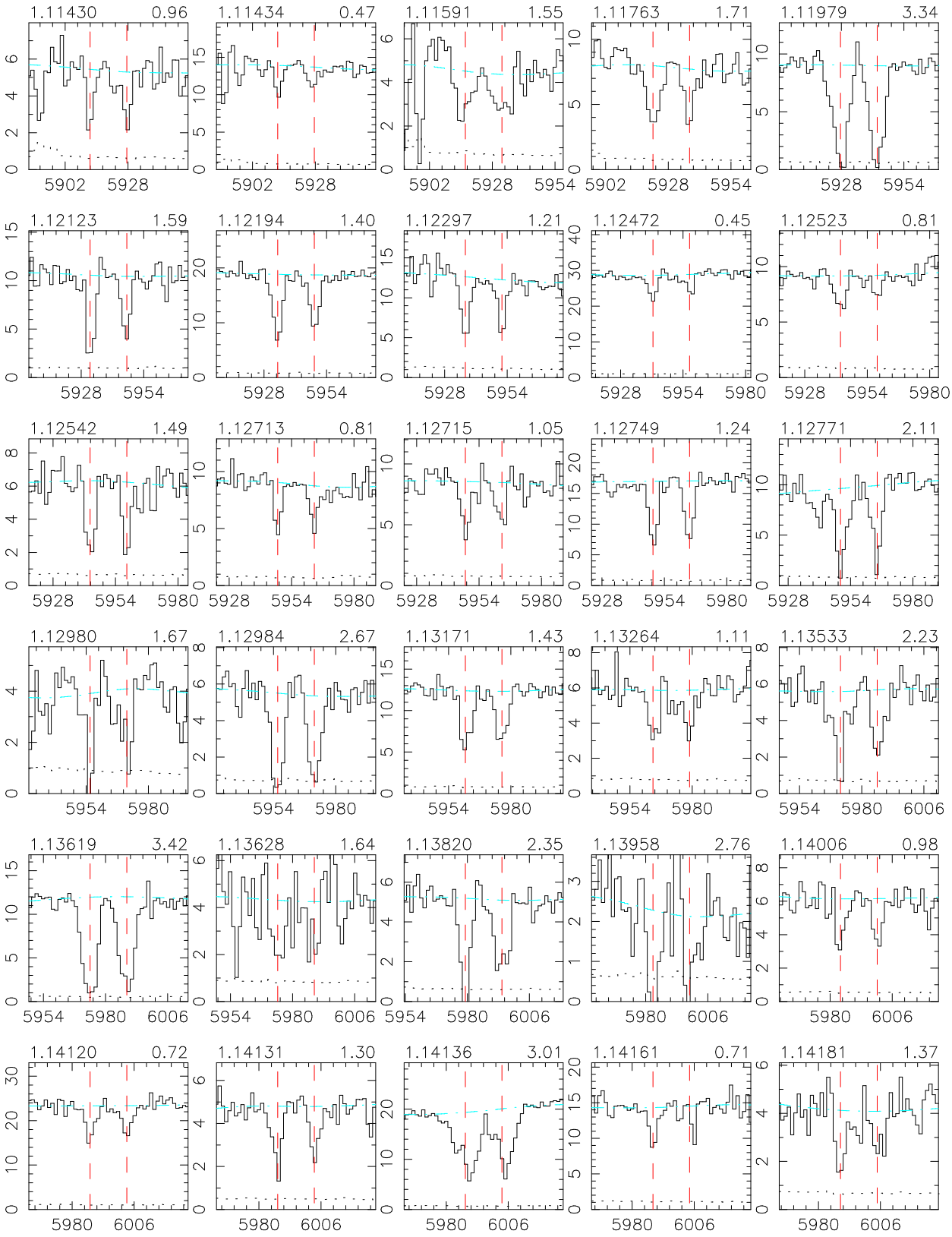
SDSS EDR
1.11430 0.96
1.11434 0.47
1.11591 1.55
1.11763 1.71
1.11979 3.34
1.12123 1.59
1.12194 1.40
1.12297 1.21
1.12472 0.45
1.12523 0.81
1.12542 1.49
1.12713 0.81
1.12715 1.05
1.12749 1.24
1.12771 2.11
1.12980 1.67
1.12984 2.67
1.13171 1.43
1.13264 1.11
1.13533 2.23
1.13619 3.42
1.13628 1.64
1.13820 2.35
1.13958 2.76
1.14006 0.98
1.14120 0.72
1.14131 1.30
1.14136 3.01
1.14161 0.71
1.14181 1.37

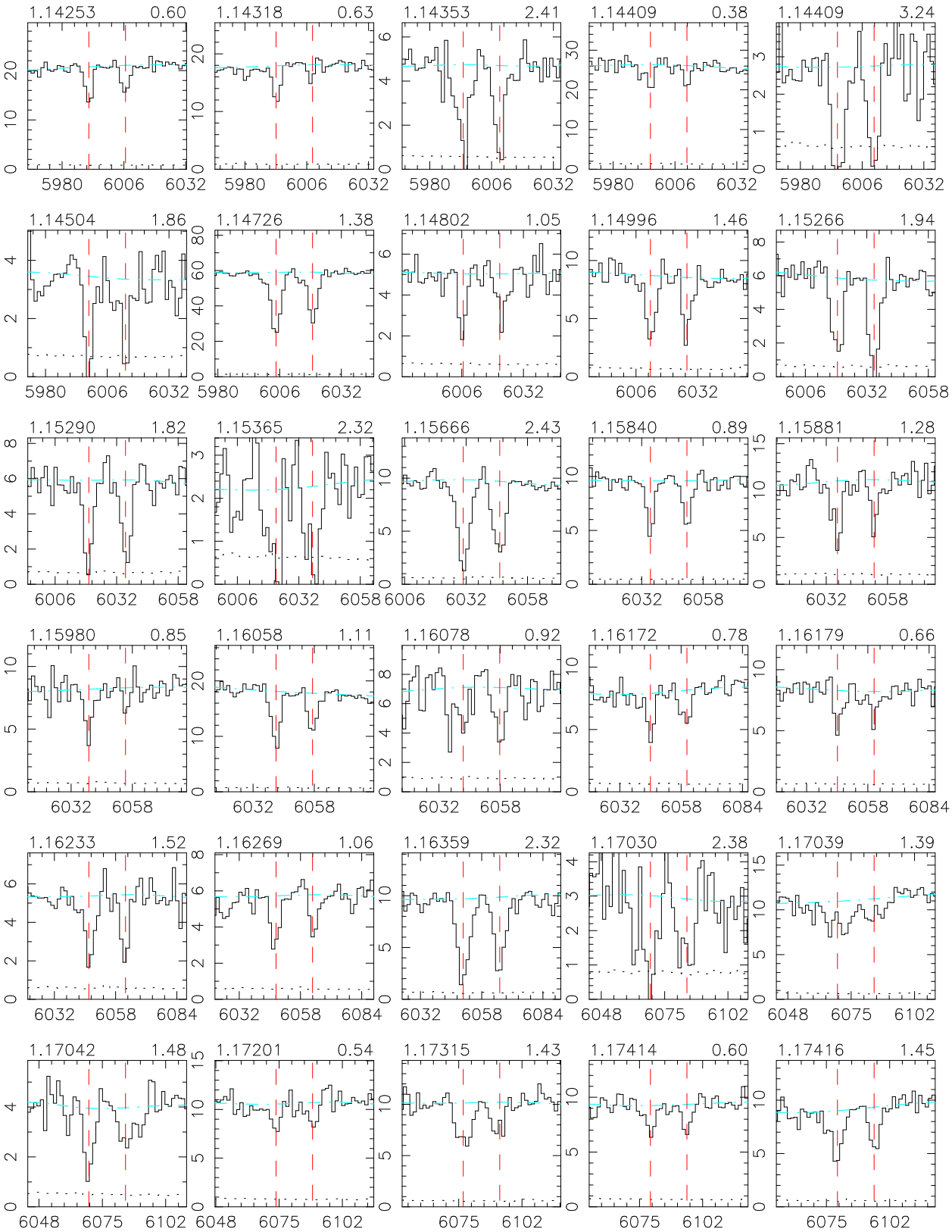
SDSS EDR
1.14253 0.60
1.14318 0.63
1.14353 2.41
1.14409 0.38
1.14409 3.24
1.14504 1.86
1.14726 1.38
1.14802 1.05
1.14996 1.46
1.15266 1.94
1.15290 1.82
1.15365 2.32
1.15666 2.43
1.15840 0.89
1.15881 1.28
1.15980 0.85
1.16058 1.11
1.16078 0.92
1.16172 0.78
1.16179 0.66
1.16233 1.52
1.16269 1.06
1.16359 2.32
1.17030 2.38
1.17039 1.39
1.17042 1.48
1.17201 0.54
1.17315 1.43
1.17414 0.60
1.17416 1.45

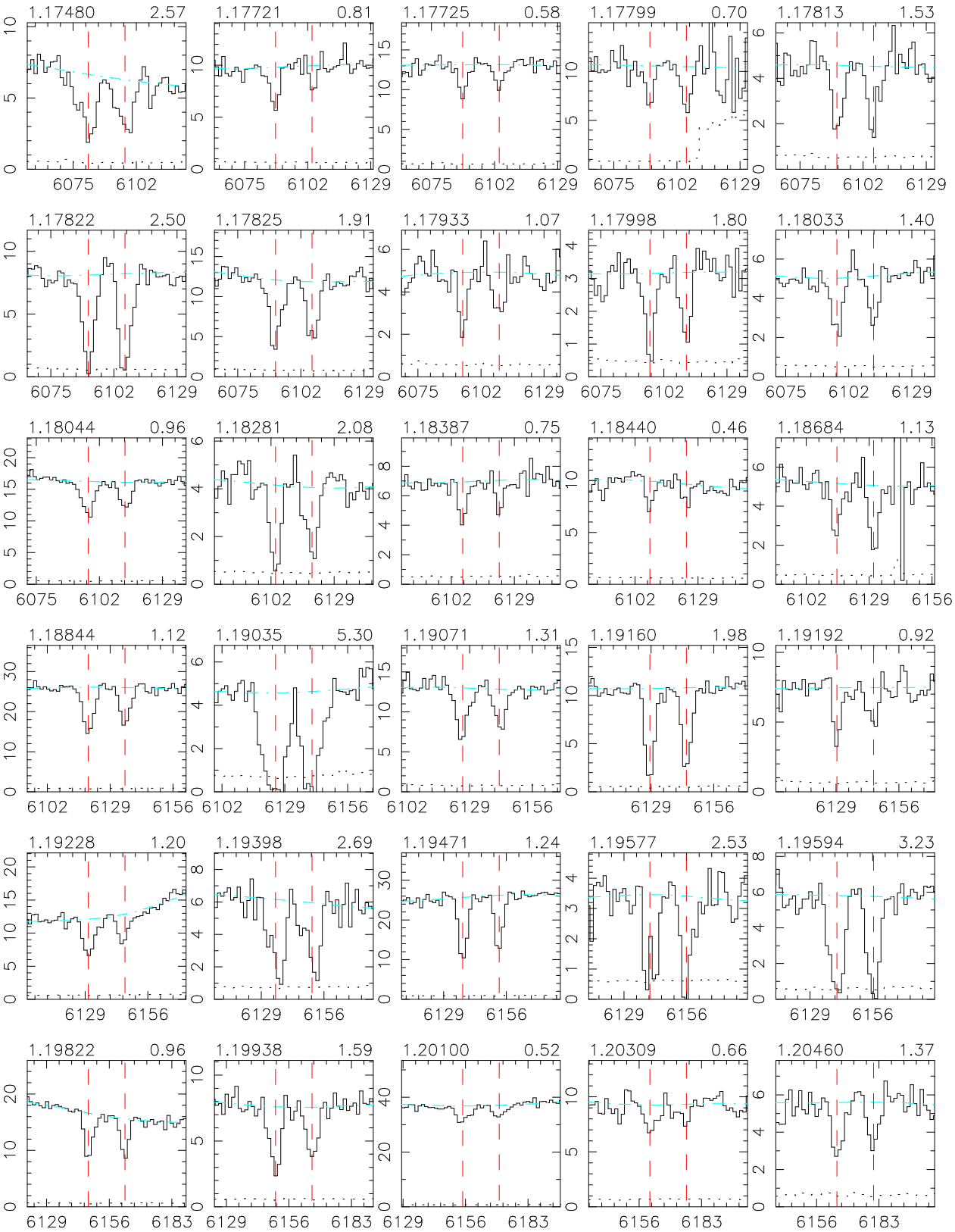
SDSS EDR
1.17480 2.57
1.17721 0.81
1.17725 0.58
1.17799 0.70
1.17813 1.53
1.17822 2.50
1.17825 1.91
1.17933 1.07
1.17998 1.80
1.18033 1.40
1.18044 0.96
1.18281 2.08
1.18387 0.75
1.18440 0.46
1.18684 1.13
1.18844 1.12
1.19035 5.30
1.19071 1.31
1.19160 1.98
1.19192 0.92
1.19228 1.20
1.19398 2.69
1.19471 1.24
1.19577 2.53
1.19594 3.23
1.19822 0.96
1.19938 1.59
1.20100 0.52
1.20309 0.66
1.20460 1.37

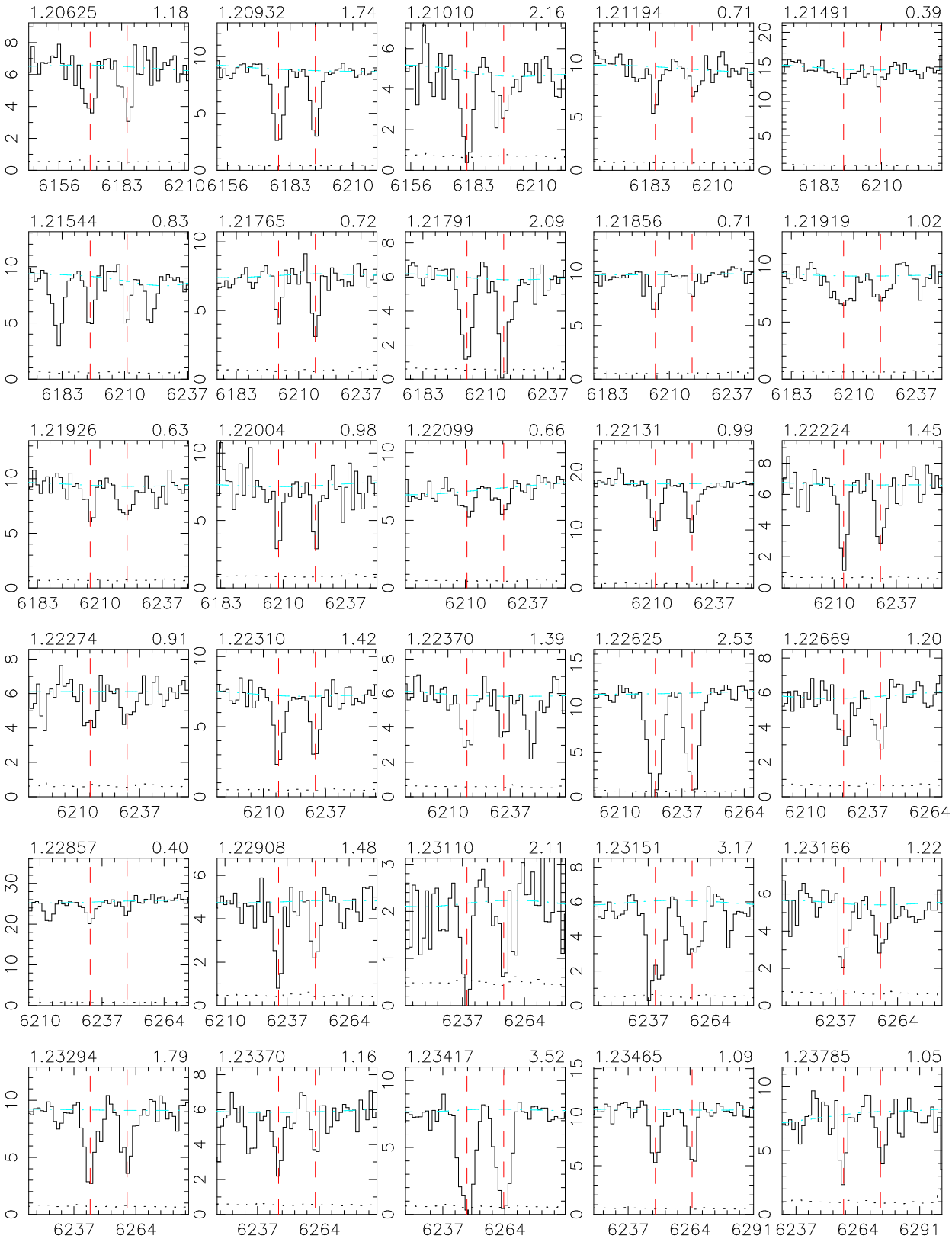
SDSS EDR
1.20625 1.18
1.20932 1.74
1.21010 2.16
1.21194 0.71
1.21491 0.39
1.21544 0.83
1.21765 0.72
1.21791 2.09
1.21856 0.71
1.21919 1.02
1.21926 0.63
1.22004 0.98
1.22099 0.66
1.22131 0.99
1.22224 1.45
1.22274 0.91
1.22310 1.42
1.22370 1.39
1.22625 2.53
1.22669 1.20
1.22857 0.40
1.22908 1.48
1.23110 2.11
1.23151 3.17
1.23166 1.22
1.23294 1.79
1.23370 1.16
1.23417 3.52
1.23465 1.09
1.23785 1.05

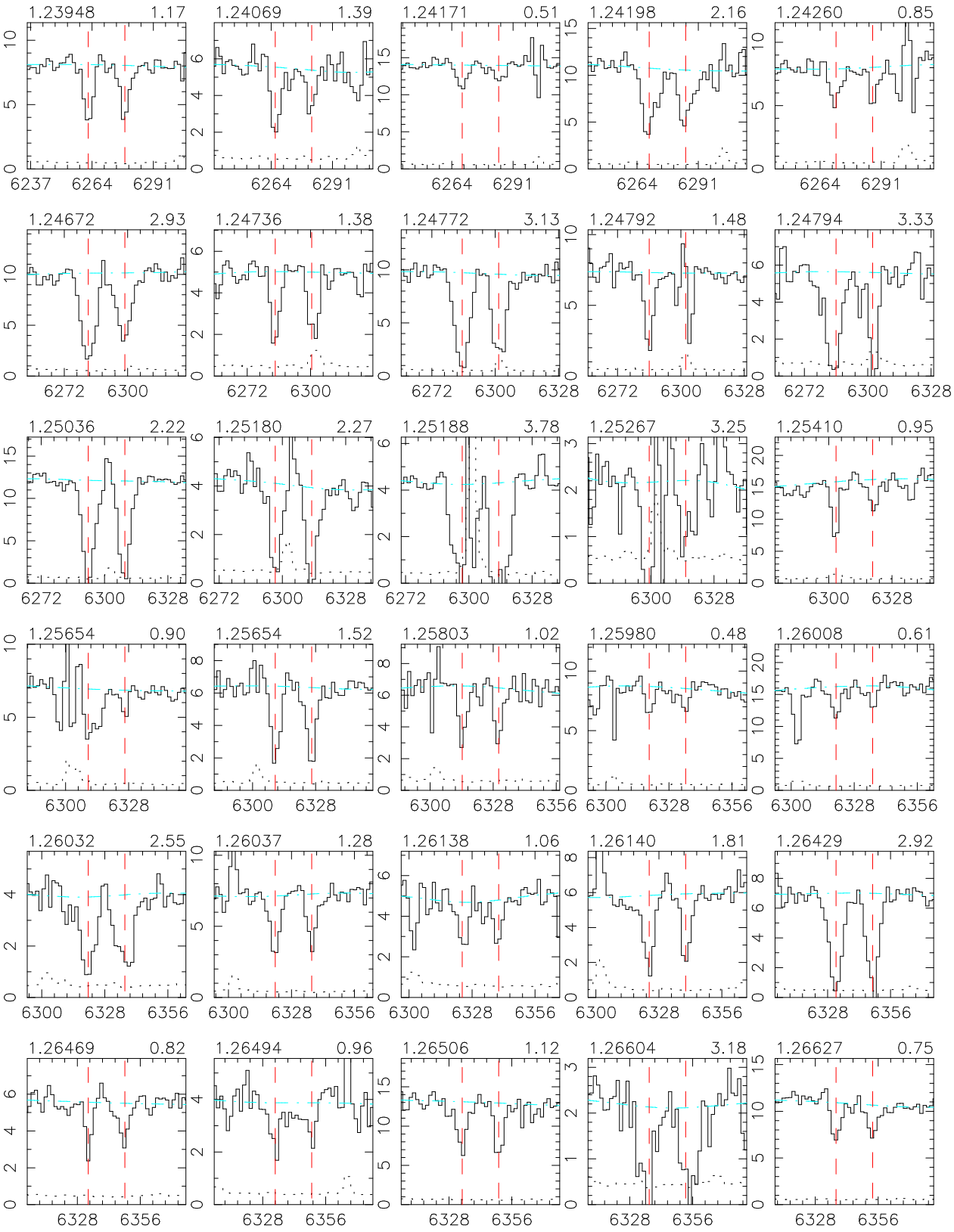
SDSS EDR
1.23948 1.17
1.24069 1.39
1.24171 0.51
1.24198 2.16
1.24260 0.85
1.24672 2.93
1.24736 1.38
1.24772 3.13
1.24792 1.48
1.24794 3.33
1.25036 2.22
1.25180 2.27
1.25188 3.78
1.25267 3.25
1.25410 0.95
1.25654 0.90
1.25654 1.52
1.25803 1.02
1.25980 0.48
1.26008 0.61
1.26032 2.55
1.26037 1.28
1.26138 1.06
1.26140 1.81
1.26429 2.92
1.26469 0.82
1.26494 0.96
1.26506 1.12
1.26604 3.18
1.26627 0.75

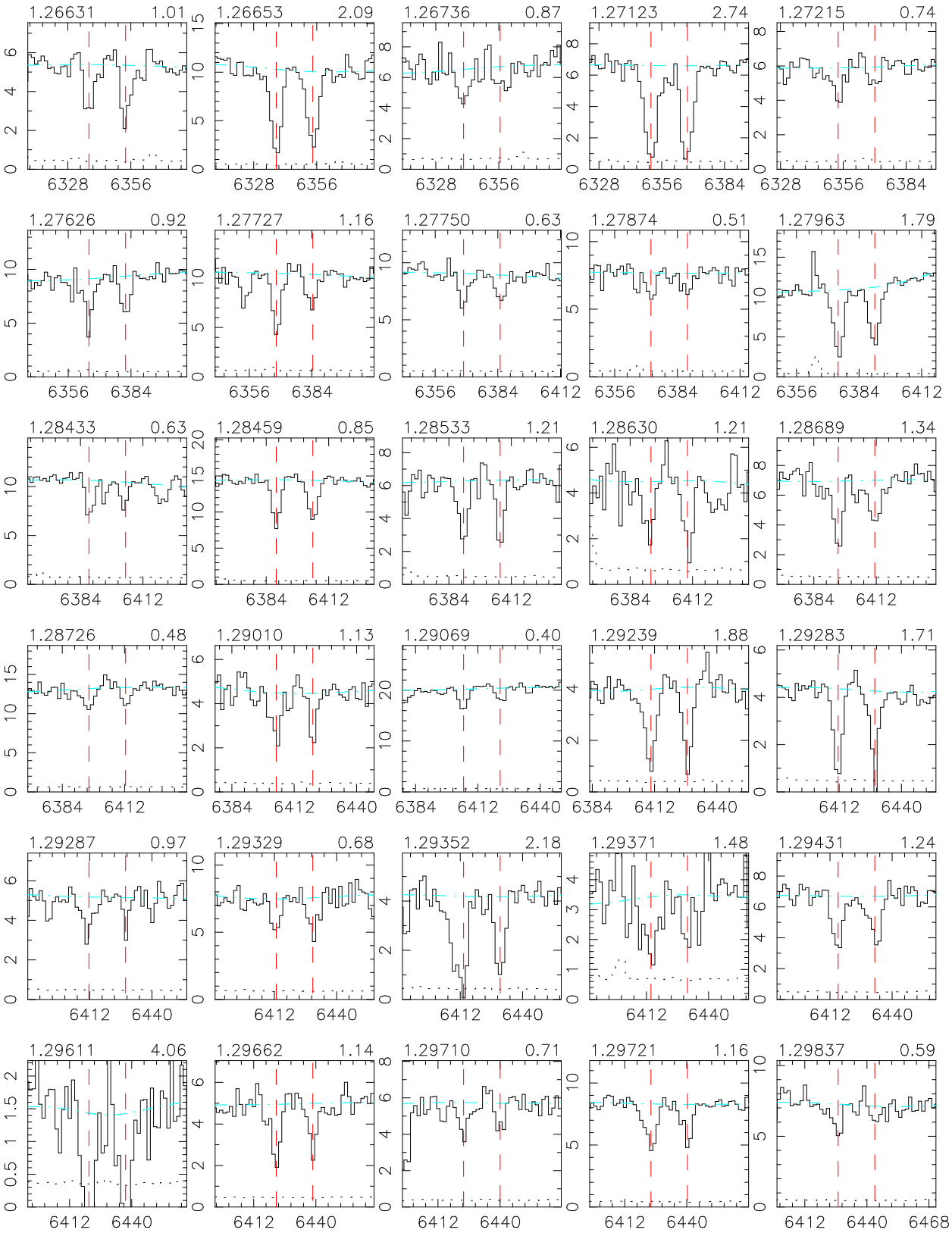
SDSS EDR
1.26631 1.01
1.26653 2.09
1.26736 0.87
1.27123 2.74
1.27215 0.74
1.27626 0.92
1.27727 1.16
1.27750 0.63
1.27874 0.51
1.27963 1.79
1.28433 0.63
1.28459 0.85
1.28533 1.21
1.28630 1.21
1.28689 1.34
1.28726 0.48
1.29010 1.13
1.29069 0.40
1.29239 1.88
1.29283 1.71
1.29287 0.97
1.29329 0.68
1.29352 2.18
1.29371 1.48
1.29431 1.24
1.29611 4.06
1.29662 1.14
1.29710 0.71
1.29721 1.16
1.29837 0.59

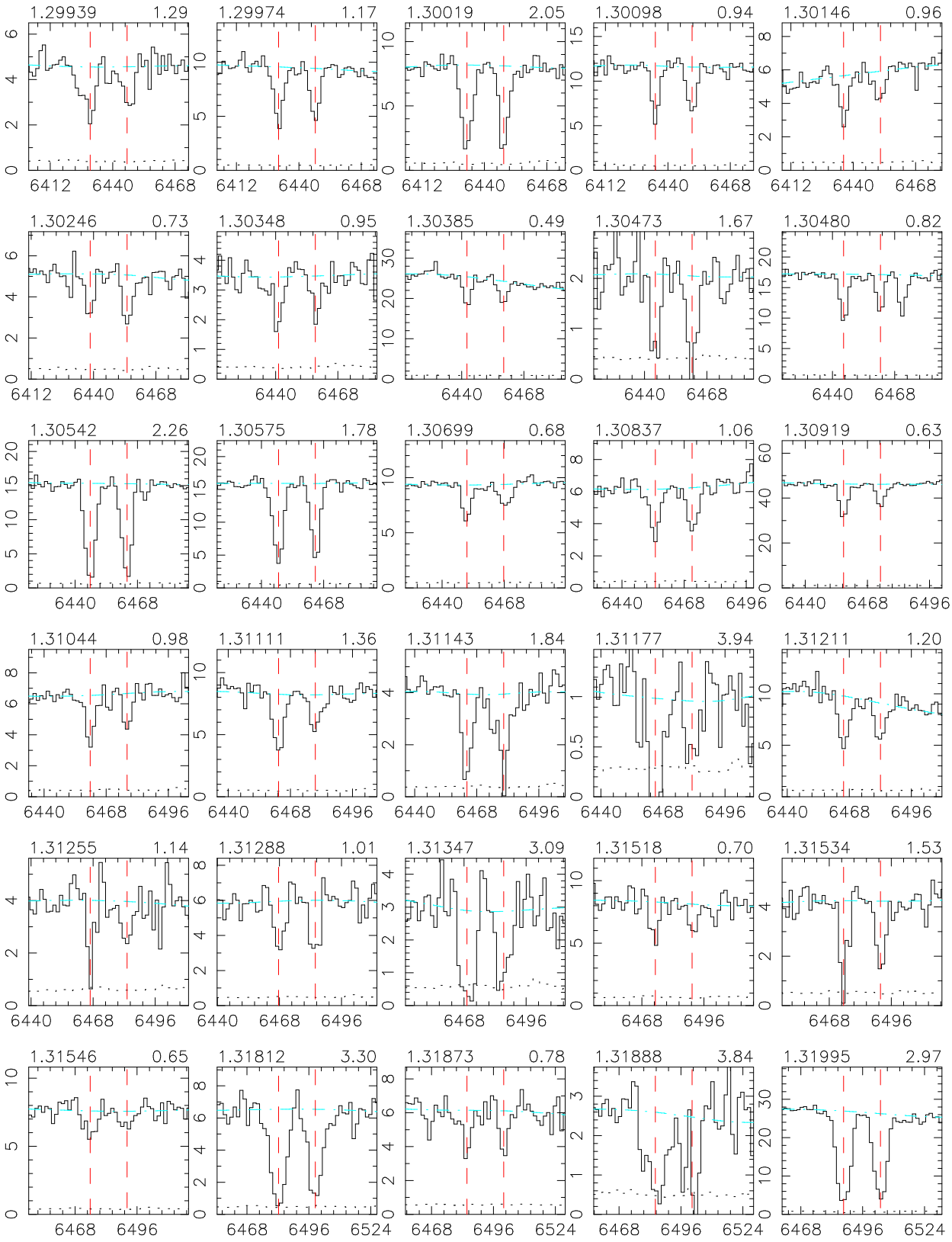
SDSS EDR
1.29939 1.29
1.29974 1.17
1.30019 2.05
1.30098 0.94
1.30146 0.96
1.30246 0.73
1.30348 0.95
1.30385 0.49
1.30473 1.67
1.30480 0.82
1.30542 2.26
1.30575 1.78
1.30699 0.68
1.30837 1.06
1.30919 0.63
1.31044 0.98
1.31111 1.36
1.31143 1.84
1.31177 3.94
1.31211 1.20
1.31255 1.14
1.31288 1.01
1.31347 3.09
1.31518 0.70
1.31534 1.53
1.31546 0.65
1.31812 3.30
1.31873 0.78
1.31888 3.84
1.31995 2.97

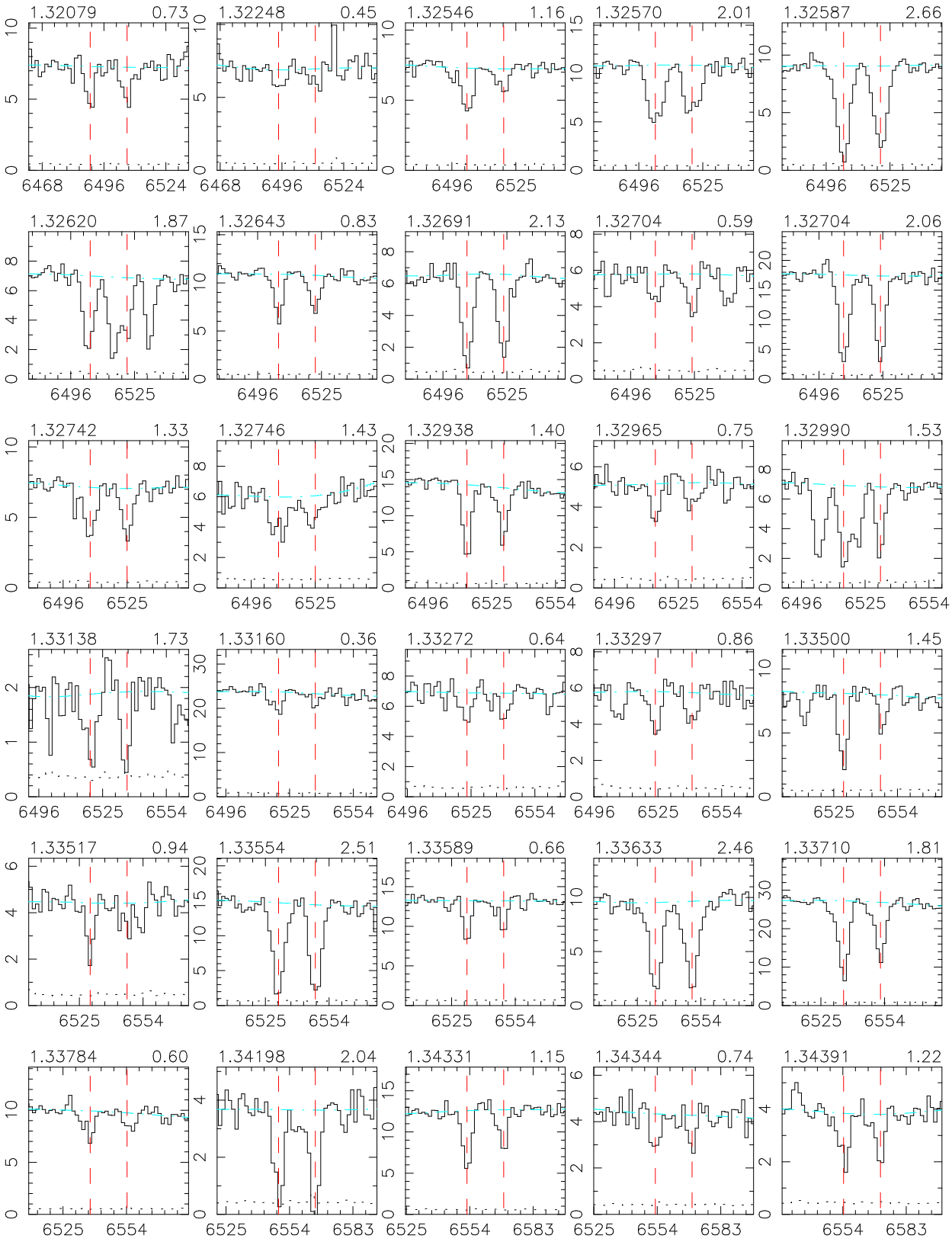
SDSS EDR
1.32079 0.73
1.32248 0.45
1.32546 1.16
1.32570 2.01
1.32587 2.66
1.32620 1.87
1.32643 0.83
1.32691 2.13
1.32704 0.59
1.32704 2.06
1.32742 1.33
1.32746 1.43
1.32938 1.40
1.32965 0.75
1.32990 1.53
1.33138 1.73
1.33160 0.36
1.33272 0.64
1.33297 0.86
1.33500 1.45
1.33517 0.94
1.33554 2.51
1.33589 0.66
1.33633 2.46
1.33710 1.81
1.33784 0.60
1.34198 2.04
1.34331 1.15
1.34344 0.74
1.34391 1.22

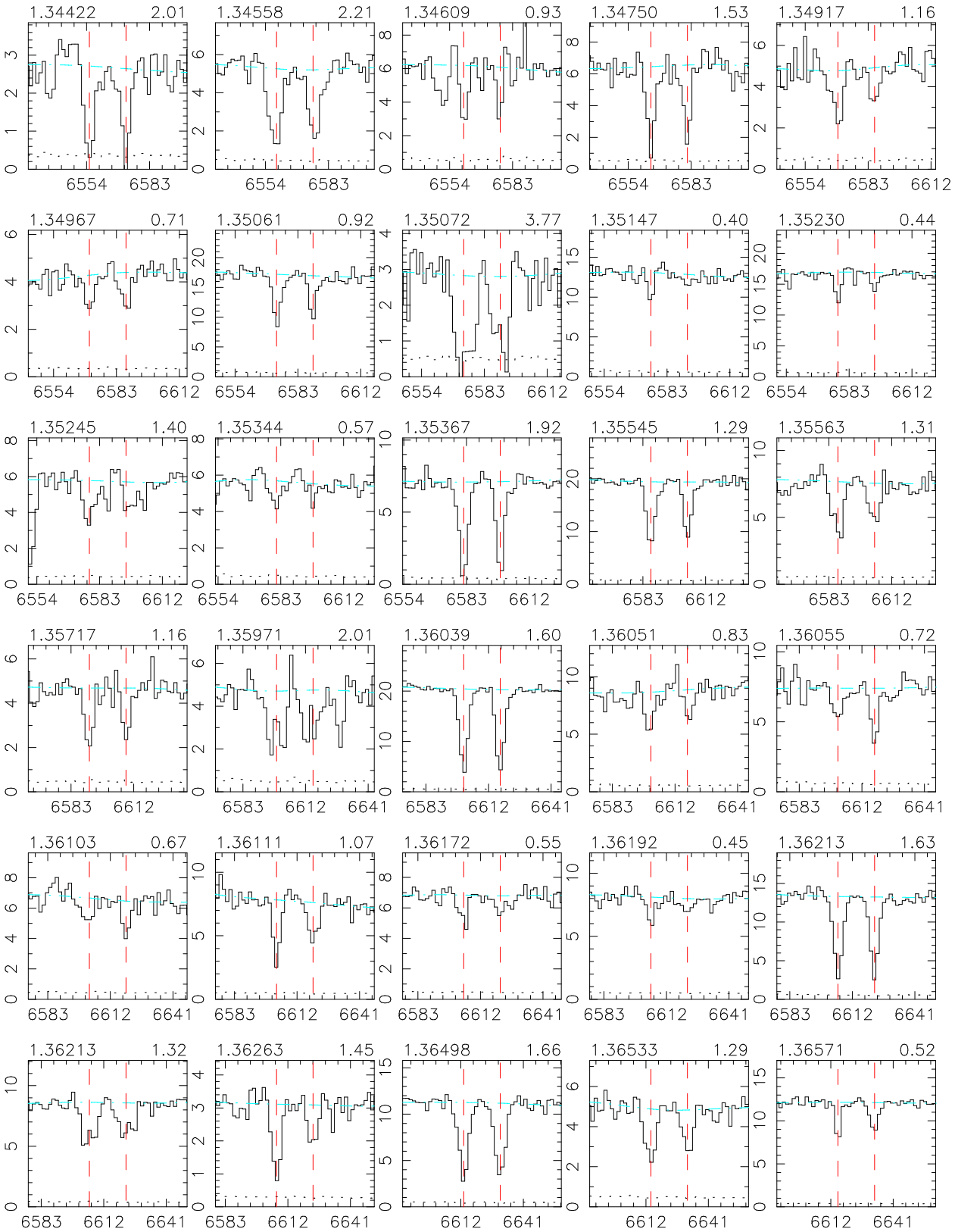
SDSS EDR
1.34422 2.01
1.34558 2.21
1.34609 0.93
1.34750 1.53
1.34917 1.16
1.34967 0.71
1.35061 0.92
1.35072 3.77
1.35147 0.40
1.35230 0.44
1.35245 1.40
1.35344 0.57
1.35367 1.92
1.35545 1.29
1.35563 1.31
1.35717 1.16
1.35971 2.01
1.36039 1.60
1.36051 0.83
1.36055 0.72
1.36103 0.67
1.36111 1.07
1.36172 0.55
1.36192 0.45
1.36213 1.63
1.36213 1.32
1.36263 1.45
1.36498 1.66
1.36533 1.29
1.36571 0.52

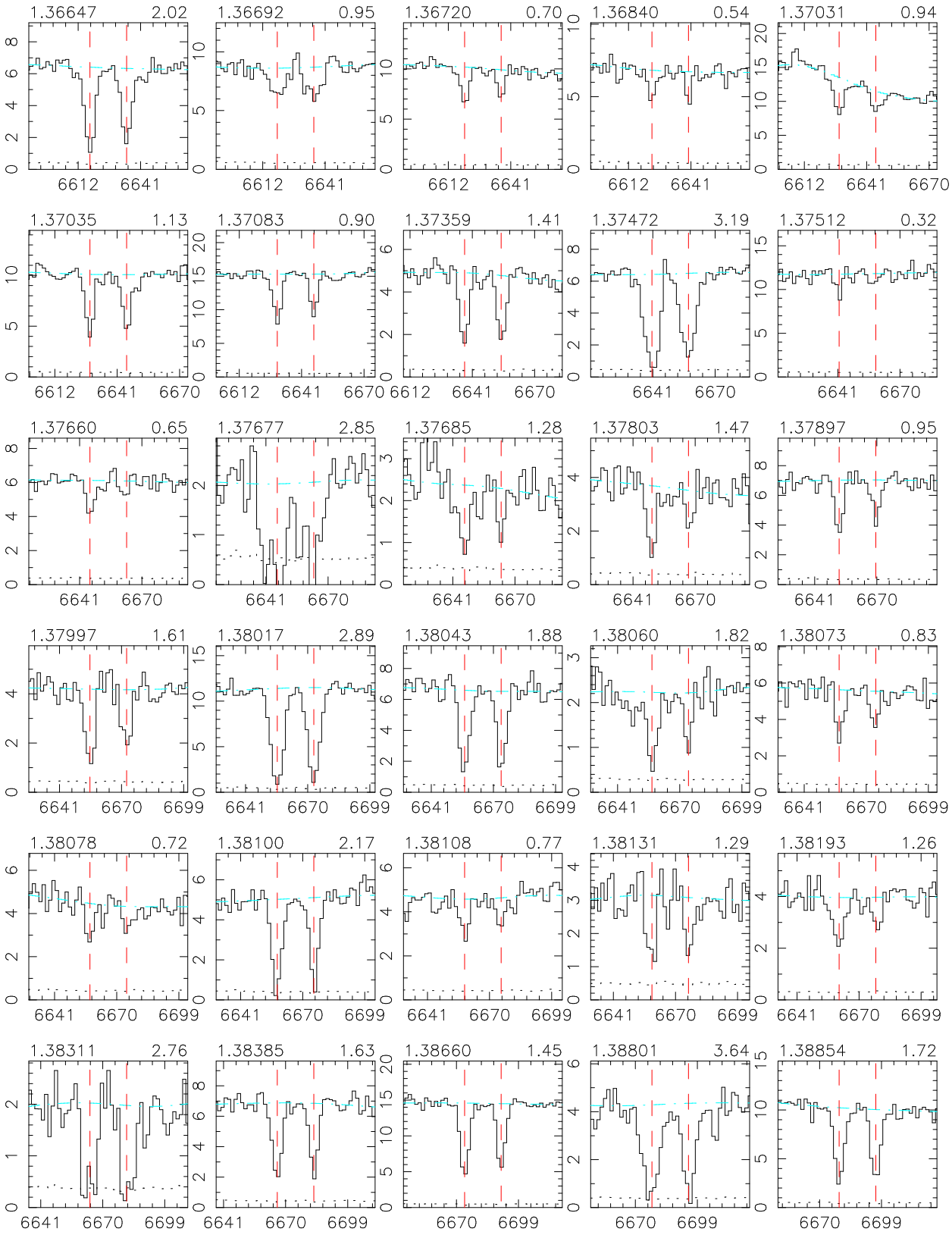
SDSS EDR
1.36647 2.02
1.36692 0.95
1.36720 0.70
1.36840 0.54
1.37031 0.94
1.37035 1.13
1.37083 0.90
1.37359 1.41
1.37472 3.19
1.37512 0.32
1.37660 0.65
1.37677 2.85
1.37685 1.28
1.37803 1.47
1.37897 0.95
1.37997 1.61
1.38017 2.89
1.38043 1.88
1.38060 1.82
1.38073 0.83
1.38078 0.72
1.38100 2.17
1.38108 0.77
1.38131 1.29
1.38193 1.26
1.38311 2.76
1.38385 1.63
1.38660 1.45
1.38801 3.64
1.38854 1.72

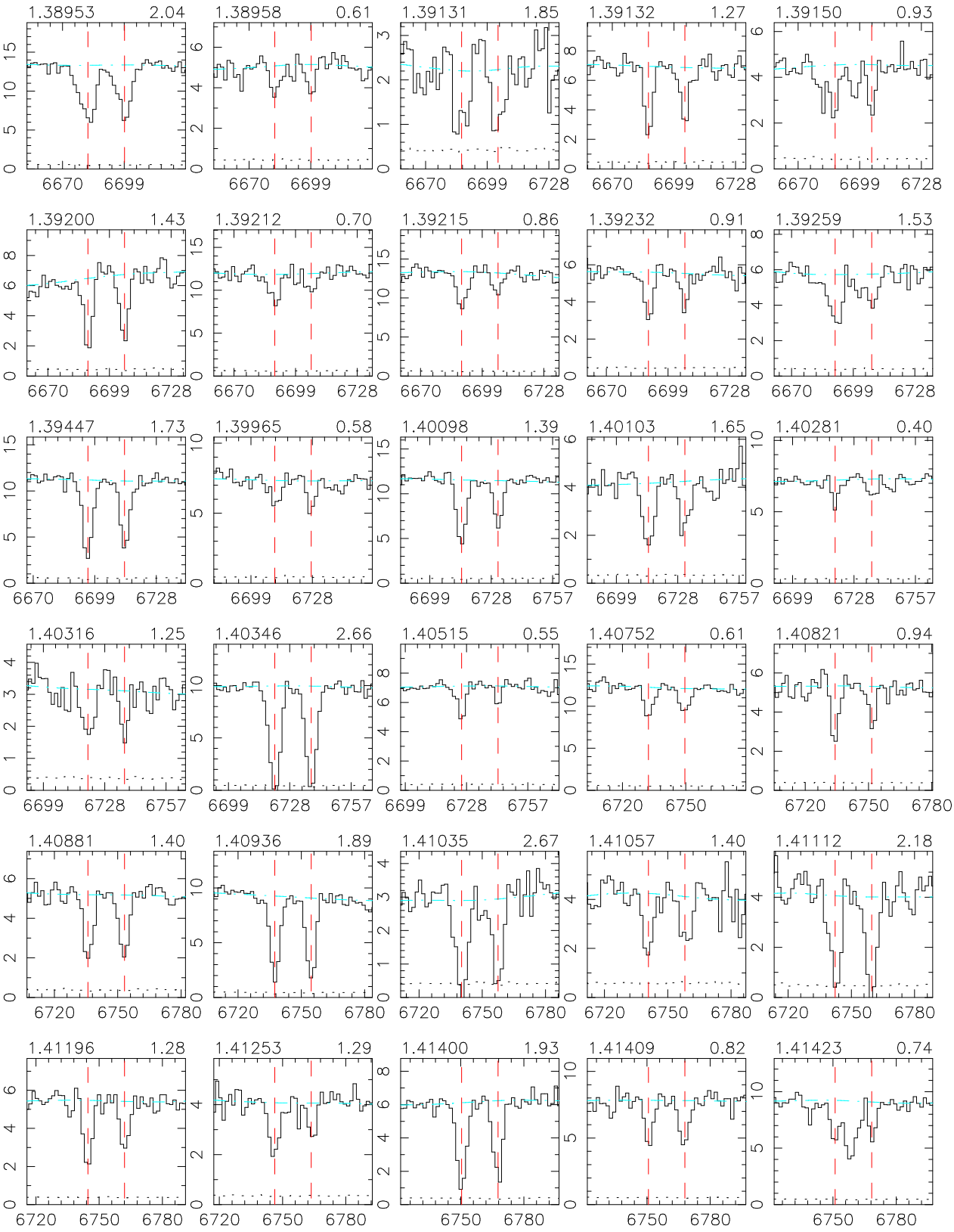
SDSS EDR
1.38953 2.04
1.38958 0.61
1.39131 1.85
1.39132 1.27
1.39150 0.93
1.39200 1.43
1.39212 0.70
1.39215 0.86
1.39232 0.91
1.39259 1.53
1.39447 1.73
1.39965 0.58
1.40098 1.39
1.40103 1.65
1.40281 0.40
1.40316 1.25
1.40346 2.66
1.40515 0.55
1.40752 0.61
1.40821 0.94
1.40881 1.40
1.40936 1.89
1.41035 2.67
1.41057 1.40
1.41112 2.18
1.41196 1.28
1.41253 1.29
1.41400 1.93
1.41409 0.82
1.41423 0.74

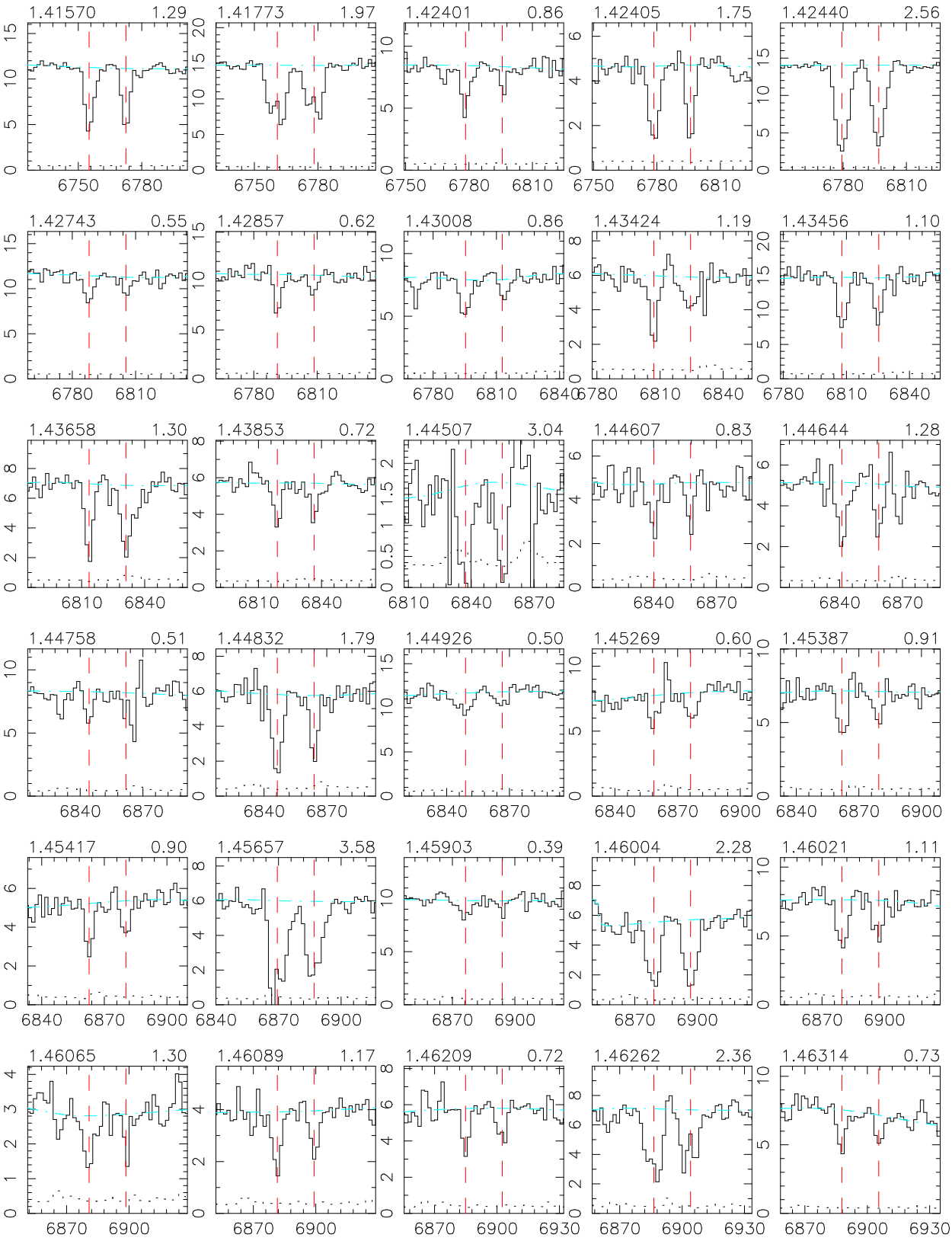
SDSS EDR
1.41570 1.29
1.41773 1.97
1.42401 0.86
1.42405 1.75
1.42440 2.56
1.42743 0.55
1.42857 0.62
1.43008 0.86
1.43424 1.19
1.43456 1.10
1.43658 1.30
1.43853 0.72
1.44507 3.04
1.44607 0.83
1.44644 1.28
1.44758 0.51
1.44832 1.79
1.44926 0.50
1.45269 0.60
1.45387 0.91
1.45417 0.90
1.45657 3.58
1.45903 0.39
1.46004 2.28
1.46021 1.11
1.46065 1.30
1.46089 1.17
1.46209 0.72
1.46262 2.36
1.46314 0.73

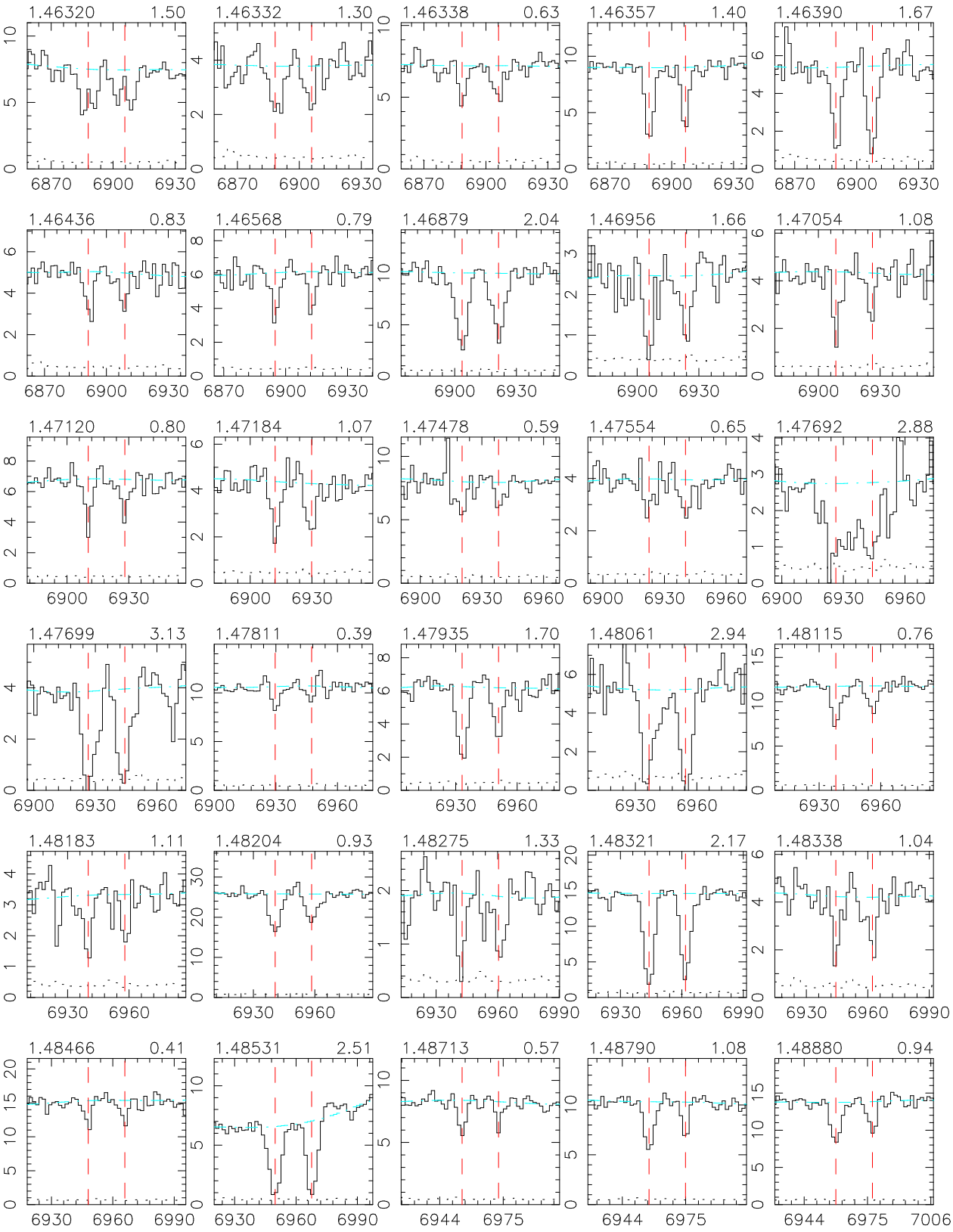
SDSS EDR
1.46320 1.50
1.46332 1.30
1.46338 0.63
1.46357 1.40
1.46390 1.67
1.46436 0.83
1.46568 0.79
1.46879 2.04
1.46956 1.66
1.47054 1.08
1.47120 0.80
1.47184 1.07
1.47478 0.59
1.47554 0.65
1.47692 2.88
1.47699 3.13
1.47811 0.39
1.47935 1.70
1.48061 2.94
1.48115 0.76
1.48183 1.11
1.48204 0.93
1.48275 1.33
1.48321 2.17
1.48338 1.04
1.48466 0.41
1.48531 2.51
1.48713 0.57
1.48790 1.08
1.48880 0.94

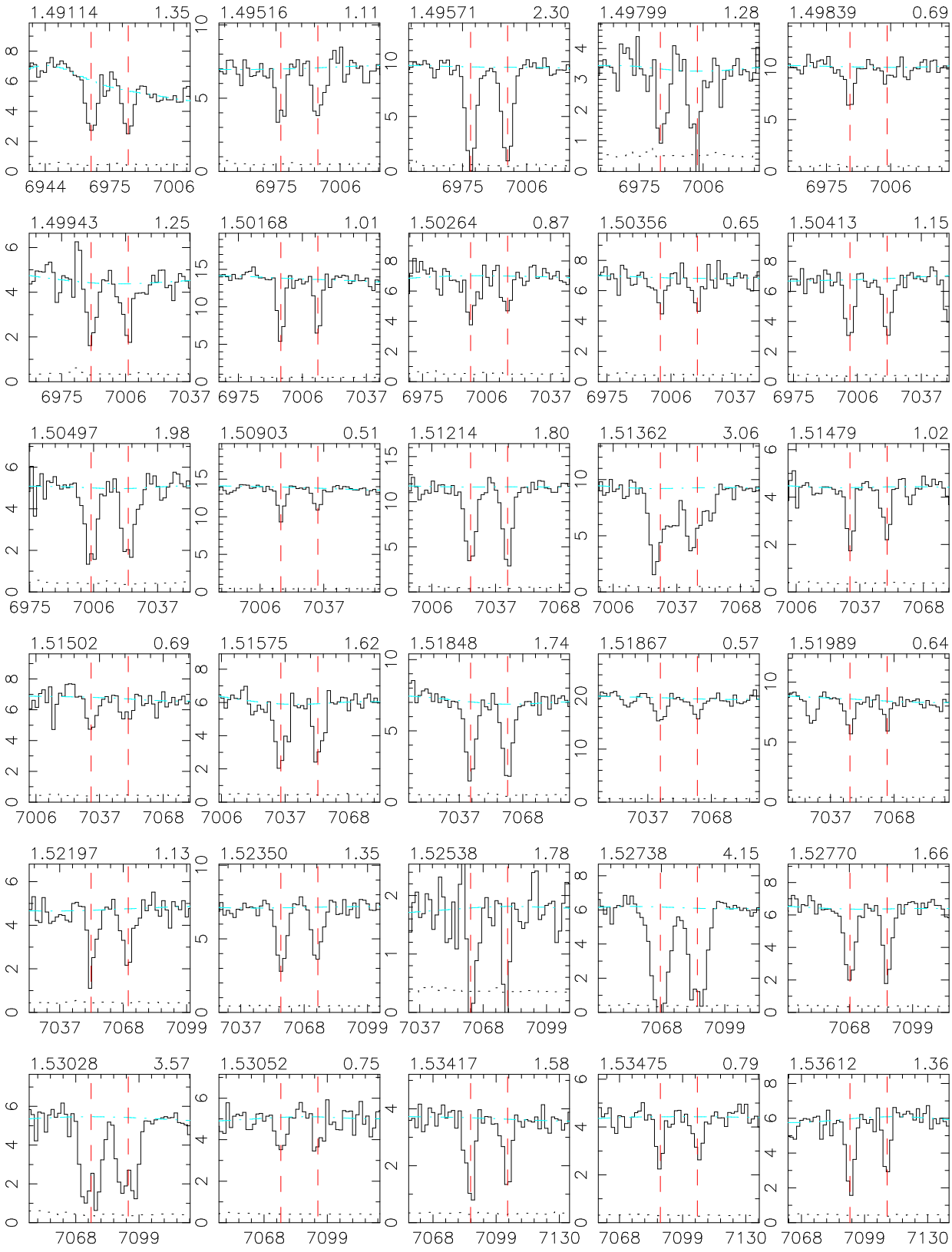
SDSS EDR
1.49114 1.35
1.49516 1.11
1.49571 2.30
1.49799 1.28
1.49839 0.69
1.49943 1.25
1.50168 1.01
1.50264 0.87
1.50356 0.65
1.50413 1.15
1.50497 1.98
1.50903 0.51
1.51214 1.80
1.51362 3.06
1.51479 1.02
1.51502 0.69
1.51575 1.62
1.51848 1.74
1.51867 0.57
1.51989 0.64
1.52197 1.13
1.52350 1.35
1.52538 1.78
1.52738 4.15
1.52770 1.66
1.53028 3.57
1.53052 0.75
1.53417 1.58
1.53475 0.79
1.53612 1.36

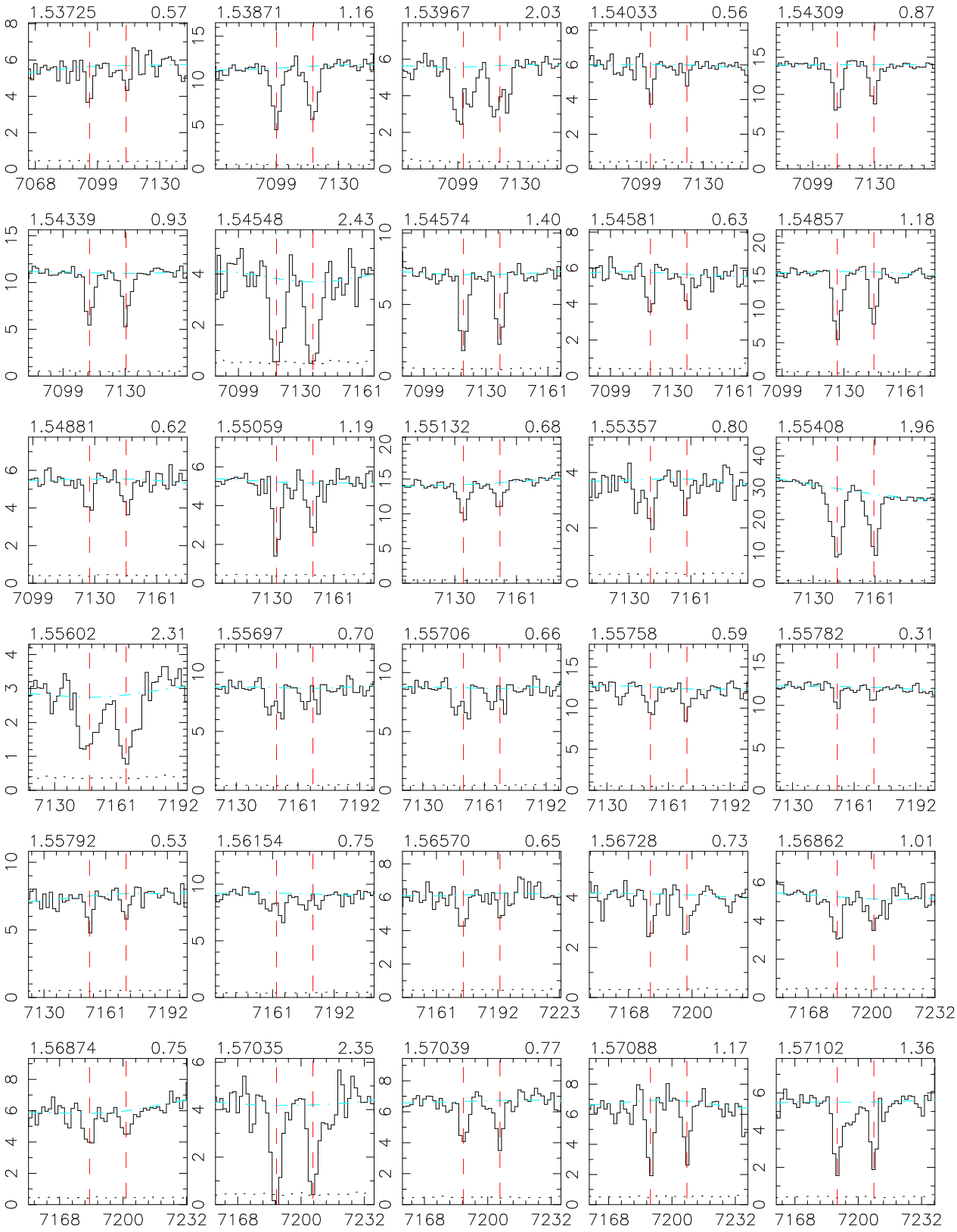
SDSS EDR
1.53725 0.57
1.53871 1.16
1.53967 2.03
1.54033 0.56
1.54309 0.87
1.54339 0.93
1.54548 2.43
1.54574 1.40
1.54581 0.63
1.54857 1.18
1.54881 0.62
1.55059 1.19
1.55132 0.68
1.55357 0.80
1.55408 1.96
1.55602 2.31
1.55697 0.70
1.55706 0.66
1.55758 0.59
1.55782 0.31
1.55792 0.53
1.56154 0.75
1.56570 0.65
1.56728 0.73
1.56862 1.01
1.56874 0.75
1.57035 2.35
1.57039 0.77
1.57088 1.17
1.57102 1.36

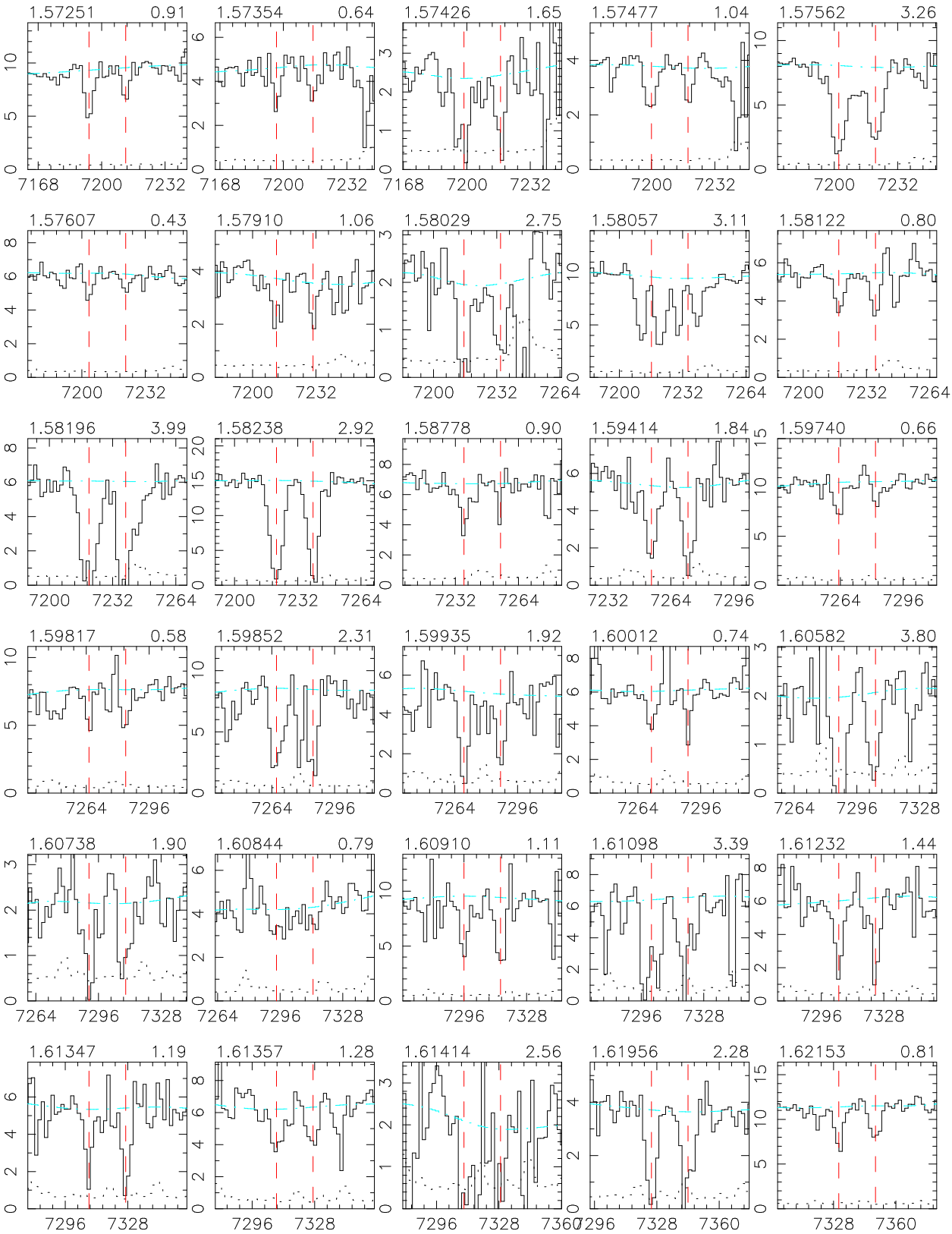
1.57251 0.91
1.57354 0.64
1.57426 1.65
1.57477 1.04
1.57562 3.26
1.57607 0.43
1.57910 1.06
1.58029 2.75
1.58057 3.11
1.58122 0.80
1.58196 3.99
1.58238 2.92
1.58778 0.90
1.59414 1.84
1.59740 0.66
1.59817 0.58
1.59852 2.31
1.59935 1.92
1.60012 0.74
1.60582 3.80
1.60738 1.90
1.60844 0.79
1.60910 1.11
1.61098 3.39
1.61232 1.44
1.61347 1.19
1.61357 1.28
1.61414 2.56
1.61956 2.28
1.62153 0.81

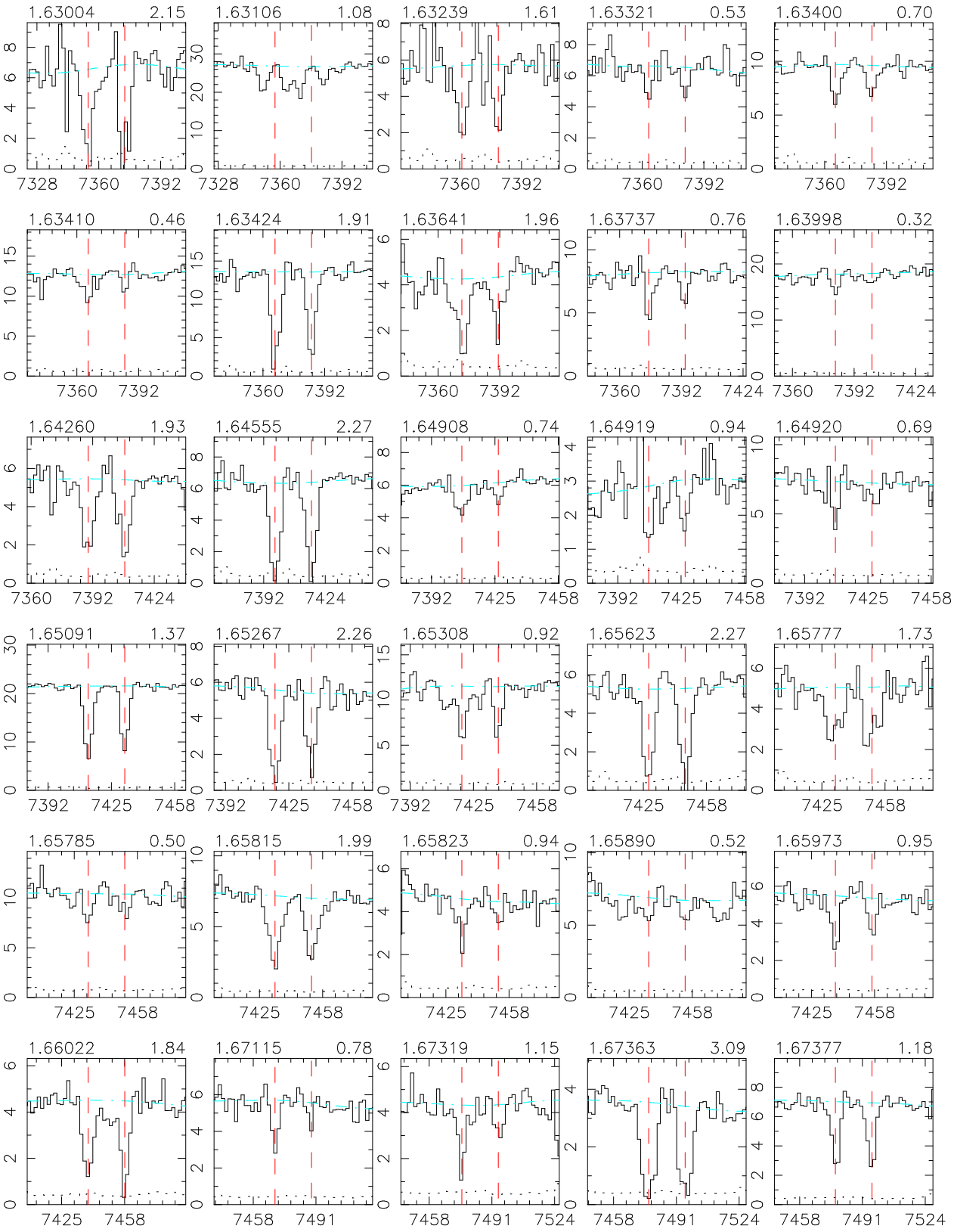
SDSS EDR
1.63004 2.15
1.63106 1.08
1.63239 1.61
1.63321 0.53
1.63400 0.70
1.63410 0.46
1.63424 1.91
1.63641 1.96
1.63737 0.76
1.63998 0.32
1.64260 1.93
1.64555 2.27
1.64908 0.74
1.64919 0.94
1.64920 0.69
1.65091 1.37
1.65267 2.26
1.65308 0.92
1.65623 2.27
1.65777 1.73
1.65785 0.50
1.65815 1.99
1.65823 0.94
1.65890 0.52
1.65973 0.95
1.66022 1.84
1.67115 0.78
1.67319 1.15
1.67363 3.09
1.67377 1.18

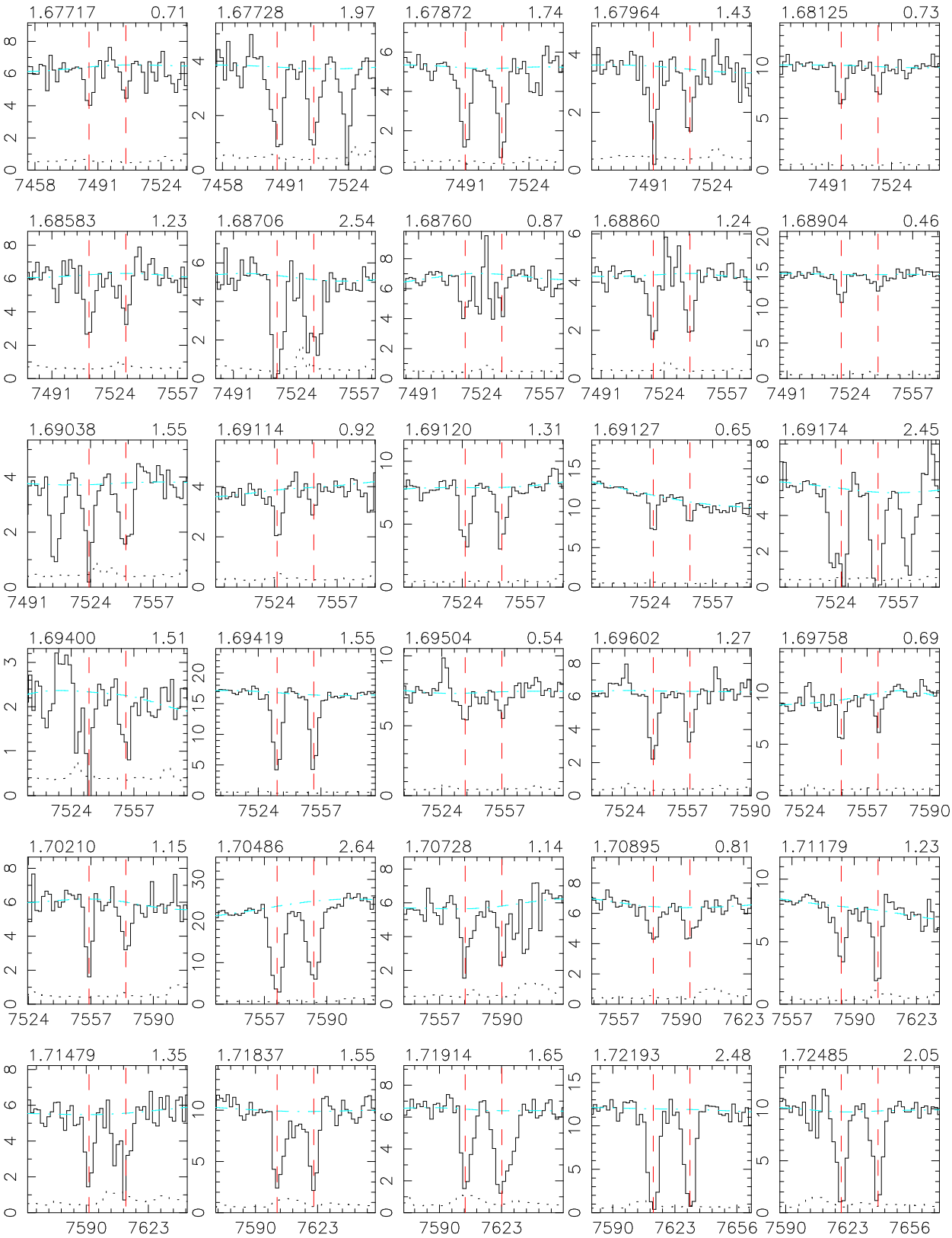
SDSS EDR
1.67717 0.71
1.67728 1.97
1.67872 1.74
1.67964 1.43
1.68125 0.73
1.68583 1.23
1.68706 2.54
1.68760 0.87
1.68860 1.24
1.68904 0.46
1.69038 1.55
1.69114 0.92
1.69120 1.31
1.69127 0.65
1.69174 2.45
1.69400 1.51
1.69419 1.55
1.69504 0.54
1.69602 1.27
1.69758 0.69
1.70210 1.15
1.70486 2.64
1.70728 1.14
1.70895 0.81
1.71179 1.23
1.71479 1.35
1.71837 1.55
1.71914 1.65
1.72193 2.48
1.72485 2.05

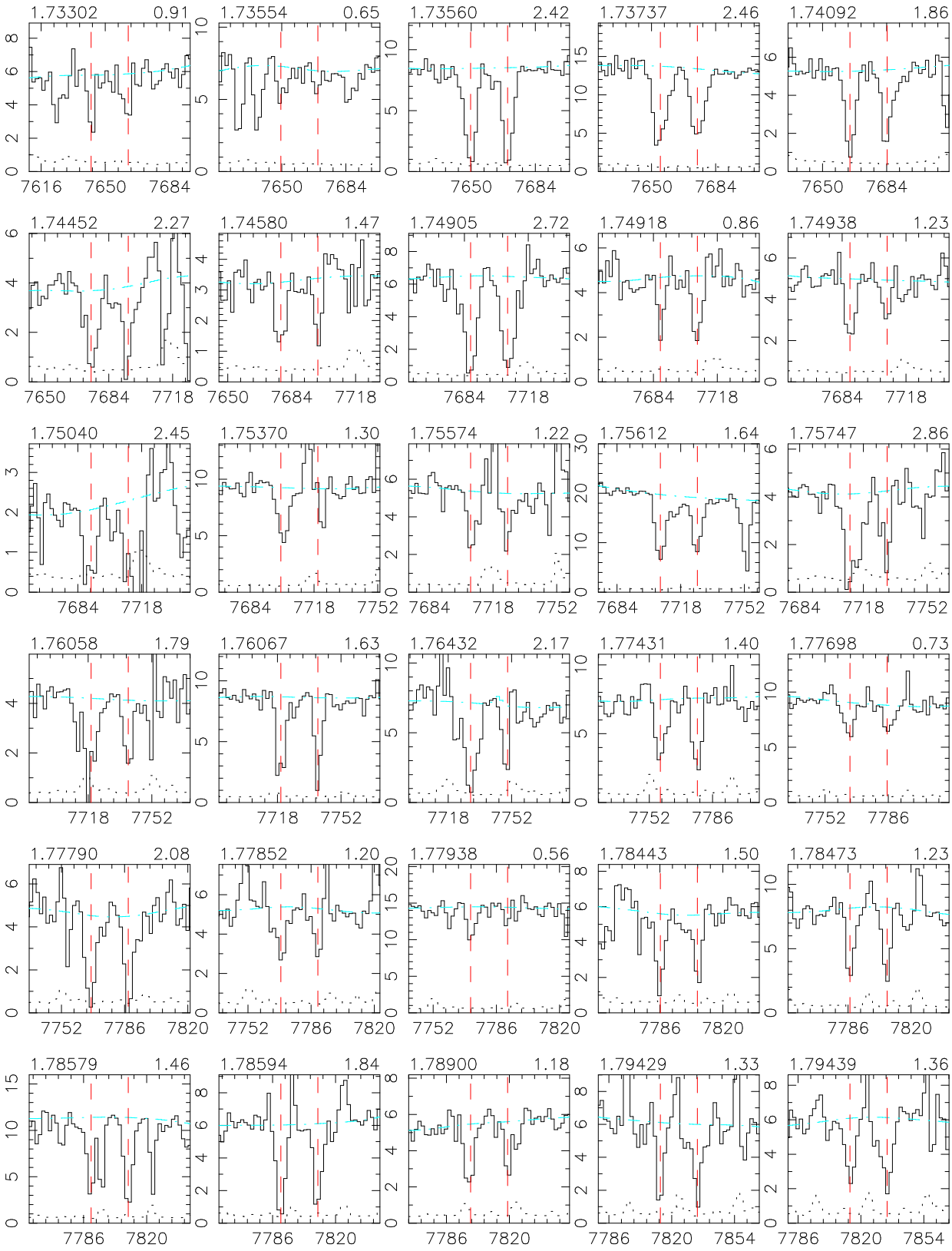
SDSS EDR
1.73302 0.91
1.73554 0.65
1.73560 2.42
1.73737 2.46
1.74092 1.86
1.74452 2.27
1.74580 1.47
1.74905 2.72
1.74918 0.86
1.74938 1.23
1.75040 2.45
1.75370 1.30
1.75574 1.22
1.75612 1.64
1.75747 2.86
1.76058 1.79
1.76067 1.63
1.76432 2.17
1.77431 1.40
1.77698 0.73
1.77790 2.08
1.77852 1.20
1.77938 0.56
1.78443 1.50
1.78473 1.23
1.78579 1.46
1.78594 1.84
1.78900 1.18
1.79429 1.33
1.79439 1.36

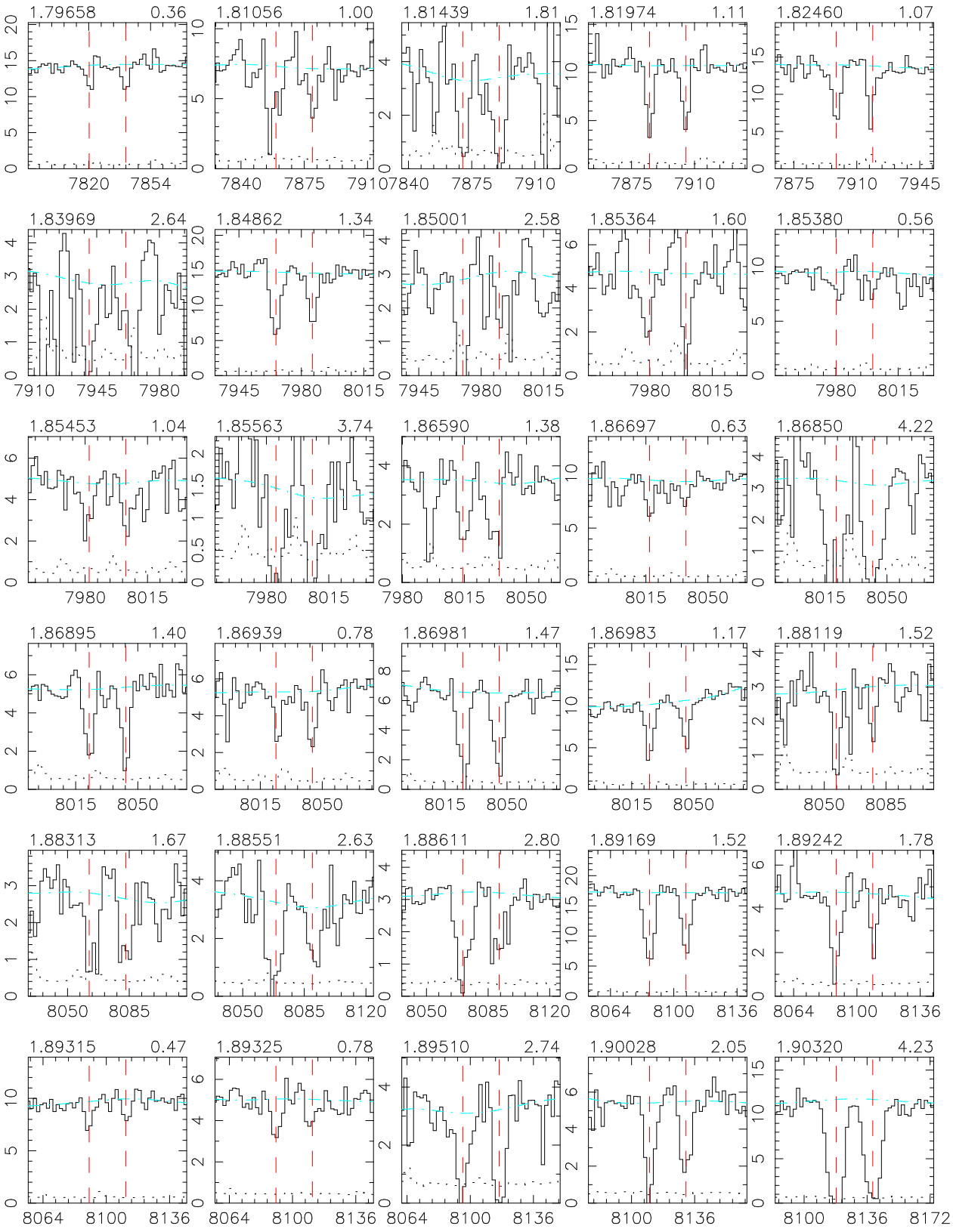
SDSS EDR
1.79658 0.36
1.81056 1.00
1.81439 1.81
1.81974 1.11
1.82460 1.07
1.83969 2.64
1.84862 1.34
1.85001 2.58
1.85364 1.60
1.85380 0.56
1.85453 1.04
1.85563 3.74
1.86590 1.38
1.86697 0.63
1.86850 4.22
1.86895 1.40
1.86939 0.78
1.86981 1.47
1.86983 1.17
1.88119 1.52
1.88313 1.67
1.88551 2.63
1.88611 2.80
1.89169 1.52
1.89242 1.78
1.89315 0.47
1.89325 0.78
1.89510 2.74
1.90028 2.05
1.90320 4.23

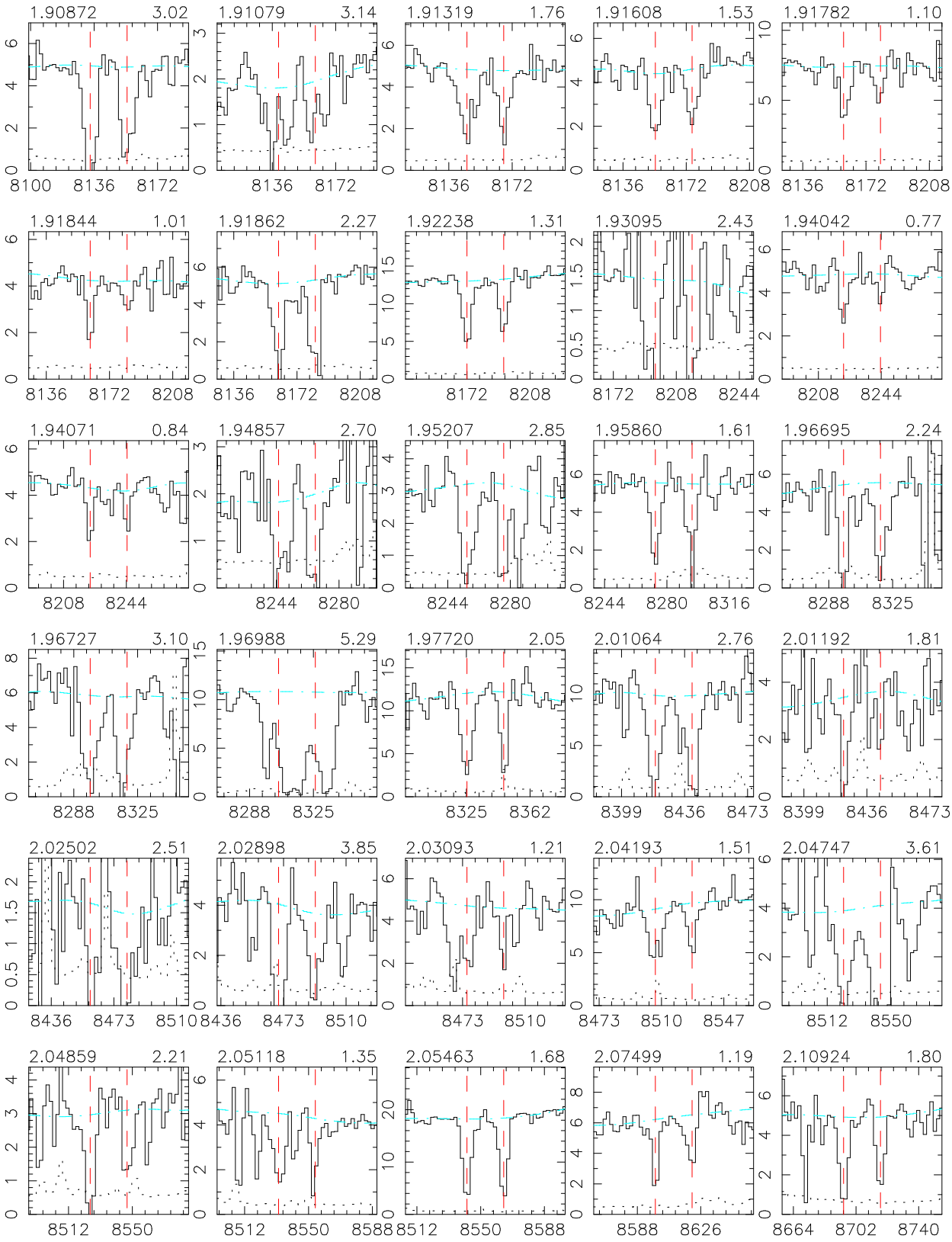
SDSS EDR
1.90872 3.02
1.91079 3.14
1.91319 1.76
1.91608 1.53
1.91782 1.10
1.91844 1.01
1.91862 2.27
1.92238 1.31
1.93095 2.43
1.94042 0.77
1.94071 0.84
1.94857 2.70
1.95207 2.85
1.95860 1.61
1.96695 2.24
1.96727 3.10
1.96988 5.29
1.97720 2.05
2.01064 2.76
2.01192 1.81
2.02502 2.51
2.02898 3.85
2.03093 1.21
2.04193 1.51
2.04747 3.61
2.04859 2.21
2.05118 1.35
2.05463 1.68
2.07499 1.19
2.10924 1.80

SDSS EDR

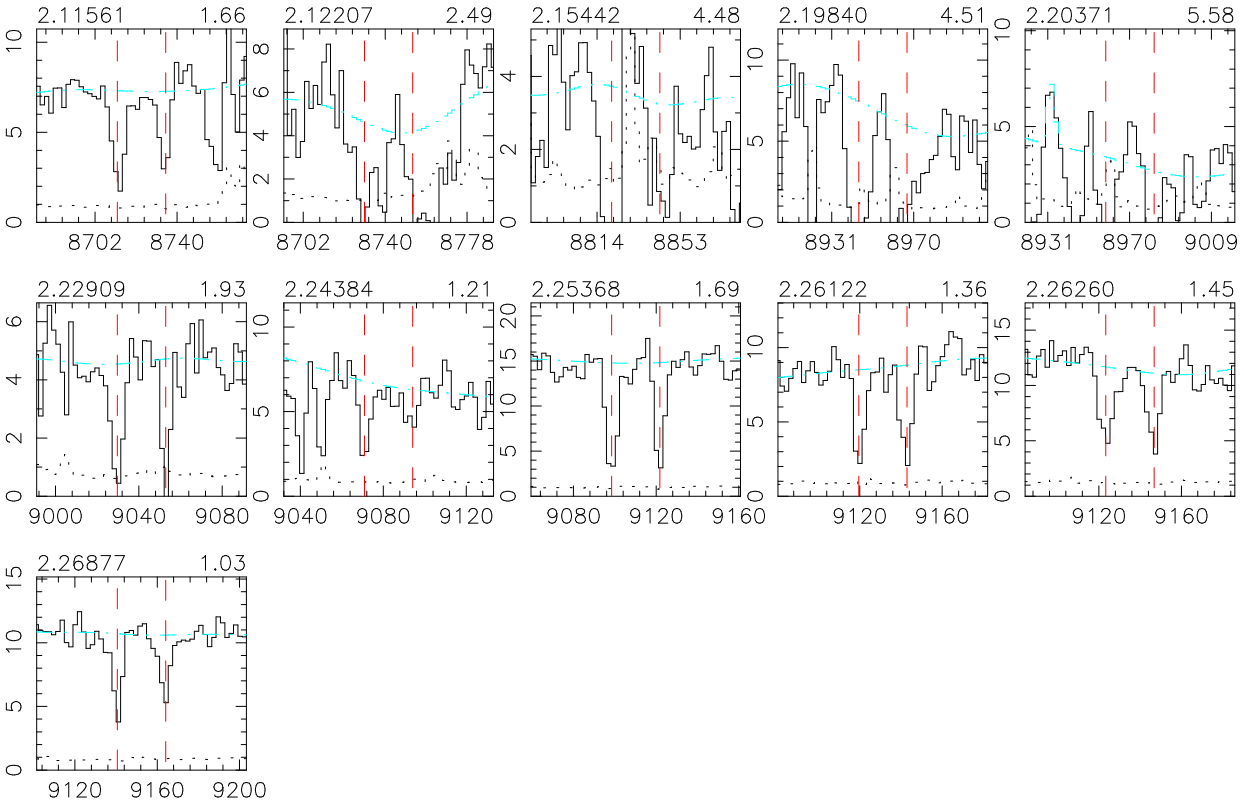
2.11561 1.66
2.12207 2.49
2.15442 4.48
2.19840 4.51
2.20371 5.58
2.22909 1.93
2.24384 1.21
2.25368 1.69
2.26122 1.36
2.26260 1.45
2.26877 1.03

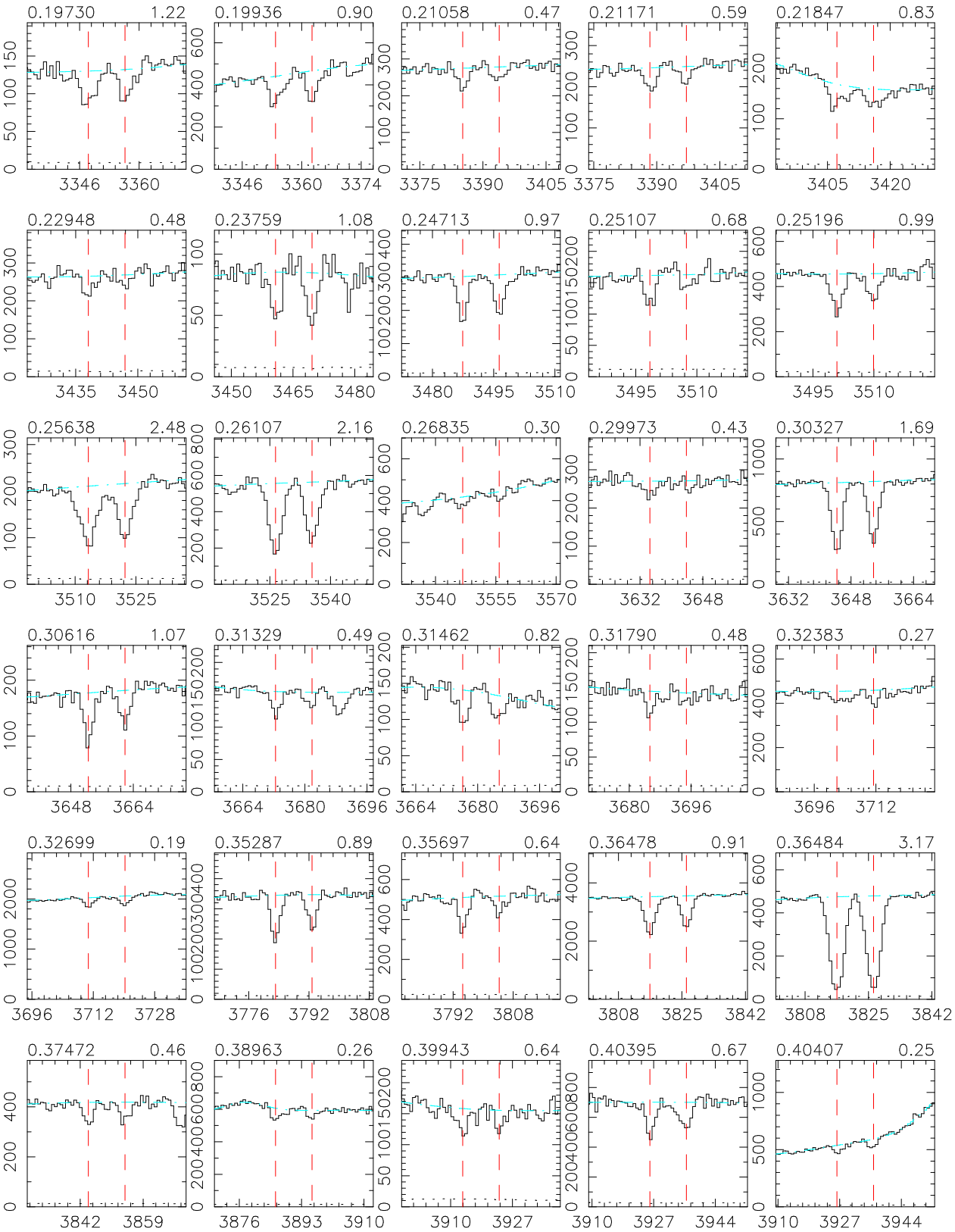
MMT
0.19730 1.22
0.19936 0.90
0.21058 0.47
0.21171 0.59
0.21847 0.83
0.22948 0.48
0.23759 1.08
0.24713 0.97
0.25107 0.68
0.25196 0.99
0.25638 2.48
0.26107 2.16
0.26835 0.30
0.29973 0.43
0.30327 1.69
0.30616 1.07
0.31329 0.49
0.31462 0.82
0.31790 0.48
0.32383 0.27
0.32699 0.19
0.35287 0.89
0.35697 0.64
0.36478 0.91
0.36484 3.17
0.37472 0.46
0.38963 0.26
0.39943 0.64
0.40395 0.67
0.40407 0.25

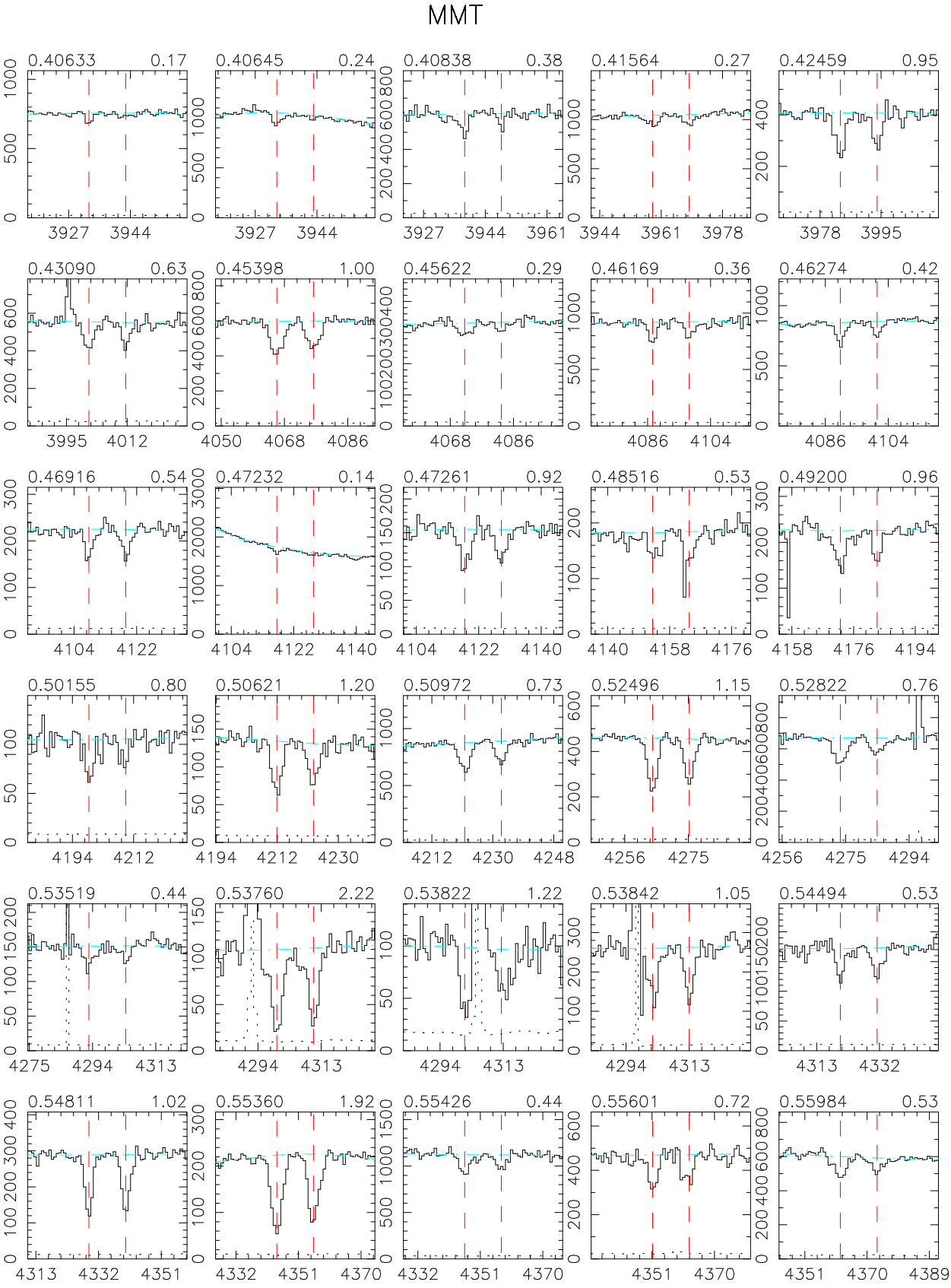
MMT
0.40633 0.17
0.40645 0.24
0.40838 0.38
0.41564 0.27
0.42459 0.95
0.43090 0.63
0.45398 1.00
0.45622 0.29
0.46169 0.36
0.46274 0.42
0.46916 0.54
0.47232 0.14
0.47261 0.92
0.48516 0.53
0.49200 0.96
0.50155 0.80
0.50621 1.20
0.50972 0.73
0.52496 1.15
0.52822 0.76
0.53519 0.44
0.53760 2.22
0.53822 1.22
0.53842 1.05
0.54494 0.53
0.54811 1.02
0.55360 1.92
0.55426 0.44
0.55601 0.72
0.55984 0.53

MMT

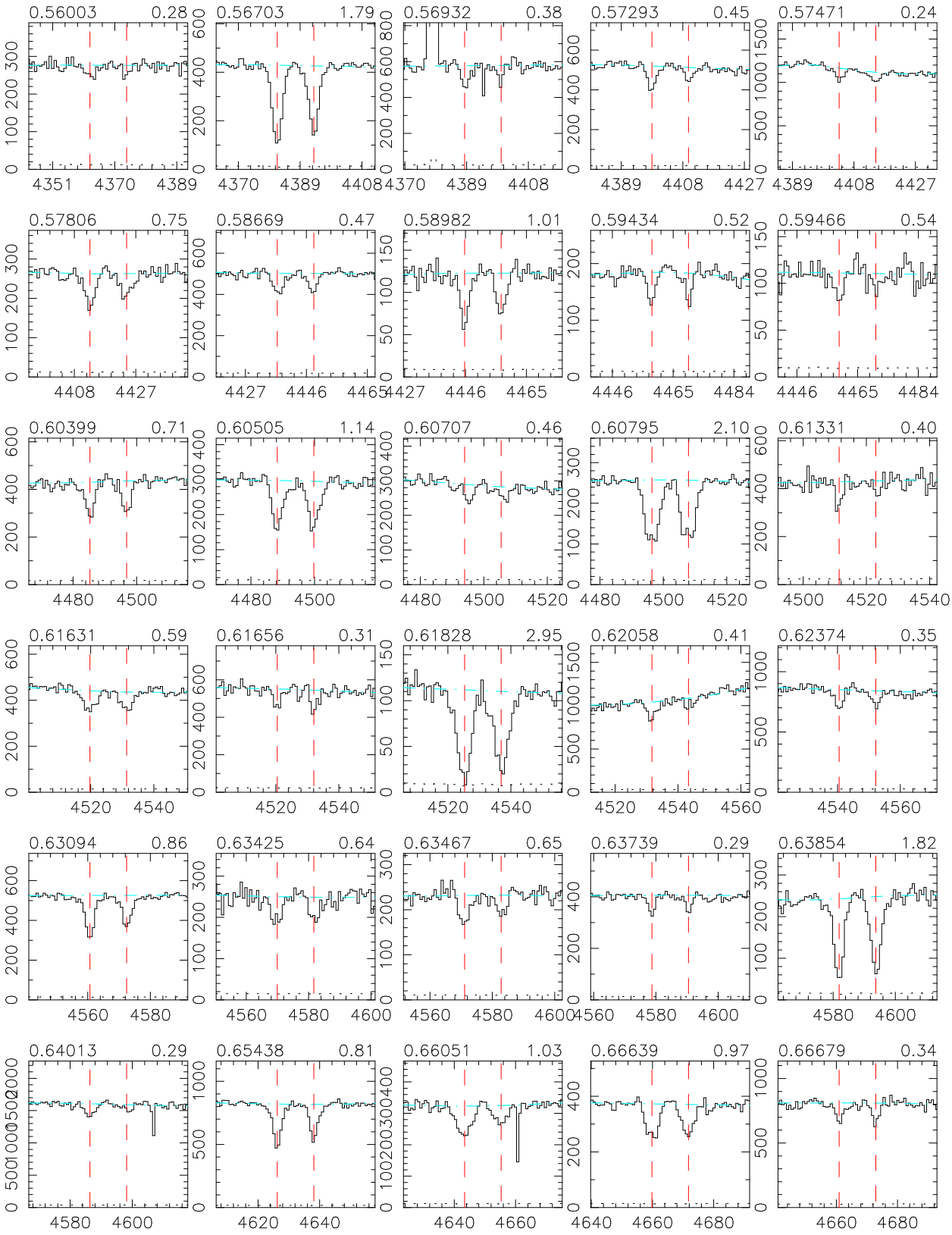
0.56003 0.28
0.56703 1.79
0.56932 0.38
0.57293 0.45
0.57471 0.24
0.57806 0.75
0.58669 0.47
0.58982 1.01
0.59434 0.52
0.59466 0.54
0.60399 0.71
0.60505 1.14
0.60707 0.46
0.60795 2.10
0.61331 0.40
0.61631 0.59
0.61656 0.31
0.61828 2.95
0.62058 0.41
0.62374 0.35
0.63094 0.86
0.63425 0.64
0.63467 0.65
0.63739 0.29
0.63854 1.82
0.64013 0.29
0.65438 0.81
0.66051 1.03
0.66639 0.97
0.66679 0.34

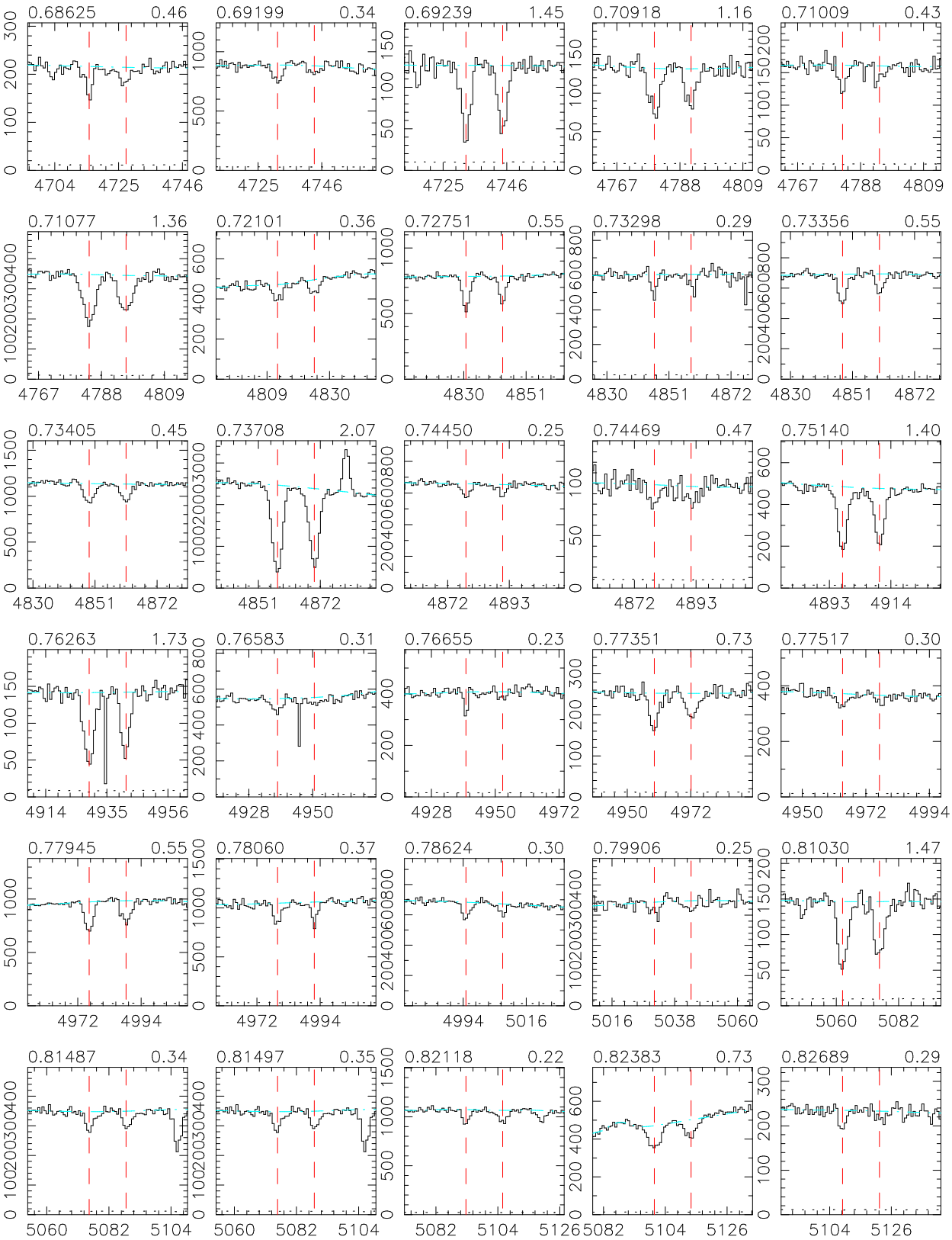
MMT
0.68625 0.46
0.69199 0.34
0.69239 1.45
0.70918 1.16
0.71009 0.43
0.71077 1.36
0.72101 0.36
0.72751 0.55
0.73298 0.29
0.73356 0.55
0.73405 0.45
0.73708 2.07
0.74450 0.25
0.74469 0.47
0.75140 1.40
0.76263 1.73
0.76583 0.31
0.76655 0.23
0.77351 0.73
0.77517 0.30
0.77945 0.55
0.78060 0.37
0.78624 0.30
0.79906 0.25
0.81030 1.47
0.81487 0.34
0.81497 0.35
0.82118 0.22
0.82383 0.73
0.82689 0.29

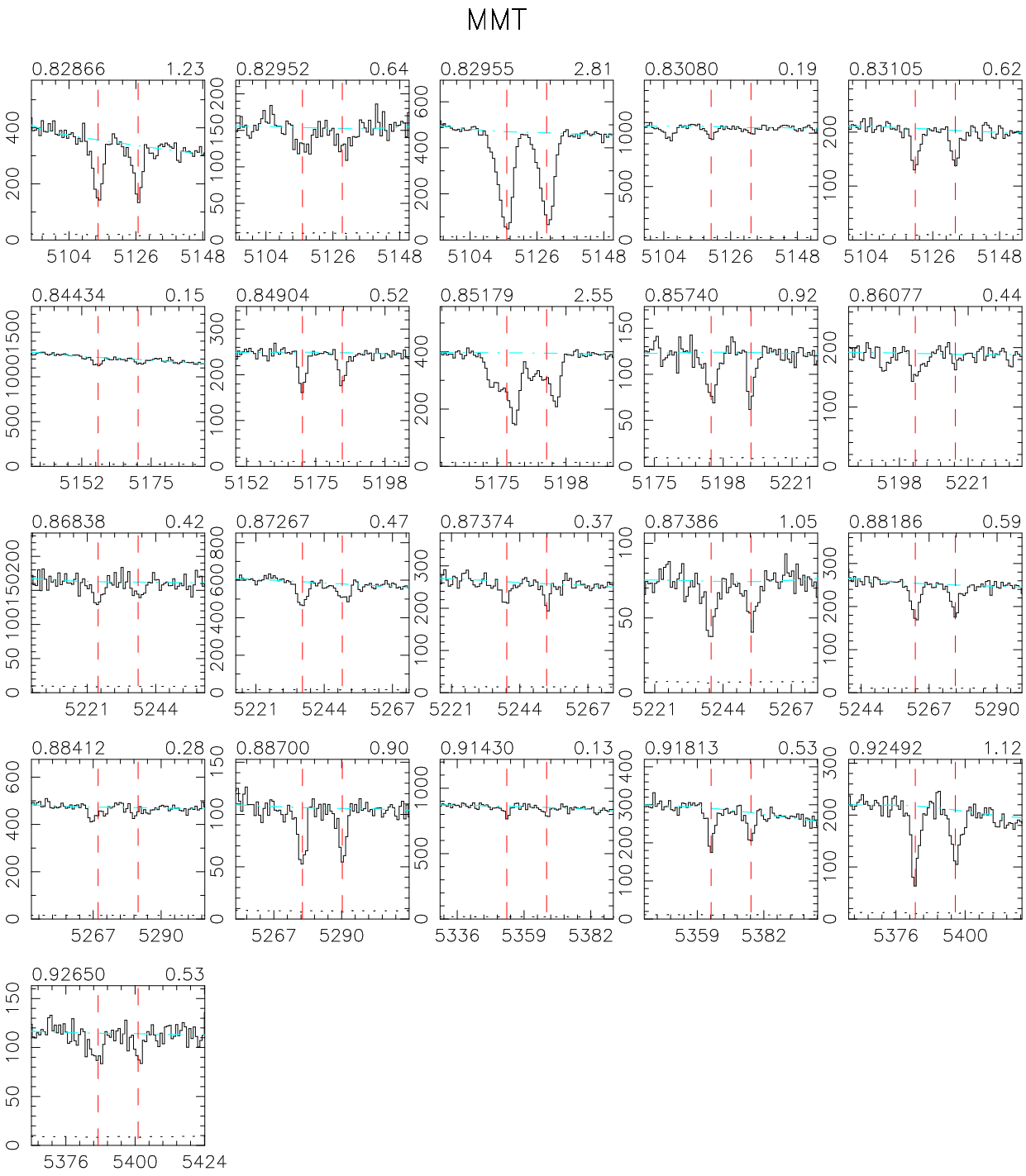
MMT
0.82866 1.23
0.82952 0.64
0.82955 2.81
0.83080 0.19
0.83105 0.62
0.84434 0.15
0.84904 0.52
0.85179 2.55
0.85740 0.92
0.86077 0.44
0.86838 0.42
0.87267 0.47
0.87374 0.37
0.87386 1.05
0.88186 0.59
0.88412 0.28
0.88700 0.90
0.91430 0.13
0.91813 0.53
0.92492 1.12
0.92650 0.53

BIBLIOGRAPHY

J. Afonso, B. Mobasher, B. Chan, and L. Cram. Discovery of an Extremely Red Galaxy at $z = 0.65$ with Dusty Star Formation and Nuclear Activity. *Astrophysical Journal*, 559: L101–L104, October 2001.

T. L. Aldcroft, J. Bechtold, and M. Elvis. Mg II absorption in a sample of 56 steep-spectrum quasars. *The Astrophysical Journal Supplement Series*, 93:1–46, July 1994.

D. G. Barnes, L. Staveley-Smith, W. J. G. de Blok, T. Oosterloo, I. M. Stewart, A. E. Wright, G. D. Banks, R. Bhathal, P. J. Boyce, M. R. Calabretta, M. J. Disney, M. J. Drinkwater, R. D. Ekers, K. C. Freeman, B. K. Gibson, A. J. Green, R. F. Haynes, P. te Lintel Hekkert, P. A. Henning, H. Jerjen, S. Juraszek, M. J. Kesteven, V. A. Kilborn, P. M. Knezek, B. Koribalski, R. C. Kraan-Korteweg, D. F. Malin, M. Marquarding, R. F. Minchin, J. R. Mould, R. M. Price, M. E. Putman, S. D. Ryder, E. M. Sadler, A. Schröder, F. Stootman, R. L. Webster, W. E. Wilson, and T. Ye. The H I Parkes All Sky Survey: southern observations, calibration and robust imaging. *Monthly Notices of the Royal Astronomical Society*, 322:486–498, April 2001.

P. D. Barthel, D. R. Tytler, and B. Thomson. Optical spectra of distant radio loud quasars. I - Data: Spectra of 67 quasars. *Astronomy and Astrophysics Supplement Series*, 82: 339–389, February 1990.

J. Bergeron and P. Boisse. A sample of galaxies giving rise to Mg II quasar absorption systems. *Astronomy and Astrophysics*, 243:344–366, March 1991.

E. Bertschinger. Simulations of Structure Formation in the Universe. *Annual Review of Astronomy and Astrophysics*, 36:599–654, 1998.

J. C. Blades, D. A. Turnshek, and C. A. Norman, editors. *QSO absorption lines: Probing the universe; Proceedings of the QSO Absorption Line Meeting, Baltimore, MD, May 19-21, 1987*, 1988.

M. Bolzonella, J.-M. Miralles, and R. Pelló. Photometric redshifts based on standard SED fitting procedures. *Astronomy and Astrophysics*, 363:476–492, November 2000.

N. Bouché, J. D. Lowenthal, J. C. Charlton, M. A. Bershady, C. W. Churchill, and C. C.

Steidel. Hα Imaging with Hubble Space Telescope-NICMOS of an Elusive Damped Lyα Cloud at $z = 0.6$. *Astrophysical Journal*, 550:585–592, April 2001.

G. Bruzual A. and S. Charlot. Spectral evolution of stellar populations using isochrone synthesis. *Astrophysical Journal*, 405:538–553, March 1993.

E. M. Burbidge, E. A. Beaver, R. D. Cohen, V. T. Junkkarinen, and R. W. Lyons. AO 0235 + 164 and Surrounding Field: Surprising HST Results. *Astronomical Journal*, 112: 2533–2540, December 1996.

D. Calzetti, L. Armus, R. C. Bohlin, A. L. Kinney, J. Koornneef, and T. Storchi-Bergmann. The Dust Content and Opacity of Actively Star-forming Galaxies. *Astrophysical Journal*, 533:682–695, April 2000.

J. A. Cardelli, G. C. Clayton, and J. S. Mathis. The relationship between infrared, optical, and ultraviolet extinction. *Astrophysical Journal*, 345:245–256, October 1989.

S. Casertano, D. de Mello, M. Dickinson, H. C. Ferguson, A. S. Fruchter, R. A. Gonzalez-Lopezlira, I. Heyer, R. N. Hook, Z. Levay, R. A. Lucas, J. Mack, R. B. Makidon, M. Mutchler, T. E. Smith, M. Stiavelli, M. S. Wiggs, and R. E. Williams. WFPC2 Observations of the Hubble Deep Field South. *Astronomical Journal*, 120:2747–2824, December 2000.

A. Caulet. The evolution of low ionization QSO absorption systems. *Astrophysical Journal*, 340:90–116, May 1989.

J. C. Charlton and C. W. Churchill. The Kinematic Composition of Mg II Absorbers. *Astrophysical Journal*, 499:181–197, May 1998.

H. Chen, K. M. Lanzetta, and J. K. Webb. The Origin of C IV Absorption Systems at Redshifts $z < 1$: Discovery of Extended C IV Envelopes around Galaxies. *Astrophysical Journal*, 556:158–163, July 2001a.

H. Chen, K. M. Lanzetta, J. K. Webb, and X. Barcons. The Gaseous Extent of Galaxies and the Origin of Lyα Absorption Systems. V. Optical and Near-Infrared Photometry of Lyα-absorbing Galaxies at $z < 1$. *Astrophysical Journal*, 559:654–674, October 2001b.

J. N. Chengalur and N. Kanekar. Giant Metrewave Radio Telescope observations of low-z damped Lyα absorbers. *Monthly Notices of the Royal Astronomical Society*, 302:L29–L32, January 1999.

C. W. Churchill. Mg II Absorber Number Density at $z \simeq 0.05$: Implications for Ω_{DLA} Evolution. *Astrophysical Journal*, 560:92–100, October 2001.

C. W. Churchill, R. R. Mellon, J. C. Charlton, B. T. Jannuzi, S. Kirhakos, C. C. Steidel, and D. P. Schneider. Low- and High-Ionization Absorption Properties of Mg II Absorption-selected Galaxies at Intermediate Redshifts. I. General Properties. *The Astrophysical Journal Supplement Series*, 130:91–119, September 2000. (C2000).

C. W. Churchill, J. R. Rigby, J. C. Charlton, and S. S. Vogt. The Population of Weak Mg II Absorbers. I. A Survey of 26 QSO HIRES/Keck Spectra. *The Astrophysical Journal Supplement Series*, 120:51–75, January 1999. (CRCV99).

C. W. Churchill and S. S. Vogt. The Kinematics of Intermediate-Redshift Mg II Absorbers. *Astronomical Journal*, 122:679–713, August 2001.

C. W. Churchill, S. S. Vogt, and J. C. Charlton. The Physical Conditions of Intermediate-Redshift Mg II Absorbing Clouds from Voigt Profile Analysis. *Astronomical Journal*, 125: 98–115, January 2003.

A. Cimatti, E. Daddi, S. di Serego Alighieri, L. Pozzetti, F. Mannucci, A. Renzini, E. Oliva, G. Zamorani, P. Andreani, and H. J. A. Röttgering. New clues on the nature of extremely red galaxies. *Astronomy and Astrophysics*, 352:L45–L50, December 1999.

A. Cimatti, D. Villani, L. Pozzetti, and S. di Serego Alighieri. The density of extremely red objects around high-z radio-loud active galactic nuclei. *Monthly Notices of the Royal Astronomical Society*, 318:453–461, October 2000.

L. L. Cowie, J. P. Gardner, E. M. Hu, A. Songaila, K.-W. Hodapp, and R. J. Wainscoat. The Hawaii K-band galaxy survey. 1: Deep K-band imaging. *Astrophysical Journal*, 434: 114–127, October 1994.

E. Daddi, A. Cimatti, and A. Renzini. EROs and the formation epoch of field ellipticals. *Astronomy and Astrophysics*, 362:L45–L48, October 2000.

R. Davé, L. Hernquist, N. Katz, and D. H. Weinberg. The Low-Redshift Lyα Forest in Cold Dark Matter Cosmologies. *Astrophysical Journal*, 511:521–545, February 1999.

A. Dey, J. R. Graham, R. J. Ivison, I. Smail, G. S. Wright, and M. C. Liu. Observations of a $z = 1.44$ Dusty, Ultraluminous Galaxy and Implications for Deep Submillimeter Surveys. *Astrophysical Journal*, 519:610–621, July 1999.

M. Dickinson and C. C. Steidel. Galaxy Evolution from QSO Absorption-Line Selected Samples. In *IAU Symp. 171: New Light on Galaxy Evolution*, pages 295–298, 1996.

A. Dobrzycki, J. Bechtold, J. Scott, and M. Morita. A Uniform Analysis of the Lyα Forest at $z = 0 - 5$. IV. The Clustering and Evolution of Clouds at $z \leq 1.7$. *Astrophysical Journal*, 571:654–664, June 2002.

M. J. Drinkwater, R. L. Webster, and P. A. Thomas. On the nature of Mg II absorption line systems in quasars. *Astronomical Journal*, 106:848–868, September 1993.

S. P. Driver, A. Fernandez-Soto, W. J. Couch, S. C. Odewahn, R. A. Windhorst, S. Phillips, K. Lanzetta, and A. Yahil. Morphological Number Counts and Redshift Distributions to $I < 26$ from the Hubble Deep Field: Implications for the Evolution of Ellipticals, Spirals, and Irregulars. *Astrophysical Journal*, 496:L93–L96, April 1998.

N. Drory, R. Bender, G. Feulner, U. Hopp, C. Maraston, J. Snigula, and G. J. Hill. The Munich Near-Infrared Cluster Survey. II. The K-Band Luminosity Function of Field Galaxies to $z \sim 1.2$. *Astrophysical Journal*, 595:698–711, October 2003.

R. S. Ellis. Faint Blue Galaxies. *Annual Review of Astronomy and Astrophysics*, 35:389–443, 1997.

S. L. Ellison, C. W. Churchill, S. A. Rix, and M. Pettini. The Number Density of $0.6 < z < 1.7$ MgII Systems from CORALS: Observational Biases at Intermediate Redshift. astro-ph/0407237, July 2004. Accepted for publication in Astrophysical Journal.

S. L. Ellison, G. Mallén-Ornelas, and M. Sawicki. The Absorption and Emission Kinematics in the $z = 0.7450$ Mg II Absorber toward Q1331+17. *Astrophysical Journal*, 589:709–721, June 2003.

S. L. Ellison, L. Yan, I. M. Hook, M. Pettini, J. V. Wall, and P. Shaver. The CORALS survey I: New estimates of the number density and gas content of damped Lyman alpha systems free from dust bias. *Astronomy and Astrophysics*, 379:393–406, November 2001.

Y. Fang, R. C. Duncan, A. P. S. Crotts, and J. Bechtold. The Size and Nature of Lyman-alpha Forest Clouds Probed by QSO Pairs and Groups. *Astrophysical Journal*, 462:77–88, May 1996.

H. C. Ferguson, M. Dickinson, and R. Williams. The Hubble Deep Fields. *Annual Review of Astronomy and Astrophysics*, 38:667–715, 2000.

M. Giavalisco. Lyman-Break Galaxies. *Annual Review of Astronomy and Astrophysics*, 40: 579–641, 2002.

N. Grevesse and A. J. Sauval. Standard Solar Composition. *Space Science Reviews*, 85: 161–174, August 1998.

P. Guillemin and J. Bergeron. Evolution of quasar absorption-selected galaxies. *Astronomy and Astrophysics*, 328:499–509, December 1997.

M. G. Haehnelt, M. Steinmetz, and M. Rauch. Damped Ly alpha Absorber at High Redshift: Large Disks or Galactic Building Blocks? *Astrophysical Journal*, 495:647–658, March 1998.

T. S. Hamilton, S. Casertano, and D. A. Turnshek. The Luminosity Function of QSO Host Galaxies. *Astrophysical Journal*, 576:61–74, September 2002.

D. W. Hogg. Distance Measures in Cosmology. astro-ph/9905116, December 2000.

A. M. Hopkins. On the evolution of star forming galaxies. astro-ph/0407170, July 2004. Accepted for publication in Astrophysical Journal.

J. C. Howk and K. R. Sembach. Ionized Gas in Damped Lyα Systems and Its Effects on Elemental Abundance Studies. *Astrophysical Journal*, 523:L141–L144, October 1999.

E. M. Hu, T. Kim, L. L. Cowie, A. Songaila, and M. Rauch. The Distribution of Column Densities and B Values in the Lyman-Alpha Forest. *Astronomical Journal*, 110:1526–1543, October 1995.

M. Im, R. E. Griffiths, A. Naim, K. U. Ratnatunga, N. Roche, R. F. Green, and V. L. Sarajedini. The Morphologically Divided Redshift Distribution of Faint Galaxies. *Astrophysical Journal*, 510:82–89, January 1999.

M. Im, R. E. Griffiths, K. U. Ratnatunga, and V. L. Sarajedini. Luminosity Functions of Elliptical Galaxies at $z < 1.2$. *Astrophysical Journal*, 461:L79–L82, April 1996.

N. Kanekar and J. N. Chengalur. H I 21cm absorption in low vec z damped Lyman-alpha systems. *Astronomy and Astrophysics*, 369:42–48, April 2001.

R. C. Kennicutt. A spectrophotometric atlas of galaxies. *The Astrophysical Journal Supplement Series*, 79:255–284, April 1992a.

R. C. Kennicutt. The integrated spectra of nearby galaxies - General properties and emission-line spectra. *Astrophysical Journal*, 388:310–327, April 1992b.

A. Klypin, A. V. Kravtsov, O. Valenzuela, and F. Prada. Where Are the Missing Galactic Satellites? *Astrophysical Journal*, 522:82–92, September 1999.

M. J. Kukula, J. S. Dunlop, R. J. McLure, L. Miller, W. J. Percival, S. A. Baum, and C. P. O'Dea. A NICMOS imaging study of high-z quasar host galaxies. *Monthly Notices of the Royal Astronomical Society*, 326:1533–1546, October 2001.

G. Lake, R. A. Schommer, and J. H. van Gorkom. The H I distribution and kinematics in four low-luminosity elliptical galaxies. *Astrophysical Journal*, 314:57–69, March 1987.

W. Lane, A. Smette, F. Briggs, S. Rao, D. Turnshek, and G. Meylan. H I 21 Centimeter Absorption in Two Low-Redshift Damped Lyα Systems. *Astronomical Journal*, 116:26–30, July 1998a.

W. M Lane. *H I 21cm Absorbers at Moderate Redshift*. PhD thesis, Rijksuniversiteit Groningen, 2000.

W. M. Lane, F. H. Briggs, and A. Smette. Detection of Warm and Cold Phases of the Neutral ISM in a Damped Lyα Absorber. *Astrophysical Journal*, 532:146–151, March 2000.

W. M. Lane, F. H. Briggs, D. A. Turnshek, and S. M. Rao. The Damped Lyman-alpha absorbers at $z = 0.0912$ and $z = 0.2212$ towards the QSO B0738+313. *Bulletin of the American Astronomical Society*, 30:1249, December 1998b.

K. M. Lanzetta, H. W. Chen, J. Webb, and N. Yahata. On the Relationship Between Galaxies and Absorbers. In J. Mulchaey and J. Stocke, editors, *ASP Conf. Ser. 254: Extragalactic Gas at Low Redshift*, page 78, 2002. astro-ph/0108068.

K. M. Lanzetta, A. M. Wolfe, and D. A. Turnshek. An absorption-line survey of 32 QSOs at red wavelengths - Properties of the Mg II absorbers. *Astrophysical Journal*, 322:739–769, November 1987.

V. Le Brun, J. Bergeron, P. Boisse, and J. M. Deharveng. The nature of intermediate-redshift damped Lyα absorbers. *Astronomy and Astrophysics*, 321:733–748, May 1997.

J. Loveday. The K-band luminosity function of nearby field galaxies. *Monthly Notices of the Royal Astronomical Society*, 312:557–566, March 2000.

A. H. Maller, J. X. Prochaska, R. S. Somerville, and J. R. Primack. Damped Lyman alpha systems and galaxy formation models - I. The radial distribution of cold gas at high z. *Monthly Notices of the Royal Astronomical Society*, 326:1475–1488, October 2001.

S. Mao, H. J. Mo, and S. D. M. White. The evolution of galactic discs. *Monthly Notices of the Royal Astronomical Society*, 297:L71–L75, July 1998.

C. Marinoni, P. Monaco, G. Giuricin, and B. Costantini. The Nearby Optical Galaxy Sample: The Local Galaxy Luminosity Function. *Astrophysical Journal*, 521:50–63, August 1999.

P. J. McCarthy. High redshift radio galaxies. *Annual Review of Astronomy and Astrophysics*, 31:639–688, 1993.

P. McDonald and J. Miralda-Escudé. Galaxy Formation and the Kinematics of Damped Lyα Systems. *Astrophysical Journal*, 519:486–500, July 1999.

K. K. McLeod and G. H. Rieke. Near-infrared imaging of low-redshift quasar host galaxies. *Astrophysical Journal*, 420:58–67, January 1994.

R. J. McLure, J. S. Dunlop, and M. J. Kukula. Two-dimensional modelling of optical Hubble Space Telescope and infrared tip-tilt images of quasar host galaxies. *Monthly Notices of the Royal Astronomical Society*, 318:693–702, November 2000.

H. J. Mo, S. Mao, and S. D. M. White. The formation of galactic discs. *Monthly Notices of the Royal Astronomical Society*, 295:319–336, April 1998.

H. J. Mo and J. Miralda-Escude. Gaseous Galactic Halos and Quasi-stellar Object Absorption-Line Systems. *Astrophysical Journal*, 469:589–604, October 1996.

B. Moore, S. Ghigna, F. Governato, G. Lake, T. Quinn, J. Stadel, and P. Tozzi. Dark Matter Substructure within Galactic Halos. *Astrophysical Journal*, 524:L19–L22, October 1999.

D. B. Nestor, S. M. Rao, D. A. Turnshek, and D. Vanden Berk. Damped Lyα Gas Metallicities at Redshifts $z = 0.9 - 2.0$ from Sloan Digital Sky Survey Spectra. *Astrophysical Journal*, 595:L5–L8, September 2003.

D. B. Nestor, D. A. Turnshek, and S. M. Rao. Mg II Absorption Systems in SDSS QSO Spectra. 2004. Submitted to *Astrophysical Journal*.

J. H. Oort. The force exerted by the stellar system in the direction perpendicular to the galactic plane and some related problems. *Bulletin of the Astronomical Institute of the Netherlands*, 6:249–287, August 1932.

P. J. E. Peebles. *Principles of Physical Cosmology*. Princeton University Press, 1993.

S. V. Penton, J. T. Stocke, and J. M. Shull. The Local Lyα Forest. III. Relationship between Lyα Absorbers and Galaxies, Voids, and Superclusters. *Astrophysical Journal*, 565:720–742, February 2002.

S. V. Penton, J. T. Stocke, and J. M. Shull. The Local Lyα Forest. IV. Space Telescope Imaging Spectrograph G140M Spectra and Results on the Distribution and Baryon Content of H I Absorbers. *The Astrophysical Journal Supplement Series*, 152:29–62, May 2004.

P. Petitjean. QSO Absorption Line Systems. In O. Le Fevre and S. Charlot, editors, *Proceedings of the Les Houches school: Formation and Evolution of Galaxies*. Springer-Verlag, 1998. astro-ph/9810418.

P. Petitjean and J. Bergeron. Mg II quasar absorption systems and properties of gaseous haloes. *Astronomy and Astrophysics*, 231:309–326, May 1990.

P. Petitjean and S. Charlot, editors. *Structure and evolution of the intergalactic medium from QSO absorption line system*, 1997.

M. Pettini, A. Boksenberg, and R. W. Hunstead. Metal enrichment, dust, and star formation in galaxies at high redshifts. I - The $z = 2.3091$ absorber toward PHL 957. *Astrophysical Journal*, 348:48–56, January 1990.

M. Pettini, S. L. Ellison, C. C. Steidel, and D. V. Bowen. Metal Abundances at $z < 1.5$: Fresh Clues to the Chemical Enrichment History of Damped Lyα Systems. *Astrophysical Journal*, 510:576–589, January 1999.

B. M. Poggianti. K and evolutionary corrections from UV to IR. *Astronomy and Astrophysics Supplement Series*, 122:399–407, May 1997.

J. X. Prochaska, E. Gawiser, A. M. Wolfe, S. Castro, and S. G. Djorgovski. The Age-Metallicity Relation of the Universe in Neutral Gas: The First 100 Damped Lyα Systems. *Astrophysical Journal*, 595:L9–L12, September 2003.

J. X. Prochaska and A. M. Wolfe. On the Kinematics of the Damped Lyman-alpha Protogalaxies. *Astrophysical Journal*, 487:73–95, September 1997.

J. X. Prochaska and A. M. Wolfe. Protogalactic Disk Models of Damped Lyα Kinematics. *Astrophysical Journal*, 507:113–130, November 1998.

J. X. Prochaska and A. M. Wolfe. Chemical Abundances of the Damped Lyα Systems at $z > 1.5$. *The Astrophysical Journal Supplement Series*, 121:369–415, April 1999.

S. Rao and F. Briggs. Neutral Hydrogen in Galaxies at the Present Epoch. *Astrophysical Journal*, 419:515–523, December 1993.

S. M. Rao, D. B. Nestor, D. A. Turnshek, W. M. Lane, E. M. Monier, and J. Bergeron. Low-Redshift Damped Lyα Galaxies toward the Quasars B2 0827+243, PKS 0952+179, PKS 1127-145, and PKS 1629+120. *Astrophysical Journal*, 595:94–108, September 2003.

S. M. Rao and D. A. Turnshek. Discovery of $z = 0.0912$ and $z = 0.2212$ Damped Ly alpha Absorption-Line Systems toward the Quasar OI 363: Limits on the Nature of Damped Lyα Galaxies. *Astrophysical Journal*, 500:L115–L119, June 1998.

S. M. Rao and D. A. Turnshek. Discovery of Damped Lyα Systems at Redshifts Less than 1.65 and Results on Their Incidence and Cosmological Mass Density. *The Astrophysical Journal Supplement Series*, 130:1–35, September 2000. (RT00).

M. Rauch. The Lyman Alpha Forest in the Spectra of QSOs. *Annual Review of Astronomy and Astrophysics*, 36:267–316, 1998.

J. R. Rigby, J. C. Charlton, and C. W. Churchill. The Population of Weak Mg II Absorbers. II. The Properties of Single-Cloud Systems. *Astrophysical Journal*, 565:743–761, February 2002.

E. Ryan-Weber, B. S. Koribalski, L. Staveley-Smith, H. Jerjen, R. C. Kraan-Korteweg, S. D. Ryder, D. G. Barnes, W. J. G. de Blok, V. A. Kilborn, R. Bhathal, P. J. Boyce, M. J. Disney, M. J. Drinkwater, R. D. Ekers, K. C. Freeman, B. K. Gibson, A. J. Green, R. F. Haynes, P. A. Henning, S. Juraszek, M. J. Kesteven, P. M. Knezek, S. Mader, M. Marquarding, M. Meyer, R. F. Minchin, J. R. Mould, J. O'Brien, T. Oosterloo, R. M. Price, M. E. Putman, E. M. Sadler, A. Schröder, I. M. Stewart, F. Stootman, M. Waugh, R. L. Webster, A. E. Wright, and M. A. Zwaan. The 1000 Brightest HIPASS Galaxies: Newly Cataloged Galaxies. *Astronomical Journal*, 124:1954–1974, October 2002.

E. M. Sadler, T. A. Oosterloo, R. Morganti, and A. Karakas. H I in Four Star-forming Low-Luminosity E/S0 and S0 Galaxies. *Astronomical Journal*, 119:1180–1196, March 2000.

W. L. W. Sargent, C. C. Steidel, and A. Boksenberg. C IV absorption in a new sample of 55 QSOs - Evolution and clustering of the heavy-element absorption redshifts. *The Astrophysical Journal Supplement Series*, 68:539–641, December 1988a.

W. L. W. Sargent, C. C. Steidel, and A. Boksenberg. Mg II absorption in the spectra of high and low redshift QSOs. *Astrophysical Journal*, 334:22–33, November 1988b.

W. L. W. Sargent, P. J. Young, A. Boksenberg, and D. Tytler. The distribution of Lyman-alpha absorption lines in the spectra of six QSOs - Evidence for an intergalactic origin. *The Astrophysical Journal Supplement Series*, 42:41–81, January 1980.

B. D. Savage and K. R. Sembach. Interstellar Abundances from Absorption-Line Observations with the Hubble Space Telescope. *Annual Review of Astronomy and Astrophysics*, 34:279–330, 1996.

D. P. Schneider, G. F. Hartig, B. T. Jannuzi, S. Kirhakos, D. H. Saxe, R. J. Weymann, J. N. Bahcall, J. Bergeron, A. Boksenberg, W. L. W. Sargent, B. D. Savage, D. A. Turnshek, and A. M. Wolfe. The Hubble Space Telescope quasar absorption line key project. II - Data calibration and absorption-line selection. *The Astrophysical Journal Supplement Series*, 87:45–62, July 1993.

J. M. Schombert, R. A. Pildis, J. Eder, and A. J. Oemler. Dwarf Spirals. *Astronomical Journal*, 110:2067–2074, November 1995.

R. K. Sheth and G. Tormen. Large-scale bias and the peak background split. *Monthly Notices of the Royal Astronomical Society*, 308:119–126, September 1999.

A. Smette, J. Surdej, P. A. Shaver, C. B. Foltz, F. H. Chaffee, R. J. Weymann, R. E. Williams, and P. Magain. A spectroscopic study of UM 673 A and B - On the size of Lyman-alpha clouds. *Astrophysical Journal*, 389:39–62, April 1992.

G. P. Smith, T. Treu, R. Ellis, I. Smail, J.-P. Kneib, and B. L. Frye. Near-Infrared Spectroscopy and Hubble Space Telescope Imaging of a Dusty Starburst Extremely Red Object. *Astrophysical Journal*, 562:635–640, December 2001.

D. N. Spergel, L. Verde, H. V. Peiris, E. Komatsu, M. R. Nolta, C. L. Bennett, M. Halpern, G. Hinshaw, N. Jarosik, A. Kogut, M. Limon, S. S. Meyer, L. Page, G. S. Tucker, J. L. Weiland, E. Wollack, and E. L. Wright. First-Year Wilkinson Microwave Anisotropy Probe (WMAP) Observations: Determination of Cosmological Parameters. *The Astrophysical Journal Supplement Series*, 148:175–194, September 2003.

C. C. Steidel. The Properties of Absorption-Line Selected High-Redshift Galaxies. In *ASSL Vol. 188: The Environment and Evolution of Galaxies*, page 263, 1993.

C. C. Steidel, M. Dickinson, D. M. Meyer, K. L. Adelberger, and K. R. Sembach. Quasar Absorbing Galaxies at $z \leq 1$. I. Deep Imaging and Spectroscopy in the Field of 3C 336. *Astrophysical Journal*, 480:568–588, May 1997.

C. C. Steidel, M. Dickinson, and S. E. Persson. Field galaxy evolution since z approximately 1 from a sample of QSO absorption-selected galaxies. *Astrophysical Journal*, 437:L75–L78, December 1994.

C. C. Steidel, J. A. Kollmeier, A. E. Shapley, C. W. Churchill, M. Dickinson, and M. Pettini. The Kinematic Connection between absorbing Gas toward QSOs and Galaxies at Intermediate Redshift. *Astrophysical Journal*, 570:526–542, May 2002.

C. C. Steidel and W. L. W. Sargent. Mg II absorption in the spectra of 103 QSOs - Implications for the evolution of gas in high-redshift galaxies. *The Astrophysical Journal Supplement Series*, 80:1–108, May 1992. (SS92).

L. J. Storrie-Lombardi and A. M. Wolfe. Surveys for $z > 3$ Damped Lyα Absorption Systems: The Evolution of Neutral Gas. *Astrophysical Journal*, 543:552–576, November 2000.

C. Stoughton, R. H. Lupton, M. Bernardi, M. R. Blanton, S. Burles, F. J. Castander, A. J. Connolly, D. J. Eisenstein, J. A. Frieman, G. S. Hennessy, R. B. Hindsley, Ž. Ivezić, S. Kent, P. Z. Kunszt, B. C. Lee, A. Meiksin, J. A. Munn, H. J. Newberg, R. C. Nichol, T. Nicinski, J. R. Pier, G. T. Richards, M. W. Richmond, D. J. Schlegel, J. A. Smith, M. A. Strauss, M. SubbaRao, A. S. Szalay, A. R. Thakar, D. L. Tucker, D. E. Vanden Berk, B. Yanny, J. K. Adelman, J. E. Anderson, S. F. Anderson, J. Annis, N. A. Bahcall, J. A. Bakken, M. Bartelmann, S. Bastian, A. Bauer, E. Berman, H. Böhringer, W. N. Boroski, S. Bracker, C. Briegel, J. W. Briggs, J. Brinkmann, R. Brunner, L. Carey, M. A. Carr, B. Chen, D. Christian, P. L. Colestock, J. H. Crocker, I. Csabai, P. C. Czarapata, J. Dalcanton, A. F. Davidsen, J. E. Davis, W. Dehnen, S. Dodelson, M. Doi, T. Dombeck, M. Donahue, N. Ellman, B. R. Elms, M. L. Evans, L. Eyer, X. Fan, G. R. Federwitz, S. Friedman, M. Fukugita, R. Gal, B. Gillespie, K. Glazebrook, J. Gray, E. K. Grebel, B. Greenawalt, G. Greene, J. E. Gunn, E. de Haas, Z. Haiman, M. Haldeman, P. B. Hall, M. Hamabe, B. Hansen, F. H. Harris, H. Harris, M. Harvanek, S. L. Hawley, J. J. E. Hayes, T. M. Heckman, A. Helmi, A. Henden, C. J. Hogan, D. W. Hogg, D. J. Holmgren, J. Holtzman, C. Huang, C. Hull, S. Ichikawa, T. Ichikawa, D. E. Johnston, G. Kauffmann, R. S. J. Kim, T. Kimball, E. Kinney, M. Klaene, S. J. Kleinman, A. Klypin, G. R. Knapp, J. Korienek, J. Krolik, R. G. Kron, J. Krzesiński, D. Q. Lamb, R. F. Leger, S. Limmongkol, C. Lindenmeyer, D. C. Long, C. Loomis, J. Loveday, B. MacKinnon, E. J. Mannery, P. M. Mantsch, B. Margon, P. McGehee, T. A. McKay, B. McLean, K. Menou, A. Merelli, H. J. Mo, D. G. Monet, O. Nakamura, V. K. Narayanan, T. Nash, E. H. Neilsen, P. R. Newman, A. Nitta, M. Odenkirchen, N. Okada, S. Okamura, J. P. Ostriker, R. Owen, A. G. Pauls, J. Peoples, R. S. Peterson, D. Petravick, A. Pope, R. Pordes, M. Postman, A. Prosapio, T. R. Quinn, R. Rechenmacher, C. H. Rivetta, H. Rix, C. M. Rockosi, R. Rosner, K. Ruthmansdorfer, D. Sandford, D. P. Schneider, R. Scranton, M. Sekiguchi, G. Sergey, R. Sheth, K. Shimasaku, S. Smee, S. A. Snedden, A. Stebbins, C. Stubbs, I. Szapudi, P. Szkody, G. P. Szokoly, S. Tabachnik, Z. Tsvetanov, A. Uomoto, M. S. Vogeley, W. Voges, P. Waddell, R. Walterbos, S. Wang, M. Watanabe, D. H. Weinberg, R. L. White, S. D. M. White, B. Wilhite, D. Wolfe, N. Yasuda, D. G. York, I. Zehavi, and W. Zheng. Sloan Digital Sky Survey: Early Data Release. *Astronomical Journal*, 123:485–548, January 2002.

D. A. Turnshek, D. B. Nestor, S. M. Rao, and D. vanden Berk. The Cosmic Neutral-Gas Metallicity at $0.9 < z < 2.2$. *Elemental Abundances in Old Stars and Damped Lyman-α Systems, 25th meeting of the IAU, Joint Discussion 15, 22 July 2003, Sydney, Australia*, 15, 2003.

D. A. Turnshek, S. Rao, D. Nestor, W. Lane, E. Monier, J. Bergeron, and A. Smette. The $z = 0.0912$ and $z = 0.2212$ Damped Lyα Galaxies along the Sight Line toward the Quasar OI 363. *Astrophysical Journal*, 553:288–298, May 2001.

D. A. Turnshek, S. M. Rao, and D. B. Nestor. A Comparative Study of Damped Lyα Galaxies. In *ASP Conf. Ser. 254: Extragalactic Gas at Low Redshift*, pages 42–50, 2002. astro-ph/0108142.

D. Tytler. An Overview and Introduction to Quasar Absorption in Cosmology. In P. Petitjean and S. Charlot, editors, *Structure and Evolution of the Intergalactic Medium from QSO Absorption Line Systems*, pages 5–15, 1997.

D. Tytler, A. Boksenberg, W. L. W. Sargent, P. Young, and D. Kunth. High-resolution spectra of 24 low-redshift QSOs - The properties of Mg II absorption systems. *The Astrophysical Journal Supplement Series*, 64:667–702, August 1987.

A. Ulmer. Strong Clustering in the Low-Redshift Ly alpha Forest. *Astrophysical Journal*, 473:110–116, December 1996.

S. J. Warren, P. Møller, S. M. Fall, and P. Jakobsen. NICMOS imaging search for high-redshift damped Lyα galaxies. *Monthly Notices of the Royal Astronomical Society*, 326: 759–773, September 2001.

M. L. Weil, V. R. Eke, and G. Efstathiou. The formation of disc galaxies. *Monthly Notices of the Royal Astronomical Society*, 300:773–789, November 1998.

R. J. Weymann, R. F. Carswell, and M. G. Smith. Absorption lines in the spectra of quasistellar objects. *Annual Review of Astronomy and Astrophysics*, 19:41–76, 1981.

R. J. Weymann, B. T. Jannuzi, L. Lu, J. N. Bahcall, J. Bergeron, A. Boksenberg, G. F. Hartig, S. Kirhakos, W. L. W. Sargent, B. D. Savage, D. P. Schneider, D. A. Turnshek, and A. M. Wolfe. The Hubble Space Telescope Quasar Absorption Line Key Project. XIV. The Evolution of Lyα Absorption Lines in the Redshift Interval $z = 0 - 1.5$. *Astrophysical Journal*, 506:1–18, October 1998.

R. E. Williams, B. Blacker, M. Dickinson, W. V. D. Dixon, H. C. Ferguson, A. S. Fruchter, M. Giavalisco, R. L. Gilliland, I. Heyer, R. Katsanis, Z. Levay, R. A. Lucas, D. B. McElroy, L. Petro, M. Postman, H. Adorf, and R. Hook. The Hubble Deep Field: Observations, Data Reduction, and Galaxy Photometry. *Astronomical Journal*, 112:1335–1389, October 1996.

A. M. Wolfe, K. M. Lanzetta, C. B. Foltz, and F. H. Chaffee. The Large Bright QSO Survey for Damped Lyα Absorption Systems. *Astrophysical Journal*, 454:698–725, December 1995.

A. M. Wolfe and J. X. Prochaska. Ionized Gas in Damped Lyα Protogalaxies. II. Comparison between Models and the Kinematic Data. *Astrophysical Journal*, 545:603–624, December 2000.

A. M. Wolfe, D. A. Turnshek, H. E. Smith, and R. D. Cohen. Damped Lyman-alpha absorption by disk galaxies with large redshifts. I - The Lick survey. *The Astrophysical Journal Supplement Series*, 61:249–304, June 1986.

B. Yanny, D. G. York, and J. S. Gallagher. The extent of nebular emission associated with the $z = 0.525$ absorber near AO 0235 + 164. *Astrophysical Journal*, 338:735–742, March 1989.

D. G. York, J. Adelman, J. E. Anderson, S. F. Anderson, J. Annis, N. A. Bahcall, J. A. Bakken, R. Barkhouser, S. Bastian, E. Berman, W. N. Boroski, S. Bracker, C. Briegel, J. W. Briggs, J. Brinkmann, R. Brunner, S. Burles, L. Carey, M. A. Carr, F. J. Castander, B. Chen, P. L. Colestock, A. J. Connolly, J. H. Crocker, I. Csabai, P. C. Czarapata, J. E. Davis, M. Doi, T. Dombeck, D. Eisenstein, N. Ellman, B. R. Elms, M. L. Evans, X. Fan, G. R. Federwitz, L. Fiscelli, S. Friedman, J. A. Frieman, M. Fukugita, B. Gillespie, J. E. Gunn, V. K. Gurbani, E. de Haas, M. Haldeman, F. H. Harris, J. Hayes, T. M. Heckman, G. S. Hennessy, R. B. Hindsley, S. Holm, D. J. Holmgren, C. Huang, C. Hull, D. Husby, S. Ichikawa, T. Ichikawa, Ž. Ivezić, S. Kent, R. S. J. Kim, E. Kinney, M. Klaene, A. N. Kleinman, S. Kleinman, G. R. Knapp, J. Korienek, R. G. Kron, P. Z. Kunszt, D. Q. Lamb, B. Lee, R. F. Leger, S. Limmongkol, C. Lindenmeyer, D. C. Long, C. Loomis, J. Loveday, R. Lucinio, R. H. Lupton, B. MacKinnon, E. J. Mannery, P. M. Mantsch, B. Margon, P. McGehee, T. A. McKay, A. Meiksin, A. Merelli, D. G. Monet, J. A. Munn, V. K. Narayanan, T. Nash, E. Neilsen, R. Neswold, H. J. Newberg, R. C. Nichol, T. Nicinski, M. Nonino, N. Okada, S. Okamura, J. P. Ostriker, R. Owen, A. G. Pauls, J. Peoples, R. L. Peterson, D. Petravick, J. R. Pier, A. Pope, R. Pordes, A. Prosapio, R. Rechenmacher, T. R. Quinn, G. T. Richards, M. W. Richmond, C. H. Rivetta, C. M. Rockosi, K. Ruthmansdorfer, D. Sandford, D. J. Schlegel, D. P. Schneider, M. Sekiguchi, G. Sergey, K. Shimasaku, W. A. Siegmund, S. Smee, J. A. Smith, S. Snedden, R. Stone, C. Stoughton, M. A. Strauss, C. Stubbs, M. SubbaRao, A. S. Szalay, I. Szapudi, G. P. Szokoly, A. R. Thakar, C. Tremonti, D. L. Tucker, A. Uomoto, D. Vanden Berk, M. S. Vogeley, P. Waddell, S. Wang, M. Watanabe, D. H. Weinberg, B. Yanny, and N. Yasuda. The Sloan Digital Sky Survey: Technical Summary. *Astronomical Journal*, 120:1579–1587, September 2000.

M. Zwaan, F. H. Briggs, and M. Verheijen. Reconciling Damped Ly-α Statistics and 21cm Studies at $z = 0$. In *ASP Conf. Ser. 254: Extragalactic Gas at Low Redshift*, pages 169–178, 2002. astro-ph/0108498.

M. A. Zwaan, L. Staveley-Smith, B. S. Koribalski, P. A. Henning, V. A. Kilborn, S. D. Ryder, D. G. Barnes, R. Bhathal, P. J. Boyce, W. J. G. de Blok, M. J. Disney, M. J. Drinkwater, R. D. Ekers, K. C. Freeman, B. K. Gibson, A. J. Green, R. F. Haynes, H. Jerjen, S. Juraszek, M. J. Kesteven, P. M. Knezek, R. C. Kraan-Korteweg, S. Mader, M. Marquarding, M. Meyer, R. F. Minchin, J. R. Mould, J. O'Brien, T. Oosterloo, R. M. Price, M. E. Putman, E. Ryan-Weber, E. M. Sadler, A. Schröder, I. M. Stewart, F. Stootman, B. Warren, M. Waugh, R. L. Webster, and A. E. Wright. The 1000 Brightest HIPASS Galaxies: The H I Mass Function and Ω_{HI}. *Astronomical Journal*, 125:2842–2858, June 2003.